Aus dem Institut für Laboratoriumsmedizin der
Ludwig-Maximilians-Universität München

Direktor: Univ.-Prof. Dr. med. Daniel Teupser

Identification of novel atherosclerosis modifiers in mice

Dissertation

zum Erwerb des Doktorgrades der Naturwissenschaften
an der Medizinischen Fakultät
der Ludwig-Maximilians-Universität München

vorgelegt von

Alexandros Nicolaou

aus

Paphos (Zypern)

2018

Mit Genehmigung der Medizinischen Fakultät
der Ludwig-Maximilians-Universität München

Betreuerin:	Prof. Dr. med. Dr. rer. nat. Lesca Holdt
Zweitgutachter:	Prof. Dr. rer. nat. Jürgen Bernhagen
Dekan:	Prof. Dr. med. dent. Reinhard Hickel
Tag der mündlichen Prüfung:	05.09.2019

Meinen Eltern

Abstract

Atherosclerosis is a chronic inflammatory condition of the large and medium-sized vasculature. It is a complex, progressive disease determined by genetic as well as environmental factors. This PhD thesis aims to make a contribution in identifying new determinants of atherosclerosis by investigating two recently reported, yet still uncharacterized atherosclerosis susceptibility loci on mouse chromosomes 3 and 12, which were identified in an intercross of atherosclerosis-susceptible C57BL/6 (B6) and atherosclerosis-resistant FVB mice on the LDL-receptor deficient background (*Ldlr*$^{-/-}$).

We genetically dissected the locus on chromosome 3 by quantitative trait locus (QTL) fine-mapping and, subsequently, by creating congenic mice that carried the B6 risk genetic interval in an otherwise FVB background. To identify candidate effector genes at the locus, we performed differential expression analysis in congenics using mRNA microarrays, and expression QTL (eQTL) mapping in 227 F2 mice as complementing strategy. We revealed two overlapping, yet independent subloci for atherosclerosis susceptibility, one associated with increased expression of *vascular cell adhesion molecule 1* (*Vcam1*), a well-known atherosclerosis modifier, and the other associating with down-regulation of the secreted phospholipase *Pla2g12a* in atherosclerosis-susceptible B6.*Ldlr*$^{-/-}$ mice. *Pla2g12a* was highly expressed in endothelial cells and PLA2G12A protein prevented binding of cultured blood monocytes to these cells. Our data indicate that PLA2G12A is a novel atherosclerosis modifier that protects from atherosclerosis, by reducing the adhesiveness of vascular cells entering atherosclerotic lesions.

In the same QTL mapping effort, the metalloprotease *a disintegrin and metalloprotease 17* (*Adam17*) has emerged as candidate effector of the second atherosclerosis risk locus on chromosome 12. ADAM17 is well-known as protease that processes dozens of membrane-resident factors, including signaling molecules. To study the effect of *Adam17* on atherosclerosis, we crossed *Adam17* hypomorphic mutant mice into an *Ldlr*$^{-/-}$ background. We found that ADAM17 exhibited an atheroprotective effect *in vivo*, which was unexpected given its presumed pro-inflammatory role in other diseases. Using proteomic screening of candidate cleavage products of a range of established ADAM17 substrates, we found that shedding of Tumor necrosis factor receptor 2

(TNFR2) and of Tumor necrosis factor-α (TNFα) from the cell membrane was impaired in *Adam17*-deficient vascular cells. Impaired cleavage increased membrane-resident TNFR2 and TNFα, which remained, however, signaling-active. Consequently, TNFR2 pathway activation augmented adhesion and proliferation and impaired apoptosis of macrophages and vascular smooth muscle cells. Together, our data indicate that normal levels of ADAM17 are required to dampen TNFR2 signaling on vascular membranes in order to protect from atherosclerosis.

Finally, in a third study, we also report that ADAM17 exerted yet another role in vascular biology. We revealed arterial dilation and changes in elastin fibers in brachiocephalic arteries of *Adam17* mutant mice. This phenotype was reminiscent of early-phase arterial aneurysm onset. Our data indicate a function of ADAM17 in maintaining a proper elastin network in the extracellular matrix (ECM) of arteries to protect the integrity of the arterial wall.

Summarizing, we have identified and characterized one novel atherosclerosis modifier, PLA2G12A, and have revealed that ADAM17 had a previously unrecognized protective role in vascular disease, which was due to TNFR2 signaling and ECM regulation.

Abstract-German

Die Atherosklerose ist eine chronische, entzündliche Erkrankung der großen und mittleren Arterien, die sowohl durch genetische als auch durch Umweltfaktoren bestimmt wird. Die vorliegende Doktorarbeit beschäftigt sich mit der Identifizierung und funktionellen Charakterisierung neuer genetischer Determinanten der Atherosklerose an zwei Genorten der Atherosklerose auf den Chromosomen 3 und 12 der Maus. Diese Genorte wurden in Vorabeiten der Arbeitsgruppe mit Hilfe eines hypothesenfreien Ansatzes in einer F2-Kreuzung atheroskleroseempfindlicher C57BL/6 (B6)- und atheroskleroseresistenter FVB-Mäuse auf dem LDL-Rezeptor defizienten Hintergrund (*Ldlr*$^{-/-}$) identifiziert. Welche genetischen Varianten an diesen zwei Loci dem gesteigerten Atheroskleroserisiko zugrundelagen war bislang unbekannt.

Der Chromosom 3 Genort wurde zunächst mit Hilfe von quantitative trait locus (QTL) Analysen feinkartiert und kongene Mäuse, die ein definiertes genomisches Intervall des B6-Risiko Lokus auf einem ansonsten FVB.*Ldlr*$^{-/-}$ Hintergrund trugen, hergestellt. Um Kandidaten-Effektorgene am Locus zu identifizieren, wurden differentielle Genexpressionsanalysen in kongenen und FVB Mäusen unter Verwendung von mRNA-Mikroarrays und eine Expressions-QTL (eQTL)-Kartierung als ergänzende Strategie in 227 F2 Mäusen der Kreuzung durchgeführt. Auf diese Weise wurden zwei überlappende, jedoch unabhängige Subloci für die Atheroskleroseempfindlichkeit gefunden. Ein Lokus war assoziiert mit einer erhöhten Expression des *vaskulären Zelladhäsionsmoleküls* 1 (*Vcam1*), einem bekannten Atherosklerose-Modifikator. Der zweite Lokus war hingegen mit einer Herunterregulation der sezernierten Phospholipase *Pla2g12a* in atheroskleroseempfindlichen B6.*Ldlr*$^{-/-}$ *Mäusen* assoziiert. *Pla2g12a* war in Endothelzellen stark exprimiert und PLA2G12A Protein verhinderte die Bindung von kultivierten Blutmonozyten an vaskuläre Endothelzellen. Unsere Daten zeigen, dass PLA2G12A ein neuer Atherosklerose-Modifikator ist, der vor Atherosklerose schützt, indem er die Adhäsion von Gefäßzellen, die in atherosklerotische Läsionen einwandern, verringert.

In der gleichen QTL-Kartierung wurde *a disintegrin and metalloprotease 17* (*Adam17)* als Effektorgen des Atherosklerose Risikogenorts auf Chromosom 12 etabliert. ADAM17 ist eine Metalloprotease, die dutzende membranständige Faktoren, einschließlich Signalmoleküle, spaltet und somit freisetzt. Um den Effekt von *Adam17* auf die Atherosklerose zu untersuchen, kreuzten wir *Adam17* hypomorphe Mäuse auf den *Ldlr*$^{-/-}$ Hintergrund, und konnten zeigen, dass ADAM17 *in vivo* eine atheroprotektive Wirkung besitzt. Dies war unerwartet, da ADAM17 bislang hauptsächlich mit der Freisetzung von inflammatorischen Molekülen in Verbindung gebracht worden ist. Durch proteomisches Screening etablierter ADAM17-Substrate konnten wir zeigen, dass die Freisetzung von Tumor necrosis factor receptor 2 (TNFR2) und Tumor necrosis factor-α (TNFα) von *Adam17*-defizienten Gefäßzellen beeinträchtigt war und konsekutiv die Mengen von membranständigem TNFR2 und TNFα erhöht waren. Da TNFR2 und TNFα an der Membran weiterhin aktiv als Signaltransduktionsmoleküle blieben, kam es zur Überaktivierung des TNFR2-Signalwegs in *Adam17*-defizienten Zellen, was schlussendlich zu einer gesteigerten Adhäsion und Proliferation führte und die Apoptose von Makrophagen und vaskulären glatten Muskelzellen beeinträchtigte. Zusammenfassend zeigen unsere Daten, dass ADAM17 durch Kontrolle des TNFR2-Signalwegs vor Atherosklerose schützt.

Schließlich konnten wir in einer dritten Studie zeigen, dass ADAM17 eine weitere Rolle in der vaskulären Biologie spielt und *Adam17*-Defizienz zu arterieller Dilatation und Veränderungen von Elastinfasern im hypomorphen Mausmodell führt. Dieser Phänotyp erinnert an die Frühphase der Ausbildung eines arteriellen Aneurysmas. Weitere Analysen zeigten, dass ADAM17 für die Aufrechterhaltung des Elastin-Netzwerks in der extrazellulären Matrix (ECM) von Arterien und somit für den Schutz der Integrität der Arterienwand wichtig zu sein scheint.

Zusammenfassend haben wir PLA2G12A als neuen Regulator der Atherosklerose identifiziert und charakterisiert und konnten zeigen, dass die Metalloprotease ADAM17 eine bisher unbekannte protektive Rolle bei Gefäßerkrankungen besitzt, die auf die Kontrolle des TNFR2-Signalwegs und Regulation der extrazellulären Matrix zurückzuführen ist.

Table of Contents

List of Abbreviations

ABCA1	ATP Binding Cassette Transporter 1
Abcd3	*ATP-binding cassette sub-family D member 3*
ABCG5	ATP-binding cassette sub-family G member 5
ABCG8	ATP-binding cassette sub-family G member 8
Acadm	*Medium-chain specific acyl-CoA dehydrogenase*
Adam	A Disintegrin and Metalloprotease
Adam17	A Disintegrin and Metalloprotease 17
ADAM-TS	ADAMs with thrombospondin domains
Adfp	*Adipose Differentiation-Related Protein*
Adh4	*Alcohol dehydrogenase 4*
Adh7	*Alcohol dehydrogenase class 4 mu/sigma chain*
Agxt2l1	*Alanine-glyoxylate aminotransferase 2-like 1*
ALOX5AP	Arachidonate 5-lipoxygenase-activating protein
ALT	Alanine transaminase
ANRIL	Antisense non coding RNA in the INK4 locus
AoR	Aortic root
APOB	Apolipoporotein B
ApoE	Apolipoporotein E
ApoE$^{-/-}$	Apolipoporotein E deficiency
ARH	Autosomal recessive hypercholesterolemia
AST	Aspartate transaminase
ATP	Adenosine triphosphate
BCA	Brachiocephalic artery
BMDM	Bone marrow-derived macrophages
BSA	Bovine serum albumin
Ccbl2	*Kynurenine-oxoglutarate transaminase 3*
Ccl5	*Chemokine (C-C motif) ligand 5*
CD30	Cluster of Differentiation 30; TNFRSF8
CD36	Cluster of Differentiation 36
CD68	Cluster of Differentiation 68
CDKN2A	Cyclin-dependent kinase Inhibitor 2A
CDKN2B	Cyclin-dependent kinase Inhibitor 2B
cDNA	Complementary DNA
CHD	Coronary heart disease
ChE	Cholinesterase
Chol	Cholesterol
Chr	Chromosome
CHX	Cycloheximide
Coro1a	*Coronin 1A*
CSF	Colony-stimulating factor
Cth	*Cystathionine gamma-lyase*
CVA	Cerebrovascular disease
CVD	Cardiovascular disease
CX3CL1	Fractalkine
Cxcl16	*Chemokine (C-X-C motif) ligand 16*
CYP7A1	Cholesterol 7 alpha-hydroxylase/ cytochrome P450 7A1
DEPC	Diethylpyrocarbonate
DMEM	Dulbecco's Modified Eagle's Medium
DMSO	Dimethyl sulfoxide
DNA	Deoxyribonucleic acid
E.coli	*Escherichia coli*
EC	Endothelial cells
ECM	Extracellular matrix
EDTA	Ethylenediaminetetraacetic acid
EGF	Epidermal growth factor
Elovl6	*Fatty acid elongase 6*
Emilin2	*Elastin microfibril interfacer 2*
eQTL	Expression QTL
EtOH	Ethanol
Evl	*Enah/Vasp-Like*
Fbln2	Fibulin-2
Fbxl22	F-Box And Leucine Rich Repeat Protein 22
FC	Fold Change
FCS	Fetal Calf Serum
Fdps	*Farnesyl pyrophosphate synthase*
FH	Familial hypercholesterolemia
FRET	Förster Resonance Energy Transfer
GAPDH	Glyceraldehyde-3-phosphate-Dehydrogenase
Gbp3	*Guanylate-binding protein 4*
GLDH	Glutamate dehydrogenase
Gm129	*Hypothetical protein LOC229599*
GM-CSF	Granulocyte-macrophage colony-stimulating factor

gp130	Glycoprotein 130
GWAS	Genome-Wide Association Studies
h	Hours
HDL	High-Density Lipoprotein
HGP	Human Genome Project
HRP	Horseradish Peroxidase
IBD	Identity by Descent analysis
ICAM1	Intercellular Cell Adhesion Molecule-1
IFNγ	Interferon-γ
IL-1	Interleukin-1
IL-6	Interleukin-6
IL-10	Interleukin-10
IL-1β	Interleukin-1 beta
IL-1R2	Interleukin-1 Receptor 2
IL-6R	Interleukin-6 Receptor
IPA	Ingenuity Pathway Analysis
IPTG	Isopropyl β-D-1-Thiogalactopyranoside
JAM-A	Junctional Adhesion Molecule-A
KC	Keratinocyte Chemoattractant
LAS	Leica Application Suite software
LDL	Low-Density Lipoprotein
LDL-C	Low-Density Lipoprotein cholesterol
Ldlr	Low-Density Lipoprotein receptor
Ldlr$^{-/-}$	Low-Density Lipoprotein Receptor Deficiency
LDLRAP1	*Low density lipoprotein receptor adaptor protein 1*
LDLR-KO	LDL receptor knockout
LOD	Logarithm of Odds
Lpxn	*Leupaxin*
LRP6	LDL receptor-related protein 6
LTA4H	Leukotriene A4 hydrolase
MCEC	Mouse cardiac endothelial cells
MCP-1	Monocyte Chemoattractant Protein-1
M-CSF	Macrophage colony-stimulating factor
MEF2A	Myocyte enhancer factor-2
MI	Myocardial Infarction
Mia1	*Melanoma Inhibitory Activity 1*
MIP-1α	Macrophage Inflammatory Protein 1α
MIP-1β	Macrophage Inflammatory Protein 1β
MMP	Matrix Metalloproteinases
Mmp12	*Matrix metalloproteinase-12*
Mmp3	*Matrix metalloproteinase-3*
MT-MMP	Membrane-type Matrix Metalloproteases
Myo1f	*Myosin-1f*
MΦ	Macrophages
NaCl	Sodium chloride
NIH	National Institutes of Health
NO	Nitric Oxide
OR	Odds Ratio
oxLDL	oxidized LDL
PBS	Phosphate Buffered Saline
PCR	Polymerase Chain Reaction
PCSK9	Proprotein Convertase Subtilisin/Kexin type 9
PDGF	Platelet-derived Growth Factor
Pecam1	*Platelet Endothelial Cell Adhesion Molecule-1*
Pen/Strep	Penicillin-Streptomycin
Pip5k1b	*Phosphatidylinositol-4-Phosphate 5-Kinase Type 1 Beta*
Pklr	*Pyruvate Kinase, Liver and RBC*
Pla2g12a	*Group XIIA Secretory Phospholipase A2*
PMA	Phorbol 12-myristate 13-acetate
PMSF	Phenylmethylsulfonylfluorid
Pmvk	*Phosphomevalonate kinase*
PVD	Peripheral Vascular Disease
PVDF	Polyvinylidene Fluoride
qRT-PCR	quantitative Real-Time-PCR
QTL	Quantitative Trait Locus
RANTES	Regulated on activation, normal T cell expressed and secreted
RFLPs	restriction fragment length polymorphisms
Rgs1	*Regulator of G Protein Signaling*
RNA	Ribonucleic acid
rpm	Revolutions per minute
RT	reverse transcription
s	soluble
SCR	Scrambled control
Sdc3	*Syndecan 3*
SDS	Sodium Dodecyl Sulfate
Selenbp2	*Selenium binding protein 2*
SEM	Standard Error of the Mean
SIFT	sorts intolerant from tolerant amino acid substitutions
siRNA	Small interfering RNA
Sln	*Sarcolipin*
SNPs	Single Nucleotide Polymorphisms
SR-A	Scavenger-receptor A
SR-B1	Scavenger-receptor B1
SSRs	Simple Sequence Repeats
SVMPs	Snake Venom Metalloproteinases
TG	Triglycerides
Them4	*Thioesterase superfamily member 4*
Tmod4	*Tropomodulin-4*
TNFR1	Tumor necrosis factor receptor 1
Tnfr1	*Tumor necrosis factor receptor 1*
TNFR2	Tumor necrosis factor receptor 2
Tnfr2	*Tumor necrosis factor receptor 2*
TNFα	Tumor necrosis factor-α
Tris	Tris(hydroxymethyl)aminomethane
Tuft1	*Tuftelin 1*
TUNEL	TdT-mediated dUTP Nick-End Labeling
Ucp1	*Uncoupling protein*
Unc5c	*Netrin receptor UNC5C*
U	Units
VCAM	Vascular cell adhesion molecule
Vcam1	*Vascular cell adhesion molecule 1*
VEGFR2	Vascular endothelial growth factor receptor 2
VLDL	Very low density lipoprotein
VSMCs	Vascular smooth muscle cells
vWF	von Willebrand Factor
X-Gal	5-bromo-4-chloro-3-indolyl-β-D-galactopyranoside
α-SMA	Alpha-smooth muscle actin

1 Introduction

1.1 Atherosclerosis and cardiovascular disease

Atherosclerosis is a chronic inflammatory condition of the large and medium-sized vasculature and the main cause of cardiovascular disease (CVD). The three major manifestations of CVD are peripheral vascular disease (PVD), cerebrovascular disease (CVA) and coronary heart disease (CHD). Atherosclerosis is a complex and progressive disease that is affected by genetic (polygenic disease) as well as environmental factors [3]. It is a disease that occurs over a lifetime and is influenced by numerous factors, including excessive dietary fat, smoking, diabetes, sedentary lifestyle and genetic factors [4]. Over the time, locally confined sites in the vascular wall develop fibrous, fatty lesions (plaques) characterized by inflammation, and abnormal cell proliferation and apoptosis. Plaque progression may lead to rupture and subsequent thrombus formation, which is the most important cause of acute cardiovascular events such as myocardial infarction and stroke [5].

CVD is the leading cause of morbidity and mortality in Germany as well as worldwide [6]. Worldwide, it was estimated that there were 422.7 million cases of CVD and 17.92 million CVD deaths, accounting for one-third of all deaths, in the year 2015 [7]. Of these deaths, an estimated 7.4 million were due to coronary heart disease and 6.7 million were due to stroke [8]. Each year, CVD causes over 4 million deaths in Europe and 1.9 million deaths in the European Union (EU)[9]. Thus, CVD is responsible for approximately 47 % of all deaths in Europe and 40 % in the EU. About 60 % of all CVD deaths occur in people over 75 years, 1.4 millions under the age of 75 and about 700,000 under the age of 65 years [10]. Overall, CVD is estimated to cost the European Union economy almost € 210 billion a year [11]. In Germany, CVD are with 38.9 % or 338,056 deaths, the leading cause of mortality each year. Of these, 148,538 (43.9 %) account for men and 189,518 (56.1 %) for women. Furthermore, myocardial infarction is responsible for the death of 50,104 people or 5.8 % of all deaths [12].

1.2 Pathophysiology of atherosclerosis

Atherosclerosis is a focal disease process that occurs predominantly at sites of disturbed laminar flow, notably, arterial branch points and bifurcations of large arteries [13]. Although much progress has been achieved over the last years, the pathogenesis of the disease is not fully understood. Various models have been proposed for the development of atherosclerosis, of which the so-called “Response to Injury” hypothesis is probably the best accepted today. This theory states that atherosclerosis occurs as a response to some form of activation of arterial endothelial cells. This can be triggered by any number of insults, either alone or in combination [14].

Arterial walls are composed of a highly ordered structure of cells and extracellular matrix (ECM) and are thicker than that of veins in order to withstand pulsatile flow and higher blood pressures. The normal muscular artery has a trilaminar structure: the tunica intima, the inner coat with a monolayer of endothelial cells and resident smooth muscle cells; the tunica media, the middle coat containing vascular smooth muscle cells (VSMCs). The media is the thickest layer and provides structural support, vasoreactivity and elasticity. The outer coat, the tunica adventitia, contains mast cells, fibroblasts, nerve endings and microvessels (Figure 1) [15].

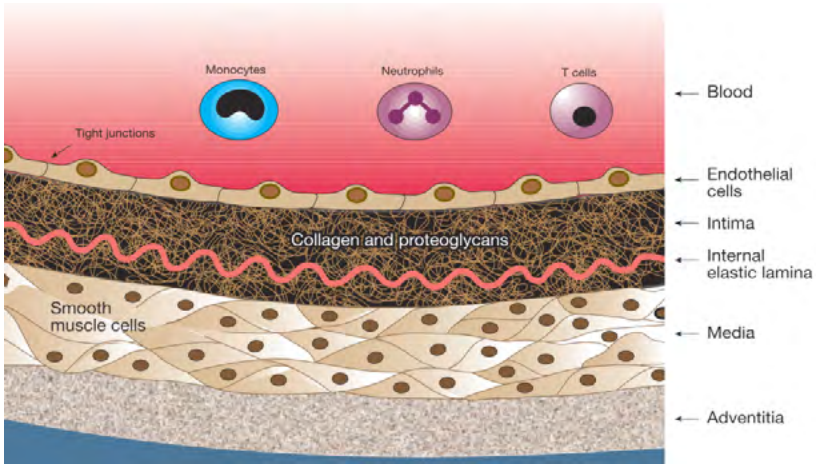

FIGURE 1: Layers of the arterial wall [1].

The ECM makes up to 60 % of the intimal volume and consists of elastic lamellae, smooth muscle cells and three major protein components, including proteoglycans, collagen and multi-adhesive matrix proteins [16].

Atherosclerosis starts with an initial damage of the vascular endothelium, which evokes endothelial dysfunction and causes a chronic inflammatory response. Intimal damage due to injury, high blood pressure, smoking, in particular of the endothelium, leads to an increased permeability and influx of lipoproteins from the blood, resulting in an increased accumulation of low-density lipoproteins (LDL) in the intima [17]. Several animal experiments, epidemiological and clinical studies established that high concentrations of cholesterol in the circulation promote atherosclerotic cardiovascular disease [18, 19]. Cholesterol is transported in the blood in lipoprotein particles, where low-density lipoproteins (LDL) particles contain esterified cholesterol and triglycerides surrounded by phospholipids, cholesterol and apolipoprotein B100 (ApoB100). Through the subendothelial retention, LDL particles are captured in the intima, the innermost layer of the artery, where they are exposed to oxidative modifications by reactive oxygen species or

enzymes like myeloperoxidase or lipooxygenases (12/15-lipoxygenase [20]) released from inflammatory cells. Otherwise, antioxidants, as α-tocopherol (Vitamin E), γ-tocopherol, α- and β-carotene and lycopene support to prevent the oxidation of LDL particles in the circulation [21, 22].

One of the first changes to which the endothelium is subjected is a reaction to the hemodynamic changes in the lumen. As arterial segments are under high shear stress, typical for normal laminar blood flow, they show a high production of nitric oxide (NO). NO acts by two mechanisms antiarteriosclerotic: on the one hand, it acts both vasodilatory and antithrombotic [23], on the other hand NO reduces the adhesiveness of the endothelium by inhibiting the expression of the vascular cell adhesion molecule (VCAM) in leukocytes. While oxidized lipoproteins inhibit the nitric oxide (NO) production in the endothelial cells, endothelial cells themselves are stimulated by the oxidized lipoproteins to attract monocytes from the blood. In the arterial segments, where the shear stress is diminished, e.g. at the crotch of arterial branches, the NO production is restricted by the endothelial cells. These segments are particularly susceptible to the development of arteriosclerotic lesions [24, 25]. Constituents of oxidized LDL can stimulate the expression of chemoattractant molecules, like monocyte chemoattractant protein-1 (MCP-1), to attract the attached leukocyte to migrate through the endothelial monolayer into the arterial intima [26]. Moreover, oxidized phospholipids stimulate the expression of adhesion molecules on the surface of vascular endothelial cells to mediate leukocyte adherence to the luminal surface of these cells. Recruitment of the leukocytes is primarily augmented by the adhesion molecules vascular cell adhesion molecule-1 (VCAM1), intercellular cell adhesion molecule-1 (ICAM1) and P-selectin on the surface of the arterial endothelial cells [27]. Once leukocytes passed through the endothelial monolayer, macrophage colony-stimulating factor (M-CSF) contributes to the differentiation of blood monocytes into macrophage foam cells [28]. These macrophage foam cells produce cytokines such Tumor Necrosis Factor-α (TNF-α) and Interleukin-1 (IL-1) and induce the expression of adhesion molecules (VCAM-1, ICAM-1) on the endothelial surface to attract more monocytes and T-lymphocytes [29].

Macrophage foam cell formation is characteristic for atherosclerosis. Under normal conditions macrophages are unable to take up circulating LDL because of down regulation of the LDL-receptor gene. Monocytes, once resident in the intima and differentiated into macrophages, exhibit enhanced expression of scavenger receptors [30, 31]. Scavenger receptors such scavenger-receptor A (SR-A), scavenger-receptor B1 (SR-B1) and CD36 bind with high affinity and internalize the oxidized LDL (oxLDL) or acetyl-LDL. Since scavenger receptors are not subjected to feedback inhibition in contrast to the LDLR, they lead to uncontrolled endocytotic uptake of oxLDL in macrophages and ultimately to the formation of foam cells. These lipid-laden macrophages (foam cells), characterize the early atherosclerotic lesion. Macrophages engulfing modified lipoproteins produce cytokines and growth factors, which in turn cause further recruitment of the macrophages and vascular smooth muscle cells (VSMC) from the tunica media through the lamina elastica to the intima and consequently to the lesions [27].

The recruitment of macrophages and T cells into the atherosclerotic lesions is guided by endothelial leukocyte adhesion molecules and chemoattractants. The latter include chemokines, which belong to a large group of structurally related and secretable chemotactic cytokines [32]. Chemokines can be expressed in different vascular cells like endothelial cells but also inflammatory cells. The recruitment of leukocytes involves a sequence of rolling, firm adhesion, lateral migration and transendothelial diapedesis, controlled by chemokines [33]. Monocytes that are located in the intima are stimulated by colony-stimulating factor (CSF) produced by activated

endothelial cells to differentiate into macrophages. In the intima, macrophages upregulate their scavenger receptors that can then take up oxLDL. The subsequent cholesterol accumulation turns these macrophages into foam cells that are characteristic of the atherosclerotic lesion.

Smooth muscle cells located in the media change their phenotype after migration. This phenotypic transformation can be initiated by oxidized lipoproteins, cellular toxins, and endothelial dysfunction. SMCs take on properties that can contribute to the inflammation process. While SMCs normally have a contractile function, SMCs found in arteriosclerotic lesions have less myofilaments, but more synthetic cell organelles such as Golgi apparatus and rough endoplasmic reticulum. Smooth muscle cells in the intimal lesion are therefore able to react to growth factors and have a synthesis function [34, 35].

Atherosclerotic plaques maturate in the arterial intima over a period of years, even decades. Underneath the formed fibrous cap, many dead or dying macrophages, cellular debris and extracellular accumulations build a so-called lipid core. Arterial smooth muscle cells (SMCs) located in the media also respond to inflammation- associated mediators. Chemoattractants like platelet-derived growth factor (PDGF) produced by activated leukocytes or SMCs themselves when stimulated can enter the intimal layer [36]. An important step in the migration and proliferation of SMC is the secretion of matrix metalloproteinases (MMP), as MMP-1, MMP-8 and MMP-13, which are responsible for the degradation of the internal elastic lamina [37]. Smooth muscle cells in the intima express extracellular matrix (ECM) molecules that contribute to lesion fibrosis [38, 39]. Fibrosis is the development of a connective tissue layer predominantly collagen and the proliferation of muscle cells above the lipid core. Arterial smooth muscle cells produce interstitial collagens like type I and III collagen at the beginning and, subsequently, type IV and V, elastic fibers, and proteoglycans leading to plaque stabilization and eventually to fibrosis. Fibrous (stable) plaques have in comparison to unstable plaque relatively small nuclei and relatively thick capsules, which are rich in connective tissue and muscle cells [40]. Underneath the fibrous cap, the formed lipid core contains many macrophages, cellular debris including apoptotic bodies and extracellular lipid accumulations. Proinflammatory cytokines released from activated white cells, endothelial cells and smooth muscle cells can potentiate cells death by apoptosis in the advancing lesion. Furthermore, macrophages in the lesions secrete proteinases that degrade the macromolecules of the extracellular matrix [26]. Complicated lesions arise when a fibrous cap of an unstable plaque ruptures, and the contents with lipids and macrophages come in contact with blood. The precipitation of platelets and coagulation factors forms a thrombus.

In our study we focused on cellular mechanisms associated with the onset of atherosclerosis and not with the late thrombotic phase. This means that we focused on phenotypes including the adhesion of mononuclear blood cells to endothelial cells, proliferation of vascular SMCs and monocytes, the propensity to apoptosis of these cells types and the remodeling of ECM by these cells. Molecularly, we applied assays to measure inflammation-regulating cytokines, adhesion factors and cytoskeletal features.

1.3 Genetic factors of atherosclerosis in humans

1.3.1 Heritability of atherosclerosis

Several studies demonstrated that a family history of early coronary artery disease (CAD) is a significant risk factor for the development of this disease [41]. The heritability of various risk factors of atherosclerosis is in the meanwhile well established by several epidemiological prospective studies [42, 43] and can be predicted with increasingly improved validity [44-46]. Heritability is used to estimate how much variation in the phenotypic trait in a population is due to genetic variation among individuals in that population. In statistical genetics, the heritability is determined by comparing the frequency of a trait in interrelated individuals as opposed to not related persons. For example, in human medicine comparisons between monozygotic twins and dizygotic twins are conducted for evaluating the importance of genetic variation in susceptibility to disease. Using such models the influence and significance of environmental effects and the contribution of specific polymorphisms to the total genetic variance can be studied [47].

The known risk factors of atherosclerosis, which have an inherited component, are mainly factors of cholesterol metabolism. For example, the heritability for elevated LDL-cholesterol is 88 % and decreased HDL-cholesterol 66 % [48]. A heritability of 41-78 % was found for other classical risk factors, such as hypertension [49] and 72 % for diabetes mellitus [50].

Lloyd and Colditz have shown that in the determination of the individual risk of atherosclerosis, family history plays a decisive role. Also after adjustment for classical risk factors (for example overweight, hypercholesterolemia), the risk of atherosclerosis in patients with positive family history is higher than in patients without positive family history [51, 52]. These findings indicate that atherosclerosis is, in significant parts, a genetically determined disease. This hypothesis was studied in numerous twin studies, where clear indications of the genetic influence on atherosclerosis was found: the relative risk to contract disease after the death of a twin from coronary heart disease (CHD), is in case of monozygotic twins twice as high compared to dizygotic twins [53]. Furthermore, Zdravkovic et al., showed in twin studies, that heritability of fatal myocardial infarction in male twins is 57 %, and in female twins 38 % [54]. In the German heart attack family study, a heritability of 50 % has also recently been demonstrated for the development of a proximal stenosis with existing coronary heart disease [55]. A morphological sign of a subclinical manifestation of atherosclerosis is the increased intima-media thickness of the carotid artery. In this case, a significant heritability of 38 % was shown [56-58].

1.3.2 Monogenic contributions to atherosclerosis

Atherosclerosis risk can be conferred either by mutations in single genes (monogenic type of atherogenesis) or be due to variation in multiple genes (polygenic model). First candidate genes of atherosclerosis were identified through their possible role in atherosclerosis development particularly in signal or metabolic pathways. Most of these genes have an influence on fat metabolism, coagulation, inflammation, endothelial dysfunction or even blood pressure regulation. In the following, monogenetic defects that lead to atherosclerosis and in consequence to a cardiovascular disease will be reviewed.

The Familial Hypercholesterolemia (FH), first identified by Brown and Goldstein, was the first monogenic disorder that was shown to cause elevated plasma cholesterol levels and especially high levels of low-density lipoprotein cholesterol (LDL-C) [59]. The frequency of heterozygous FH is 1:500, while homozygous FH is reported to be 1:1,000,000. Responsible for FH are mutations in the low-density lipoprotein receptor (*LDLR*), apolipoporotein B (*APOB*) or the protein convertase subtilisin/kexin type 9 (*PCSK9*) genes. *LDLR* is located on chromosome 19 and in the meanwhile more than 800 allelic variations are described [60]. Due to the mutations, the LDL receptor loses its ability to mediate the binding, internalization, or degradation of LDL [61]. This leads to extreme high cholesterol levels (>600 mg/dl) in homozygous patients and little lower in heterozygous patients (~400 mg/dl). Human APOB is located on chromosome 2 and codes for the main apolipoprotein of chylomicrons and LDL. Cholesterol levels of these patients are lower than those of FH, but still highly elevated. PCSK9 is an enzyme encoded by the *PCSK9* gene in humans on chromosome 1. PCSK9 plays a key role in regulating cholesterol homeostasis. It reduces hepatic low-density lipoprotein receptors (LDLRs) thereby increasing LDL-cholesterol. Furthermore, the autosomal recessive hypercholesterolemia (ARH), a disorder with similar characteristics to individuals carrying LDLR mutations have two defective copies of the *LDLRAP1 (low density lipoprotein receptor adaptor protein 1*) gene [62]. Sitosterolemia shows a similar clinical picture like Familial Hypercholesterolemia. It is a rare autosomal recessive disorder of the plant sterol metabolism, based on mutations in ABCG5 and ABCG8 [63, 64]. In a linkage analysis Mani et al. identified LRP6 (LDL receptor-related protein 6) as the putative causal gene in a family study with apparent autosomal dominant inheritance of premature CAD/MI and metabolic syndrome [65, 66]. Through genome-wide linkage analysis the myocyte enhancer factor-2 (MEF2A), arachidonate 5-lipoxygenase-activating protein (ALOX5AP) and leukotriene A4 hydrolase (LTA4H) were also detected to be associated with CAD [67-69]. ApoE is another key protein of the lipid transporting system which regulates serum cholesterol and participates in the formation of high density lipoproteins (HDL). Furthermore, ATP Binding Cassette Transporter 1 Gene (ABCA1) functions as a cholesterol efflux pump in the apolipoprotein mediated cellular lipid removal pathway [60]. Mutations of the *ABCA1* gene have been described in the case of Tangier disease and the hereditary HDL deficiency [70]. Another gene involved in cholesterol metabolism is the *CYP7A1* gene. *CYP7A1* plays a role in the conversion of cholesterol into bile acids. Genetic variations in the *CYP7A1* gene were associated in some studies with hypercholesterolemia [60].

1.3.3 *Genome-wide association studies (GWAS)*

The identification of genetic variants that contribute to atherosclerosis risk via polygenic effects was made possible by the complete sequencing of the human genome by the Human Genome Project and the development of high throughput genotyping technology as a prerequisite of genome-wide association studies (GWAS).

The international Human Genome Project (HGP) was founded 1990 and was completed 2003 with the near-complete sequencing of the approximately 3 billion base pairs of the human genome. To this end, the international HapMap project also contributed a key role. This research project aimed to develop a haplotype map of the human genome, the HapMap, which describes the common patterns of human DNA sequence variation [71]. Due to how genetic material is inherited by recombination between homologous chromosomes in the process of meiosis [72] and given that humans have a confined common ancestry, genetic variants are seen to be inherited together

in longer segments of DNA that are called haplotype blocks (a set of associated SNP alleles in a region of a chromosome). These haplotype blocks gain limited variation across generations and are shared by most of the human population. Therefore they can be used to associate genetic differences in human DNA sequences with diseases. A major type of sequence variation in the haplotype blocks is called single nucleotide polymorphisms (SNPs). In the meanwhile, more than 80 million SNPs exist in human populations [73]. Some SNPs in the haplotype blocks are redundant, so that only few SNPs are needed to indicate that there is genetic diversity of the entire block. These few "tag" SNPs can provide information on the pattern of genetic variation in larger genomic region. This haplotype structure of the human genome makes it possible, by genotyping approximately 500,000 SNPs, to associate genetic loci with the risk of a disease [74].

A number of high-throughput genotyping technologies have been developed that allow parallel genotyping of a high number of genetic markers in DNA. Using DNA microarrays it is possible to genotype multiple genomic markers in patients – up to 500,000 SNPs at a time [75]. The evaluation of these markers in combination with the meta-analysis of case-control samples leads to the identification of genetic variants which are highly and reproducibly associated with the risk for CAD and MI [77].

Genome-wide association studies (GWAS) are applied to associate genetic polymorphisms with phenotypes or certain diseases. Representing a hypothesis-free approach, a typical GWAS analyses a large number of genetic loci spread over the whole genome with the aim of identifying new, and possibly unanticipated genetic variants in a large unrelated population associated with a given trait of interest.

For widespread diseases, such as cancer, diabetes, or coronary heart disease, GWAS provided hundreds of genetic markers. The first large-scale, case-control association study to myocardial infarction (MI) was performed in 2002 in a Japanese population showing that the homozygosity in two SNPs in lymphotoxin A (LTA) at 6p21 was significantly associated with increased risk (odds ratio [OR] = 1.78) [76] (See Chapter 1.5 for details on the calculation of OR). In the meanwhile, several genome-wide association studies have been performed with relation to coronary artery disease (CAD) and myocardial infarction (MI) and more than 66 genetic variants were identified at 'genome-wide significance' ($P < 5 \times 10^{-8}$) [77-80]. The chromosome 9p21 (Chr9p21) locus, emerging from multiple GWAS, is the strongest genetic risk factor of atherosclerosis known today [85]. This locus has been replicated in several studies [81-83] and can be considered the most robust genetic marker of atherosclerotic cardiovascular disease. Investigating this locus in more depth, the first studies identified two genes located at this locus, *CDKN2A* and *CDKN2B*. Subsequent studies identified that the risk/non-risk alleles at the 9p21 locus are related to different isoforms of *ANRIL*, a long non-coding RNA. ANRIL is thought to affect not only the expression of *CDKN2A* and *CDKN2B* but also of many other genes, causing effects on cell proliferation and apoptosis and inflammation [84, 85]. Table 1 shows an overview of the replicated CAD-linked loci in European populations, the closest genes in the neighbourhood of the lead SNP, putative functions of these genes and possible relevance to CAD, the name of the lead SNPs, the effect allele frequency and the odds ratio that were detected during the past years through genome-wide association studies [86]:

TABLE 1: Replicated genome-wide significant loci for CAD [86].

Chr	Closest Gene(s)	Putative Functions of Possible Relevance to CAD	Lead SNP	EAF	OR
1	PPAP2B	Regulation of cell-cell interactions	rs17114036	0.92	1.13
1	PCSK9	Regulation of LDL receptor recycling	rs11206510	0.85	1.08
1	SORT1	Regulate apoB secretion and LDL catabolism	rs599839	0.78	1.11
1	IL6R	IL-6 receptor, immune response	rs4845625	0.46	1.05
1	MIA3	Collagen secretion	rs17465637	0.73	1.08
2	LINC00954	LncRNA of unknown function	rs16986953	0.07	1.09
2	APOB	Major apolipoprotein of LDL	rs515135	0.78	1.07
2	ABCG5/G8	Cholesterol absorption and secretion	rs6544713	0.29	1.05
2	VAMP5/8-GGCX	Intracellular vesicle trafficking	rs1561198	0.47	1.06
2	ZEB2-AC074093.1	ZEB2-transcriptional repressor	rs2252641	0.44	1.03
2	WDR12	Component of nucleolar protein complex	rs6725887	0.14	1.14
3	MRAS	Cell growth and differentiation	rs9818870	0.15	1.07
4	EDNRA	Receptor for endothelin-vasoconstriction	rs1878406	0.16	1.06
4	GUCY1A3	Nitric oxide signaling	rs7692387	0.80	1.07
4	REST-NOA1	REST maintains VSMCs in a quiescent state	rs17087335	0.21	1.06
5	SLC22A4/A5	Organic cation transporter	rs273909	0.14	1.06
6	ANKS1A	May inhibit PDGF-induced mitogenesis	rs17609940	0.82	1.03
6	PHACTR1	Regulates protein phosphatase 1 activity	rs12526453	0.71	1.10
6	KCNK5	Potassium channel protein	rs10947789	0.78	1.05
6	TCF21	Transcriptional regulator	rs12190287	0.64	1.06
6	SLC22A3-LPAL2-LPA	Lipoprotein(a)	rs2048327	0.35	1.06
			rs3789220	0.02	1.42
6	PLG	Fibrinolysis	rs4252120	0.74	1.03
7	NOS3	Production of nitric oxide	rs3918226	0.06	1.14
7	HDAC9	Represses MEF2 activity/beige adipogenesis	rs2023938	0.10	1.08
7	ZC3HC1	Encodes NIPA, regulator of cell proliferation	rs11556924	0.69	1.08
8	LPL	Lipolysis of TG-rich lipoproteins	rs264	0.85	1.06
8	TRIB1	TG, MAPK signaling, SMC proliferation	rs2954069	0.55	1.04
9	CDKN2BAS	Cellular proliferation, platelet function	rs10757274	0.48	1.21
9	ABO	IL-6, E-selectin, LDL-C levels	rs579459	0.21	1.08
10	KIAA1462	Component of endothelial cell-cell junctions	rs2505083	0.40	1.07
10	CXCL12	Endothelial regeneration; neutrophil migration	rs501120	0.81	1.08
			rs2047009	0.48	1.06
10	LIPA	Intracellular hydrolysis of cholesteryl esters	rs1412444	0.37	1.07
			rs11203042	0.45	1.04
10	CYP17A1-CNNM2-NT5C2	steroidogenic pathway	rs12413409	0.89	1.08
11	PDGFD	Role in SMC proliferation	rs974819	0.33	1.07
11	SWAP70	Leukocyte and VSMC migration and adhesion	rs10840293	0.55	1.06
11	ZNF259 APOA5 APOC3	TG-rich lipoprotein metabolism	rs964184	0.18	1.05
12	SH2B3	Negative regulator of cytokine signaling	rs3184504	0.42	1.07
12	ATP2B1	Intracellular calcium homeostasis	rs7136259	0.43	1.04
12	KSR2	Suppressor of Ras2 – cell proliferation; obesity	rs11830157	0.36	1.12

Chr	Closest Gene(s)	Putative Functions of Possible Relevance to CAD	Lead SNP	EAF	OR
13	FLT1	VEGFR family; angiogenesis	rs9319428	0.31	1.04
13	COL4A1/A2	Type IV collagen chain of basement membrane	rs4773144	0.43	1.05
			rs9515203	0.76	1.07
14	HHIPL1	Unknown	rs2895811	0.41	1.04
15	ADAMTS7	Proliferative response to vascular injury	rs7173743	0.56	1.08
15	SMAD3	Downstream mediator of TGF-β signaling	rs56062135	0.79	1.07
15	ATP2B1	MFGE8: lactadherin–VEGF neovascularization	rs8042271	0.90	1.10
15	FURIN	Endoprotease-TGF-β1 precursor and type I MMP	rs17514846	0.44	1.05
17	BCAS3	Rudhira-EC polarity and angiogenesis	rs7212798	0.15	1.08
17	RAI1-PEMT-RASD1	PEMT encoded protein converts PE to PC	rs12936587	0.61	1.03
17	SMG6	Role in nonsense mediated RNA decay	rs216172	0.35	1.05
17	UBE2Z	Protein ubiquination; apoptosis	rs46522	0.51	1.04
18	PMAIP1-MC4R	PMAIP1: HIF1A-induced proapoptotic gene; MC4R: leptin signaling-obesity	rs663129	0.26	1.06
19	LDLR	LDL clearance	rs1122608	0.77	1.08
19	APOE	LDL and VLDL clearance	rs4420638	0.17	1.10
19	ZNF507	Unknown	rs12976411	0.09	0.67
21	KCNE2	Maintains cardiac electric stability	rs9982601	0.13	1.12
22	POM121L9P-ADORA2A	Adenosine A2a receptor: infarct-sparing effects	rs180803	0.97	1.20

EAF, effect allele frequency; OR, odds ratio

The identified loci explain only around 10 % of the heritability of coronary artery disease and most genome-wide significant hits were not related to traditional risk factors [87]. The main traditional risk factors that show some evidence for association with CAD-associated single-nucleotide polymorphisms (SNPs) are lipid and blood pressure traits [87].

The two atherosclerosis risk loci that we have investigated in our study do not overlap with known hits from GWAS for CAD (see above) nor with hits from GWAS for CAD risk factors.

1.4 Mouse models in atherosclerosis

Currently, the mouse is the most frequently and widely used model for atherosclerosis studies. Atherosclerosis studies in mice are important for both, identification of novel candidate genes of the disease using hypothesis-free approaches, as well as for hypothesis-driven validations of candidate genes *in vivo.* 75 % of mouse genes have an equivalent orthologous gene class in humans, making mice ideal for studying different diseases.

Genetic analysis in isogenic (inbred) mice provides an excellent example of a viable strategy to gene discovery for complex human diseases like atherosceloris. Inbred strains are produced using not less than 20 consecutive generations of brother x sister or offspring x parent mating. At least 98.6 % of the loci in each mouse are homozygous and therefore the individual animals are considered as being genetically identical (isogenic)[88]. Many inbred strains are well characterized and crossing of phenotypically different inbred strains enables mapping of quantitative or qualitative trait loci [89].

Wild-type mice are actually resistant to spontaneous atherosclerotic lesion formation. Compared to other vertebrate species, mice have an antiatherogenic lipoprotein profile with high levels of High-density lipoproteins (HDL) and low levels of Low-density lipoproteins (LDL) in blood [90]. However, through induced mutations it was possible to develop mouse strains that are susceptible to atherosclerosis. Three different atherosclerosis mouse models are used to induce and examine atherosclerosis. A diet-induced model, secondly the *apolipoprotein E*-deficient model, and third, *LDL receptor*-deficient mice. Paigen developed a cholesterol-cholate diet ("Paigen diet") consisting of 15 % high-fat, 1.25 % high-cholesterol and 0.5 % cholic acid to induce atherosclerosis in wild-type mice [91]. Nonetheless, atherosclerotic lesion formation remained small, therefore this mouse model was not extensively used [92]. In the year 1992, two independent research groups created hyperlipidemic *apolipoprotein E*-deficient mice using gene targeting through homologous recombination in embryonic stem cells [93, 94]. ApoE is a major apoprotein of chylomicrons and intermediate-density lipoproteins (IDLs). *ApoE* K0 mice lack the primary lipoprotein required for the uptake of the lipoproteins through the hepatic receptors. In the year 1993, gene targeting in embryonic stem cells was also used to create *LDL receptor* knockout (*LDLR*-KO) mice, a model of familial hypercholesterolemia. These mice lack the primary receptor for LDL cholesterol uptake. *LDL receptor* deficient mice have a more modest lipoprotein abnormality than the apolipoprotein E deficient mice, with increased levels of LDL- and VLDL-cholesterol leading to a total plasma cholesterol of about 250 mg/dl on a chow diet [95]. Apolipoprotein E deficient mice are characterized by the plasma accumulation of plasma VLDL particles and spontaneously develop atherosclerotic lesions on a low-fat diet. LDL receptor deficient mice accumulate plasma LDL and develop higher levels of atherosclerosis when fed a high-cholesterol diet [90]. Furthermore, in 1994, ApoE and LDL-receptor (LDLr) double knockout (ApoE/LDLr-DKO) mice were generated [96], representing a new mouse model that develops severe hyperlipidemia and atherosclerosis [97]. The following figure shows the progression of atherosclerosis in the above-described mouse models [98].

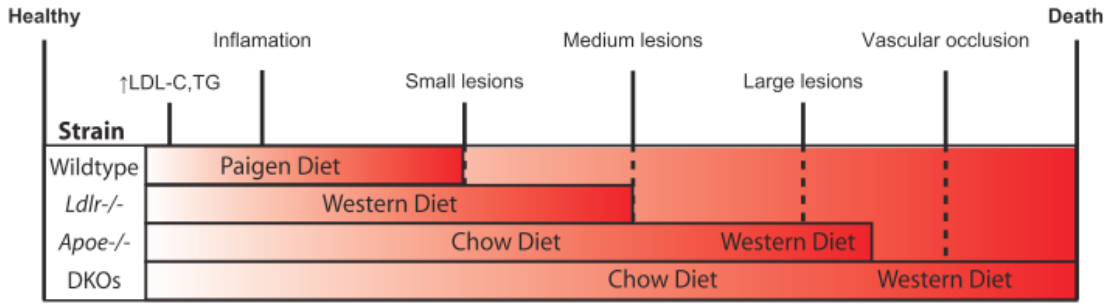

FIGURE 2: Atherosclerosis phenotyping in mice and corresponding mouse models [98].

Teupser et al. succeeded to induce hypercholesterolemia in mice for atherosclerosis development using a semisynthetic diet by adding cholesterol at different concentrations (0.02 %-0.15 %). The aim was to establish a diet that would achieve hypercholesterolemia and atherosclerosis in LDLR$^{-/-}$ mice without toxicity from very high cholesterol and cholic acid components and without the weight gain induced by high-fat feeding [99]. This semisynthetic diet consisted of standardized components: 19 % protein (mainly casein), 67 % carbohydrates (corn starch, maltodextrin, sucrose) and 4.3 % fat (soybean oil, cocoa butter). The rest is made up of vitamins, fiber and trace elements. In semisynthetic diets with 0.00 % and 0.02 % cholesterol, the plasma cholesterol

level was similar (10 mmol/l) and significantly lower compared to diets with higher cholesterol. While in the two diets with the lowest cholesterol shares no steatosis was observed, the animals showed a significant steatosis of the liver on diets with 0.15 % to 0.50 % cholesterol. The semi-synthetic diet containing 0.02 % cholesterol did not induce hepatic impairment. Therefore we triggered atherosclerosis by feeding a semisynthetic diet to *Ldlr*$^{-/-}$ mutant mice for all our atherosclerosis studies.

1.5 Quantitative trait locus (QTL) mapping for atherosclerosis susceptibility

Quantitative trait locus (QTL) analysis is a method that is applied to identify loci making a significant impact on a phenotype, for example identifying genetic factors of atherosclerosis in mice. Mouse genetic mapping methods rely on the presence of inbred mouse models. For a QTL analysis, two or more inbred mouse strains are needed that differ genetically with regard to the trait of interest. Furthermore, genetic markers are required that distinguish between the parental F0 strains. Various markers are used for genotyping, as single nucleotide polymorphisms (SNP), simple sequence repeats (SSRs), restriction fragment length polymorphisms (RFLPs) and transposable elements [100-102]. There are several variants in QTL mapping methods: the F2 generation can either be generated by crossing the littermates of the F1 generation or by backcrossing the F1 generation with the parental F0 strains (N2 generation). Inbred F0 mice are genetically identical and homozygous at all loci and, consequently, the F1 generation is heterozygous. The resulted F2 mice are genetically distinct from each other, since the paternally and maternally derived chromosomes recombine before segregating into gametes.

In this regard, genetic linkage analysis is used for mapping heritable trait genes to defined chromosomal regions. The frequency of recombination between two genetic markers is greater, the further apart they are. Accordingly, the smaller the distance between to genes, the more unlikely it is that these genes will be separated by meiotic crossing-over. Analyzing the separation of distinguishing genetic variants over several generations in genetic crosses, the relative distance between two genes can be determined via the recombination frequency. Disease candidate genes are identified by using genetic markers, whose position is known in the genome. These markers, though representing genetic variants are use solely for mapping, and have nothing to do with the disease *per se*. Therefore, if some disease is passed to offsprings along with specific marker-genes, then it can be concluded that the gene(s) which are responsible for the disease are located close on the chromosomal location of these markers. In the classical parametric linkage analysis, the probability that a gene important for a disease is linked to a genetic marker is studied through the log of the odds ratio (LOD) score. This score assesses the probability that a given pedigree, where the disease and the marker are cosegregating, is due to the existence of genetic linkage (with a given linkage value) as opposed to segregation by chance [103].

Mouse models using inbred strains have been proven useful for identifying candidate genes of atherosclerosis. All mice of the F2 generation are analyzed genome-wide with polymorphic microsatellite markers to define the genotype at each locus. Three different genotypes occur in an intercross of AxB mice: Either homozygous (AA or BB) or heterozygous (AB). QTL software is then used to define the correlations between genotype and phenotype, and the output is given as likelihood ratio statistic or as a log of the LOD score [90]. The LOD score ratio is used as a measure of a linkage analysis. The ratio (odds ratio) is calculated from the probability that

the observed data are linked and the probability that they are not linked. The logarithm of this quotient, the LOD score (logarithm of the odds), serves as a measure of linkage probability. For monogenic features or diseases, a LOD score of 3.0 is considered to be evidence of linkage (i.e., the probability that linkage is present, would be 1000 times greater than the likelihood of no linkage). In our studies, linkage analyses in mice were used to identify novel candidate genes for atherosclerosis susceptibility. Therefore, atherosclerosis-susceptible inbred C57BL/6 (B6) and atherosclerosis-resistant FVB mice on the LDL receptor-deficient (*Ldlr*$^{-/-}$) background were intercrossed to generate a heterozygous F1 generation [104]. F1 mice were then mated by brother-sister mating to generate F2 mice. Recombination in F2 was assessed with a genome-wide scan involving 192 microsatellite markers [104]. Subsequently, a correlation of the genotype of the F2 generation with the phenotype was performed to generate a LOD score (logarithm of odds) of each genetic marker.

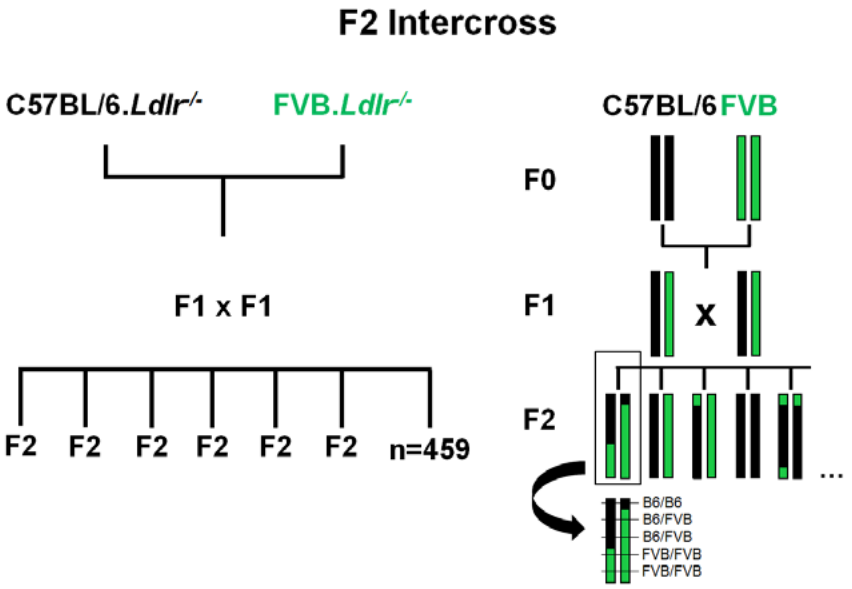

FIGURE 3: Atherosclerosis-susceptible C57BL/6 and atherosclerosis-resistant FVB mice on the *Ldlr*$^{-/-}$ background were intercrossed to generate F1 mice. Heterozygous F1 mice were mated by brother-sister mating to generate 459 F2. Recombination in the F2 was assessed with a complete genome scan involving 192 microsatellite markers [104].

In principle, QTL analysis in mouse models investigates phenotypes, which differ between the two parental strains. In preliminary works, the size of atherosclerotic lesions as well as HDL- and LDL-cholesterin levels had been determined. Figure 4 shows the lesion sizes as the phenotype of a QTL experiment of an atherosclerosis-susceptible C57BL/6.*Ldlr*$^{-/-}$ and atherosclerosis-resistant FVB.*Ldlr*$^{-/-}$ cross-breeding and subsequent generations. The F1 generation has a heterozygous phenotype and intermediate atherosclerotic lesions, formed by crossing of the parental inbred strains (atherosclerosis-susceptible C57BL/6 [B6] and atherosclerosis resistant FVB). The F2 generation differs in its characteristic expression with respect to the phenotype, according to the proportion of the genes from the grandparental generations (Figure 4).

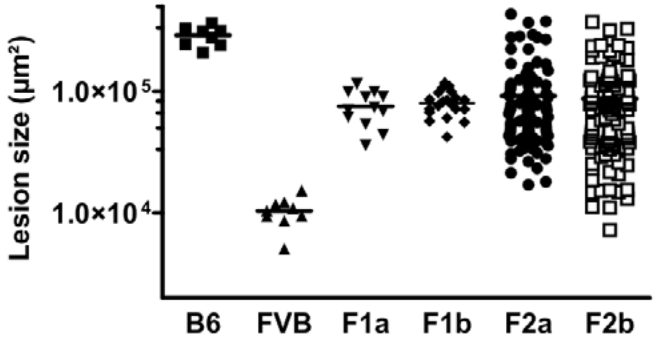

FIGURE 4: Atherosclerotic lesion size (phenotype) in female mice of an intercross of atherosclerosis-susceptible C57BL/6 and atherosclerosis-resistant FVB mice on the *Ldlr*$^{-/-}$ background [104].

A correlation of the genotypes of the F2 generation with the phenotype (atherosclerotic lesion sizes) was performed to generate a LOD score (logarithm of odds) of each genetic marker. For the areas between the markers the LOD score is being estimated.

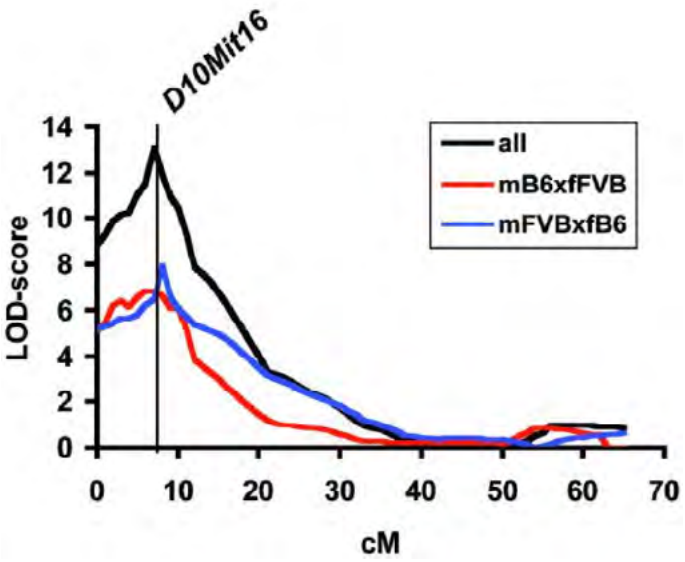

FIGURE 5: Atherosclerosis LOD score on chromosome 10 [104].

Here, a significant LOD score for atherosclerosis was identified on chromosome 10.

1.6 Atherosclerosis loci in mice

Through quantitative trait locus mapping analysis of mice on the *ApoE*$^{-/-}$, *Ldlr* deficient background or the Paigen diet, a variety of novel atherosclerosis loci were identified. The following table gives an overview of the identified atherosclerosis loci [98]. The chromosome, peak location, mouse model, QTL name (if available) and potential identified candidate gene are given.

TABLE 2: Quantitative trait loci of atherosclerosis in different mouse models [98].

Chromosome	Peak Location or Interval	Mouse Model	QTL Name	Proven Gene
1		*Paigen diet*	*Ath1*	*Tnfsf4*
1		*ApoE$^{-/-}$*	*Ath30*	
1	105.4	*ApoE$^{-/-}$*	*QTL-#*	
1	166.3	*ApoE$^{-/-}$*	*QTL-#*	
1	176.6	*ApoE$^{-/-}$*	*Ath9*	
2		*Paigen diet*	*Ath2*	
2		*ApoE$^{-/-}$*	*Ath28*	
2	148.5	*Ldlr$^{-/-}$*	*Athla1*	
3		*ApoE$^{-/-}$*	*Ath23*	
3	115.5	*Ldlr$^{-/-}$*	*Ascla4*	
3	147.8	*Ldlr$^{-/-}$*	*Ascla3*	
4	137.4-150.9	*Ldlr$^{-/-}$*	*Athsq1*	
4	45.-105	*Paigen diet, ApoE$^{-/-}$*	*Ath8*	
5		*ApoE$^{-/-}$*	*Ath24*	
6		*Ldlr$^{-/-}$*	*Artles*	*Alox5*
6		*Ldlr$^{-/-}$*	*Ath38*	
6		*Ldlr$^{-/-}$*	*Athsq2*	
6	116.6-128.5	*Ldlr$^{-/-}$*	*Ath37*	
7	57	*Paigen diet*	*Aorls2*	
7		*Paigen diet*	*Ath3*	
7		*ApoE$^{-/-}$*	*Ath31*	
9	65.3	*ApoE$^{-/-}$*	*Ath29*	
10	82.1	*Paigen diet*	*Aorls1*	
10		*ApoE$^{-/-}$*	*Ath11*	
10	20.1	*Paigen diet*	*Ath20*	
10	67.7	*Paigen diet*	*Ath17*	
10	18.5	*Ldlr$^{-/-}$*	*Ascla2*	
10	21.4	*Ldlr$^{-/-}$*	*Ascla1*	
11	108.6	*Paigen diet*	*Ath19*	
12		*Paigen diet*	*Ath21*	
12		*Paigen diet*	*Ath6*	
12	35.9	*Paigen diet*	*Ath18*	
12	14.3	*Ldlr$^{-/-}$*	*Ascla5*	*Adam17*
12	55.1	*Ldlr$^{-/-}$*	*Ascla6*	
12		*ApoE$^{-/-}$*	*Cath1*	
13		*ApoE$^{-/-}$*	*Ath25*	
13		*ApoE$^{-/-}$*	*Ath32*	
14	51.9-165.9	*ApoE$^{-/-}$*	*Ath13*	
15		*ApoE$^{-/-}$*	*Ath22*	
15		*ApoE$^{-/-}$*	*Ath33*	
17		*ApoE$^{-/-}$*	*Ath26*	
18		*ApoE$^{-/-}$*	*Ath27*	
19	38.5	*ApoE$^{-/-}$*	*Ath16*	

1.7 Atherosclerosis susceptibility loci on mouse chromosome 3 and 12

In preliminary work to this thesis, quantitative trait locus (QTL) mapping in atherosclerosis-susceptible C57BL/6 (B6) and atherosclerosis-resistant FVB mice on the Ldl-receptor-deficient background (*Ldlr*$^{-/-}$) led to the identification of three novel significant atherosclerosis susceptibility loci on chromosomes 3, 10, and 12 [104]. In this work we focused on the identified atherosclerosis loci on chromosomes 3 and 12 (Figure 6).

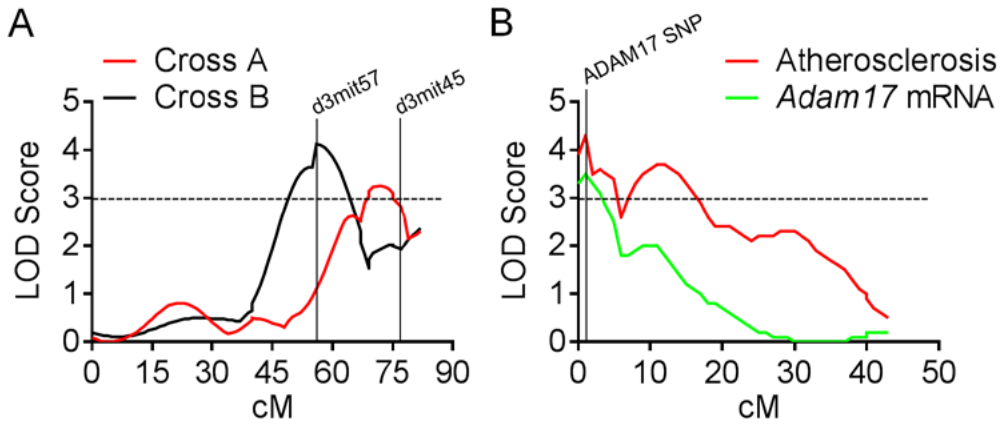

FIGURE 6: LOD scores for atherosclerosis on mouse chromosome (**A**) 3 and (**B**) 12, respectively [104, 105].

The Chr3 locus was gender-dependent and only present in female F2 mice [104]. Different LOD score maxima were observed in different female crosses according to the breeding scheme of the F0 generation (Figure 6 A). In cross A, male B6 mouse was mated with female FVB (F0 = male B6xfemale FVB), the maximum LOD score of atherosclerosis was 3.3 at marker d3mit45. In cross B, a male FVB mouse was mated with a female B6 mouse (F0 = male FVBxfemale B6), with a maximum atherosclerosis LOD score of 4.1 at marker d3mit57 [104]. Lineage-dependency of loci at chromosome 3 suggested that different molecular mechanisms might underlie the two distinct female atherosclerosis loci.

On the atherosclerosis locus on mouse chromosome 12, the *Adam17* gene was previously identified as the candidate gene underlying this atherosclerosis locus through eQTL mapping (Figure 6 B) [105]. In that study, however, no further functional validations *in vitro* or *in vivo* were performed to investigate whether *Adam17's* role in atherogenesis was causal [105]. On the following an overview will be given of the family of metalloproteases and especially the ADAM17 structure and functions.

1.8 Adam17 as a candidate gene of atherosclerosis and the family of metalloproteases

Based on common structural features, motifs and folding patterns in their protein sequence, metalloproteases are classified in five major superfamilies [106]. These superfamilies are the gluzincins, inuzincins, metzincins, carboxypeptidases and DD carboxypeptidases [107]. The superfamily of metzincins is characterized by a protease domain with a HEXXHXXGXXH zinc-binding motif at the active site and a methionine-containing Met-turn [108]. The family of metzincins includes four subfamilies: the astacins, serralysins, matrixins and the adamalysins [Figure7])[107,109].

The matrixins comprise the matrix metalloproteases (MMPs). These enzymes are responsible for extracellular matrix degradation and remodeling and play substantial roles in development and the pathology of diseases such as arthritis and cancer [110]. Members of the astacin family are induced in embryonic stages of development, and are implicated in processes like dorsal-ventral patterning, hatching, and eggshell matrix degradation [111]. Serralysins are bacterial Zn-endopeptidases that act as a virulence factor to cause tissue damage and anaphylactic response [112].

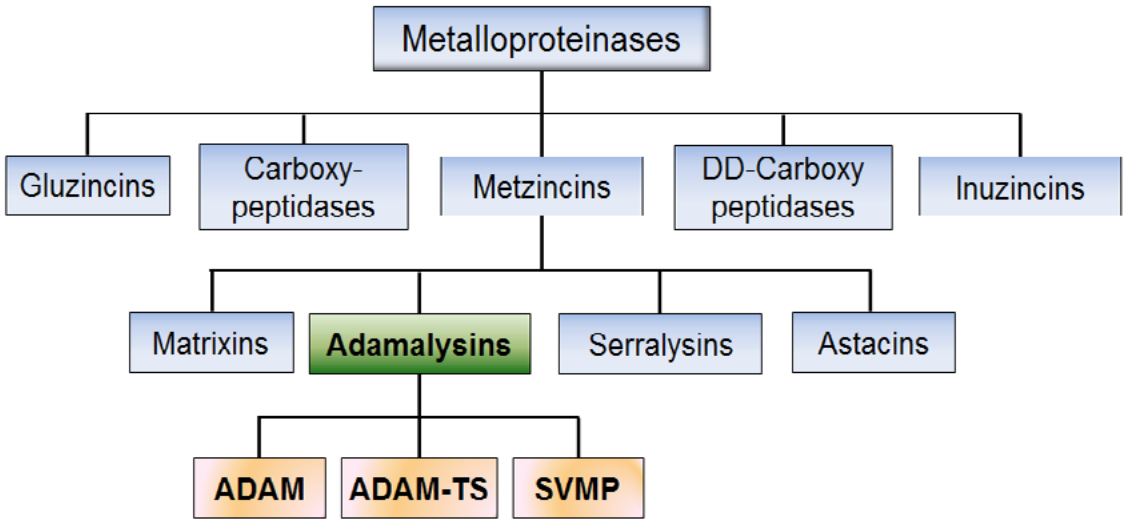

FIGURE 7: Protein family of Zn^{2+} dependent metalloproteases.

Due to structural homologies, the adamalysin family is further divided into three protein families: ADAM (A disintegrin And Metalloprotease), ADAM-TS (thrombospondin motif) and SVMPs (Snake Venom Metalloprotease).

ADAM enzymes are structurally closely related to other metalloenzymes such as ADAM-TSs (ADAMs with thrombospondin domains), matrix metalloproteinases (MMPs) and snake venom metalloproteinases (SVMP) [121]. ADAMs and the membrane-type matrix metalloproteases (MT-MMP) are membrane-bound enzymes that are capable of shedding a multitude of proteins from the cell surface. All proteases have a signal sequence, a pro-domain and a catalytic domain. The structure of ADAMs is closely related to the family of snake venom metalloproteases, which are responsible for the hemorrhage effects and massive tissue necrosis seen after snake bites. SVMP are soluble proteins in contrast to ADAMs since they have no transmembrane and cytoplasmic domain [113]. ADAMs have also a similar domain structure as the matrix metalloproteases with two distinct differences. They do not contain the characteristic hemopexin-like domain but instead have three additional domains, the cysteine-rich domain, the Epidermal Growth Factor (EGF)-like repeat domain and the disintegrin domain [114]. Other subclasses of MMPs have an additional fibronectin type II-like sequence. ADAM-TSs are all secreted, extracellular enzymes that have diverse roles in tissue morphogenesis and pathophysiological remodeling, in inflammation and vascular biology [115]. Like ADAMs, all ADAM-TS enzymes share a signal peptide, a prodomain, a catalytic domain, a disintegrin-like domain and possess further a central thrombospondin (TS) repeat, a cysteine-rich- and a spacer domain.

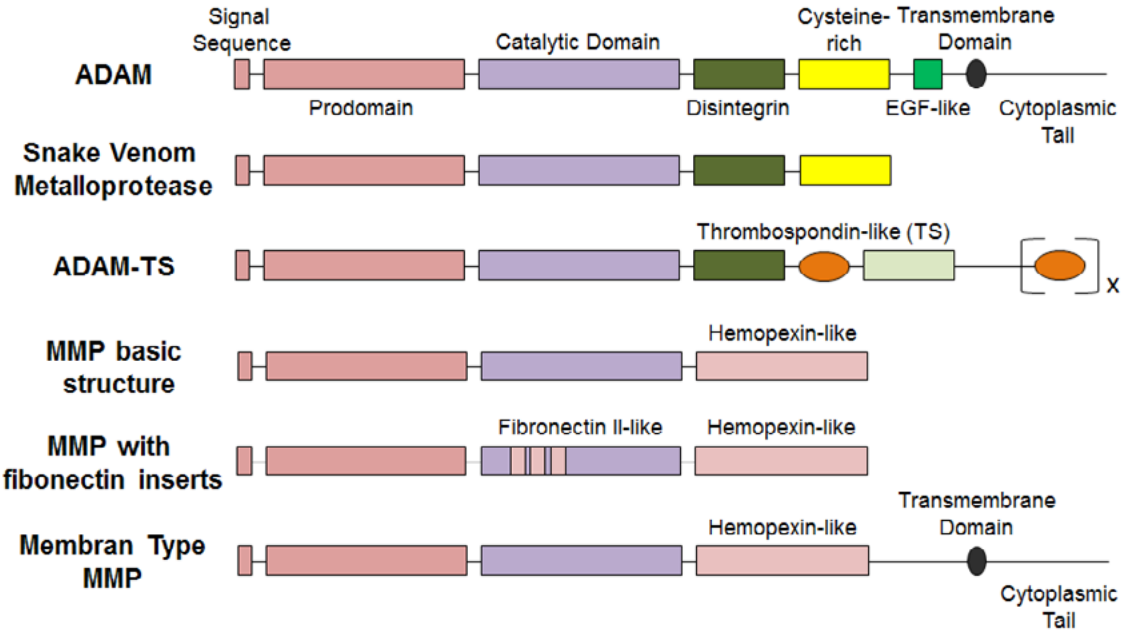

FIGURE 8: Schematic representation of the domain structure of metzincin proteases, modified after [116].

As mentioned in 1.6 (Atherosclerosis Loci in mice), several quantitative trait loci (QTL) for atherosclerosis were identified in different mouse crosses. A QTL mapping in atherosclerosis-resistant FVB and atherosclerosis-susceptible C57BL/6 (B6) mice on the *Ldl*-receptor deficient (*Ldlr*$^{-/-}$) background [104] led to the identification of a novel atherosclerosis locus on chromosome 12 and subsequently to the identification of metalloproteinase a disintegrin and metalloprotease 17 (*Adam17*) as a candidate gene of atherosclerosis [105].

ADAM17 belongs to one of 34 members of the ADAM family that have been described so far in a variety of species [117]. ADAM proteins are structurally similar but only few of them are proteolytically active [118]. ADAM17 is a type I transmembrane protein [119] and it was first identified as an enzyme that convertes membrane-bound tumor necrosis factor (TNF)-α precursor to a soluble form [120]. It is a multi-domain protein starting with a signal sequence (1-17 aa), followed by a prodomain (18-214 aa), a metalloproteinase or catalytic domain (215-473 aa) with the typical HEXXHXXGXXH sequence, a disintegrin domain (474-572 aa), a cysteine-rich domain (603-671 aa), followed by a transmembrane domain (672-694 aa) and a intracellular tail (695-824 aa). ADAM17 has very little sequence similarities with other ADAMs; its closest relative is ADAM10 [121].

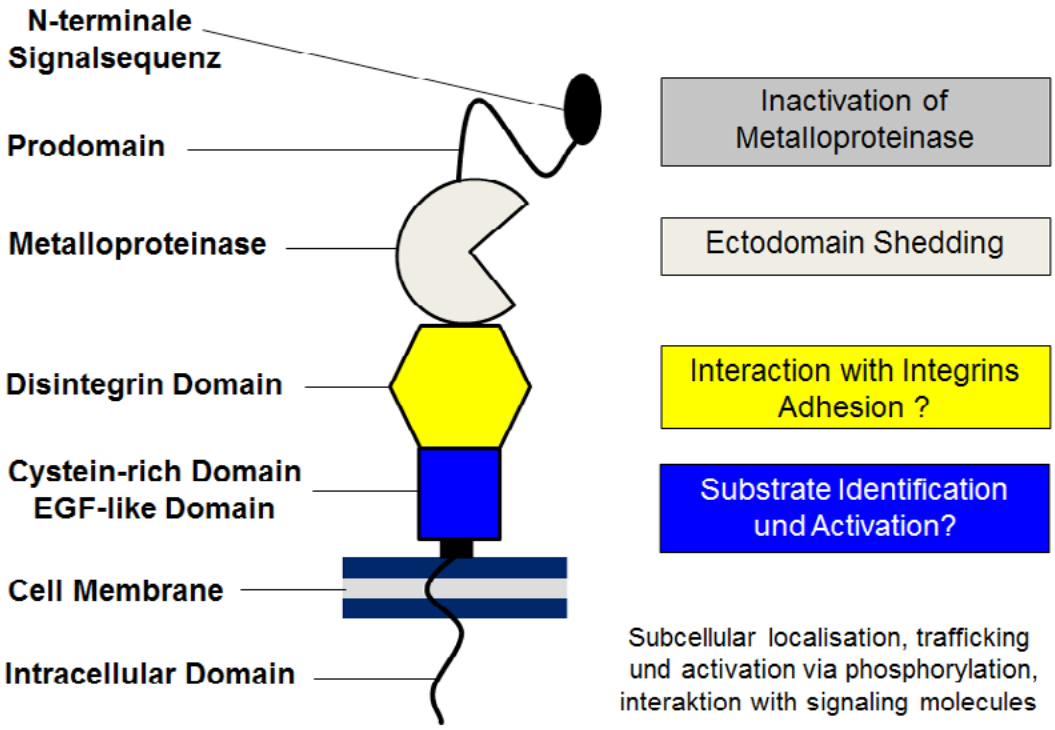

FIGURE 9: ADAM17 domains and structure, modified after [122].

The enzymatic activity of ADAM17 is inhibited through its prodomain during translation [123]. The prodomain of ADAM17 is cleaved by furin, a proprotein convertase, in the trans-Golgi at the last 4 amino acids (RVKR) before the catalytic domain [124]. Latest reports show that iRhom2, a proteolytically inactive member of the rhomboid family, binds ADAM17 and promotes its exits from the endoplasmic reticulum [125]. The catalytic (metalloproteinase) domain of ADAM17 contains the Zn^{2+} chelating sequence HEXXHXXGXXH (X being any amino acid residue) and is responsible for shedding membrane-bound proteins. ADAM17 substrates such as adhesion molecules VCAM1, ICAM1, L-selectin and JAM-A as well as cytokines and receptors TNFα, TNFR1, TNFR2, IL-6R and CX3CL1 play an important role in cell-cell adhesion, intra- and extracellular signaling, inflammation and cell proliferation [121, 122, 126]. So far, 76 ADAM17 substrates were identified. Table 3 gives an overview of some of the most important ADAM17 substrates.

TABLE 3: Substrates of ADAM17 [122].

Cytokines, Growth factors		Receptors		Adhesion molecules
TNFα	SEMAD4D	TNFR1	SORT1	ICAM1
TGFα	LAG-3	TNFR2	Notch1	VCAM1
AREG	DLL1	IL-6R	LOX-1	NCAM
HB-EGF	MICA	IL1-R2	ErbB4	ALCAM
EPGN	MICB	NTRK1	TNFRSF5	EpCAM
Fractalkine/CX3CL1	LTA	CSF1R	TNFRSF8	CD62L
CSF-1	FLT-3L	SORL1	VEGFR2	JAM-A
Jagged	TMEFF2	EPCR	IGF2-R	CD44
Other molecules				
MUC-1	CAS9	PRNP	LYPD3	CD163
APP	GP	KL	VASN	PMEL17

The disintegrin domain of ADAM17 can, in some cases, interact with integrins to influence cell adhesion and cell-cell interactions [127]. Furthermore, the disintegrin and the EGF-like domains are thought to be involved in substrate recognition and dimerization [128]. Furthermore, ADAM17 is acting as a sheddase for epidermal growth factor ligands [129]. In line with this, ADAM17 has been established in the pathogenesis of several types of inflammatory diseases, such as rheumatoid arthritis, inflammatory bowel disease, psoriasis and pulmonary inflammation [121]. Since inflammatory components play a crucial role in the pathogenesis of atherosclerosis [33], these findings support the hypothesis that ADAM17 might be involved in this frequent disease [130].

Studies of ADAM17 in mice have been hampered by the fact that *Adam17* knockout mice (*Adam17*$^{\Delta Zn/\Delta Zn}$) are not viable. These animals die within several hours after birth and show severe epithelial abnormalities [131]. Only recently, hypomorphic *Adam17* mice (*Adam17*$^{ex/ex}$) have been generated, which are partially deficient for *Adam17* and have barely detectable levels of *Adam17* in all tissues [132]. Until now, conditional knockout mice with *Adam17*-deletions in myeloid cells [133], in thymic epithelial cells [134], in osteochondroprogenitor cells [135], leucocytes [136] and endothelial cells [137, 138] were used to study inflammation (rheumatoid arthritis) and cancer. A mouse model overexpressing *Adam17* showed no enhanced shedding activity *in vivo* despite higher *Adam17* mRNA and protein expression [139]. To date, none of these mouse models was used to study the effect of ADAM17 on atherosclerosis [130].

1.9 Goal of this thesis

Atherosclerotic cardiovascular disease has a strong heritable component. Over the last decade, several atherosclerosis susceptibility loci were identified across the entire mouse genome through quantitative trait locus mapping in different crosses from atherosclerosis-susceptible and atherosclerosis resistant mice. About 50 % of the risk for developing atherosclerosis is genetically determined, but only a fraction of this percentage genetically annotated. Thus, the identification of novel candidate genes for atherosclerosis susceptibility remains important.

Through quantitative trait locus (QTL) mapping in atherosclerosis-susceptible C57BL/6 (B6) and atherosclerosis-resistant FVB mice on the Ldl-receptor-deficient background (*Ldlr*$^{-/-}$), two novel atherosclerosis susceptibility loci were identified [104], an atherosclerosis locus on chromosome 3 and a separate risk locus on chromosome 12. It was the goal of this thesis was to identify and characterize the underlying effector genes at these loci.

This PhD thesis is divided in three major projects with the following aims:

1. Chromosome 3 atherosclerosis locus:

The identified chromosome 3 atherosclerosis locus was gender-dependent and only presented in the female F2 generation in crosses of atherosclerosis-susceptible C57BL/6 (B6) and atherosclerosis-resistant FVB mice. Interestingly, risk differed depending on whether risk alleles were transmitted from grandfathers or from grandmothers suggesting that more than one single molecular mechanisms or several distinct subloci might underlie this locus. The aim was to identify the genes affecting risk through this locus by establishing a congenic mouse model and to unravel their potential molecular role in atherogenesis by investigating their function in pathophysiologically relevant vascular cells in cell culture models.

2. Chromosome 12 atherosclerosis locus:

On the atherosclerosis locus on mouse chromosome 12, the *Adam17* gene had been previously identified as the candidate gene underlying this atherosclerosis locus [105]. This study had revealed that an allele that led to higher *Adam17* mRNA expression associated with reduced susceptibility to atherosclerosis, indicating an unexpected antiatherogenic role of ADAM17, but leaving open the mode of ADAM17's molecular action in atheroprotection [105]. Since mice with complete *Adam17*-deficiency are not viable, it was the aim of the current study to study Adam17 function in adult mice *in situ* taking advantage of the fact that hypomorphic *Adam17* mutants, with strongly reduced Adam17 mRNA and protein expression, survive ($Adam17^{ex/ex}$) [132]. For this, *Adam17* hypomorphic mice should be crossed onto the low-density lipoprotein receptor (Ldlr)-deficient background to be able to induce atherosclerosis and to histologically test for the function of Adam17. Finally, the role of ADAM17 should be investigated related to cellular functions known to be involved in the etiology of atherogenesis, like apoptosis, proliferation, and adhesion in atherosclerosis-relevant cell lines of macrophages, vascular smooth muscle cells and endothelial cells.

3. Chromosome 12 atherosclerosis locus (elastic stability):

Adam17 has also been studied in other vascular diseases, such as aneurysms. Its role therein remained controversial, with one study reporting reduced ADAM17 expression in aneurysms [140], and other studies showing a positive correlation between expression and aneurysm risk or occurrence [141-143]. The aim of project 3 was to specifically address whether and how Adam17 functionally regulated aneurysm onset by taking advantage of the *Adam17* hypomorphic mouse model established in project 2. In aneurysms the integrity of the arterial wall is compromised by inflammatory processes and other extracellular matrix (ECM)-degrading factors, impairing elastin lamellae that support and transmit mechanical load to the cellular cytoskeleton [144, 145]. Therefore we wanted to quantify whether ADAM17 affected arterial wall elasticity and ECM properties in different arteries [146].

2 Material and Methods

2.1 Mouse models

2.1.1 Generation of F2 intercross-mice linkage analysis (C57BL/6-FVB)

This PhD thesis is based on the F2 intercross from atherosclerosis-susceptible C57BL/6 (B6) and atherosclerosis resistant FVB mice on the Ldl receptor-deficient background generated by Prof. Teupser in the year 2006 [104]. B6 mice on the *Ldlr*$^{-/-}$ background were obtained from The Jackson Laboratory (B6.129S7-Ldlrtm1HerJ, stock no.002207, henceforth called B6.Ldlr$^{-/-}$). FVB mice on the *Ldlr*$^{-/-}$ background (henceforth called FVB.LDLR$^{-/-}$) were generated in the laboratory [99]. Mice of the F1 and F2 generation were generated in two ways: In cross A "mB6xfFVB," male B6.Ldlr$^{-/-}$ mice were crossed to female FVB.*Ldlr*$^{-/-}$ mice and the resulting F1 generation, was intercrossed by brother-sister mating to generate 107 female and 112 male F2 mice. In cross B "mFVBxfB6," male FVB.*Ldlr*$^{-/-}$ mice were crossed to female B6.Ldlr$^{-/-}$ mice and the resulting F1 generation was intercrossed to generate 120 female and 120 male F2 mice [104]. Working material of all 459 mice from this intercross was at our disposal for further experiments.

2.1.2 Genetic analysis of the F2 generation

By cross-breeding the inbred parental strains B6 and FVB, a heterozygous F1 generation is formed. Mating heterozygous F1 mice by brother-sister, an F2 generation is formed with a genetic recombination. During recombination, pieces of DNA are broken and recombined to produce new combinations of alleles. This recombination process creates genetic diversity at the level of genes that reflects differences in the DNA sequences of different organisms [147]. A complete genome scan with genetic markers from each of the 459 animals of the F2 generation is available. Genetic recombination in the F2 generation was assessed with 192 microsatellite markers. Genomic DNA

was isolated from mouse tissues (liver, tail) by digestion with proteinase K and precipitation with ethanol. Genotyping was performed with microsatellite markers with known polymorphisms between B6 and FVB mice. The genome scan was first performed with 154 markers in approximately 10 cM intervals and with an additional set of 54 markers to allow a finer mapping, or to repeat marker, where the analysis was unclear [104].

2.1.3 *Generation of chromosome 3 congenic mice*

Congenic strains are produced by transferring a mutation from one genetic background to a specific inbred strain through repeated backcrossing. Congenic mice are strains of mice that differ only in restricted regions of the genome. They are generated by mating two inbred strains and backcrossing the descendants 5-10 generations with one of the original strains, known as recipient strain.

Chromosome 3 congenic mice were generated by crossing B6 and FVB mice and backcrossing the resulting heterozygous $Chr3^{FVB/B6}$ F1 mice onto the FVB.*Ldlr*$^{-/-}$ background for 10 generations. Heterozygous FVB.$Chr3^{FVB/B6}$ (carrying an interval from megabases [Mb] 80 to 160 from Chr3 of B6 mice in an otherwise FVB background) were intercrossed to generate FVB.$Chr3^{B6/B6}$, FVB.$Chr3^{FVB/B6}$ and wild-type FVB.$Chr3^{FVB/FVB}$ control mice [148]. To allow identification of the respective congenic and subcongenic mice SNP assays were designed across the chromosome 3 interval from 80 to 160 Mb. All SNPs used for the genotyping are listed in Table 30 of the appendix.

2.1.4 *Generation of hypomorphic Adam17$^{ex/ex}$.Ldlr$^{-/-}$ mice*

Hypomorphic *Adam17*$^{ex/ex}$ mice were obtained from the laboratory of Prof. Rose-John from the Institute of Biochemistry, University of Kiel [132]. Chalaris et al. developed a novel strategy to generate mice with barely detectable levels of ADAM17 in all tissues. The strategy is based on the generation of a new exon within the *Adam17* gene, which starts with an in-frame translational stop codon and which was flanked by splice donor/acceptor sites, which slightly deviated from the canonical consensus sequence. Homozygous mice used the new exon for about 95 % of the *Adam17* mRNAs, resulting in a dramatic loss of ADAM17 protein in all cell types. The hypomorphic *Adam17*$^{ex/ex}$ mice on the C57BL/6 (B6) background were backcrossed onto the Ldl receptor deficient background with C57BL/6 LDLR$^{-/-}$ mice for 6 generations and B6.Ldlr$^{-/-}$Adam17$^{wt/wt}$ (*Adam17*$^{wt/wt}$.*Ldlr*$^{-/-}$), B6.Ldlr$^{-/-}$Adam17$^{wt/ex}$ (*Adam17*$^{wt/ex}$.*Ldlr*$^{-/-}$) and B6.Ldlr$^{-/-}$Adam17$^{ex/ex}$ (*Adam17*$^{ex/ex}$.*Ldlr*$^{-/-}$) mice were generated for further atherosclerosis studies.

2.1.5 *Atherosclerotic studies in mice*

In all atherosclerosis studies, mice were weaned at 28 days of age and fed a semisynthetic diet containing 0.02 % cholesterol until they were killed at 20 weeks of age [99]. Whole blood samples, plasma and tissues were collected from all mice. The aortic root and the brachiocephalic artery were embedded in mounting medium (OCT compound, Tissue-Tek) as described below.

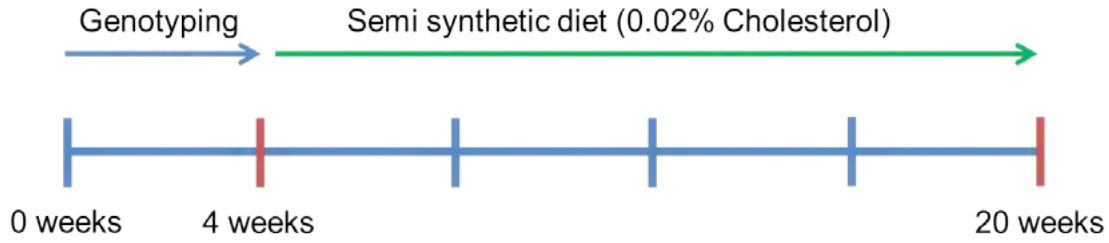

FIGURE 10: Study design of atherosclerosis experiments.

2.2 *Mouse section*

2.2.1 *Removal of organs and vessels*

Mice were euthanized by intraperitoneal anesthesia using 0.2 ml Rompun + 0.6 ml Ketamine. Blood was collected from the right ventricle with 1 ml syringe containing EDTA and subsequently the mouse heart was rinsed with 10 ml PBS containing Heparin. 40 µl of the whole blood was used for determination of the blood parameters and the remaining blood was centrifuged by 8000 rpm for 10 min to collect plasma. Tissues (liver, spleen, kidney, lung, gut, muscle, brain, parametrial/subcutaneous/perirenal fat) were collected from all mice and immediately put into liquid nitrogen and stored at -80 °C. Plasma supernatant was collected for clinical chemistry analyses and determination of lipoprotein subfractions. For atherosclerotic studies, the aortic root (AoR) and the brachiocephalic artery (BCA) were embedded in mounting medium (OCT compound, Tissue-Tek) as described below. Bone marrow was isolated from both femurs and tibias using 10 ml heparinized PBS. The bone marrow was homogenized and the collected cell suspension was drained through a cell strainer (40 µm, Nylon, BD) and centrifuged for 5 minutes at 1000 rpm. The supernatant was discarded and the cell pellet was resuspended in 1.5 ml DMEM (10 % FCS, 1% Pen-Strep) and split into 3 tubes à 500 µl. 400 µl fetal calf serum (FCS) and 100 µl Dimethyl Sulfoxide (DMSO) were added. After gradual freezing at -80 °C for 24h, cells were transferred into liquid nitrogen as cryopreservation for further studies.

2.2.2 *Laboratory analysis*

Clinical chemistry parameters (alanine transaminase [ALT], aspartate transaminase [AST], cholinesterase [ChE], glutamate dehydrogenase [GLDH], Glucose, Urea, Cholesterol [Chol], Triglycerides [TG]) were measured on automated analyzers (Modular PPE, Roche). For determination of blood cell parameters (white blood cells) an automated hematology analyzer (Sysmex) was used. Lipoproteins were determined quantitative by sequential ultracentrifugation (Beckman Coulter, Optima LE-80K Ultracetrifuge, Rotor Ti42.2) from plasma at densities (d) < 1.006 g/ml (very low-density lipoprotein [VLDL]), 1.006 ≤ d ≤ 1.063 g/ml (intermediate-density lipoprotein [ILDL] and low-density lipoprotein [LDL]), and d > 1.063 g/ml (high-density lipoprotein [HDL]) [149]. 60 µl mouse plasma were overlayed with 60 µl PBS in a Thickwall Cellulose Propionate Tube (7x20 mm) (Beckman Coulter) and centrifuged at 4 °C and 40,000 U/min for 3 hours. 60 µl of the lower and the upper phase were transfered to two separate ultracentrifuge tubes, respectively. 60 µl potassium bromide (KBr) (d=1.12 g/ml) were added to the lower phase and centrifuged again for 18 hours at 4 °C and 40,000 U/min. 60 µl of the resulting fractions containing LDL (lower phase) and HDL (upper phase) were transferred to 1.5 ml Eppendorf tubes each. Subsequently, 60 µl of the upper phase, obtained from the first centrifugation step, were mixed with the same volume of PBS and centrifuged for 18 hours at 4 °C and 40,000 U/min. The resulting lower phase contained LDL, whereas VLDL was received from the upper phase. Both fractions were transfered to 1.5 ml Eppendorf tubes as well. Enzymatic colorimetric assays (Roche) were used to determine the cholesterol (cholesterol oxidase-phenol-aminophenazone: CHOD-PAP [150]) and triglyceride (glycerol phosphate oxidase-p-aminophenazone: GPO-PAP) concentration in the lipoprotein fractions (LDL, HDL, VLDL). The measurement was performed with a fluorescence and absorbance reader (SpectraMax Paradigm Multi-Mode Microplate Reader, Molecular Devices) at 500 nm.

2.3 *Histological, histochemical and immunohistochemical methods*

2.3.1 *Quantitative analysis of atherosclerotic lesions*

Atherosclerosis was quantified at the aortic root and the brachiocephalic artery (BCA) as described by [99, 151]. All cryosections were performed with the cryostat LEICA CM1850 from Leica Biosystems.

2.3.1.1 *Brachiocephalic artery (BCA) section*

For quantification of atherosclerosis in the OCT-compound-embedded brachiocephalic artery (BCA), transverse cryosections of 10 µm were prepared in a proximal direction from the bifurcation with the right common carotid artery and right subclavian artery to the aortic arch. Two sections were prepared per slide. At a distance of 200, 400, and 600 µm (Figure 11) proximal from the bifurcation of the BCA the sections (1A, 2A, 3A) were mounted on glass slides and used for oil red O staining and subsequent lesion quantification. The remaining sections (B, C, D) were cryopreserved and used for immunohistochemical stainings.

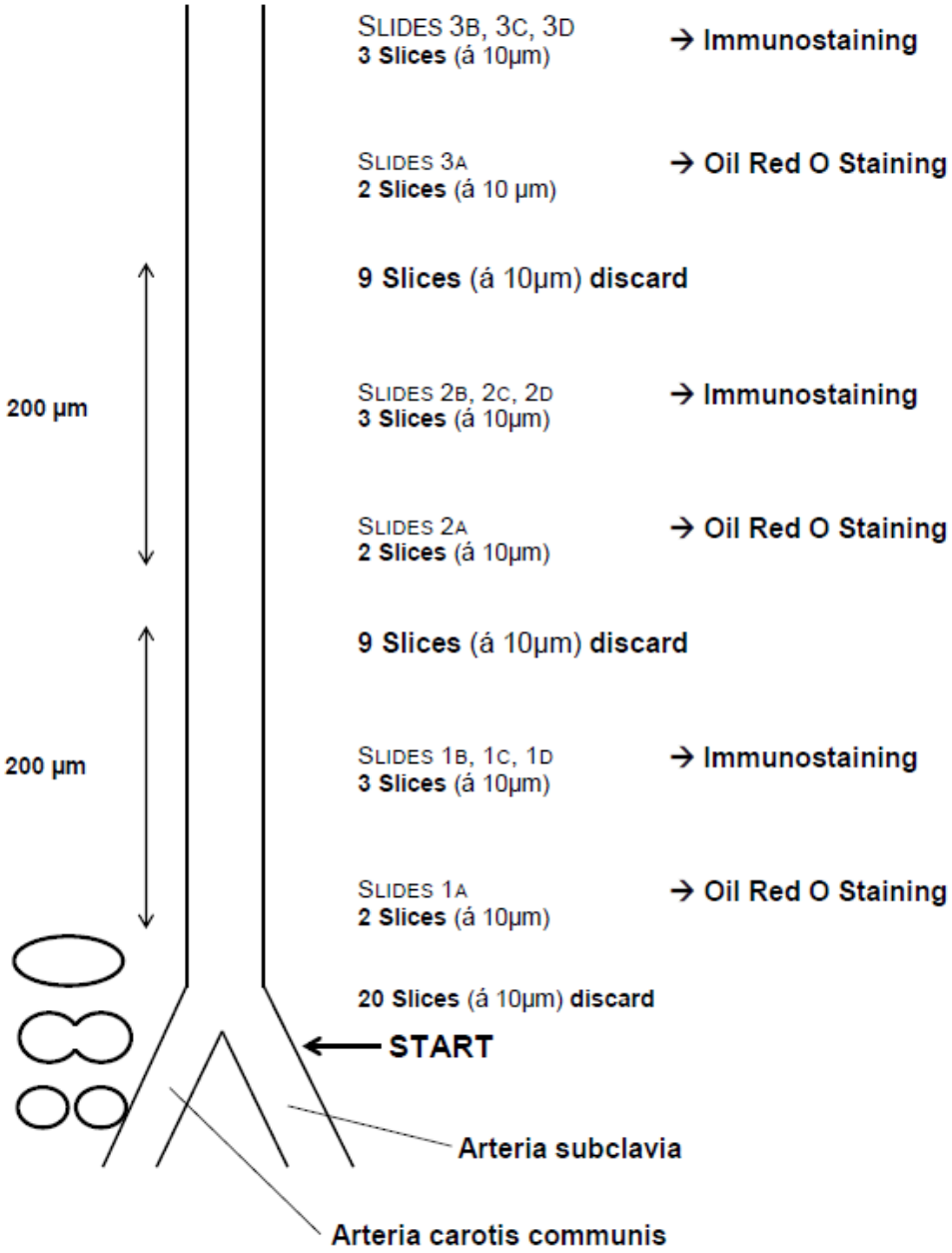

FIGURE 11: Scheme for the preparation of cryosections of the BCA for atherosclerotic and immunohistochemical studies [99].

2.3.1.2 *Aortic root (AoR) preparation*

Determination of atherosclerotic lesions at the aortic root was performed according to a method described by Paigen et al. [151, 152]. Embedded hearts were cut parallel to the valvular level at 10 µm thickness. Preparation of cryosections of the aortic root started when two out of three aortic valves were completely visible, until no aortic valves were observable. 2 sections were preserved per slide (Figure 12).

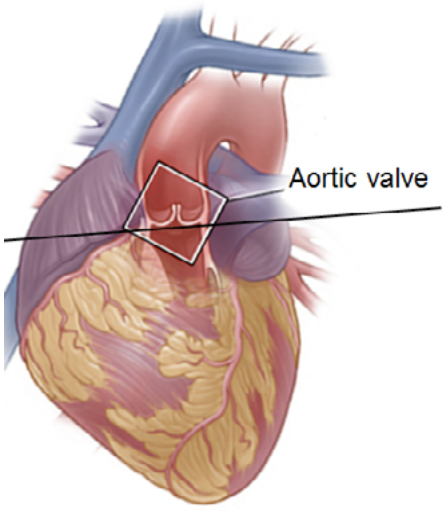

1a Oil Red O 2 Slices
1b Immunostaining 2 Slices
1c Immunostaining 2 Slices
2a Oil Red O 2 Slices
2b Immunostaining 2 Slices
2c Immunostaining 2 Slices
3a Oil Red O 2 Slices
3b Immunostaining 2 Slices
3c Immunostaining 2 Slices
4a Oil Red O 2 Slices
4b Immunostaining 2 Slices
4c Immunostaining 2 Slices
5a Oil Red O 2 Slices
5b Immunostaining 2 Slices
5c Immunostaining 2 Slices
6a Oil Red O 2 Slices
6b Immunostaining 2 Slices
6c Immunostaining 2 Slices
7a Oil Red O 2 Slices
7b Immunostaining 2 Slices
7c Immunostaining 2 Slices

FIGURE 12: Scheme for preparation of cryosections of the aortic root (modified from Healthwise, Incoporated [https://myhealth.alberta.ca]).

All (a) sections were used for oil-red O staining while (b) and (c) sections were used for immunohistochemical stainings. All cryosections were stored at -80 °C for further usage.

2.3.1.3 *Oil red O staining (atherosclerosis staining)*

Quantitative and qualitative analysis of the aortic roots and the brachiocephalic arteries was performed using oil red O (Sigma-Aldrich) for staining neutral triglycerides and lipids, Light Green SF yellowish (Merck) for collagen and Haematoxylin (Sigma-Aldrich) for cell nuclei. Before staining, the cryosections were fixed in formalin solution overnight at 4 °C. The staining was performed with an automatic slide stainer (Bavimed).

TABLE 4: Protocol used for oil red O staining:

Solution	Time
H_2O	1′
H_2O	1′
60 % Isopropanol	30″
oil red O 0.24 %	10′
60 % Isopropanol	2″
H_2O	1′
H_2O	1′
Haematoxylin Solution	2′
Bluing Solution	1′
H_2O	1′
Light Green 0.25 %	30″
H_2O	

Upon oil red oil staining, all sections were mounted with warmed (55 °C) glycerol gelatine (Sigma-Aldrich) and coverslips (VWR).

2.3.1.4 *Quantification of atherosclerotic lesions*

The quantification of atherosclerotic lesions was performed on oil red O-stained sections using a Leitz DMRD fluorescent phase contrast microscope and the Leica Application Suite 4.4 (LAS) software (Leica). All (a) sections of the BCA (5x magnification) and the aortic root (5x magnification) were imaged and lesions were manually quantified with the LAS software (Leica). Only intraluminal lesions were quantified. Atherosclerotic lesions at the BCA were determined as mean value of lesion quantification of the 1A, 2A, and 3A sections. At the aortic root, atherosclerotic lesions were determined as mean value of five sequenced (a)-sections. Aortic root quantification started when 2 of the 3 aortic valves leaflets were no longer visible and then counted back the last five sections (8a-4a or 10a-6a) [153].

2.3.2 *Immunohistochemical staining*

Immunohistochemical staining of serial sections (10 µm) of the aortic root and the brachiocephalic artery was performed using primary antibodies. Frozen sections were fixed in ice-cold methanol-acetone (1:1) solution for 10 min, dried at room temperature for 5 min and washed 3 times with PBS. Peroxidases were quenched with 3 % H_2O_2 for 3 min at RT. Sections were washed and blocked with 2.5 % normal horse (Vector Laboratories) or goat serum for 30 min. The primary antibodies were incubated overnight at 4 °C and then washed with Tween PBS (0.125 % Tween20) and incubated with horseradish peroxidase (HRP-) conjugated secondary antibody for 30 min. After washing, peroxidase was visualized by incubating with Nova Red (Vector Laboratories) and counterstained with hematoxylin. Sections were dried and permanently mounted with Vecta-Mount mounting medium (Vector Laboratories) and photographed with a Leitz DMRD fluorescent phase contrast microscope (Leica). All antibodies and their dilutions used for the immunohistochemical stainings are presented in Table 28 of the appendix.

2.3.3 *Immunofluorescence staining*

Immunofluorescence stainings of PLA2G12A (sc-1043029, Santa Cruz Biotechnology) and ADAM17 (ab39163) and co-staining with CD68 positive macrophages (MCA1957, Serotec), Mac2 positive macrophages (CL8942AP, Cedarlane), α-SMA-positive smooth muscle cells (ab5694; Abcam), von Willebrand Factor (vWF) positive endothelial cells (ab11713, Abcam) and Ki67 proliferating cells (ab15580) was performed on serial cryosections (10 µm) of the aortic root. Cryosections were dried at 50 °C for 10 min and subsequently fixed with 4 % PFA for 15 min. After repeated washing with PBS and PBST (PBS, 0.2 % Triton X-100) cryosections were blocked with 5 % donkey normal serum (X0907, Dako) for 1 h. Samples were incubated with first antibodies overnight at 4 °C in a humidified chamber and afterwards with fluorescently labeled secondary antibodies (Alexa Fluor 594 Donkey anti Rabbit F(ab')2, Dianova; Alexa Fluor 488 Donkey anti Sheep F(ab')2, Dianova; Alexa Fluor 488 Donkey anti Rat F(ab')2, Dianova; Alexa Fluor 488 Donkey anti Goat F(ab')2, Dianova) for 1 h. After washing in PBS, sections were mounted in Fluorescence Mounting Medium (Dako) and photographed with a Leitz DMRD microscope (Leica). Immunostaining results for Ki67, a-SMA and Mac-2 were analyzed by counting the number of $Ki67^+$, $a\text{-}SMA^+$ and $Mac\text{-}2^+$ in the lesions, relative to the number of DAPI-stained nuclei and are expressed as the percentage of the total number of lesional cells [130].

2.3.4 *TUNEL staining*

TUNEL staining for apoptosis detection of serial cryosections (10 µm) of the aortic root was performed using the DeadEnd™ Fluorometric TUNEL System from Promega. Sections were washed by immersion in 0.9 % NaCl and PBS for 5 min, respectively. Subsequently, sections were fixed in 4 % PFA for 15 min and washed twice with PBS for 5 min. Permeabilization was performed by adding 20 µg/ml Proteinase K solution and incubation for 10 min at RT. Sections were washed in PBS and fixed with 4 % PFA. After washing with PBS the sections were incubated for 10 min with equilibration buffer. Labelling of the fragmented DNA of apoptotic cells was accomplished by adding the Terminal Deoxynucleotidyl Transferase (TdT) mix for 1h at 37 °C in a humidified chamber. The reaction was stopped by immersion in 2xSCC solution for 15 min. After repeated washing in PBS sections were mounted in VECTASHIELD Antifade Mounting Medium with DAPI (Vector Laboratories) for staining nuclei. Sections were analyzed by fluorescence microscopy, detecting green fluorescence of apoptotic tissue (520 ± 20 nm) and DAPI stained nuclei in blue (460 nm). To analyze TUNEL staining, the number of $TUNEL^+$ cells in the lesions was counted, relative to the number of DAPI-stained nuclei and plague area [130].

2.3.5 *Collagen and elastin-fiber staining*

Arterial extracellular matrix (ECM) properties were determined by assessing elastic fibers with Verhoeff-Van Gieson staining and by quantifying total collagen fiber content by PicroSirius Red imaging using polarized light.

To study the collagen properties of brachiocephalic arteries (BCA) of wild-type *Adam17*$^{wt/wt}$.*Ldlr*$^{-/-}$ and homozygous *Adam17*$^{ex/ex}$.*Ldlr*$^{-/-}$ mice, cryosections of 10 µm were stained by PicroSirius Red (1.2 % Sirius Red F3 [w/v] [CI 35780, Direct Red, Sigma Aldrich] in saturated picric acid [0.5 % acetic acid]) for 1 h. Cryosections were washed twice with acidified water, dehydrated in three changes of 100 % ethanol and mounted with DPX Mounting medium (Sigma-Aldrich). Images were shot using polarization microscope (Axio Imager.M2, Carl Zeiss Microimaging GmbH, Jena, Germany) and converted to greyscale images. The collagen density was analyzed using the imaging software KS400 (AxioVision KS400, Zeiss).

Staining of elastic fibers was performed by Verhoeff-Van Gieson method. Cryosections were hydrated to distilled water and stained in Verhoeff's solution (5 % alcoholic hematoxylin, 10 % ferric chloride, Weigert's iodine solution) for 1 hour. The slides were rinsed in tap water for 3 times and differentiated in 2 % ferric chloride for 2 minutes. The differentiation was stopped with several changes of tap water and subsequently treated with 5 % sodium thiosulfate for 1 minute. The slides were washed in running tap water for 5 minutes and counterstained in Van Gieson's solution for 5 minutes. The slides were dehydrated through 95 % Ethanol and 2 changes of 100 % Ethanol, cleared in 2 changes of xylene for 3 minutes each and mounted with DPX Mounting medium (Sigma-Aldrich). To quantify the fiber length, we determined the length of individual elastic fibers within sub-segments of identical length (20 µm).

2.3.6 *Labelling of cell surface proteins by biotin*

Cell-membrane proteins of BMDM of mice were labeled using the EZ-Link Sulfo-NHS-SS-Biotin (1 mg/ml in PBS) from Thermo Scientific. EZ-Link Sulfo-NHS-SS-Biotin is a water-soluble, NHS-ester biotinylation reagent with a spacer arm which includes a cleavable disulfide bond for reversible labeling of proteins. It is a negatively charged reagent that does not permeate cell membranes. Cells were incubated with the labeling reagent at 4 °C under gentle agitation for 30 min. The biotin solution was removed by decanting and cells were washed three times with ice-cold PBS. The cells were incubated with 50 mM glycine in PBS solution for 15 min at 4 °C with gentle rocking to block unbound biotin. After repeated washing with PBS, the cells were scraped with RIPA lysis buffer (50 mM Tris pH8, 150 mM NaCl, 1 % Igepal CA-630, 1 % sodium deoxycholate, 0.1 % SDS) supplemented with cOmplete™ Protease Inhibitor Cocktail (Roche); 0.1 mM phenymethylsulfonylfluorid (PMSF); 20 µM metalloproteinase inhibitor BB-2519 (Tocris Bioscience); 10 mM 1,10-phenathroline (Sigma-Aldrich) and 1 mM sodium orthovanadate (NEB). Cells were incubated for 1 hour on ice to swell and homogenized with 25 strokes in a loose-fitting Dounce homogenizer. The whole cell lysate was incubated with Dynabeads MyOne Streptavidin C1 Beads (Invitrogen) overnight at 4 °C to bind the biotin-labeled membrane proteins. The beads were washed three times with PBS buffer and eluted with 1x Laemmli buffer (2 % SDS; 10 % glycerol; 62.5 mM Tris-HCl pH 6.8; 5 % β-mercaptoethanol; 50 mM DTT; bromophenol blue) [130].

2.4 Cell culture

2.4.1 *Cultivation of cells*

Cell culture experiments were performed in murine RAW264.7 macrophages, vascular smooth muscle cells MOVAS, mouse cardiac endothelial cells (MCEC) cells and bone marrow-derived macrophages (BMDM). RAW264.7 cells are a macrophage-like cell line derived from Balb/c mice. RAW264.7 cells were cultivated in Dulbecco's Modified Eagle Medium (DMEM, *Life* Technologies) with 10 % fetal bovine serum (FBS, Millipore) and 1 % penicillin/streptomycin (Pen/Strep, Gibco-*Life* Technologies) as additive. MOVAS (immortalized with SV40 large T antigen smooth muscle cells derived from a C57/BL/6 mouse) were purchased from ATCC (CRL-2797) and cultivated in DMEM (Cat.# 30-2002, ATCC) medium with 10 % FCS and 0.2 mg/ml G-418. Mouse cardiac endothelial cells (MCEC) were purchased from Cedarlane (Cat.# CLU510) and cultivated in DMEM (D5796, Sigma Aldrich) medium with 10 mM penicillin/streptomycin, 10 mmol/L HEPES (Gibco) and 5 % FCS. L929 mouse fibroblasts were cultivated to obtain cell culture supernatant (= L-cell-conditioned medium), containing the macrophage colony-stimulating factor (M-CSF) as an important growth factor for bone marrow cells [154]. Fibroblasts were incubated with DMEM, 10 % FCS and 1 % Pen/Strep for 48h; the supernatant (L-cell-conditioned medium) was separated, filtered and stored at -80 °C thereafter.

Cryo-preserved bone marrow cells were thawed and differentiated into macrophages (BMDM) in the presence of L-cell-conditioned medium for 14 days. BMDM were cultivated in DMEM with the presence of 20 % L-cell-conditioned medium, 10 % FCS, 1 % Pen/Strep and 1 % Partricin as antimycotic. For functional studies, BMDM were incubated with 100 nmol/L Phorbol-12-myristate-13-acetate (PMA, Sigma Aldrich) for 1 h. All cell types were cultured at 37 °C and 5 % CO_2 (Binder incubator).

2.4.2 *Cell culture functional assays*

Cell proliferation, apoptosis and adhesion are all cellular processes which are key regulators in the development of atherogenesis [1].

Cell proliferation was performed in a 96- or 384-well plate with a clear bottom using quadruplicates and was determined by CellTiter-Glo® Luminescent Cell Viability Assay (Promega). The assay is a homogeneous method to determine the number of viable cells based on quantitation of the ATP present, which signals the presence of metabolically active cells (Promega). Upon cell seeding, the single reagent (CellTiter-Glo® Reagent) is given directly to the cultured cells, incubated for 10 minutes and subsequently the luminescence is measured.

Cell apoptosis was performed in a 96-well white flat bottom plate using quadruplicates. Apoptosis was induced for 24 hours with cycloheximide (CHX, Sigma Aldrich), an inhibitor of protein biosynthesis, in concentrations of 10 µg/ml and 50 µg/ml and staurosporine (Merck-Millipore), a protein kinase inhibitor that prevents ATP of binding to the kinase, in concentrations of 0.125 mM and 0.25 mM. The Caspase-Glo® 3/7 Assay (Promega) is a luminescent assay that measures caspase-3 and -7 activities in cultured cells. The reagent is optimized for caspase activity, luciferase activity and cell lysis. Adding the single Caspase-Glo® 3/7 reagent to the cells results in cell lysis, followed by caspase cleavage of the substrate and generation of a luminescent signal. After 1 hour of incubation, protected from light, the luminescence was measured.

Cell adhesion experiments of RAW264.7 macrophages were performed in a 96-well white flat bottom plate using quadruplicates. Initially, the 96-well plate was coated with matrigel and collagen in different dilutions to allow cells to adhere. Treated cells were given to the precoated wells and left 1 hour to allow adhesion. Subsequently, the 96-wells were washed and the number of adherent cells was determined using the CellTiter-Blue® Cell Viability Assay (Promega) in relation to standard curves of the respective cell line. The CellTiter-Blue® assay is a fluorometric method for estimating the number of viable cells present in multiwell plates. It is based on the ability of living cells to convert a redox dye (resazurin) into a fluorescent end product (resorufin). Viable cells retain the ability to reduce resazurin into resorufin. For quantifying adhesion of bone marrow-derived BMDMs to endothelial cells, two different experimental setups were investigated: first, siRNA-treated ECs were preplated on uncoated 96-well plates at 28,000 cells per well 24 hours before the adhesion experiments. BMDMs were seeded on top of preplated MCECs, incubated for 45 min, washed twice with cell culture medium and BMDMs' adhesion was measured with an IncuCyte Live Cell Analysis System (Essen Bioscience). The IncuCyte Live Cell Analysis System allows quantitative live cell imaging and analysis while cells remain within the controlled environment of a standard cell incubator. Adhesion is determined by quantifying the number of macrophages attached on endothelial cells using phase contrast imaging to differentiate between the respective cell types. Quadruplicate measurements per condition were performed. Independently, BMDM were treated with siRNA for 24 hours and subsequently were allowed to adhere to non-treated preplated ECs. Adherent cells were quantified as described above. Cell adhesion assays of RAW264.7 macrophages were performed in 96-well plates coated with Matrigel (BD Biosciences) or on uncoated dishes. Cells were allowed to adhere for 40 min in both conditions. Numbers of adherent cells were determined in relation to standard curves using CellTiter-Glo (Promega). All fluorescence and luminescence measurements were performed with the SpectraMax Paradigm Multi-Mode Microplate Reader from Molecular Devices [130, 148].

2.4.3 *RNAi (small interfering RNA)*

Small interfering RNA (siRNA) consist of approximately 20 (deoxy)ribonucleotides or chemically modified analogs. siRNAs are applied to suppress gene expression in a specific manner [155, 156]. Once the oligonucleotide crosses the cell membrane, it has the ability to bind with high affinity to the target messenger RNA sequence through Watson-Crick base pairing and therefore blocks the protein translation process. siRNA knock-down was performed in murine RAW 264.7 cells, MOVAS, MCEC and Bone Marrow-Derived Macrophages (BMDM) using Lipofectamine2000 (Cat. # 11668030, *Life* Technologies) and the Amaxa Nucleofector Technology (4D-Nucleofector System, Lonza). Lipofectamine is a cationic liposome formulation that forms complexes with negatively charged nucleic acid. These complexes are then taken up by the cell through endocytosis and then released in the cytoplasm (Thermo Fisher Scientific). The Amaxa Nucleofector is basically a electroporation, where cell membranes are made permeable exposing them to short pulses of an intense electric field. For the BMDMs we used the P2 Primary Cell 4D-Nucleofector X Kit L (Catalog # V4XP-2024), for the MCECs the P5 Primary Cell 4D-Nucleofector X Kit L (Catalog # V4XP-5024) and for the RAW264.7 macrophages the SF Cell Line 4D-Nucleofector X Kit L (Catalog # V4XC-2024). Knock-down efficiency was determined by quantitative RT-PCR after 48 h of incubation. siRNAs used for transfection studies are listed below in Table 5.

TABLE 5: siRNAs used for transfection studies.

siRNA	Product No.	Supplier
Adam17	SASI_Mm01_00083937	Sigma Aldrich
Tnfr2	SASI_Mm01_00134452	Sigma Aldrich
Pla2g12a	Cat# s83067	Ambion
Gapdh	Cat#: 4390849	Ambion
SCR	Cat#: 4390843	Ambion

2.5 Molecular biological methods

2.5.1 RNA isolation

RNA isolation from cells and tissues was performed with the monophasic phenol and guanidine isothiocyanate solution (TRIzol, *Life* Technologies) according to the manufacturer's protocol. Mouse tissue (50 mg) homogenization was performed in a Precellys24 homogenizer (PeqLab) using CK24 ceramic beads and 900 µl TRIzol. Subsequently, 600 µl TRIzol was added to the homogenized tissue, which was incubated for 5 min at room temperature (RT). The mixture was centrifuged at 4 °C and 12,000 g for 10 min and the supernatant was transfered to a new Eppendorf tube. After 300 µl chloroform was added, shaken (15 s) and incubated for 2 min at RT, the tube was centrifuged for 20 min at 4 °C. The upper aqueous phase was taken over, mixed with 750 µl isopropanol and precipitated for 10 min at RT, followed by a centrifugation step (10 min, 12,000 g, 4 °C) to pellet the RNA. The RNA pellet was washed twice with 1 ml 75 % ethanol, dried and finally dissolved in Diethyl-pyrocarbonate (DEPC) water (55 °C, 10 min). RNA was stored at -80 °C. RNA isolation from RAW267.4 cells, MOVAS smooth muscle cells, mouse cardiac endothelial cells (MCEC) and bone-marrow-derived macrophages was conducted by lysis of the respective cells with 750 µl TRIzol and addition of 150 µl chloroform. Precipitation was performed using 375 µl isopropanol. The following steps were performed as described before.

2.5.2 RNA isolation of the aortic arch (RNAqueous-Micro Kit)

For isolation of total RNA from the aortic arch of mice the RNAqueous®-Micro Kit (*Life* Technologies) was applied, which is made for micro-sized samples using a guanidinium-based lysis/denaturant and a glass fiber filter separation technology.

150 µl lysis buffer were given in 2 ml screw-cap tubes prefilled with ceramic beads and the aortic arch. The samples were homogenized with the Precellys24 homogenizer for 2 x 20 sec at 5,000 rpm. The lysate was mixed with 75 µl ethanol and centrifuged at RT at 15,000 g for 1 min. 150 µl of the mixture was applied to a silica-based filter that selectively binds RNA. The filter was washed with 180 µl Wash Solution 1 and twice with Wash Solution 2/3. The flow-through was discarded and the filter was centrifuged for 1 min at maximum speed. The RNA was eluted into a new micro elution tube with 20 µl preheated (75 °C) Elution Solution. To remove remaining genomic DNA the sample was subsequently treated with DNase I. 2 µl 10xDNase I Buffer and 1 µl DNase I were added to the sample and mixed gently. After incubation for 20 min at 37 °C, 2 µl of DNase Inactivation Reagent were added, mixed well and left at room temperature for 2 min. The reaction was centrifuged at maximum speed to pellet the DNase Inactivation Reagent and the RNA was transferred to a new RNase-free tube.

2.5.3 *Determination of concentration and purity of nucleic acids*

Nucleic acids and proteins have absorbance maxima at 260 and 280 nm, respectively. To determine the purity and concentration of nucleic acids, we measured the absorbance with the NanoDrop System (Thermo Scientific). The absorbance ratio at these wavelengths has been used as a measure of purity in both nucleic acid and protein extractions. The ratio E_{260}/E_{280} should be 1.8 for DNA and 2.0 for RNA in 1 x TE buffer. Furthermore, the absorbance at 238 nm is accepted as being the result of other contamination. Therefore the ratio of A_{260}/A_{230} was also calculated. The ratio E_{260}/E_{230} for "pure" nucleic acid is commonly in the range of 2.0-2.2.

2.5.4 *Complementary DNA (cDNA) synthesis by reverse transcription (RT)*

Reverse transcription (RT reaction) is a process in which single-stranded RNA is reverse transcribed into a stable complementary DNA (cDNA) for PCR amplification. RNA from mouse tissue, RAW264.7 cells, MCECs, MOVAS and bone marrow-derived macrophages was reversed transcribed into cDNA using Superscript II reverse transcriptase (Invitrogen) and random hexamer primers. 100 ng-2 µg dissolved RNA was diluted with DEPC-H_2O to a final volume of 10 µl. 1 µl random hexamer primers (500 µg/ml, Roche) was added and incubated for 10 min at 68 °C, followed by the addition of 9 µl master mix and the incubation for 60 minutes at 42 °C.

TABLE 6: Master mix composition for the reverse transcription.

1 µl Recombinant RNAsin Ribonuclease (10,000 U, Promega)
1 µl dNTPs (10 mM, Invitrogen)
2 µl DTT (0.1 M, Invitrogen)
4 µl 5 x First Strand Buffer (FSB, Invitrogen)
1 µl Superscript II Reverse Transcriptase (200 U/µl, Invitrogen)

The samples were diluted with 1xTE buffer at a ratio of 1:15. Aortic arches were diluted at a ratio of 1:5. cDNA samples were stored at -20 °C until further use.

2.5.5 *Whole genome mRNA expression analysis*

Whole genome expression analysis was performed in liver RNA from congenic FVB.Chr3$^{B6/B6}$ (n = 4) and FVB (n = 4) mice, as well as in the aortic arch and bone marrow-derived macrophages (with and without PMA stimulation) from wild-type *Adam17*$^{wt/wt}$.*Ldlr*$^{-/-}$ (n = 4) and homozygous *Adam17*$^{ex/ex}$.*Ldlr*$^{-/-}$ (n = 4) mice. The total RNA was labeled and hybridized to Illumina Ref8V2 BeadChips and imaged using the iScan System at the Interdisciplinary Center for Clinical Research Leipzig (PD Dr. Knut Krohn, Faculty of Medicine, University of Leipzig). Bead level data preprocessing was done in Illumina Genome Studio, the integrated data analysis software platform. Upstream regulator analysis was performed using transcripts with expression changes of < 0.7 and > 1.3 using the Ingenuity Pathway Analysis (IPA) software (www.ingenuity.com).

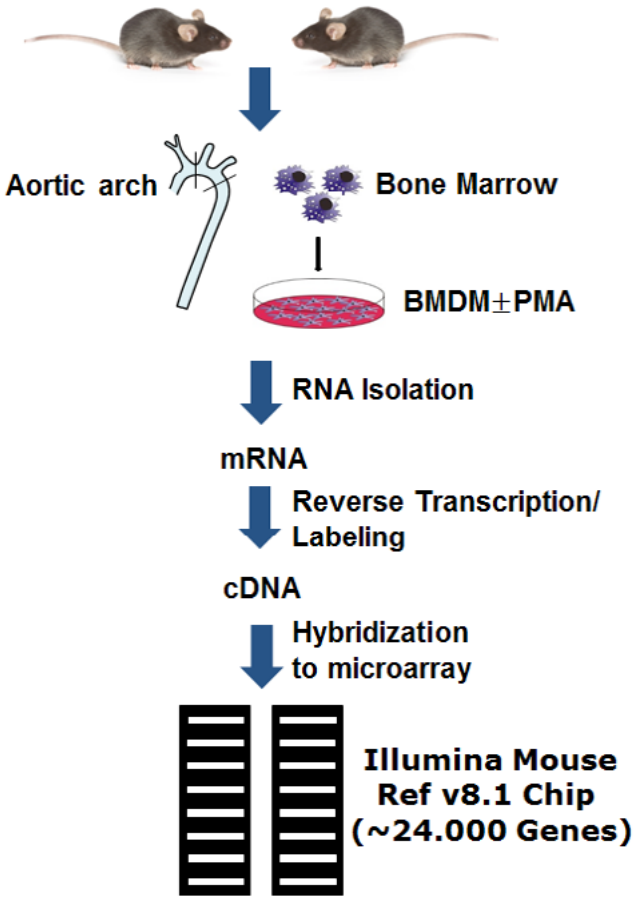

FIGURE 13: Whole genome expression analysis in mice.

2.5.6 *Isolation of genomic DNA from mice*

DNA from tails or ear tags of mice was isolated using lysis buffer (50 mM Tris, pH8; 100 mM EDTA; 100 mM NaCl; 1 % SDS), proteinase K and 100 % isopropanol for precipitation. A tail- or ear-tag biopsy was incubated in a thermomixer at 55 °C overnight with 500 µl lysis buffer and 50 µl proteinase K (Roche, 10 mg/ml). After incubation, the samples were centrifuged at maximum speed for 10 minutes. The supernatant was transferred to a new tube and an equal volume of 100 % isopropanol was added. The solution was mixed by inversion several times and subsequently centrifuged at 10,000 xg for 10 minutes. The supernatant was carefully removed and the DNA pellet was washed with 500 µl of 70 % ice-cold ethanol. After centrifugation for 10 min at 4 °C and maximum speed, EtOH was removed and the tubes were turned upside down to air-dry. The dried DNA pellets were dissolved to a concentration of 30-50 ng/µl with 0.1xTE (10 mM Tris, pH 8.0; 1 mM EDTA). DNA was stored at 4 °C until further analyses.

2.5.7 *Genotyping*

Genotyping is used for the determination of differences in the DNA sequence of an individual compared to that of another individual or a reference sequence. Single nucleotide polymorphisms (SNPs) have emerged as genetic markers of choice because of their high-density and relatively even distribution in the human genomes [157-159]. SNPs typically have three genotypes, denoted generically as homozygous for AA, heterozygous for Aa or homozygous for aa. Genotyping was performed in *Adam17* hypomorphic mice and in chromosome 3 congenic mice via melting curve analysis as described below.

2.5.7.1 *Adam17 genoytping (hypomorphic Adam17 mice)*

Genotyping of hypomorphic *Adam17* mice was performed by polymerase chain reaction (PCR) as described by Chalaris et al. [132]. To construct a targeting vector for the *Adam17* gene, Chalaris et. al inserted a loxP sequence followed by a noncanonical donor splice site downstream of a cryptic acceptor splice site within intron11. This manipulation generated a new exon between exons 11 and 12, which started with an in-frame translational stop codon. Whereas in wild-type animals only a band of 380 bp (wt/wt) was detected, heterozygous ADAM17$^{wt/ex}$ mice showed an additional band of 550 bp (wt/ext) corresponding to the insertion of the new exon. Homozygous *Adam17* mice showed only a band at 550 bp (ex/ex) (Agarose gel Figure 14). *Adam17* genotyping was performed in a FlashGel™ System (LONZA) with the FlashGel™ DNA marker 50 bp - 1.5 kb (LONZA).

TABLE 7: *Adam17* genotyping by PCR (Master mix and cycle parameter).

DNA Template	2.0 µl
AmpliTaq Gold 360 Mastermix	6.25 µl
360 GC Enhancer	1.25 µl
ADAM17_DNA_Fwd	0.625 µl
ADAM17_DNA_Rev	0.625 µl
Dest. H_2O	1.75 µl
Total	**12.5 µl**

Cycle – Parameter:

95 °C	5′	
95 °C	1′	43 x
52 °C	1′	
72 °C	1′	
72 °C	5′	
4 °C	∞	

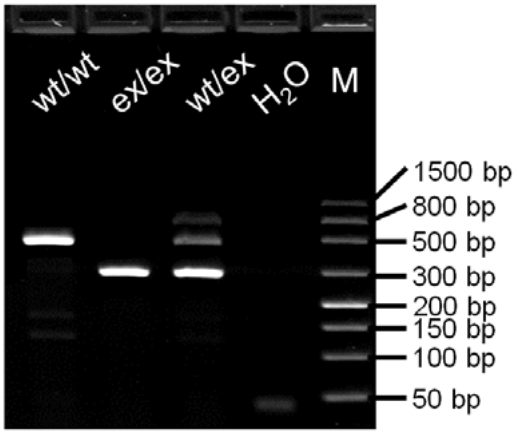

FIGURE 14: Agarose gel of *Adam17* genotyping.

2.5.7.2 *SNP genotyping via melting curve analysis (chromosome 3)*

The chromosome 3 genotyping was performed using known single nucleotide polymorphisms (SNP) between the two parental strains B6 and FVB. To find known SNPs across the required interval (80-160 Mb) on chromosome 3 we used Phenome Jax (www.phenomejax.de), a mouse database, were SNPs of different mouse strains are listed.

SNP genotyping was performed using melting curve analysis with a single dual-label probe, at the end of a classic PCR-reaction amplifying the DNA region in which the mutation of interest lies. In contrast to a standard qRT-PCR-protocol, the probe is not hydrolyzed through the 5′-exonuclease activity of the Taq-polymerase. To avoid hydrolysis of the probe during the PCR-reaction, the melting point of the probe was chosen 10 °C below the annealing temperature of the PCR primers. Melting curve analysis was performed by stepwise increase of the temperature and continuous detection of the fluorescence signal. The probe dissociates from the DNA with the mutated allele at a lower temperature than from the DNA with the homozygote wild-type allele (Figure 14). The here described method is based on the decrease of the FRET (Förster resonance energy transfer) phenomenon, when the probe is released from the target sequence and achieves a random single-stranded conformation. The distance between the reporter and the quencher molecules of the melted probe becomes shorter resulting in a FRET effect, which is inversely proportional to the sixth power of this distance. Therefore, a difference in the fluorescence emission between the hybridized and the melted configurations of the probe is detectable [160]. Primers were designed using the Primer Express software (*Life* Technologies) and probes with the freeware MELT-CALC (www.meltcalc.de) purchased by Eurofins Genomics. Primers hat a final concentration of 100 and 900 nM respectively, whereas the primer with the lower concentration is located on the strand where the probe has its binding site. The probe had a final concentration of 100 nM.

All reactions were performed in 384-well plates in the LightCycler480 II (Roche) under the following conditions:

TABLE 8: Master mix, cycle parameter and melting curve analysis parameter for SNP genotyping via melting curve analysis.

Reagent	Stock	Final	1 x Reaction [µl]
$MgCl_2$ [mM] – Solis Biodyne	25 mM	4	2.00
10 x Buffer – Solis Biodyne	10 x	1	1.25
dNTP Mix [mM] – Promega	2.5 mM	0.25	1.25
FIREPol DNA Polymerase I [U/µl] – Solis Biodyne	5 U/µl	0.05	0.13
Probe [µM] – MWG	10 µM	0.1	0.13
Primer Fwd [µM] – MWG	20 µM	0.1	0.06
Primer Rev [µM] – MWG	20 µM	0.9	0.56
BSA [mg/ml] – NEB	10 mg/ml	0.5	0.63
H_20-Lichrosolv			4.00
+ DNA-Template			2.50
Total			**12.50**

Cycle – Parameter:

95 °C	5′	
95 °C	1′	43 x
62.5 °C	1′	
72 °C	1′	
72 °C	5′	
4 °C	∞	

Subsequently a melting curve analysis was performed, using the following parameters:

95 °C	3′
20 °C	2.5′
20 °C to 95 °C	ramp rate of 5 °C/min
95 °C	15″

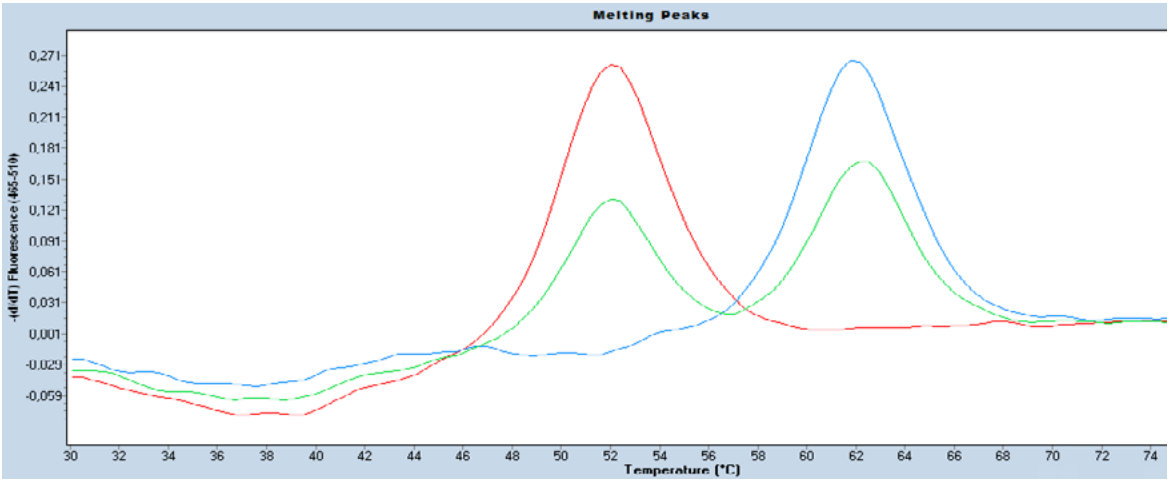

FIGURE 14: Using melting curve analysis of Real-Time PCR we can detect single-nucleotide polymorphisms (SNP) and can distinguish between homozygous wildtype (red), heterozygous (green) and homozygous (blue) mutant alleles.

2.5.8 *Polymerase chain reaction (PCR)*

The polymerase chain reaction (PCR) is used for the amplification of specific DNA or cDNA sequences. The method relies on repeated cycles of three temperature-dependent steps: denaturation of the double-stranded DNA into single-stranded DNA; annealing of the specific primers to the single-stranded template DNA; elongation of the primers by Taq-Polymerase and therefore duplication of the DNA-fragment between the primers. Specific primers for the amplification of genes were designed with the Primer Express 2.0 software (Applied Biosystems). Primer pairs annealed at two sequenced exons of the cDNA of the candidate genes. The synthesis of primers used was carried out at MWG Biotech (Ebersberg). Tables 9 and 10 show the PCR protocol and the cycling conditions.

TABLE 9: Standard-protocol for PCR.

DNA- or cDNA-*Template*	2.5 µl
10 x PCR-Puffer (Roche)	2.5 µl
$MgCl_2$ (25 mM, Solis Biodyne)	5.0 µl
dNTPs (1250 µM)	2.5 µl
Forward-Primer (20 pmol/µl)	0.5 µl
Reverse-Primer (20 pmol/µl)	0.5 µl
Ampli Taq Gold DNA-Polymerase (Roche)	0.25 µl
H_20	13.75 µl
Total	**25.00 µl**

TABLE 10: Cycling conditions for the PCR.

	T [°C]	t [min]	Cycles
Initial Denaturation	95 °C	10:00	
Denaturation	95 °C	0:10	40 x
Annealing/Elongation	60 °C	1:00	
Final Elongation	60 °C	2:00	
	4 °C	∞	

2.5.9 *Agarose gel electrophoresis*

Agarose gel electrophoresis is used for separating DNA fragments of varying sizes. The phosphate backbone of the DNA (or the RNA) molecule is negatively charged, therefore when placed in an electric field, DNA (and RNA) will move to the positively charged anode. Fragments of DNA migrate through the pores of the gel at a rate which is inversely proportional to the log of their molecular weight.

DNA and RNA were separated using TAE-gels with different concentrations of agarose (0.8-3 %), dependent on the expected fragment size. The molecular-weight size marker X (Roche Diagnostics) was used as standard to identify the approximate size of the respective fragments. The electrophoresis buffer consisted of 2 M Tris-acetate and 5 mM Na_2EDTA (pH 8.0). After running the gel for 30-90 min at 80 Volt, it was stained with ethidium bromide (1 ng/ml) for 5 min, destained for 5 min in distilled water and the visualization of bands was performed an UV transilluminator (Fusion X, PeqLab).

2.5.10 *Subcloning of PCR fragments into PCR® II-TOPO*

Cloning of PCR-products was performed with the TOPO TA Cloning Kit (Invitrogen) according to the manufacturer's instructions. 10-20 ng of PCR-product were ligated into the 3950 bp pCR® II-TOPO vector (TOPO™ TA Cloning Kit, Invitrogen) and then transformed into *Escherichia coli* cells (Top10 One Shot, Invitrogen). Successfully transformed bacteria are selected based on their ampicillin resistance. Furthermore, the blue-white selection allows the identification of successful products of cloning reactions through the colour of the bacterial colony. The LB agar plates contain apart from ampicillin, IPTG and X-Gal. The multiple cloning site (MCS) of the pCR® II-TOPO vector is flanked by the lacZ sequence. After a successful incorporation of a PCR-product a functional β-galactosidase enzyme is not produced. If β-galactosidase is produced, X-Gal is hydrolyzed, which spontaneously dimerizes to produce an insoluble blue pigment. The colonies therefore appear blue while the recombinant ones appear white. The white recombinant colonies are picked and cultured.

LB-Medium and LB-Agar were prepared as follows and autoclaved overnight.

TABLE 11: LB-Medium and LB-Agar.

LB-Medium	LB-Agar
5 g Tryptone (BD)	5 g Tryptone (BD)
2.5 g Yeast extract (BD)	2.5 g Yeast extract (BD)
5 g NaCl (Roth)	5 g NaCl (Roth)
ad 500 ml H_20 dest	7.5 g Bacto Agar (BD)
	ad 500 ml H_20 dest

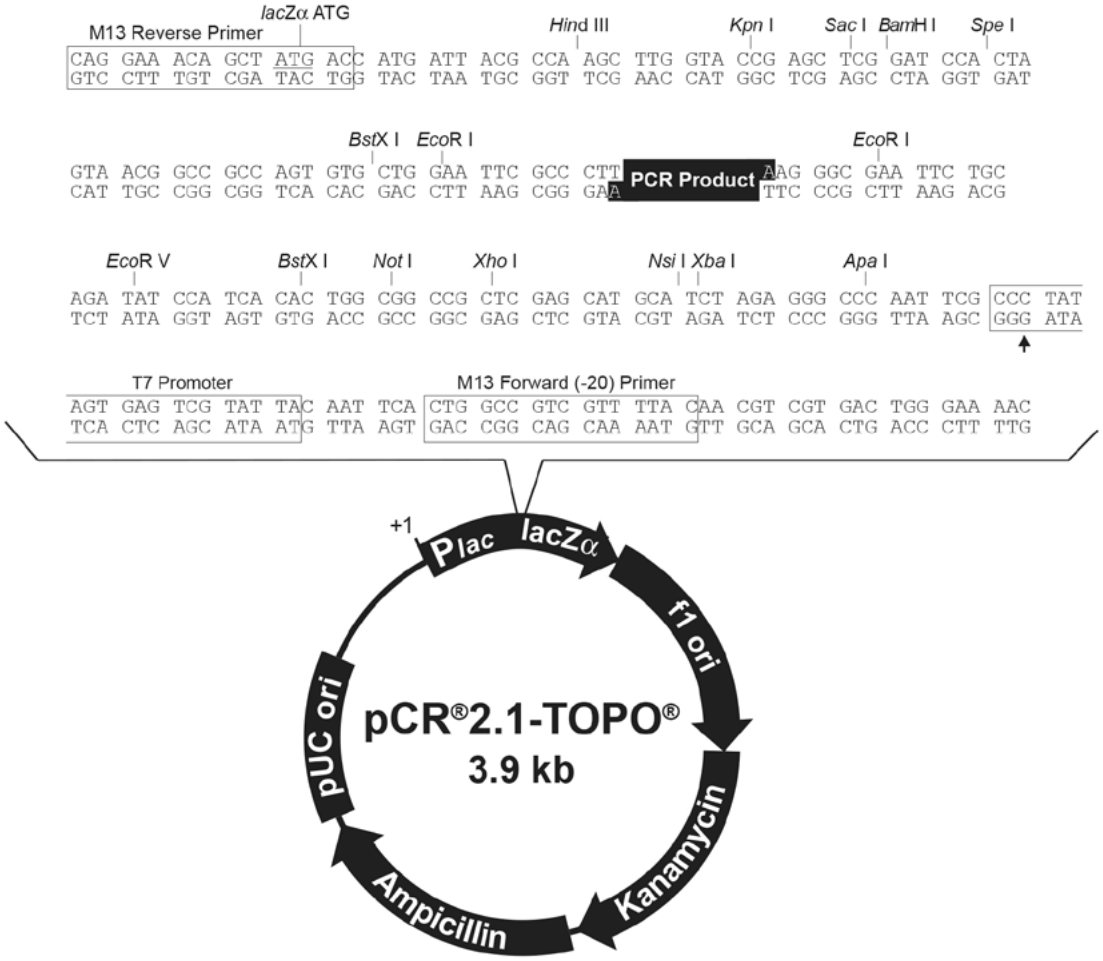

FIGURE 15: pCR 2.1-TOPO vector.

2.5.11 *Preparation of plasmid-DNA (plasmid-mini preparation)*

Mini-preparation of plasmid DNA was performed using the Fast Plasmid Mini Kit (5Prime). This Kit uses a single solution for cell resuspension, lysis and DNA trapping. This single solution contains a mixture of enzymes and detergents that lyse bacterial cells, denatures and solubilizes cellular components, degrades RNA and traps DNA on a matrix, all in one step (5Prime).

In brief, 1.5 ml of fresh bacterial culture were pellet at maximum speed. The medium was removed by decanting. 400 µl of ice-cold Complete Lysis Solution were added and mixed thoroughly by constant vortexing for 30 seconds. The lysate was incubated at room temperature for 3 minutes and transferred to a Spin Column Assembly by decanting. The Spin Column Assembly was centrifuged for 60 seconds at maximum speed. 400 µl of DILUTED Wash Buffer were added to the Spin Column Assembly and centrifuged for 60 seconds at maximum speed. Subsequently the Spin Column was centrifuged again at maximum speed for 1 minute to dry the Spin Column. The Spin Column was then transferred into a Collection Tube. 50 µl Elution Buffer were directly added to the center of the Spin Column membrane and centrifuged at maximum speed 60 seconds.

The plasmids were analyzed by restriction analysis to confirm the presence of the insert. The insertion site of the pCR® II-TOPO vector is flanked by EcoRI restriction sites. 1 µl Plasmid was incubated for 2h at 37 °C with 20 U EcoRI (New England Biolab, Frankfurt/Main), the respective reaction buffer and 0.5 µl RNAse (0.5 µg/µl; Boehringer, Mannheim) in a final volume of 10 µl. The size of the resulting fragments was checked on an agarose gel.

2.5.12 *DNA-sequencing*

Sequencing was performed to confirm that the fragment is cloned into the plasmid in the correct orientation. Primers M13 fwd and M13 rev (Invitrogen) were used, which hybridize on both sides of the pCR® II-TOPO insertion site.

TABLE 12: Master mix for the sequencing reaction.

Reagent	1x Reaction
Big Dye 5x Dilution Buffer (Applied Biosystems)	2.0 µl
Big Dye 3.1 Reaction Mix (Applied Biosystems)	1.5 µl
M13-Primer forward or reverse (5 µM)	1.0 µl
Plasmid (m ~ 1.0 µg)	
H_2O	ad 10.0 µl

TABLE 13: Cycling conditions.

T [°C]	t [min]	Cylcles
96 °C	1:00	
96 °C	0:10	25 x
50 °C	0:05	
60 °C	2:00	

After cycle sequencing, reactions were cleaned up by ethanol precipitation to remove unincorporated dye nucleotides. The samples were mixed with 10 µl H_20, 2 µl 3 M Na-Acetate (pH 5.2) and 55 µl 100 % Ethanol, centrifuged for 20 min at 14,000 xg and 4 °C and the supernatant was discarded. The pellet was washed with 250 µl 70 % Ethanol and centrifuged again. The final pellet was dried for 10 min at 68 °C. Sanger sequencing of the respective samples was performed at MWG Eurofins.

2.5.13 *Standard curve preparation for qRT-PCR (TaqMan)*

Plasmids containing cloned target sequences were used as standards in quantitative RT-PCR. Initially the plasmid standard was linearized with a restriction endonuclease, which cuts the vector (not the insert) at a single restriction site.

3 µg Plasmid-DNA, 4 µl 10x Restriction-Buffer, 40 U HindIII (or XhoI) (New England Biolabs) and DEPC.H_2O to a final volume of 40 µl were incubated at 37 °C overnight. The restriction enzyme was inactivated for 20 min at 65 °C. The result of the restriction was initially checked on an agarose gel and the concentration of the linearized plasmid-DNA was measured with the NanoDrop System (Thermo Scientific).

The clone picked as standard was diluted to 10^9 single-strand molecules/µl with 1xTE buffer. Dilution to the required copy number of the standard curve was performed with 1xTE buffer containing 0.06 % 5 x First Strand Buffer.

2.5.14 *Quantitative real-time PCR (TaqMan)*

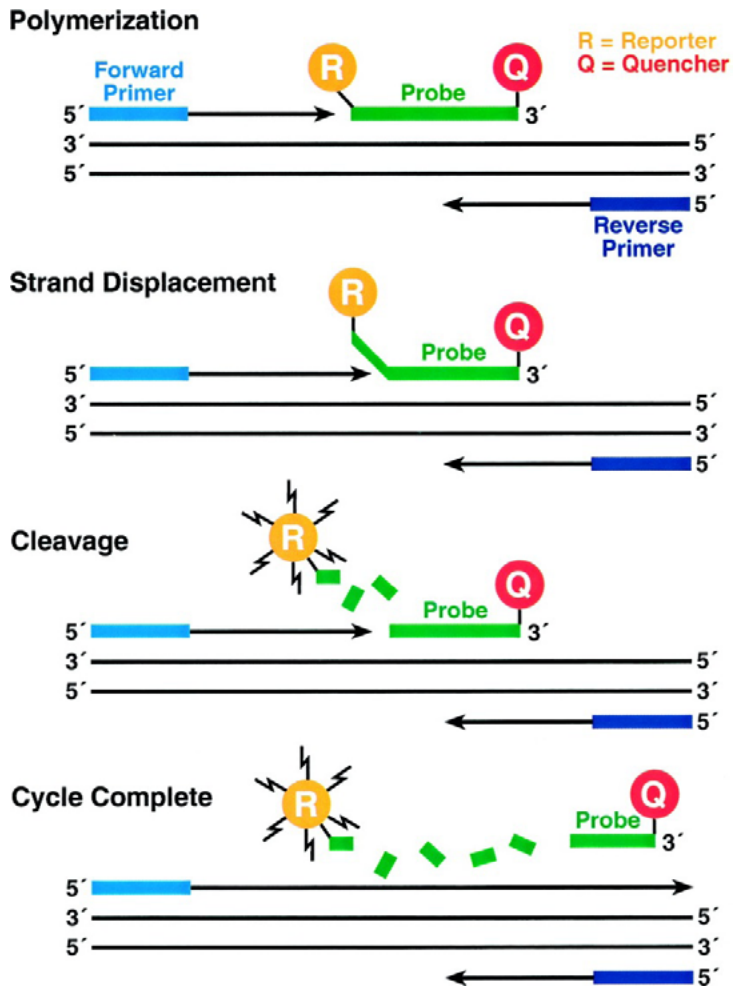

FIGURE 16: Principle of TaqMan probe-based assays [2].

Real-time quantitative PCR allows the specific detection of PCR-products generated during each PCR-cycle, which are directly proportional to the amount of template prior to the start of the PCR process. TaqMan probes are labeled on the 5` end with a fluorescent dye reporter (FAM) and a quencher dye which is attached to the 3´ end (TAMRA). TaqMan probes spann the exon/exon junction to avoid significant amplification of contaminative genomic DNA. The TaqMan probe anneals downstream from one of the primer sites and as long as the probe is intact FRET (fluorescence resonance energy transfer) occurs and the fluorescence emission of the reporter dye is absorbed by the quenching dye. The probe is cleaved by the 5´ nuclease activity of the Taq polymerase enzyme during the extension phase of the PCR. Cleavage of the probe separates the reporter and quencher dyes, thereby increasing the fluorescence from the reporter dye. The increase in the intensity of fluorescence is proportional to the formation of PCR products.

2.5.14.1 *Quantification of candidate genes*

Quantification of gene expression was performed on ViiA 7 Real-Time PCR-System (Life Technologies). All primers and probes used for the candidate genes quantification are listed in Table 29 of the appendix. Cloned cDNA fragments of the template were used as standards in serial dilutions and *Beta actin* (*Ba*) was used as housekeeping gene. Quantification of candidate genes was performed in quadruplicates in a 384-well plate.

The following protocol was used for all qRT PCRs:

TABLE 14: PCR conditions.

Reagent	**1 X Reaction**
H_2O	4.56 µl
$MgCl_2$ (25 mM Stock)	2.5 µl
10xPCR Buffer	1.25 µl
dNTPs	1 µl
Forward primer (300 nM)	0.1875 µl
Reverse primer (300 nM)	0.1875 µl
Probe (10 µM Stock)	0.25 µl
Ampli TaqGold Polymerase (Thermo Fisher)	0.0625 µl
Total	ad 10.0 µl
+ cDNA/Standard	2.5 µl
Reaction volume	**12.5 µl**

TABLE 15: Cycling conditions.

	T [°C]	**t [min]**	**Cycles**
Initial Denaturation	95 °C	10:00	
Denaturation	95 °C	0:10	40 x
Annealing/Elongation	60 °C	1:00	
Final Elongation	60 °C	2:00	
	4 °C	∞	

2.6 Functional analysis

2.6.1 Western blotting

Proteins are separated using gel electrophoresis followed by the transfer of proteins to a membrane. Now the proteins can be detected with specific antibodies.

Western blots were performed with mice tissues, whole cell lysates (RAW264.7, MOVAS, MCEC and BMDM) and isolated cell membrane proteins of BMDM (3.1.) of mice. Cells were scraped with RIPA lysis buffer (50 mM Tris pH8, 150 mM NaCl, 1 % Igepal CA-630, 1 % sodium deoxycholate, 0.1 % SDS) supplemented with cOmplete™ Protease Inhibitor Cocktail (Roche); 0.1 mM phenymethylsulfonylfluorid (PMSF); 20 µM metalloproteinase inhibitor BB-2519 (Tocris Bioscience); 10 mM 1,10-phenanthroline (Sigma-Aldrich) and 1 mM sodium orthovanadate (NEB). Mouse tissue was homogenized in a Precellys24 homogenizer (PeqLab) using CK24 ceramic beads using 300 µl RIPA lysis buffer. Cells and tissues were incubated for 1 hour on ice to swell and subsequently centrifuged at 13,000 xg for 30 min and 4 °C. The supernatant was removed and the protein concentration was measured using the Pierce™ BCA Protein Assay (Thermo Scientific). The bicinchoninic acid assay (BCA assay) is a biochemical assay for determining the total concentration of protein in a solution (0.5 µg/mL to 1.5 m/mL). The principle of this method is that proteins can reduce Cu^{+2} to Cu^{+1} in an alkaline solution (biuret reaction) and result in a purple color formation by bicinchoninic acid. The absorbance was detected at 562 nm on a plate reader (SpectraMax Paradigm Multi-Mode Microplate Reader, Molecular Devices) and the concentration was determined using a standard curve (Diluted Albumin [BSA] Standards).

Equal amounts of protein (20 µg per sample) were loaded on 10 % NuPAGE Bis-Tris Mini or Midi gels (Invitrogen). Subsequently proteins were blotted to nitrocellulose or PVDF (Polyvinylidene fluoride) membranes for 1h by 135 mA. Membranes were blocked for 1 hour using PBS, 0.3 % Tween 20, 0.05 % Triton X-100 and 5 % skim milk powder, followed by incubation with the primary antibody overnight at 4 °C. Dilutions of primary and secondary antibodies are given in Table 28 of the appendix. Protein bands were visualized by chemiluminescence (AceGlow-Solution [PeqLab]) and detected with the Fusion FX image system (PeqLab). The densitometric analysis of proteins on western blots was performed using the ImageJ Software (NIH).

2.6.2 Multiplex immunoassay

The Luminex technology enables up to 100 proteins or genes to be detected simultaneously in each well of a 96 or 384-well plate, using very small sample volumes. Biomolecules (such as an oligo or antibody) are conjugated to the surface of beads, allowing the capture and detection of specific analytes from a sample. Furthermore, the beads are internally dyed with red and infrared fluorophores, marking each bead with a unique spectral signal and therefore representing a particular assay. A dual detection flow cytometer is used to sort out the different assays by bead colors in one channel and to determine the concentration of the specific analyte by measuring the reporter dye fluorescence in another channel. Common applications include the detection of cytokines, metabolic markers and phosphorylated proteins. The concentrations of released ADAM17 substrates, like receptors, cytokines, chemokines and adhesion molecules were detected in the plasma and the supernatant of BMDM of wild-type $Adam17^{wt/wt}$.$Ldlr^{-/-}$ (n = 12), heterozygous

Adam17$^{wt/ex}$.*Ldlr*$^{-/-}$ (n = 10) and hypomorphic Adam17$^{ex/ex}$.*Ldlr*$^{-/-}$ (n = 12) mice. The assays were performed using the bead-based Milliplex xMAP multiplex technology (Millipore) according to the manufacturer's instructions on the Luminex 100 instrument (Biorad). In the following table are the assays and the parameters listed that were measured.

TABLE 16: Multiplex assays and parameters mesaured in wild-type Adam17$^{wt/wt}$.*Ldlr*$^{-/-}$ (n = 12), heterozygous Adam17$^{wt/ex}$.*Ldlr*$^{-/-}$ (n = 10) and hypomorphic Adam17$^{ex/ex}$.*Ldlr*$^{-/-}$ (n = 12) mice.

Assays	Cytokines/Receptors
Milliplex Map Mouse Cytokine/Chemokine (Cat.# MCYTOMAG-70K – Millipore)	GM-CSF, IL-10, KC, MCP-1, TNF-α
Milliplex Map Mouse Cytokine/Chemokine Magnetic Bead Panel II (Cat.# MCYP2MAG-73K – Millipore)	Fractalkine
Milliplex Map Mouse Cardiovascular Disease (CVD) Panel I (Cat.# MCVD1-77AK – Millipore)	VCAM-1, ICAM1
Milliplex Map Mouse Soluble Cytokine Receptor Magnetic Bead Panel (Cat.# MSCRMAG-42K – Millipore)	sCD30, sgp130, sIL-6R, sVEGFR2, sIL-1R2, sTNFR1, sTNFR2
Bio-Plex Pro™ Mouse Cytokine Group I assay (Biorad)	sIFNγ, sIL-1b, sIL-10, sIL-6, sMIP-1α, sMIP-1β, sRANTES, sMCP-1, sEotaxin

Using standard curves, analyte concentrations were determined using the Bio-plex software.

2.7 Statistics

For statistical analysis of data the GraphPad Prism Software (Version 6.0) was used. All data are given as mean ± SEM unless otherwise indicated. Normality of distribution was assessed using the Kolmogorov-Smirnov test. Comparison of multiple groups was done using ANOVA and Tukey was performed as a post-test. Comparison of 2 groups of normally distributed samples was done using the t-test.

3 Results – Chapter I –

Quantitative trait locus mapping in mice identifies phospholipase Pla2g12a as novel atherosclerosis modifier

This work has been published in [148].

3.1 Quantitative trait locus mapping (QTL) of atherosclerosis on mouse chromosome 3

In a previous study, a novel atherosclerosis susceptibility locus on mouse chromosome (Chr) 3 was identified by quantitative trait locus (QTL) mapping in atherosclerosis-susceptible C57BL/6 (B6) and atherosclerosis-resistant FVB mice on the low density lipoprotein (LDL)-receptor-deficient background (*Ldlr*$^{-/-}$) [104]. For the initial QTL mapping, F1 animals from reciprocal crosses of male and female B6 and FVB mice were intercrossed and atherosclerosis lesion sizes were quantified in the F2 generation. The Chr3 locus was gender-dependent and only present in female F2 mice [104]. Furthermore, different LOD score maxima were observed in different female crosses according to the breeding scheme of the F0 generation (Figure 17 A, B). In cross A, male B6 mouse was mated with female FVB (F0 = male B6xfemale FVB), the maximum LOD score at 78.5 cM at marker d3mit45 was 3.3. In cross B, a male FVB mouse was mated with a female B6 mouse (F0 = male FVBxfemale B6), with a maximum LOD score of 4.1 at 55 cM at marker d3mit57.

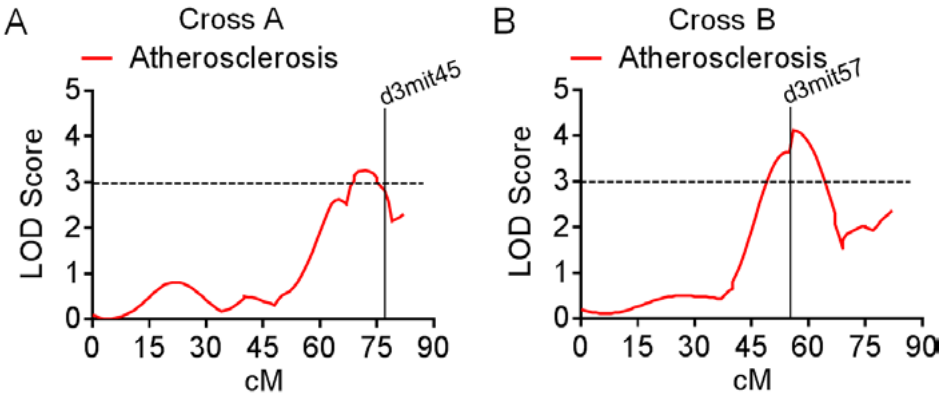

FIGURE 17: Atherosclerosis LOD scores on mouse chromosome 3. The Chr3 locus was gender-dependent and only present in female F2 mice. (**A**) LOD score in cross A was generated from male B6 and female FVB and (**B**) cross B from male FVB with a female B6 mouse.

Lineage-dependency of loci at Chr3 suggested that different molecular mechanisms might underlie the two distinct female atherosclerosis loci. This indicated that potentially independent candidate genes on the Chr3 risk QTL predisposed for atherosclerosis susceptibility in females. To validate the Chr3 atherosclerosis locus and to identify the causal genes in both subcrosses we first generated chromosome 3 congenic mice and performed expression studies in congenic and F0 mice as well as in mice of the F2 generation.

3.1.1 Fine-mapping of Chr3 subloci in female F2 mice in cross A and cross B

To fine-map the two previously identified female-specific atherosclerosis risk subloci and to reduce the number of potential candidate genes within the Chr3 QTL [104], we genotyped 107 female mice of cross A and 120 female mice of cross B with 6 additional single nucleotide polymorphisms (SNPs). The 6 additional SNPs were evenly spaced along the genome on chromosome 3 (Table 17) [148].

TABLE 17: SNPs used for fine-mapping and their chromosomal position.

Number	SNP #	Position [Mb]
1	rs4224041	87.174.360
2	rs3683384	110.052.310
3	rs36523879	122.019.140
4	rs30359806	140.072.342
5	rs30102565	150.234.187
6	rs31598641	159.008.817

QTL analysis revealed LOD score maxima for atherosclerosis at the initially identified markers d3mit45 (LOD 3.3, cross A) and marker d3mit57 (LOD 4.1, cross B), where the homozygous B6 alleles correlated with 2.3-fold and 2.2-fold more atherosclerosis [104]. Dupuis and Siegmund found that 1.5-LOD support intervals provide around 95 % coverage in the case of a dense marker Map [161]. Applying this conservative cutoff of 1.5 LOD when defining the confidence intervals, we were able to narrow down the genetic regions potentially containing candidate genes of atherosclerosis risk from 44 to 36 Mb in cross A and 54 to 44 Mb in cross B, respectively (Table 18) [148].

TABLE 18: Old and new confidence intervals (CI) in female crosses A and B [148].

	Start (Marker)	Base pairs	End (Marker)	Base pairs	Length [bp]
Cross A (old CI)	d3mit57	115.433.310	End Chr3	159.599.783	44.166.473
Cross A (new CI)	rs36523879	122.018.890	rs31598641	159.008.567	36.989.677

	Start (Marker)	Base pairs	End (Marker)	Base pairs	Length [bp]
Cross B (old CI)	d3mit51	76.802.932	d3mit254	131.611.739	54.808.807
Cross B (new CI)	rs4224041	87.174.110	d3mit254	131.611.739	44.437.629

The confidence interval (CI, green area) of cross A now spanned from SNP rs36523879 to rs31598641 (Figure 18), had a length of 36.989.677 base pairs and contained 221 genes, the previous confidence interval contained 406 annotated RefSeq transcripts [148].

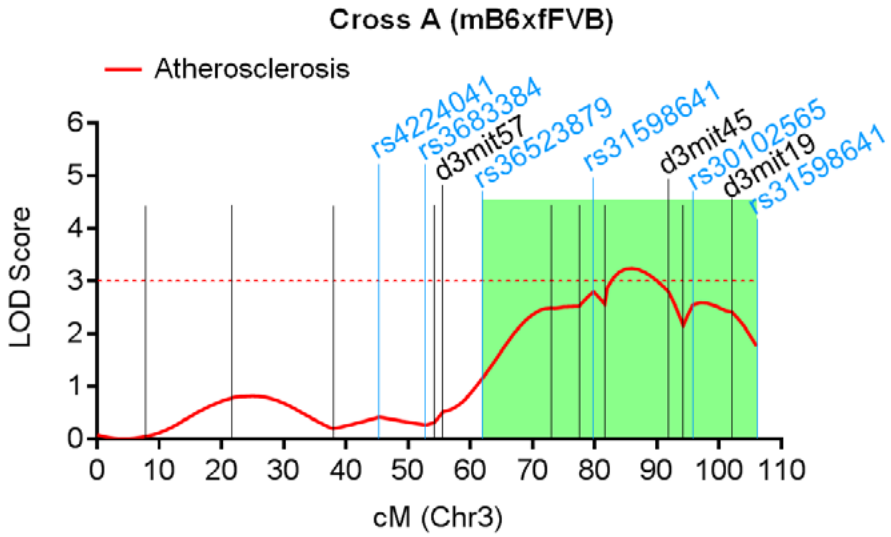

FIGURE 18: Confidence interval in cross A of mouse chromosome 3. The black lines indicate the microsatellite markers used initialy for genotyping the F2-generation mice and the blue lines the additional SNPs used to narrow the confidence intervals [148].

The confidence interval (blue area) of cross B now spanned from SNP rs4224041 to d3mit254 (Figure 19), had a length of 44.437.629 base pairs and contains 593 genes. The previous confidence interval contained 788 genes.

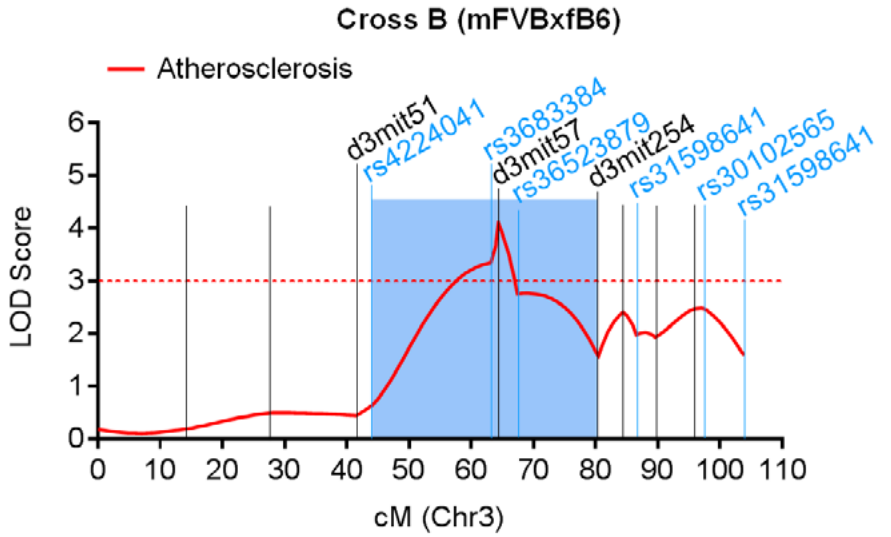

FIGURE 19: Confidence interval in cross B of mouse chromosome 3. The black lines indicate the microsatellite markers used initialy for genotyping the F2-generation mice and the blue lines the additional SNPs used to narrow the confidence intervals [148].

3.1.2 *Generation and characterization of chromosome 3 congenic mice*

To validate that the B6 allele on chromosome 3 was causal for promoting atherosclerosis, we first generated chromosome 3 congenic mice by introducing an 80 Mb long genomic stretch of Chr3 from atherosclerosis-susceptible B6 into the FVB.*Ldlr*$^{-/-}$ background. These mice were generated by crossing atherosclerosis-susceptible C57BL/6 (B6) and atherosclerosis resistant FVB mice and backcrossing the resulting heterozygous Chr3$^{FVB/B6}$ mice onto the FVB.*Ldlr*$^{-/-}$ background for 10 generations [148].

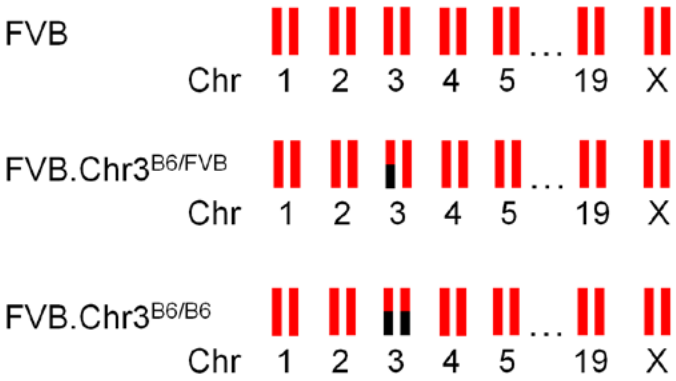

FIGURE 20: Chromosome 3 congenic mice. Chromosome 3 congenic mice carry an 80-160 Mb interval of Chr3 from B6 on the FVB background.

The identified loci on mouse chromosome 3 were female specific, thus only female mice were generated. Heterozygous FVB.Chr3$^{FVB/B6}$ mice (carrying an 80-160 Mb interval of Chr3 from B6 on the FVB background) were intercrossed to generate female homozygous FVB.Chr3$^{B6/B6}$ (n = 20), female heterozygous FVB.Chr3$^{FVB/B6}$ (n = 20) and female wild-type FVB.Chr3$^{FVB/FVB}$ (n = 20) control mice. Neither heterozygous FVB.Chr3$^{B6/FVB}$ nor homozygous FVB.Chr3$^{B6/B6}$ or wild-type FVB mice on the *Ldlr*-deficient background showed any great abnormalities and proved healthy and fertile when maintained under specific pathogen-free conditions. Mice were weaned at 4 weeks and were fed a semisynthetic diet containing 0.02 % cholesterol for 16 weeks which was previously shown to promote hypercholesterolemia and atherosclerosis and at the same time avoiding obesity with all of the attendant metabolic complications [99]. Subsequently they were sacrificed at 20 weeks of age by a standardized protocol (see Methods 3.3.1.2).

Plasma parameters were analyzed on an automated analyzer (Modular PPE, Roche) and lipoproteins were isolated by sequential ultracentrifugation. Total body weight and biochemical and clinical chemical characteristics of all mice are indicated in Table 19. Clinical chemistry parameters and plasma lipid levels showed no differences between FVB.Chr3$^{B6/B6}$, FVB.Chr3$^{B6/FVB}$ and FVB.Chr3$^{FVB/FVB}$ mice.

TABLE 19: Total body weight, biochemical characteristics and chemical clinical parameters of female FVB, FVB.Chr3$^{B6/FVB}$ and FVB.Chr3$^{B6/B6}$ mice [148].

Measurement	FVB	FVB.Chr3$^{B6/FVB}$	FVB.Chr3$^{B6/B6}$	*p*-Value		
	n = 20	n = 20	n = 20	FVB/ FVB.Chr3$^{B6/B6}$	FVB/ FVB.Chr3$^{B6/FVB}$	FVB.Chr3$^{B6/FVB}$/ FVB.Chr3$^{B6/B6}$
Weight [g]	22.1 ± 2.1	23.6 ± 2.5	24.5 ± 2.7	*0.003*	*n.s.*	*n.s.*
ALT [ukat/l]	0.65 ± 0.33	0.54 ± 0.14	0.76 ± 0.43	*0.003*	*n.s.*	*n.s.*
AST [ukat/l]	2.2 ± 1.14	2.06 ± 0.88	2.22 ± 1.32	*n.s.*	*n.s.*	*n.s.*
ChE [ukat/l]	109.3 ± 15.2	125.7 ± 19.7	136.8 ± 14.8	*n.s.*	*n.s.*	*n.s.*
Urea [mmol/l]	8.06 ± 2.02	9.1 ± 1.55	9.42 ± 3.71	*n.s.*	*n.s.*	*n.s.*
Total Protein [g/dl]	48.3 ± 3.29	50.3 ± 3.72	48.4 ± 3.8	*n.s.*	*n.s.*	*n.s.*
Triglyceride [mg/dl]	31.71 ± 14.59	38.55 ± 15.49	29.36 ± 8.28	*n.s.*	*n.s.*	*n.s.*
Cholesterol [mg/dl]	163.78 ± 26.84	191 ± 42.7	168.28 ± 37.11	*n.s.*	*n.s.*	*n.s.*
Creatinine [µmol/l]	12.32 ± 2.35	12.82 ± 3.5	11.88 ± 2.91	*n.s.*	*n.s.*	*n.s.*
VLDL-Cholesterol [mg/dl]	30.43 ± 16.58	47.61 ± 28.39	32.08 ± 15.45	*n.s.*	*n.s.*	*n.s.*
LDL-Cholesterol [mg/dl]	259.6 ± 60.6	307 ± 96.5	261 ± 69.3	*n.s.*	*n.s.*	*n.s.*
HDL-Cholesterol [mg/dl]	89.46 ± 10.67	91.36 ± 17.9	87.64 ± 11.58	*n.s.*	*n.s.*	*n.s.*
VLDL-TG [mg/dl]	106.8 ± 81.9	131.2 ± 77.2	92.4 ± 34.4	*n.s.*	*n.s.*	*n.s.*
LDL-TG [mg/dl]	63.87 ± 23.88	64.78 ± 23.36	61.8 ± 24.9	*n.s.*	*n.s.*	*n.s.*
HDL-TG [mg/dl]	22.85 ± 23.93	17.46 ± 14.09	24.44 ± 18.99	*n.s.*	*n.s.*	*n.s.*

Data are given as mean ± SD. ALT, alanine aminotransferase; AST, aspartate aminotransferase; ChE, cholinesterase; GLDH, Glutamate dehydrogenase; VLDL, very low- density lipoproteins; LDL, low-density lipoproteins; HDL, high-density lipoproteins. Comparison of multiple groups was done using ANOVA and Tukey was performed as a post-test. *n.s.* = not significant.

3.1.3 *Increased atherosclerosis in Chr3 congenic female mice*

Atherosclerotic lesion areas were quantified at the aortic root of female wild-type FVB (n = 20), heterozygous congenic FVB.Chr3$^{B6/FVB}$ (n = 20) and homozygous congenic FVB.Chr3$^{B6/B6}$ (n = 20) mice on the *Ldlr*-deficient background using oil red O staining. Oil red O is used for staining neutral triglycerides and lipids, Light Green SF yellowish for staining collagen and hematoxylin for staining cell nuclei. In Figure 21, representative oil red O stainings of chr3 congenic FVB.Chr3$^{B6/B6}$ and FVB mice are shown as well as the atherosclerosis quantification [148].

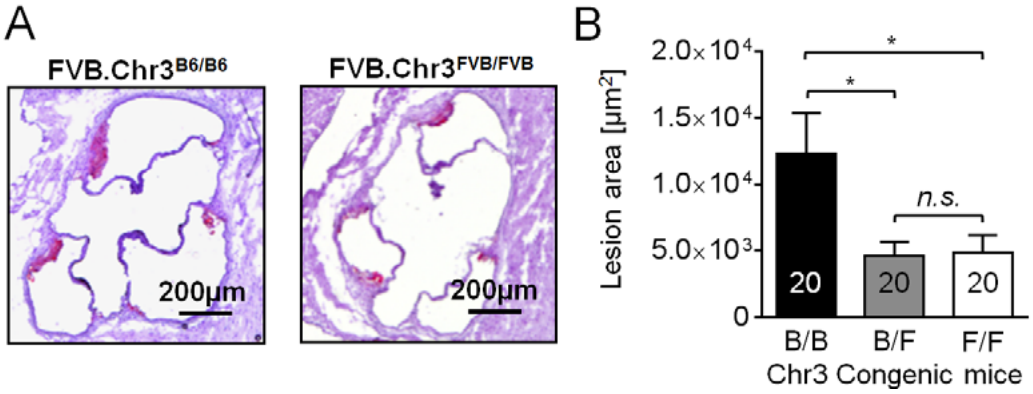

FIGURE 21: (**A**) Representative oil red O stainings of chr3 congenic FVB.Chr3$^{B6/B6}$ and FVB mice and (**B**) Atherosclerosis quantification in FVB.Chr3$^{B6/B6}$ (B/B), heterozygous FVB.Chr3$^{B6/FVB}$ (B/F) and wild-type FVB (F/F) mice. Data are given as mean ± SEM. * $p < 0.05$ [148].

Homozygous congenic FVB.Chr3$^{B6/B6}$ mice showed significantly 2.5 fold greater atherosclerotic lesion areas compared to heterozygous FVB.Chr3$^{B6/FVB}$ and wild-type FVB mice. These data confirmed that genetic factors contained within the 80 Mb at chromosome 3 conferred atherosclerosis susceptibility, and that atherogenesis was likely triggered independent of cholesterol and triglyceride metabolism as no differences were observed among all mice (Table 19) [148].

3.1.4 *Identification of novel atherosclerosis modifier genes on mouse chromosome 3*

To identify and functional characterize candidate genes for subsequent functional characterization at the atherosclerosis susceptibility locus at Chr3 we applied the following strategy (Figure 22).

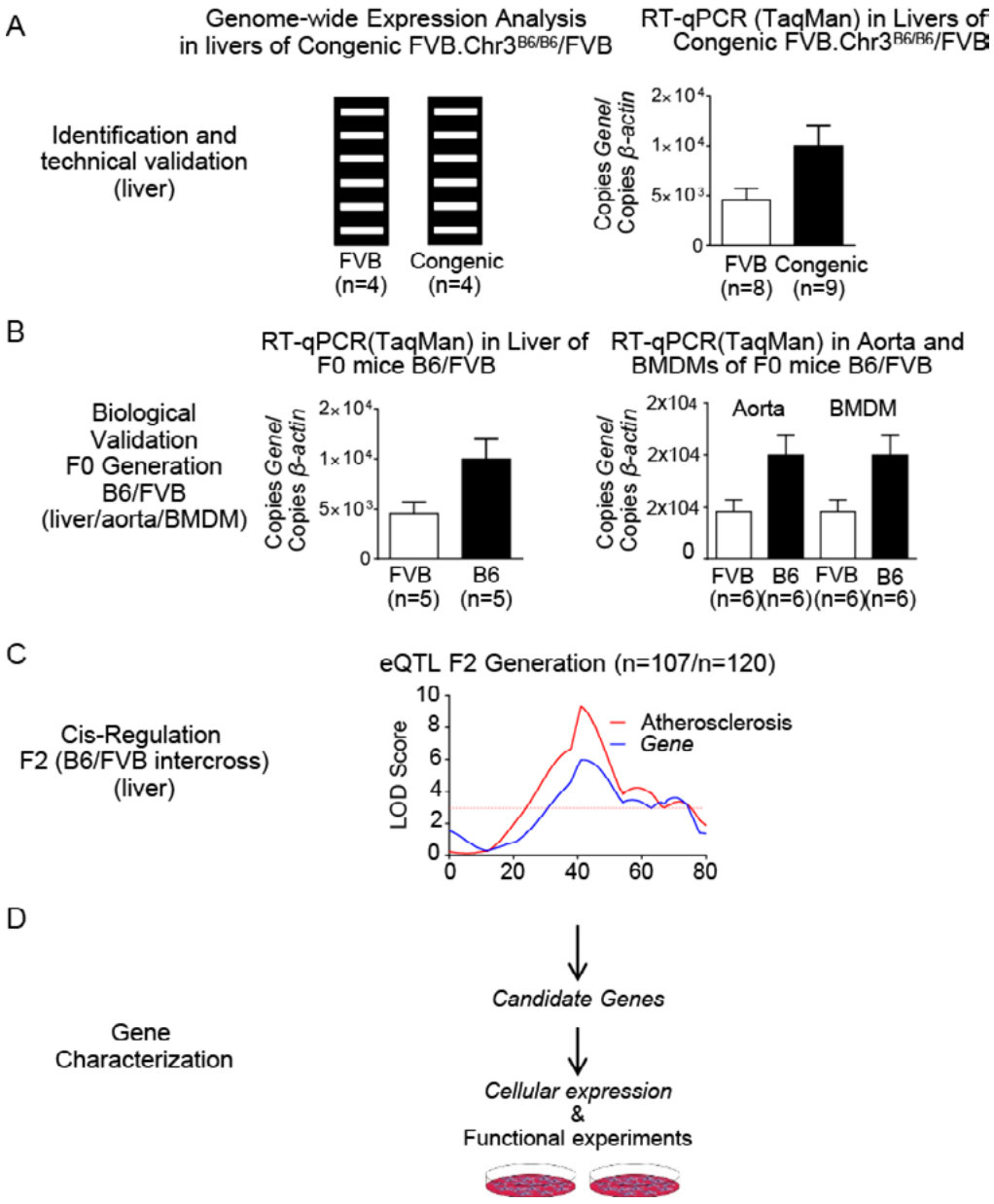

FIGURE 22: Strategy for identifying novel atherosclerosis modifier genes on mouse chr3 for subsequent functional studies. (**A**) Genome-wide expression analyses were performed in livers of congenic *FVB.Chr3*$^{B6/B6}$ (n = 4) and *FVB* (n = 4) mice using Illumina Ref8 arrays and technical validated in livers of congenic *FVB.Chr3*$^{B6/B6}$ (n = 9) and *FVB* (n = 8) mice using RT-qPCR (TaqMan) assays. (**B**) A biological validation of differentially expressed candidate genes was performed in livers (n = 5/5), aortas (n = 6/6) and bone marrow-derived macrophages (BMDM) (n = 6/6) of the parental B6 and FVB strains using RT-qPCR (TaqMan) assays. (**C**) Candidate genes that passed through the technical and biological validation were then measured in eQTL analyses in female mice of the F2-generation. (**D**) Identified genes were subsequently characterized in cellular expression and functional experiments [148].

In a first step, we performed transcriptome-wide expression analyses in RNA from livers of female congenic FVB.Chr3$^{B6/B6}$ (n = 4) mice and in FVB (n = 4) control mice to identify differentially regulated transcripts within the interval. Here, we found that 19 genes were differentially expressed with a fold change (FC) ratio > 1.4 and < 0.7, which we chose as a biologically relevant arbitrary cutoff (Table 20). 9 of these genes were located in the confidence interval of cross A, 13 genes in the interval of cross B, and 3 of these genes were in the overlap of the two intervals (Figure 23 and Table 20).

Using qPCRs we validated the differential expression of these genes by comparing their mRNA abundance firstly in preparations of livers from congenic FVB.Chr3$^{B6/B6}$ (n = 8) and FVB (n = 9) mice, and secondly by analyzing the parental F0 B6 (n = 5) and FVB (n = 5) female mice (Table 20). To examine whether the identified candidates were also differentially expressed in vascular tissue or cells known to contribute to atherosclerotic plaque formation (endothelial cells, macrophages), we next quantified candidate gene expression in parental F0 aortas (n = 6/6) and, secondly, in bone marrow-derived macrophages (BMDM, n = 6/6) (Table 20). In total, 7 genes passed the first two validation stages of expression analysis in the liver, out of which 5 were also expressed in aortic tissue and/or BMDMs: *tropomodulin-4* (*Tmod4*), *vascular cell adhesion molecule 1* (*Vcam1*), *fatty acid elongase 6* (*Elovl6*), the *group XIIA secretory phospholipase A2* (*Pla2g12a)* and *cystathionine gamma-lyase* (*Cth)* (Table 20).

Of these, *Vcam1*, *Elovl6* and *Cth* were induced, and *Tmod4* and *Pla2g12a* were repressed in mice carrying the B6 allele in the Chr3 interval (Table 20) [148].

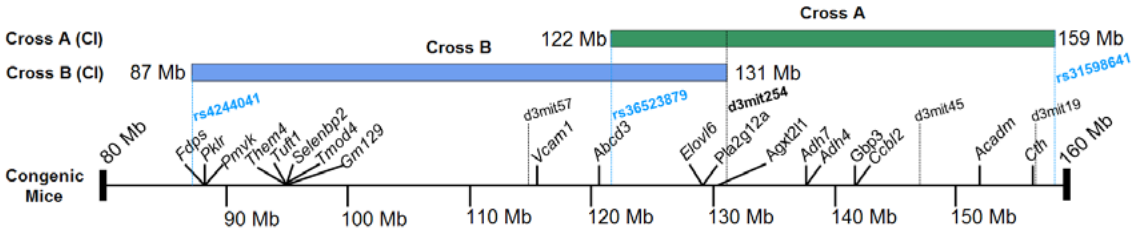

FIGURE 23: Chromosome 3 congenic mice (FVB.Chr3$^{B6/B6}$) are carrying an 80-160 Mb interval of Chr3 from B6 on the FVB background. On the 80 Mb long confidence interval are all genes listed that are differentially expressed in congenic FVB.Chr3$^{B6/B6}$ and FVB mice [148].

To remain conservative in our gene prioritization strategy we took all 7 candidates to further analyses stages [148].

TABLE 20: Identification of candidate genes through transcriptome-wide expression arrays and qPCRs [148].

Gene	**Position [Mb]**	**CI Cross A**	**CI Cross B**	**Congenic: Illumina WG-6 FC FVB.Chr3$^{B6/B6}$/FVB. Chr3$^{FVB/FVB}$ (n = 4/4)**	**Congenic: qRT-PCR FC FVB.Chr3$^{B6/B6}$/FVB.Chr3$^{FVB/FVB}$ (n = 8/9)**	**F0 Liver: qRT-PCR FC B6/FVB (n = 5/5)**	**F0 Aorta: qRT-PCR FC B6/FVB (n = 6/6)**	**F0 BMDM: qRT-PCR FC B6/FVB (n = 6/6)**	**LOD Score F2 Liver (n = 107/120)**
Fdps	88.8		X	1.86	*1.14*	*n.f.*	*n.f.*	*n.f.*	*n.f.*
Pklr	88.9		X	1.52	2.16**	2.22**	*not expr.*	*not expr.*	*4.4**
Pmvk	89.2		X	1.59	*1.24*	*n.f.*	*n.f.*	*n.f.*	*n.f.*
Them4	94.1		X	1.47*	*1.13*	*n.f.*	*n.f.*	*n.f.*	*n.f.*
Tuft1	94.1		X	0.65**	0.67	*n.f.*	*n.f.*	*n.f.*	*n.f.*
Selen-bp2	94.4		X	1.64	*0.72 ↑↓*	*n.f.*	*n.f.*	*n.f.*	*n.f.*
Tmod4	94.9		X	0.58***	0.25***	0.23***	*0.17****	*0.32****	*0.7*
Gm129	95.6		X	1.85*	*1.59*	*n.f.*	*n.f.*	*n.f.*	*n.f.*
Vcam1	115.8		X	1.46*	1.73*	2.14**	1.6**	*not expr.*	*4.4**
Abcd3	121.4		X	1.41*	*1.14*	*n.f.*	*n.f.*	*n.f.*	*n.f.*
Elovl6	129.2	X	X	1.73*	2.53*	3.09*	2.2***	*1.02*	0.95^{A}; 2.4^{B}
Pla-2g12a	129.5	X	X	0.49***	0.77*	0.53***	*0.46***	0.71*	3.6*^{A}, 2.4^{B}
Agxt2l1	130.3	X	X	2.1*	3.31***	2.01*	*not expr.*	*not expr.*	0.13^{A}; 0.5^{B}
Adh7	137.8	X		3.51***	*0.62 ↑↓*	*n.f.*	*n.f.*	*n.f.*	*n.f.*
Adh4	138.1	X		0.69**	*0.83*	*n.f.*	*n.f.*	*n.f.*	*n.f.*
Gbp3	142.2	X		1.45	*1.01*	*n.f.*	*n.f.*	*n.f.*	*n.f.*
Ccbl2	142.3	X		4.85***	1.48 *	*1.08*	*n.f.*	*n.f.*	*n.f.*
Acadm	153.5	X		0.68*	*0.78*	*n.f.*	*n.f.*	*n.f.*	*n.f.*
Cth	157.5	X		1.83*	2.76***	2.6***	0.85	3.1***	5.6*

Differentially expressed candidate genes identified by genome-wide expression arrays in homozygous chromosome 3 congenic FVB.Chr3$^{B6/B6}$ and FVB.Chr3$^{FVB/FVB}$ mice in the confidence intervals of cross A and B, respectively. As a cut off value a fold change (FC) of congenic FVB.Chr3$^{B6/B6}$ to FVB.Chr3$^{FVB/FVB}$ mice greater than 1.4 and less 0.7 was chosen. All fold changes of the validation stages are given. CI = Confidence Interval; *n.f.* = not followed; *not expr.* = not expressed; BMDM = bone marrow-derived macrophages; ^{A} Cross A; ^{B} Cross B.
*Fdps = farnesyl pyrophosphate synthase; Pklr = pyruvate kinase, liver and RBC; Pmvk = phosphomevalonate kinase; Them4 = thioesterase superfamily member 4; Tuft1 = tuftelin 1; Selenbp2 = selenium binding protein 2; Tmod4 = tropo-modulin-4; Gm129 = hypothetical protein LOC229599; Vcam1 = vascular cell adhesion molecule 1; Abcd3 = ATP-binding cassette sub-family D member 3; Elovl6 = fatty acid elongase 6; Pla2g12a = group XIIA secretory phospholipase A2; Agxt2l1 = alanine-glyoxylate aminotransferase 2-like 1; Adh7 = alcohol dehydrogenase class 4 mu/sigma chain; Adh4 = alcohol dehydrogenase 4; Gbp3 = guanylate-binding protein 4; Ccbl2 = kynurenine-oxoglutarate transaminase 3; Acadm = medium-chain specific acyl-CoA dehydrogenase; Cth = cystathionine gamma-lyase. * p < 0.05; ** p < 0.01; *** p < 0.001; * LOD > 3.3 (corresponding to a genome-wide significance level of 0.05 [162])*

3.1.5 *Identity by descent analysis (IBD)*

eQTLs can principally arise due to genetic variants contained either gene-proximally (within the transcribed RNA or the promoter/promoter-proximal regions, changing the transcription, stability or degradation kinetics of the mRNA by various mechanisms)[163], or in more distant regulatory regions [164]. We thus performed an identity by descent analysis (IBD) of chromosome 3 in C57BL/6 and FVB mice to explore if any genomic regions in the candidate gene interval could be excluded due to sharing of haplotypes (Figure 24, Table 21). Black regions indicate identical segments of C57BL/6 and FVB mice and white segments indicate segments that are inherited independently [148].

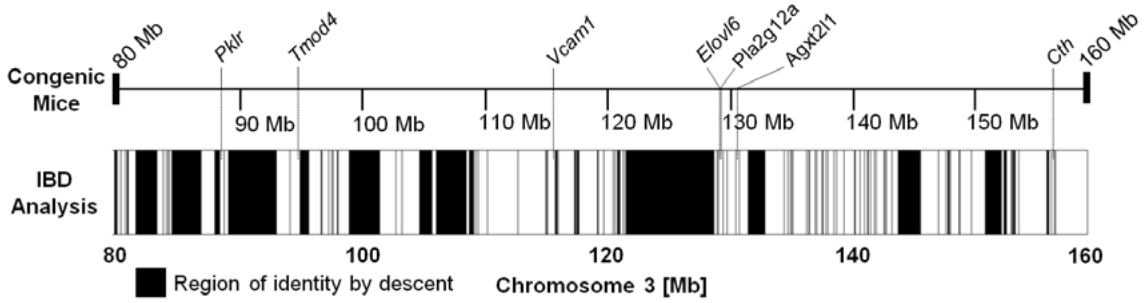

FIGURE 24: Identity by descent (IBD) analysis in the interval of 80-160 Mb of chromosome 3 in C57BL/6 and FVB mice. Presented are the 7 candidate genes that passed through the validation stages [148].

TABLE 21: Regions of identity by descent (IBD) in the confidence interval of 80-160 Mb of Chr3 in C57BL/6 and FVB mice [148].

No.	Start Position	End Position	No.	Start Position	End Position
1	80.188.361	80.227.607	54	129.973.800	129.974.021
2	80.536.900	80.594.470	55	130.258.613	130.275.265
3	80.690.601	80.829.263	56	130.961.839	130.965.944
4	81.419.232	83.180.615	57	131.263.933	131.327.493
5	83.695.103	83.697.639	58	132.024.501	133.389.556
6	83.910.647	83.970.081	59	134.979.859	135.039.822
7	84.108.613	84.109.902	60	135274.890	135.290.731
8	84.178.368	84.232.881	61	135.490.845	135.490.845
9	84.420.466	86.840.354	62	135.586.445	135.586.445
10	87.942.214	88.394.992	63	135.700.534	135.730.210
11	88.726.672	88.726.672	64	136.848.780	136.857.802
12	89.089.629	89.089.629	65	136.999.580	136.999.580
13	89.165.033	93.071.701	66	137.069.054	137.090.397
14	94.207.865	94.207.865	67	137.559.532	137.559.816
15	94.985.990	95.747.548	68	137.674.541	137.674.541
16	96.736.639	96.740.089	69	138.119.505	138.216.740
17	96.767.593	96.767.742	70	138.429.420	138.431.027
18	96.810.034	96.811.406	71	138.578.932	138.625.427
19	97.386.657	97.402.858	72	139.082.389	139.082.389

No.	Start Position	End Position	No.	Start Position	End Position
20	97.641.765	97.641.912	73	139.312.208	139.312208
21	97.731.201	97.737.430	74	139.901.711	139.901.711
22	98.090.360	98.181.483	75	140.783.381	140.886.545
23	99.040.115	101.508.142	76	141.256.960	141.256.960
24	101.563.427	101.563.427	77	141.630.571	141.631.086
25	102.893.521	102.912.926	78	141.864.016	141.947.400
26	103.434.925	103.435.289	79	142.103.827	142.123.983
27	104.862.464	105.894.207	80	142.425.542	142.425.542
28	106.251.616	107.271.160	81	142.588.681	142.588.681
29	107.324.647	108.706.370	82	143.230.029	143.232.983
30	109.004.747	109.335.491	83	143.313.362	143.352.391
31	109.492.017	109.551.155	84	143.414.498	143.416.205
32	109.693.328	109.731.513	85	143.892.533	143.907.260
33	110.457.786	110.458.378	86	144.398.993	146.266.204
34	112.984.364	112.984.364	87	147.746.587	147.746.688
35	115.294.141	115.294.599	88	148.339.778	148.382.587
36	115.355.523	115.355.761	89	148.484.699	148.484.699
37	115.442.491	115.442.491	90	148.513.159	148.580.347
38	116.078.713	116.239.710	91	148.631.065	148.631.065
39	116.323.774	116.354.251	92	148.728.333	148.728.333
40	117.643.991	117.777.467	93	149.434.141	149.434.141
41	117.894.669	118.045.948	94	149.476.617	149.502.384
42	119.571.115	119.647.899	95	150.477.760	150.477.760
43	120.092.503	120.121.442	96	151.609.744	152.891.138
44	120.838.527	120.838.527	97	152.924.161	152.924.161
45	120.993.033	120.993.033	98	153.109.774	153.316.575
46	121.197.396	121.218.386	99	153.728.658	153.828.179
47	121.288.737	121.414.004	100	153.886.960	154.038.227
48	121.692.915	121.694.285	101	154.333.765	154.390.758
49	121.837.443	121.837.443	102	156.682.833	156.838.748
50	121.917.655	122.039.421	103	157.002.851	157.062.314
51	122.101.525	129.200.388	104	157.308.021	157.316.520
52	129.442.386	129.471.180	105	157.413.336	157.413.336
53	129.556.279	129.556.279	106	157.417.299	157.417.299

The IBD analysis revealed that all 7 candidate genes indeed resided in regions that were inherited independently in both strains, and thus none of these candidates could be excluded [148].

3.1.6 *Non-synonymous protein-sequence-changing (nsSNPs)*

Furthermore, to investigate whether the 7 identified candidate genes contained any nucleotide mutations that would alter the amino acid sequence of the protein, we Identified the non-synonymous SNPs in the confidence intervals of cross A and cross B (Table 22). Subsequently, we determined the SIFT (sorts intolerant from tolerant amino acid substitutions) score, which predicts whether an amino acid substitution affects protein function, using the PolyPhen-2 Software [165]. The SIFT score ranges from 0.0 (deleterious) to 1.0 (tolerated) and can be interpreted as follows:

- ➔ 0.0 to 0.05 – Variants with scores in this range are likelly deleterious. Variants with scores closer to 0.0 are more confidently predicted to be deleterious.
- ➔ 0.05 to 1.0 – Variants with scores in this range are predicted to be tolerated (benign). Variants with scores very close to 1.0 are more confidently predicted to be tolerated.

TABLE 22: Identified nonsynonymous SNPs in the confidence intervals of cross A (122.019.140 bp-159.008.817 bp) and cross B (87.174.110 bp-131.711.739 bp) [148].

SNP ID	Coordinate (GRCm38)	Gene Symbol	C57BL/6J	FVB/NJ	SIFT Score
rs30016755	87.536.471	*Etv3*	T	C	1
rs30054575	87.556.061	*Etv3l*	A	G	-
rs31624766	87.728.530	*Arhgef11*	T	C	0.6
rs31085609	87.847.667	*Sh2d2a*	A	G	1
rs30756513	87.976.039	*Nes*	T	A	1
rs30081012	87.976.065	*Nes*	G	A	**0.04**
rs30699602	87.976.195	*Nes*	T	C	0.09
rs31201125	87.976.454	*Nes*	G	A	0.11
rs30011971	88.055.415	*Gpatch4*	C	T	0.82
rs13477249	88.247.513	*Rhbg*	A	G	0.63
rs13477251	88.854.680	*Gon4l*	C	T	**0.01**
rs30809262	88.912.751	*Msto1*	A	T	1
rs13468134	89.170.304	*Clk2*	A	G	0.95
rs30987263	89.230.775	*Muc1*	T	A	0.78
rs31327584	93.331.614	*Hrnr*	T	C	-
rs30076287	93.332.617	*Hrnr*	T	A	-
rs30991551	93.332.685	*Hrnr*	C	T	-
rs33037297	93.471.541	*Tchhl1*	G	T	**0.03**
rs30700506	94.317.417	*Them4*	C	T	0.21
rs31054855	94.770.626	*Cgn*	T	C	1
rs13459184	95.122.411	*Vps72*	C	T	0.32
rs13459184	95.122.411	*Tmod4*	C	T	0.32
rs30207972	96.442.058	*BC107364*	A	T	-
rs13477282	98.713.577	*Hsd3b2*	A	T	**0.02**
rs3653450	101.860.984	*Slc22a15*	T	G	0.64
rs30608634	102.934.877	*Sycp1*	G	A	0.15
rs13459070	104.804.630	*Mov10*	A	G	0.63

SNP ID	Coordinate (GRCm38)	Gene Symbol	C57BL/6J	FVB/NJ	SIFT Score
rs31489662	113.054.049	*Gm5548*	T	A	-
rs13466303	116.111.020	*Vcam1*	A	G	1
rs31253294	116.582.921	*Trmt13*	C	G	1
rs30057851	116.589.588	*Trmt13*	G	C	0.19
rs30359775	116.891.876	*Frrs1*	A	G	1
rs30628512	129.810.533	*Rrh*	G	T	1
rs30629454	129.810.593	*Rrh*	T	C	0.45
rs16790997	129.912.163	*Casp6*	A	G	0.5
rs31379347	134.829.672	*Tacr3*	G	C	0.86
rs13477425	134.932.375	*Tacr3*	T	C	1
rs30358046	138.065.960	*1110002E22Rik*	T	G	0.35
rs30406544	138.069.232	*1110002E22Rik*	G	A	0.07
rs30256098	138.069.604	*1110002E22Rik*	G	A	0.09
rs30902098	138.173.534	*4930579F01Rik*	C	A	0.68
rs30980112	139.193.642	*Gm4862*	G	A	-
rs30357439	142.352.761	*Pdlim5*	G	A	**0**
rs30423887	142.507.947	*Gbp5*	G	A	0.19
rs31062787	142.567.699	*Gbp3*	A	G	1
rs31036665	142.569.244	*Gbp3*	T	C	1
rs30720420	154.763.824	*Erich3*	A	C	**0**
rs30712233	154.872.125	*Tnni3k*	G	A	**0**
rs30203847	155.086.840	*Fpgt*	A	G	1

We identified 49 gene transcripts with a SIFT score from 0.0 to 0.05. However, none of the 7 identified candidate genes contained non-synonymous protein-sequence-changing SNPs. Thus, it is likely, that SNPs within regulatory regions are causal for the differential expression.

3.1.7 *Identification of cis-regulated candidate genes by expression QTL (eQTL) mapping*

To investigate if the B6-derived genetic variants that promoted atherosclerosis also regulated gene expression of our candidate genes *in cis*, we obtained mRNA preparations from livers of female F2 mice from cross A (n = 107) or from cross B (n = 120), and performed expression quantitative trait locus (eQTL) mapping for *Pklr*, *Vcam1*, *Elovl6*, *Agxt2l1*, *Cth*, *Tmod4* and *Pla2g12a* (Figures 25 and 26) [148].

In cross A, we observed significant LOD scores for *Pla2g12a* and *Cth*. These two genes were located in the defined confidence interval of cross A. *Agxt2l1* and *Elovl6* showed no significant LOD scores.

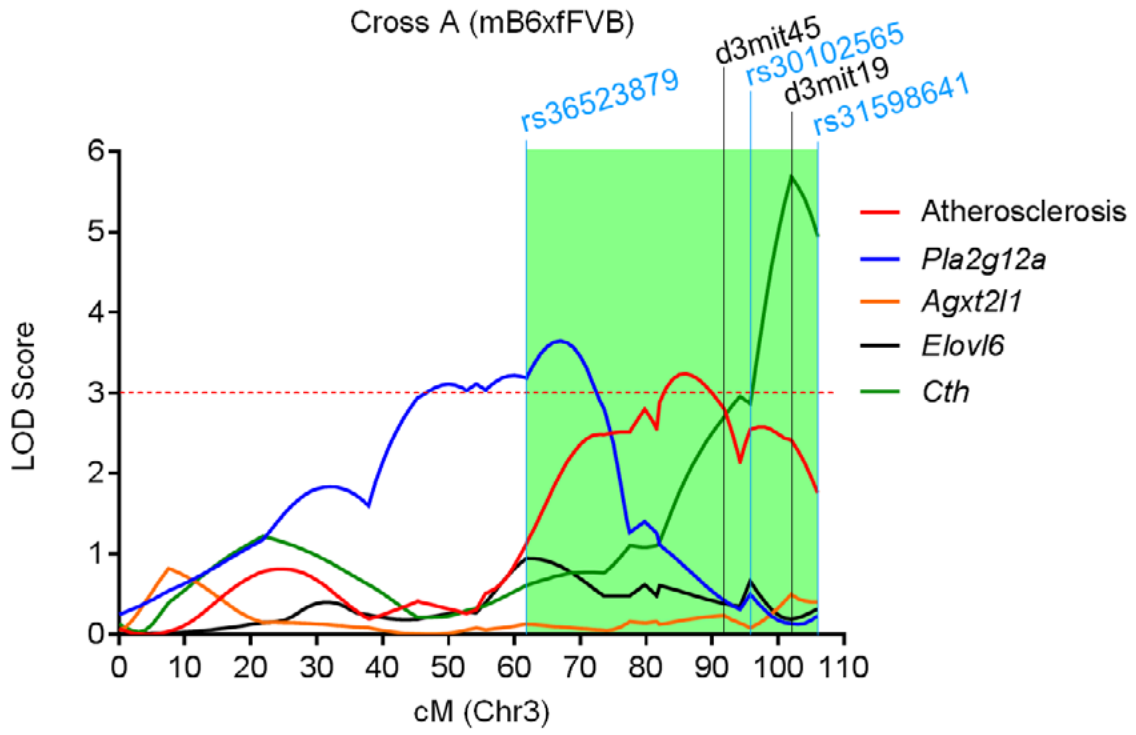

FIGURE 25: Identification of cis-regulated candidate genes by expression QTL (eQTL) mapping in cross A. Black lines- microsatellite markers [104]; blue lines- SNPs used for fine-mapping; green highlighted: confidence interval of cross A [148].

We observed a LOD score maximum of 3.6 at SNP rs36523879 for *Pla2g12a* expression in F2 females of cross A, which is 7.4 Mb 5' to the *Pla2g12a* gene and the top atherosclerosis marker d3mit45 in this subcross (Figure 25). In the same subcross, we observed a significant LOD score for *Cth* expression at marker d3mit19, which is located 9.8 Mb distal to marker d3mit45 and only 88.7 kb 3' of the *Cth* gene. Applying the same conservative cutoff of 1.5 LOD when defining the confidence interval for the *Cth* cis eQTL [161], *Cth's* spans from rs30102565 to rs31598641 (150.234.187 - 159.008.817 Mb). Thus, there is no overlap between the *Cth* cis eQTL and the maximum LOD score for atherosclerosis in this subcross making *Cth* an unlikely, candidate gene [148].

In cross B, a LOD score maximum of 4.4 for *Vcam1* was detected and overlapped most closely the location of atherosclerosis-susceptibility at marker d3mit57. We also observed a significant eQTL for *Pklr* at marker d3mit63, however, as with *Cth* in subcross A, no overlap of the confidence interval of the *Pklr* cis eQTL (d3mit203 to rs3683384; 26.8-110 Mb) with the maximum atherosclerosis LOD score was detected. *Tmod4*, *Elovl6*, *Agxt2l1* and *Pla2g12a* LOD scores showed no significance [148].

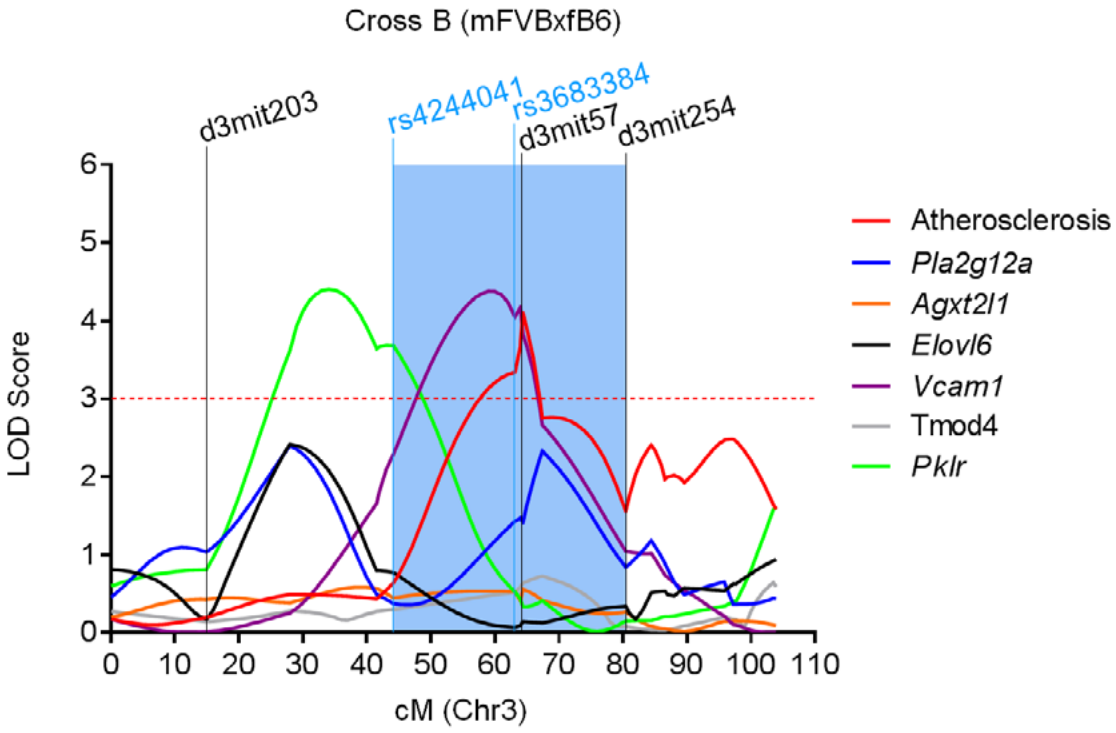

FIGURE 26: Identification of *cis*-regulated candidate genes by expression QTL (eQTL) mapping in cross B. Black lines- microsatellite markers [104]; blue lines- SNPs used for fine-mapping. blue highlighted: confidence interval of cross A [148].

Since no eQTLs for *Elovl6*, *Agxt2l1* and *Tmod4* were detected, and *Cth* and *Pklr* did not overlapped with the atherosclerosis LOD score, it is unlikely that genetic variants at Chr3 is causal for their differential expression and therefore were not further considered as candidate genes.

In addition, we examined the correlation of *Cth* in cross A and *Pklr* in cross B with atherosclerosis in mice of the F2 generation. Neither of the two genes revealed a correlation with atherosclerosis and therefore were both excluded as candidate genes as previously mentioned.

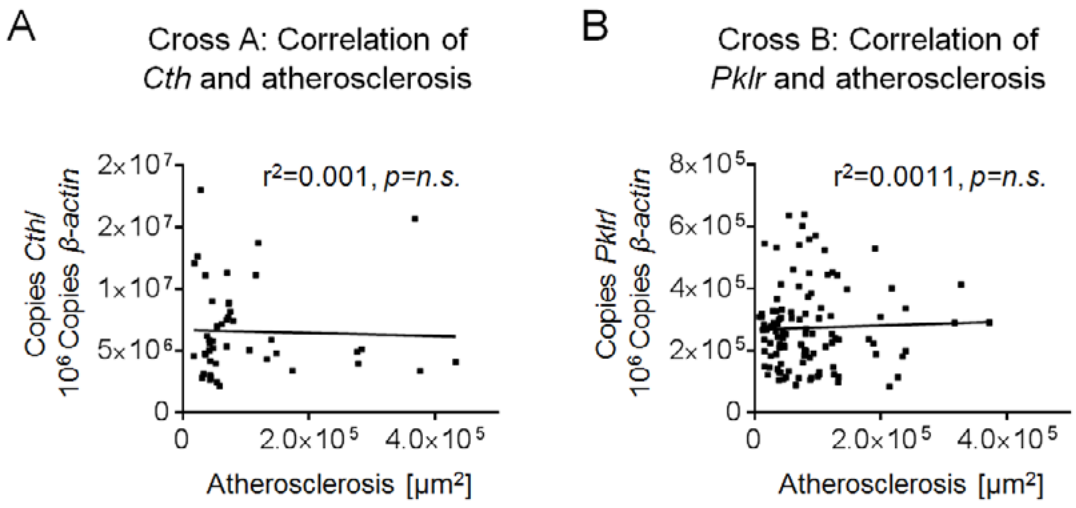

FIGURE 27: Correlation of (**A**) *Cth* and (**B**) *Pklr* with atherosclerosis in female F2 progeny from cross A and cross B, respectively [148].

Subsequently, we determined the genotypic effects of the lesion area and the *Vcam1* mRNA expression at marker d3mit57 in the female mice of cross B. There are three different genotypes, homozygous for the B6 allele (B/B), heterozygous (B/F) or homozygous for the FVB allele (F/F).

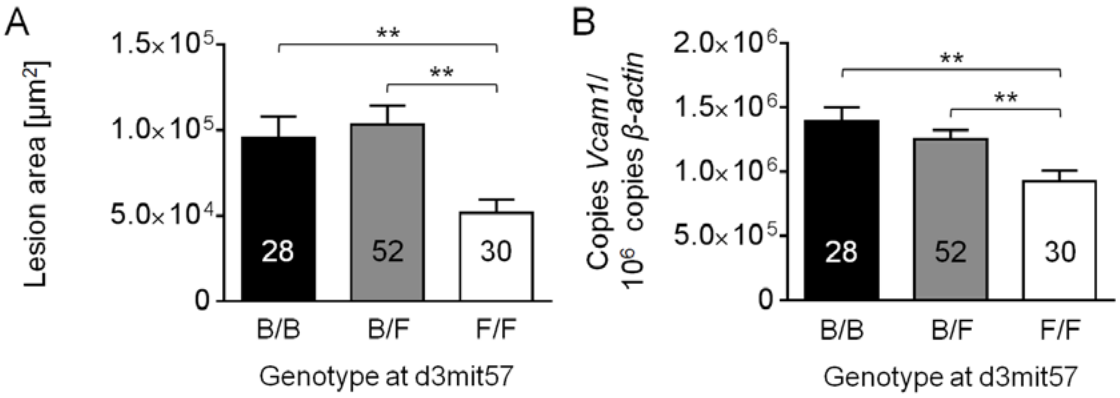

FIGURE 28: Genotypic effects for (**A**) lesion area and (**B**) *Vcam1* mRNA expression at marker d3mit57 in female mice of cross B. ** $p < 0.01$ [148].

Females, carrying two B6-alleles at d3mit57 had 1.5-fold higher *Vcam1* expression levels ($p = 0.001$) and developed 1.9-fold more atherosclerosis ($p = 0.004$). Since *Vcam1* is a well-known regulator of atherogenesis [166] and high *Vcam1* levels have been shown to promote atherosclerosis [167, 168], our data are consistent with the published literature and make *Vcam1* a likely effector gene in cross B.

Thus, from the analysis of cross A, *Pla2g12a* emerged as novel candidate atherosclerosis modifier [148].

3.1.8 *Fine-mapping in cross A with SNP rs13464244*

To improve eQTL mapping accuracy in cross A, we increased the marker coverage at the chromosomal location of *Pla2g12a* by genotyping SNP rs13464244, located only 0.24 Mb 5′ of the gene [148].

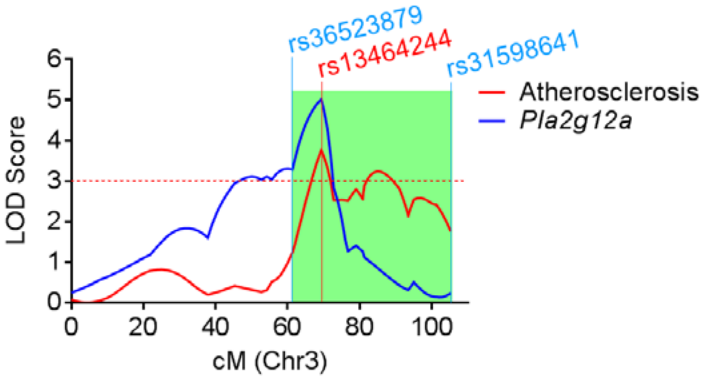

FIGURE 29: Chr3 LOD score plot for atherosclerosis and *Pla2g12a* mRNA expression in female F2 progeny of cross A after eQTL fine-mapping with SNP rs13464244 [148].

This resulted in a sharp increase of the LOD score of atherosclerosis (from 3.2 to 3.7) as well as from the LOD score of *Pla2g12a* (from 3.6 to 5.01) and a co-localization for both traits. Homozygosity for the B6 allele at rs13464244 in F2 females from cross A was associated with enlarged atherosclerotic lesions ($p = 0.0009$) (Figure 29) and decreased mRNA abundance of *Pla2g12a* compared to the FVB genotype at this position ($p = 9.6 \times 10^{-07}$) suggesting that high *Pla2g12a* expression was atheroprotective [148].

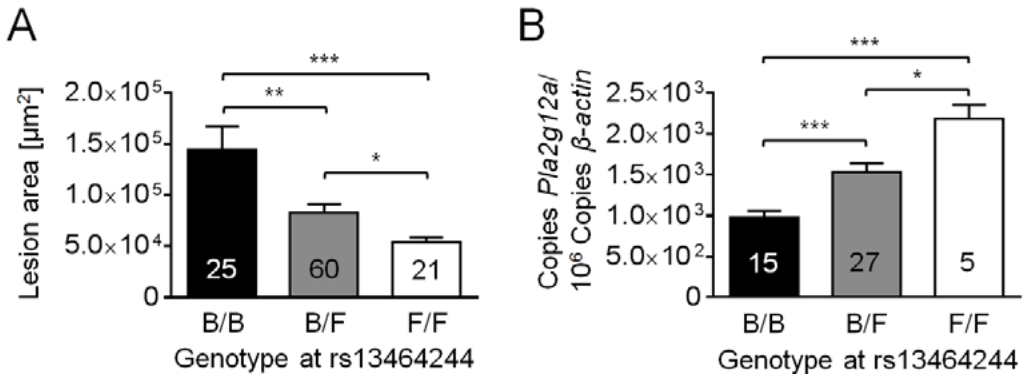

FIGURE 30: Genotypic effects for (**A**) lesion area and (**B**) *Pla2g12a* mRNA expression at SNP rs13464244. * $p < 0.05$; ** $p < 0.01$; *** $p < 0.001$ [148].

We also observed an inverse correlation of high *Pla2g12a* mRNA expression with smaller atherosclerotic lesion sizes ($r^2 = 0.18$, $p = 0.002$) further suggesting that *Pla2g12a* protects from atherosclerosis (Figure 31).

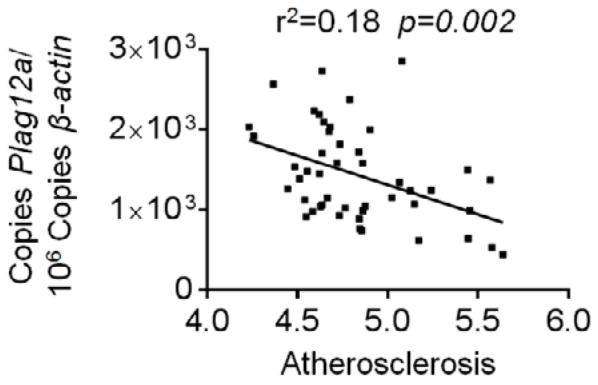

FIGURE 31: Correlation of *Pla2g12a* mRNA with atherosclerosis in female F2 mice of cross A [148].

Together, eQTL mapping in female F2 progeny from cross A identified *Pla2g12a* as an independent candidate gene for atherosclerosis susceptibility in this locus and indicated that low *Pla2g12a* expression in the arterial wall might promote atherosclerosis [148].

3.1.9 *Gender-dependence of eQTLs in F2 mice of cross A and B*

Corroborating the known gender-dependence of this Chr3 QTL (Figure 32), eQTL fine-mapping with SNP rs13464244 in F2 males of cross A revealed LOD scores for *Pla2g12a* and atherosclerosis below the significance limit of 3 [148].

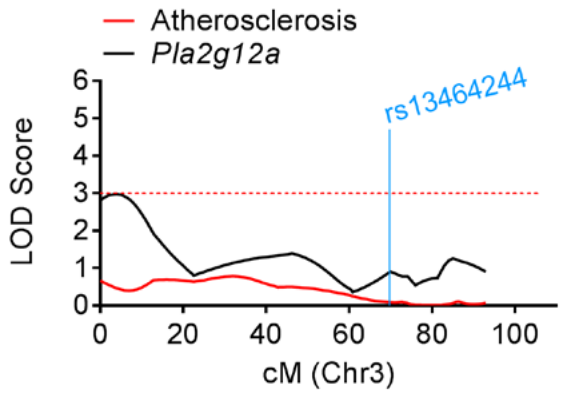

FIGURE 32: Chr3 LOD score plot for atherosclerosis and *Pla2g12a* mRNA expression in male F2 progeny of cross A after eQTL fine-mapping with SNP rs13464244 [148].

Consistently, no significant differences were observed regarding *Pla2g12a* mRNA expression and lesion area at SNP rs13464244.

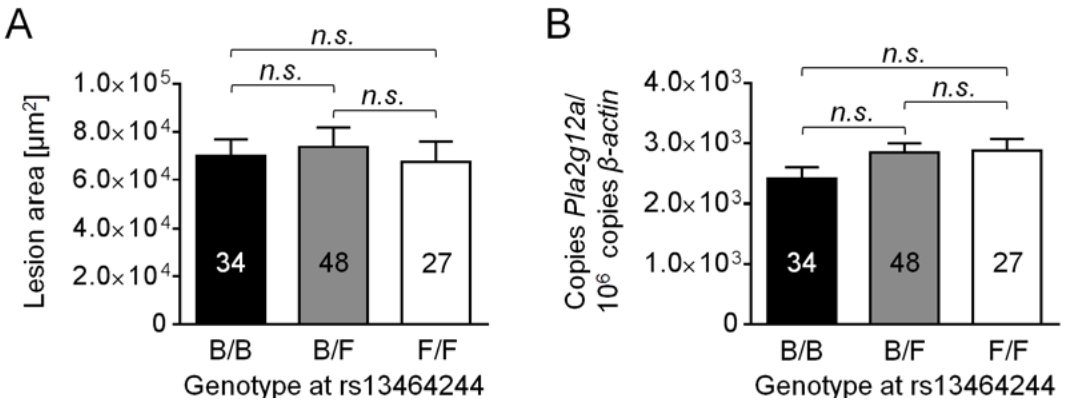

FIGURE 33: Genotypic effects at SNP rs13464244 for (**A**) lesion area and (**B**) *Pla2g12a* mRNA expression in male mice of cross A. *n.s.* = not significant [148].

Furthermore, *Pla2g12a* mRNA levels in male mice of the F2 generation were not correlated with atherosclerosis lesions size ($r^2 = 0.00006$, $p = 0.87$) [148].

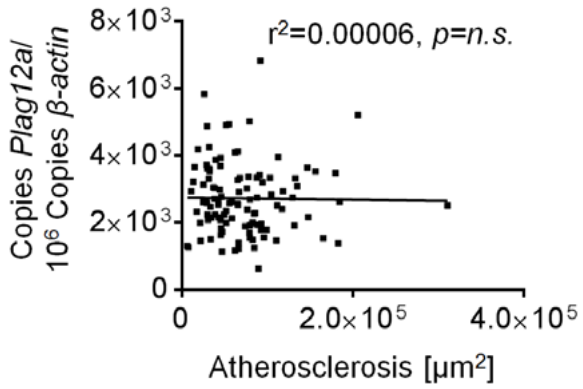

FIGURE 34: Correlation of *Pla2g12a* mRNA expression with atherosclerosis in male mice of cross A. *n.s.* = not significant [148].

Similar to the results in male mice of the F2 generation in cross A we investigated the LOD scores of atherosclerosis and *Vcam1* mRNA expression in 120 male mice of cross B at marker d3mit57. As in male mice of cross A, no significant LOD scores for atherosclerosis and *Vcam1* mRNA expression were observed.

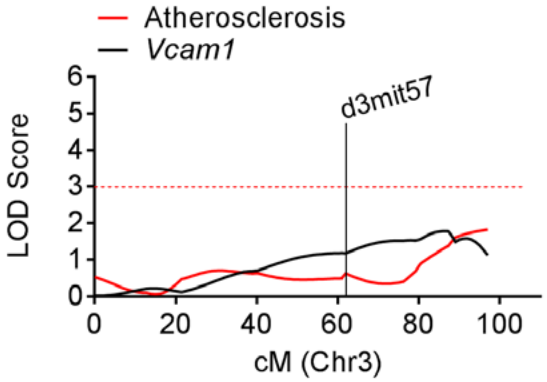

FIGURE 35: Chr3 LOD score plot for atherosclerosis and *Vcam1* mRNA expression in male F2 progeny of cross B at marker d3mit57 [148].

Consistently, no significant differences were observed regarding *Vcam1* mRNA expression and lesion area at marker d3mit57.

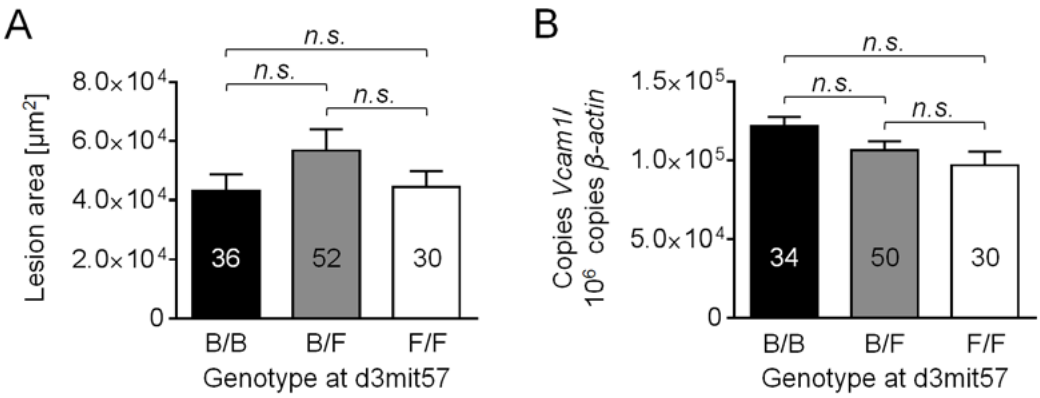

FIGURE 36: Genotypic effects at marker d3mit57 for (**A**) lesion area and (**B**) *Vcam1* mRNA expression in male mice of cross B and correlation of *Vcam1* [148].

Additionally, *Vcam1* mRNA levels in male mice of the F2 generation were not correlated with atherosclerosis lesions size ($r^2 = 0.0002$, $p = 0.87$).

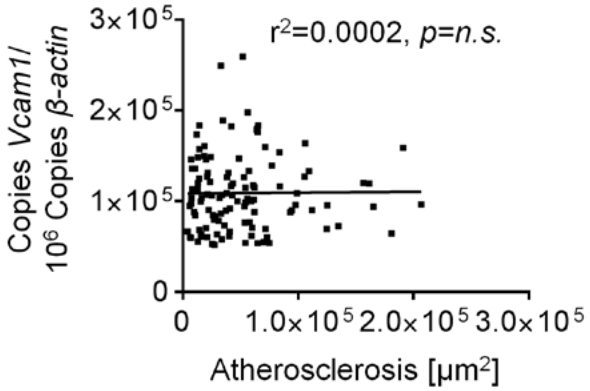

FIGURE 37: Correlation of *Vcam1* mRNA expression with atherosclerosis in male mice of cross B [148].

Together, eQTL mapping in F2 mice indicated that downregulation of *Pla2g12a* and upregulation of *Vcam1* might be causal for promoting atherosclerosis in female but not male F2 mice carrying the B6 alleles at the two atherosclerosis subloci of the Chr3 risk QTL [148].

3.1.10 *Characterization of PLA2G12A*

Whereas *Vcam1* is an established atherosclerosis modifier gene [169], the potential role of *Pla2g12a*, which belongs to the secreted phospholipase A2 enzymes ($sPLA_2$), in atherogenesis has not been investigated, yet. We thus focussed on PLA2G12A and performed qPCR analyses, immunohistochemical stainings and western blots to prioritize which vascular cell type to study in subsequent functional analyses [148].

3.1.10.1 *Expression profiling of Pla2g12a in different tissues*

In order to investigate the expression pattern of *Pla2g12a*, we first quantified its expression in different tissues from FVB mice (n = 3) with higher *Pla2g12a* expression. *Pla2g12a* mRNA expression was normalized to 10^6 copies of *β-actin* house-keeping gene.

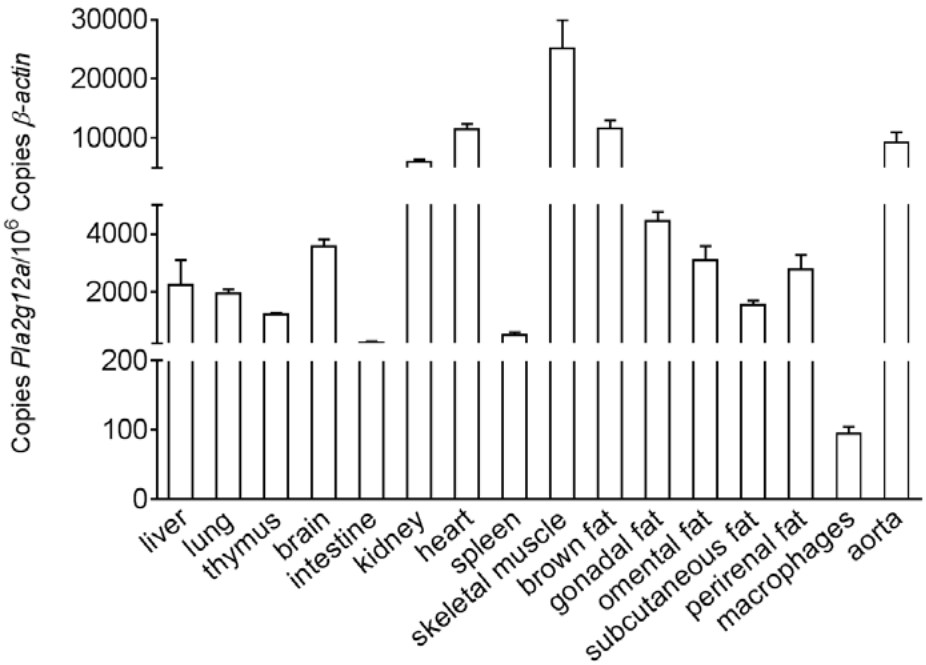

FIGURE 38: *Pla2g12a* mRNA expression in different tissues of FVB mice (n = 3).

Pla2g12a is ubiquitous expressed and highest expression was detected in skeletal muscle, heart, brown fat and aorta. Consistent with our previous results, we observed significantly lower expression levels of *Pla2g12a* in the aortic tissue of B6 (n = 17) compared to FVB (n = 17) F0 mice [148].

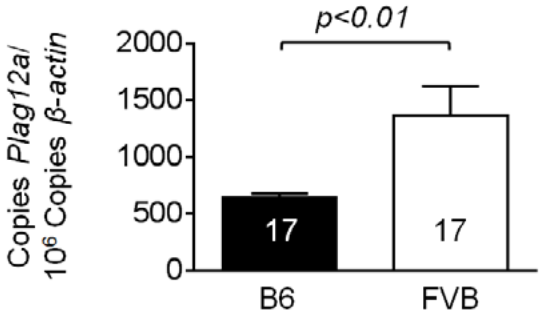

FIGURE 39: *Pla2g12a* mRNA expression in aortic tissue of B6 and FVB F0 mice [148].

3.1.10.2 *Immunohistochemical stainings and co-stainings of PLA2G12A*

To investigate which cells within atherosclerotic lesions expressed PLA2G12A, we performed immunohistochemical stainings in the aortic root of a C57BL/6 mouse co-stained with CD68 positive macrophages, von Willebrand-factor (vWF) positive endothelial cells and alpha-smooth muscle actin (α-SMA) positive smooth muscle cells in consecutive sections in the aortic root of a C57BL/6 mouse (Figure 40) [148].

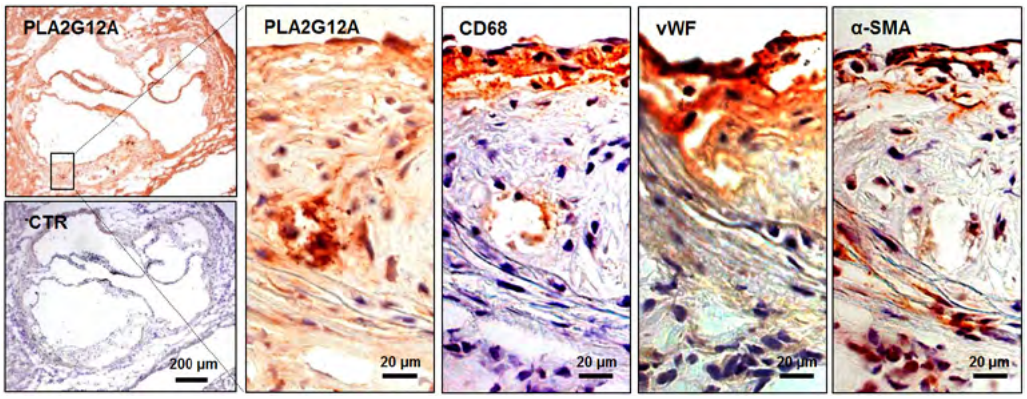

FIGURE 40: Immunohistochemical stainings of PLA2G12A, von Willebrand Factor positive endothelial cells (vWF), α-SMA positive smooth muscle cells and CD68 positive macrophages in the aortic root of a C57BL/6 mouse. Stainings were performed with Vector NovaRED so that PLA2G12A, CD68, vWF and α-SMA are stained red and hematoxylin was used to counterstain cell nuclei [148].

Immunohistochemical stainings showed that PLA2G12A was highly expressed in vascular endothelial cells (ECs) and to a lesser extent in macrophages [148].

3.1.10.3 *Increased Pla2g12a mRNA and protein expression in ECs*

Since immunohistochemical stainings demonstrated PLA2G12A expression in cells of atherosclerotic plaques, we used qPCR and Western blotting in order to identify the cell type with highest gene expression. To this end, we performed RT-qPCR in MCEC mouse cardiac endothelial cells (ECs), bone marrow-derived macrophages (BMD MΦ) of a C57B/L6 mouse and MOVAS smooth muscle cells (SMCs).

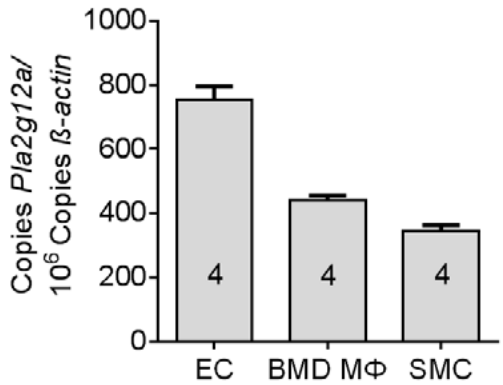

FIGURE 41: *Pla2g12a* mRNA expression in mouse cardiac endothelial cells (EC), bone marrow-derived macrophages and vascular smooth muscle cells (MOVAS) [148].

Pla2g12a was expressed most strongly in endothelial cells when compared to cultured macrophages or vascular smooth muscle cells (Figure 41) [148].

Using Western blots, this finding was validated and we also observed highest PLA2G12A protein levels in mouse endothelial cells, whereas Glyceraldehyde-3-phosphate-Dehydrogenase (GAPDH) was unaltered.

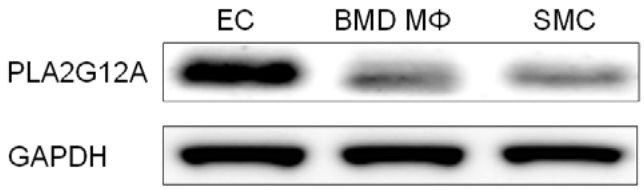

FIGURE 42: PLA2G12A protein levels in mouse cardiac endothelial cells (EC), bone marrow-derived macrophages and vascular smooth muscle cells (MOVAS) [148].

3.1.11 *Cell culture functional experiments*

3.1.11.1 *Pla2g12a-deficiency promotes adhesion between endothelial cells and macrophages*

Endothelial cell (EC) activation is one of the first cellular changes in the vasculature *en route* to atherosclerosis [170, 171]. During atherosclerosis development ECs control adhesion of circulating leukocytes to nascent atherosclerotic lesions [172]. Previous experiments showed a highly expression of *Pla2g12a* in endothelial cells, so we investigated if *Pla2g12a* was important for the adhesive capacity of ECs [148].

For the adhesion experiments, we used bone marrow-derived macrophages (BMDM) from atheroprotective FVB mice, Chr3 congenic FVB.Chr3$^{B6/B6}$ which contain the 80 Mb genomic DNA from Chr3 of C57BL/6 mice and atherosclerosis-sensitive C57BL/6 mice. Herewith, we wanted to explore, if genomic elements in the 80 Mb interval have an influence on adhesion.

For quantifying adhesion of BMDM to endothelial cells, two different experimental setups were investigated: first, *Pla2g12a* siRNA-treated endothelial cells (ECs) were preplated on uncoated 96-well plates 24 hours before adhesion experiments. BMDMs were then allowed to adhere for 45 min, washed twice and adherent cells were imaged with an IncuCyte Live Cell Analysis System (Essen Bioscience).

Second, BMDM were treated with siRNA for 24 hours and subsequently were allowed to adhere to non-treated ECs. Adherent cells were quantified as described above.

Additionally, cell adhesion assays with RAW264.7 macrophages were performed in 96-well plates coated with Matrigel or on uncoated dishes [148].

First, BMDM from FVB.*Ldlr*$^{-/-}$, chromosome 3 congenic (FVB.Chr3$^{B6/B6}$.*Ldlr*$^{-/-}$) and C57BL/6.*Ldlr*$^{-/-}$ mice were seeded on mouse cardiac endothelial cells (MCEC) that were treated with siRNAs against *Pla2g12a* or with scrambled (SCR) siRNA control oligonucleotides (Figure 43).

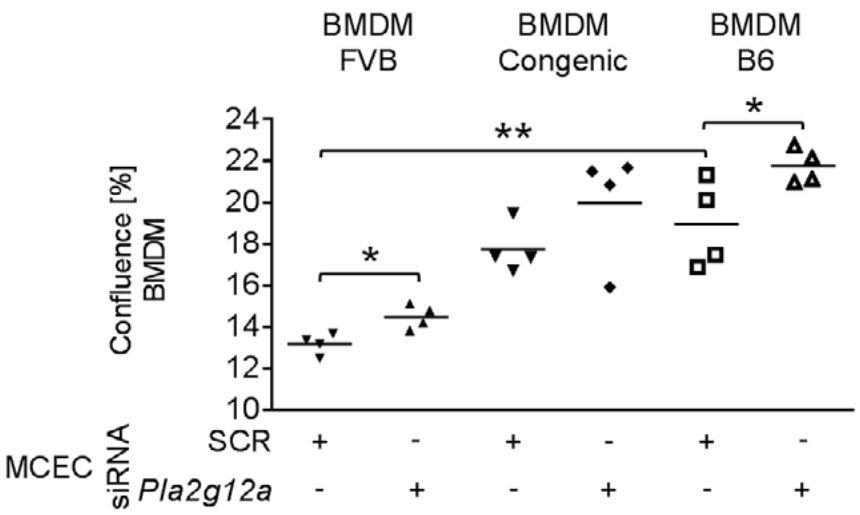

FIGURE 43: Adhesion of bone marrow-derived macrophages (BMDM) from *FVB.Ldlr*$^{-/-}$, chromosome 3 congenic (FVB.Chr3$^{B6/B6}$.*Ldlr*$^{-/-}$) and *C57BL/6.Ldlr*$^{-/-}$ mice on mouse cardiac endothelial cells that were treated with siRNAs against *Pla2g12a* or with scrambled (SCR) siRNA control oligonucleotides. Quadruplicate measurements per condition were performed. * $p < 0.05$; ** $p < 0.01$ [148].

Here, we found that BMDMs from B6 mice, as well as BMDMs derived from Chr3 congenic mice (both with lower *Pla2g12a* expression) were more adhesive than FVB BMDMs which have relatively higher *Pla2g12a* expression.

Importantly, we found that depleting *Pla2g12a* from endothelial cells in this adhesion assay further increased adhesion of BMDMs to ECs, with a comparable relative increase in adhesion of both B6-derived and FVB-derived BMDMs (Figure 43 A, B). These results indicated that PLA2G12A was exhibiting parallel atheroprotective roles in macrophages and in ECs [148].

Parallel, we determined the mRNA levels of *Pla2g12a* and *Vcam1* in the endothelial cells after *Pla2g12a* siRNA downregulation.

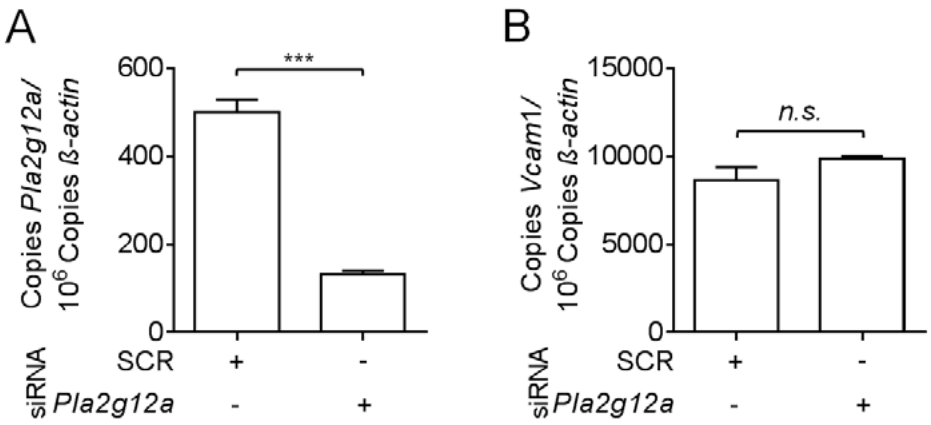

FIGURE 44: qPCR analysis of (**A**) *Pla2g12a* and (**B**) *Vcam1* mRNA expression in mouse cardiac endothelial cells (MCEC) after transfection with P*la2g12a* siRNA or using scrambled (SCR) siRNA controls. mRNA expression was normalized to 10^6 copies of β-*actin* house-keeping gene. Statistical differences are depicted relative to SCR control. *** $p < 0.001$, *n.s.* = not significant [148].

In this adhesion assay, upon loss of *Pla2g12a* (Figure 44 A), mRNA levels of the integrin ligand *Vcam1* did not change (Figure 44 B) suggesting that the change in adhesion was due to *Pla2g12a*-

dependent processes and independent of indirect transcriptional regulation of *Vcam1*. *Pla2g12a* mRNA expression was significantly reduced after *Pla2g12a* siRNA mediated knockdown.

To ask if *Pla2g12a* levels were determining the adhesive capacity also in bone marrow-derived macrophages, we depleted *Pla2g12a* in BMDM that we derived from FVB, congenic FVB.Chr3$^{B6/B6}$ and C57BL/6 mice. After 24 hours BMDMs were let to adhere on untreated endothelial cells [148].

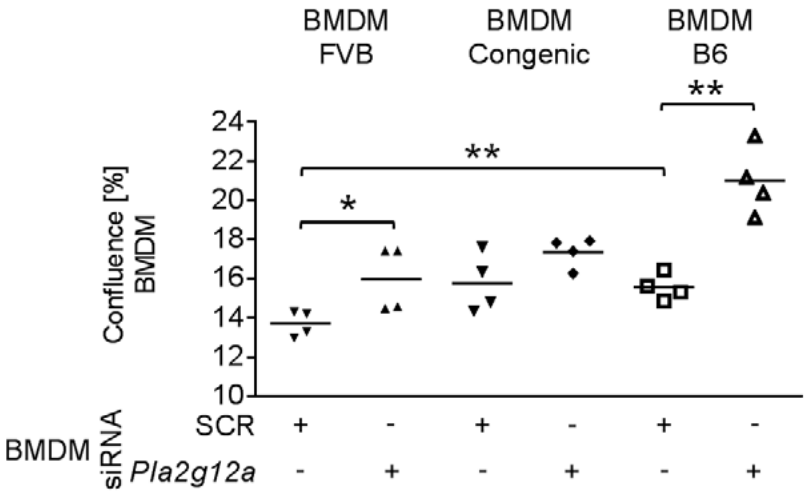

FIGURE 45: Adhesion of bone marrow-derived macrophages (BMDM) from FVB (n = 4), homozygous chromosome 3 congenics (FVB.Chr3$^{B6/B6}$ [n = 4]) or C57BL/6 (n = 4) mice that were treated with siRNAs against *Pla2g12a* or with scrambled (SCR) siRNA control on untreated mouse cardiac endothelial cells (MCEC). * $p < 0.05$; ** $p < 0.01$ [148].

Here again, we observed an increased adhesion after *Pla2g12a* knockdown in cells from all genetic backgrounds compared to cells treated with scrambled RNAi oligonucleotides (Figure 45).

Pla2g12a mRNA expression in BMDMs was significantly reduced after *Pla2g12a* siRNA knockdown (Figure 46 A) while *Vcam1* was not induced during the adhesion experiment (Figure 46 B).

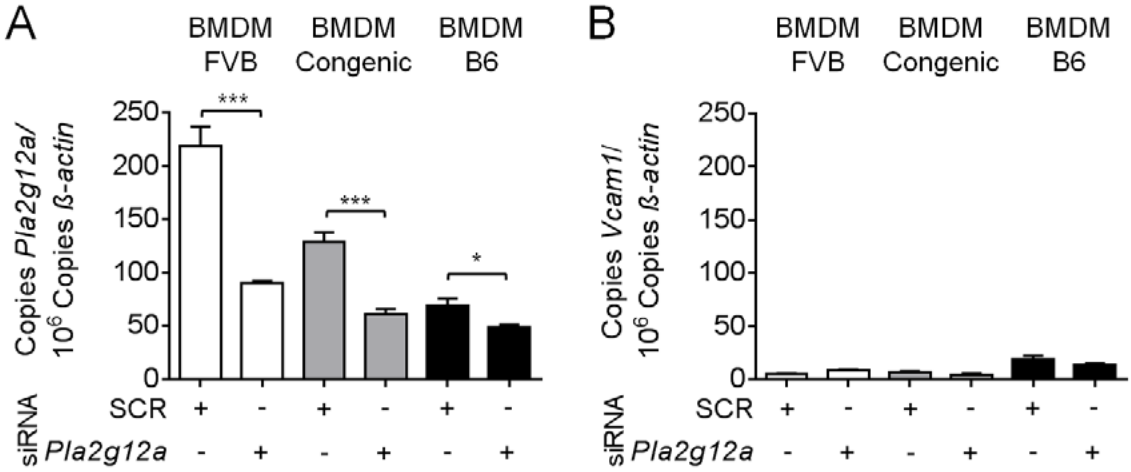

FIGURE 46: qPCR analysis of (**A**) *Pla2g12a* and (**B**) *Vcam1* mRNA expression in *FVB.Ldlr*$^{-/-}$, chromosome 3 congenic (FVB.Chr3$^{B6/B6}$.*Ldlr*$^{-/-}$) and *C57BL/6.Ldlr*$^{-/-}$ mice after transfection with *Pla2g12a* siRNA or using scrambled (SCR) siRNA controls. mRNA expression was normalized to 10^6 copies of β-*actin* housekeeping gene. Statistical differences are depicted relative to SCR control. * $p < 0.05$; *** $p < 0.001$ [148].

To test whether *Pla2g12a* was, thus, a more general determinant of adhesion, we depleted *Pla2g12a* in a cultures macrophages cell line of independent genetic origin (RAW264.7 cells from BALB/C mice).

While *Pla2g12a* siRNA mediated knockdown in RAW264.7 macrophages resulted in a significant decrease of the *Pla2g12a* mRNA expression (Figure 47 A), *Vcam1* was barely expressed (Figure 47 B), and therefore had no influence on the adhesion results.

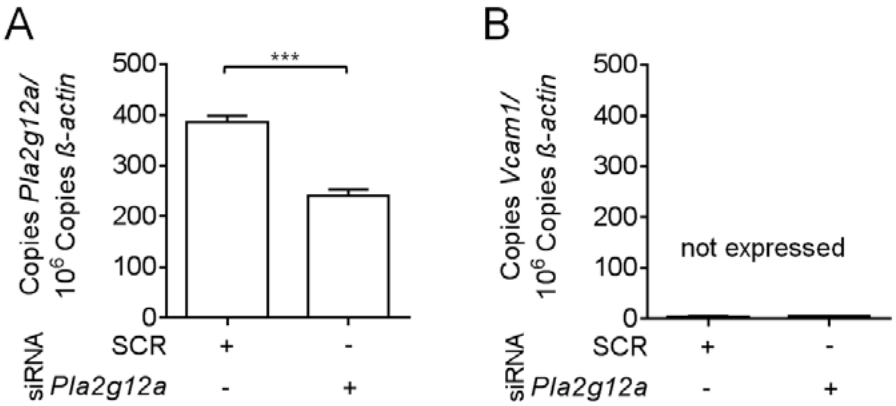

FIGURE 47: qPCR analysis of (**A**) *Pla2g12a* and (**B**) *Vcam1* mRNA expression in RAW264.7 macrophages after transfection with *Pla2g12a* siRNA or using scrambled (SCR) siRNA controls. mRNA expression was normalized to 10^6 copies of β-*actin* house-keeping gene. *** $p < 0.001$ [148].

Pla2g12a-depleted macrophages were seeded on uncoated and with matrigel-coated wells. Here again, we observed increased adhesion to both untreated culture plates as well as to matrigel-coated surfaces after *Pla2g12a* knockdown compared to cells treated with scrambled RNAi oligonucleotides [148].

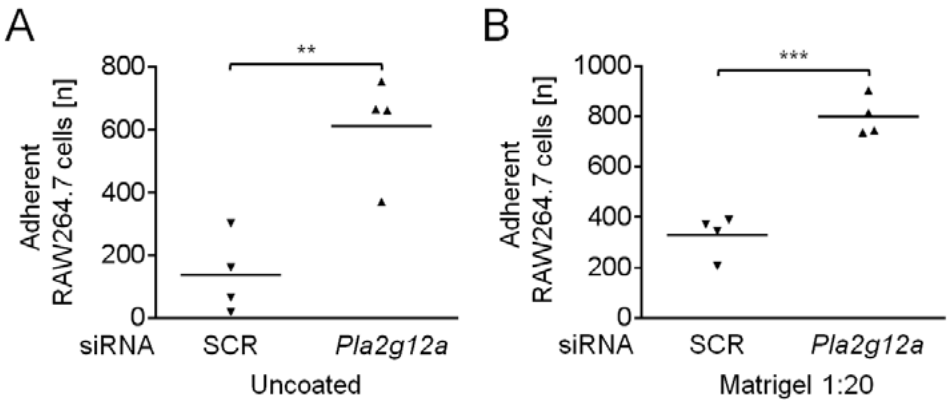

FIGURE 48: Adhesion of RAW264.7 macrophages on uncoated (**A**) and matrigel coated (**B**) membranes after siRNA-mediated knockdown of *Pla2g12a* (n = 4) or using scrambled (n = 4) control olirgonucleotides. ** $p < 0.01$; *** $p < 0.001$ [148].

These data indicate that PLA2G12A is normally functioning as anti-adhesive factor irrespective of the genetic background which is consistent with the increased sensitivity to atherosclerosis when PLA2G12A levels are low [148].

As the *Pla2g12a* expression was higher in endothelial cells we also examined the apoptotic behavior in mouse cardiac endothelial cells (MCEC) after *Pla2g12a* siRNA knockdown. Apoptosis in MCECs was stimulated with staurosporine (0.125 µM) and cycloheximide (10 ng/ml) (Figure 49).

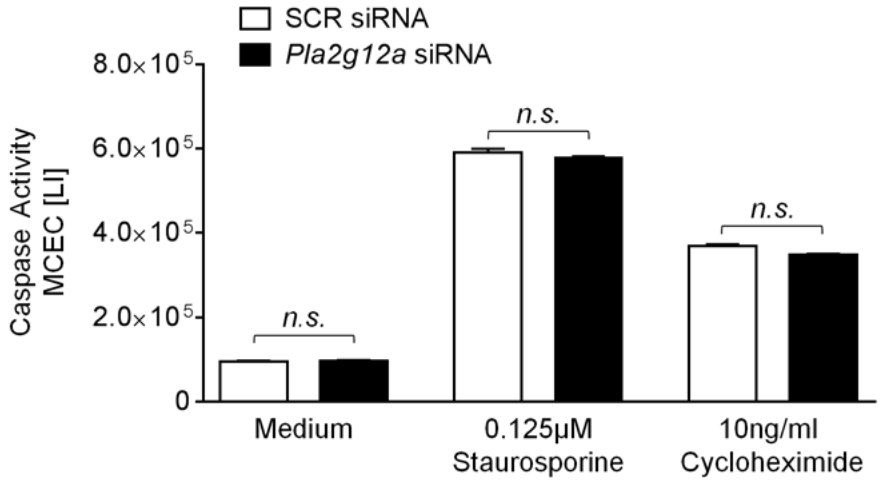

FIGURE 49: Apoptosis assay in mouse cardiac endothelial cells (MCEC) after siRNA-mediated knockdown of *Pla2g12a* (n = 4) or using scrambled (SCR) oligonucleotide controls (n = 4). Apoptosis in MCECs was stimulated with staurosporine (0.125 µM) or cycloheximide (10 ng/ml) for 24 hours. Caspase activity is given as luminescence intensity (LI). *n.s.* = not significant [148].

Depletion of *Pla2g12a* did not alter any survival properties in MCECs. Therefore, we think that this role in curbing adhesion was a specific regulatory process, because depletion of *Pla2g12a* did, for example, not alter other cellular regulatory.

Summarizing, *in vivo* as well as *in vitro* data indicate a role for *Pla2g12a* in protecting from atherosclerosis-relevant cellular functions and highlight *Pla2g12a* as novel atherosclerosis modifier in mice [148].

3 Results – Chapter II –

Adam17-deficiency promotes atherosclerosis by enhanced TNFR2 signalling in mice

This work has been published in [130].

3.2 Atherosclerosis locus on mouse chromosome 12

In the first part of this PhD thesis we focused on identifying novel candidate genes of atherosclerosis susceptibility in an atherosclerosis locus on mouse chromosome 3. In the same cross, the A*dam17* gene was previously identified as the candidate gene underlying the atherosclerosis locus on mouse chromosome 12. Figure 50 presents the LOD score of atherosclerosis and *Adam17* mRNA expression on mouse chromosome 12. The colocalization of the peak LOD score of *Adam17* mRNA expression to the peak LOD score of atherosclerosis at proximal Chr12 suggested that both phenotypes might be related [105].

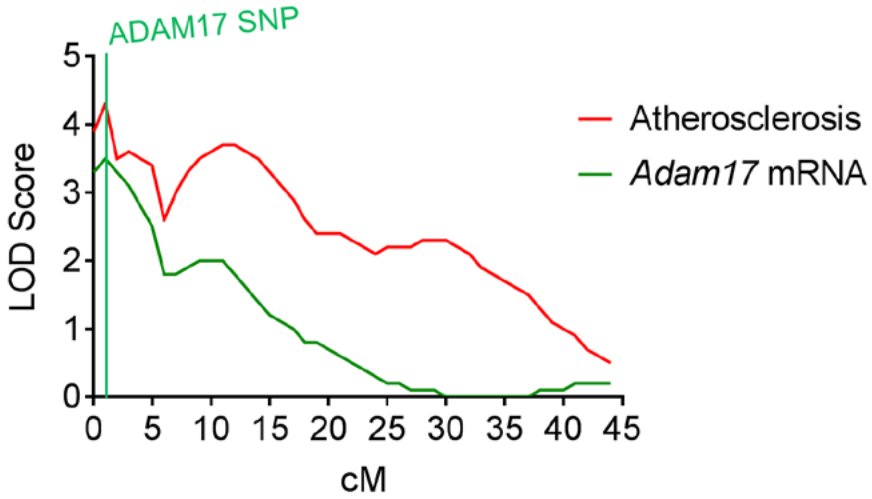

FIGURE 50: Atherosclerosis- and *Adam17* mRNA LOD score on mouse chromosome 12 [105].

Expression QTL (eQTL) mapping in female mice of the F2 generation indicated that reduced expression of *Adam17* mRNA and reduced ADAM17 activity was associated with increased atherosclerosis at the aortic root in female mice of the F2 generation [105]. This suggested that *Adam17* might confer atheroprotection, which at first seemed contradictory to its well-established role in promoting cell adhesion and inflammation [120, 131, 173-175]. Since *Adam17* knockout (Adam17$^{\Delta Zn/\Delta Zn}$) mice are not viable and die within several hours after birth having severe epithelial abnormalities [131], the direct effect of *Adam17*-deficiency on atherosclerosis development has not been investigated so far. Only recently, hypomorphic *Adam17* mice (*Adam17*$^{ex/ex}$) have been generated, which are partially deficient for Adam17 and have barely detectable levels of *Adam17* in all tissues [132]. Until now, conditional knockout mice with *Adam17* deletions in myeloid cells [133], thymic epithelial cells [134], osteochondroprogenitor cells [135], leucocytes [136], and endothelial cells [137, 138] were used to study inflammation (rheumatoid arthritis) and cancer. A mouse model overexpressing *Adam17* showed no enhanced shedding activity in vivo despite higher *Adam17* mRNA and protein expression [139]. To date, none of these mouse models have been used to study the effect of ADAM17 in atherosclerosis [130].

It was the aim of this thesis, to investigate the influence of partial *Adam17*-deficiency on atherosclerosis development and elucidated potential mechanisms of atherogenesis.

3.2.1 *Generation and characterization of Adam17$^{ex/ex}$.Ldlr$^{-/-}$ hypomorphic mice*

Hypomorphic *Adam17* mice (*Adam17*$^{ex/ex}$) were backcrossed onto the atherosclerosis-susceptible *Ldl*-receptor deficient (*Ldlr*$^{-/-}$) background for 6 generations (*Adam17*$^{ex/ex}$.*Ldlr*$^{-/-}$). Subsequently, heterozygous *Adam17*$^{wt/ex}$.*Ldlr*$^{-/-}$ mice were mated to generate male and female wild-type *Adam17*$^{wt/wt}$.*Ldlr*$^{-/-}$, heterozygous mutant *Adam17*$^{ex/wt}$.*Ldlr*$^{-/-}$ and homozygous mutant *Adam17*$^{ex/ex}$.*Ldlr*$^{-/-}$ mice. Homozygous A*dam17*$^{ex/ex}$.*Ldlr*$^{-/-}$ mice were born at a frequency clearly below the expected Mendelian distribution pattern [132], so we also mated male homozygous *Adam17*$^{ex/ex}$.*Ldlr*$^{-/-}$ mice with female heterozygous *Adam17*$^{wt/ex}$.*Ldlr*$^{-/-}$ mice. Female *Adam17*$^{ex/ex}$.*Ldlr*$^{-/-}$ mice had reduced milk duct development and were not suitable for matings [132]. The following shematic describes the matings and the generated mice used for the subsequent atherosclerosis experiments.

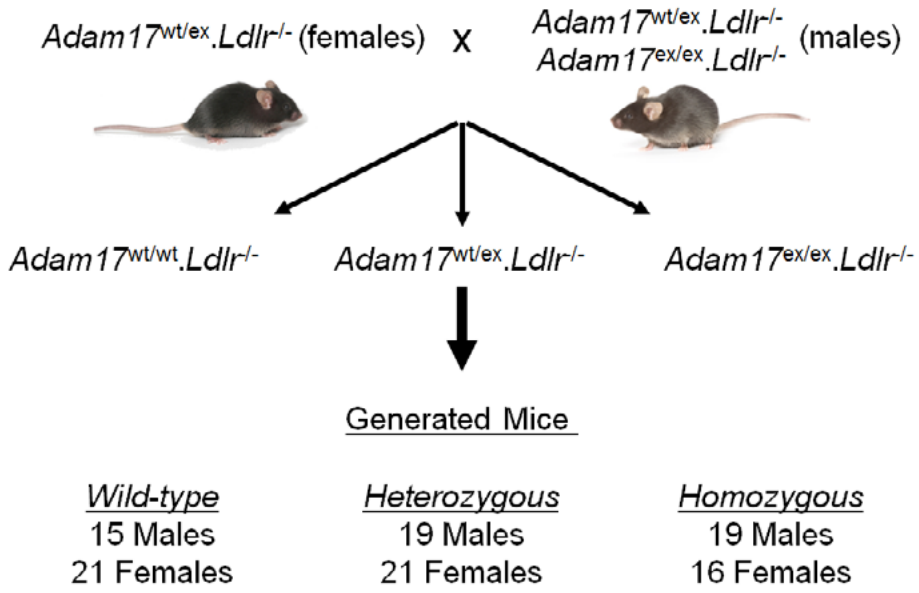

FIGURE 51: Shematic of the generation of male and female wild-type *Adam17*$^{wt/wt}$.*Ldlr*$^{-/-}$, heterozygous *Adam17*$^{wt/ex}$.*Ldlr*$^{-/-}$ and homozygous mutant *Adam17*$^{ex/ex}$.*Ldlr*$^{-/-}$ mice. A total of 111 mice were generated.

To induce atherosclerosis, male and female wild-type *Adam17*$^{wt/wt}$.*Ldlr*$^{-/-}$, heterozygous *Adam17*$^{wt/ex}$.*Ldlr*$^{-/-}$ and homozygous *Adam17*$^{ex/ex}$.*Ldlr*$^{-/-}$ mice were fed a semisynthetic diet for 16 weeks, resulting in a moderate degree of hypercholesterolemia, which is more physiological than feeding on a high-fat, high-cholesterol diet [99, 130]. Mice were sacrificed at 20 weeks of age after they were weaned at 4 weeks of age by a standardized protocol. Total body weight and biochemical characteristics and other clinical chemical parameters of male and female wild-type *Adam17*$^{wt/wt}$.*Ldlr*$^{-/-}$, heterozygous *Adam17*$^{wt/ex}$.*Ldlr*$^{-/-}$ and homozygous *Adam17*$^{ex/ex}$.*Ldlr*$^{-/-}$ mice are indicated in Tables 23 and 24.

Homozygous *Adam17*$^{ex/ex}$.*Ldlr*$^{-/-}$ mice developed eye, skin and hair defects compared to heterozygous and wild-type mice as previously described by Chalaris et al. [132]. In addition, *Adam17*$^{ex/ex}$.*Ldlr*$^{-/-}$ mice developed slightly enlarged hearts compared to wild-type *Adam17*$^{wt/wt}$.*Ldlr*$^{-/-}$ mice (4205 µm^2/3772 µm^2; 35/39 mice; $p = 3.11 \times 10^{-5}$) in accordance to TACE$^{\Delta Zn/\Delta Zn}$ null mutants, which exhibit markedly enlarged fetal hearts and die at birth [176]. Plasma parameters were analyzed in an automated analyzer (Modular PPE, Roche) and lipoproteins were isolated by sequential ultracentrifugation.

Plasma total-, LDL-, and HDL-cholesterol levels were not significantly different in female *Adam17*$^{ex/ex}$.*Ldlr*$^{-/-}$ and *Adam17*$^{wt/wt}$.*Ldlr*$^{-/-}$ mice (Tables 23 and 24). In male *Adam17*$^{ex/ex}$.*Ldlr*$^{-/-}$ mice, LDL-cholesterol was even lower than in *Adam17*$^{wt/wt}$.*Ldlr*$^{-/-}$ controls. White blood cells were significantly elevated in whole blood of *Adam17*$^{ex/ex}$.*Ldlr*$^{-/-}$ mice.

TABLE 23: Total body weight, biochemical characteristics and chemical clinical parameters of female *Adam17*$^{wt/wt}$.*Ldlr*$^{-/-}$, *Adam17*$^{wt/ex}$.*Ldlr*$^{-/-}$ and *Adam17*$^{ex/ex}$.*Ldlr*$^{-/-}$ mice [130].

Measurement	***Adam17*$^{wt/wt}$.*Ldlr*$^{-/-}$**	***Adam17*$^{wt/ex}$.*Ldlr*$^{-/-}$**	***Adam17*$^{ex/ex}$.*Ldlr*$^{-/-}$**	***p*-Value**		
n =	**21**	**21**	**16**	**wt/ex***	**wt/het†**	**het/ex‡**
Body Weight [g]	19.5 ± 1.2	19 ± 0.9	19.5 ± 2.2	*n.s.*	*n.s.*	*n.s.*
Cholesterol [mg/dl]	521.7 ± 125.9	440.5 ± 90.4	577 ± 207	*n.s.*	*0.01*	*0.009*
LDL-Chol [mg/dl]	380.8 ± 85.1	303 ± 116.1	429.7 ± 117.7	*n.s.*	*0.04*	*0.008*
HDL-Chol [mg/dl]	69.7 ± 29.8	74.2 ± 37.2	62.9 ± 14.5	*n.s.*	*n.s.*	*n.s.*
Triglycerides [mg/dl]	137.5 ± 55.3	108 ± 46.8	240.5 ± 149.3	*0.006*	*n.s.*	*0.0004*
WBC [g/l]	1.44 ± 0.61	1.51 ± 0.53	2.97 ± 2.26	*0.005*	*n.s.*	*0.006*
ALT [U/l]	30 ± 18.9	27.6 ± 9.7	43.3 ± 18.8	*0.04*	*n.s.*	*0.001*
AST [U/l]	135.6 ± 64.5	158.8 ± 85.9	136.1 ± 40.2	*n.s.*	*n.s.*	*n.s.*
Cholinesterase [KU/l]	5.6 ± 1	6.1 ± 0.9	4.7 ± 1.2	*0.005*	*n.s.*	*0.00001*
GLDH [U/l]	14.8 ± 9.1	11.8 ± 4.9	45.4 ± 29.9	5.4×10^{-5}	*n.s.*	4.5×10^{-6}
Glucose [mg/dl]	278.8 ± 48.8	298 ± 53.6	249 ± 65	*n.s.*	*n.s.*	*0.006*
Urea [mg/dl]	44.6 ± 10.2	45.2 ± 8.5	53.5 ± 14.7	*0.014*	*n.s.*	*0.012*
Total Protein [g/dl]	4.8 ± 0.4	4.4 ± 0.4	4.6 ± 1	*n.s.*	*0.002*	*0.02*

Data are given as mean ± SD. LDL-Chol, low-density lipoprotein cholesterol; HDL-Chol, high-density lipoprotein cholesterol; WBC, white blood cells; ALT, alanine aminotransferase; AST, aspartate aminotransferase; GLDH, Glutamate dehydrogenase. Comparison of multiple groups was done using ANOVA, and Tukey was performed as a post-test. * Comparison of *Adam17*$^{wt/wt}$.*Ldlr*$^{-/-}$ (wt) and *Adam17*$^{ex/ex}$.*Ldlr*$^{-/-}$ (ex) mice; † Comparison of *Adam17*$^{wt/wt}$.*Ldlr*$^{-/-}$ (wt) and *Adam17*$^{wt/ex}$.*Ldlr*$^{-/-}$ (het) mice; ‡ Comparison of *Adam17*$^{wt/ex}$.*Ldlr*$^{-/-}$ (het) and *Adam17*$^{ex/ex}$.*Ldlr*$^{-/-}$ (ex) mice.

TABLE 24: Total body weight, biochemical characteristics and chemical clinical parameters of male *Adam17*$^{wt/wt}$.*Ldlr*$^{-/-}$, *Adam17*$^{wt/ex}$.*Ldlr*$^{-/-}$ and *Adam17*$^{ex/ex}$.*Ldlr*$^{-/-}$ mice [130].

Measurement	*Adam17*$^{wt/wt}$.*Ldlr*$^{-/-}$	*Adam17*$^{wt/ex}$.*Ldlr*$^{-/-}$	*Adam17*$^{ex/ex}$.*Ldlr*$^{-/-}$	*p*-Value		
n =	15	19	19	wt/ex*	wt/het†	het/ex‡
Body Weight [g]	25.2 ± 3.3	24.5 ± 1.2	24.9 ± 2	*n.s.*	*n.s.*	*n.s.*
Cholesterol [mg/dl]	394 ± 78	401 ± 61	379 ± 68	*n.s.*	*n.s.*	*n.s.*
LDL-Chol [mg/dl]	313.5 ± 56.8	285.4 ± 70.4	265 ± 39.5	*0.009*	*n.s.*	*n.s.*
HDL-Chol [mg/dl]	91.7 ± 22.4	101.5 ± 39.4	82.9 ± 9.1	*n.s.*	*n.s.*	*n.s.*
Triglycerides [mg/dl]	127.5 ± 45.5	141.9 ± 43.5	181.6 ± 81.4	*0.02*	*n.s.*	*n.s.*
WBC [g/l]	1.52 ± 0.68	1.46 ± 0.65	2.62 ± 2.48	*n.s.*	*n.s.*	*0.04*
ALT [U/l]	30.1 ± 43.4	23.5 ± 5.6	44.7 ± 43.1	*n.s.*	*n.s.*	*0.03*
AST [U/l]	115.2 ± 87.1	172.5 ± 79	125.1 ± 43.1	*n.s.*	*0.04*	*0.048*
Cholinesterase [KU/l]	4.1 ± 0.9	4.6 ± 0.4	3.2 ± 0.7	*0.0001*	*0.02*	4.9×10^{-14}
GLDH [U/l]	16.7 ± 29.3	10.7 ± 4.1	35.4 ± 26.6	*0.04*	*n.s.*	*0.0001*
Glucose [mg/dl]	306.7 ± 74.2	322 ± 32.5	263 ± 62.5	*0.027*	*n.s.*	3.5×10^{-5}
Urea [mg/dl]	49 ± 20	45 ± 4.3	61.5 ± 17.3	*0.025*	*n.s.*	6.8×10^{-7}
Total Protein [g/dl]	4.9 ± 0.3	4.6 ± 0.2	4.6 ± 1	*0.01*	*0.0005*	*n.s.*

Data are given as mean ± SD. LDL-Chol, low-density lipoprotein cholesterol; HDL-Chol, high-density lipoprotein cholesterol; WBC, white blood cells; ALT, alanine aminotransferase; AST, aspartate aminotransferase; GLDH, Glutamate dehydrogenase. Comparison of multiple groups was done using ANOVA, and Tukey was performed as a post-test. * Comparison of *Adam17*$^{wt/wt}$.*Ldlr*$^{-/-}$ (wt) and *Adam17*$^{ex/ex}$.*Ldlr*$^{-/-}$ (ex) mice; † Comparison of *Adam17*$^{wt/wt}$.*Ldlr*$^{-/-}$ (wt) and *Adam17*$^{wt/ex}$.*Ldlr*$^{-/-}$ (het) mice; ‡ Comparison of *Adam17*$^{wt/ex}$.*Ldlr*$^{-/-}$ (het) and *Adam17*$^{ex/ex}$.*Ldlr*$^{-/-}$ (ex) mice.

3.2.2 *Tissue expression profiling in Adam17 hypomorphic mice*

We examined the *Adam17* mRNA expression in different tissues and cells of wild-type *Adam17*$^{wt/wt}$.*Ldlr*$^{-/-}$ and homozygous *Adam17*$^{ex/ex}$.*Ldlr*$^{-/-}$ mice using quantitative polymerase chain reaction (qPCR). Bone marrow cells were thawed and differentiated into macrophages (MΦ). *Adam17* copies were normalized to µg RNA.

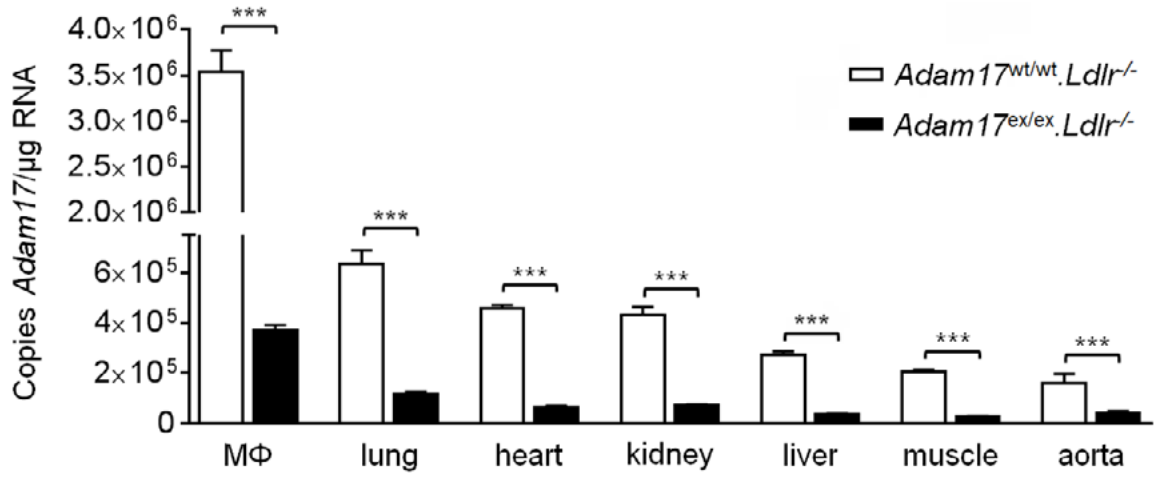

FIGURE 52: *Adam17* mRNA expression in different tissues of *Adam17*$^{wt/wt}$.*Ldlr*$^{-/-}$ (n = 6) and *Adam17*$^{ex/ex}$.*Ldlr*$^{-/-}$ (n = 6) mice. MΦ, Macrophages. *** $p < 0.001$ [130]

We validated a consistent and ubiquitous decrease of *Adam17* mRNA expression in cells and tissues of hypomorphic *Adam17*$^{ex/ex}$.*Ldlr*$^{-/-}$ mice (Figure 52). The highest *Adam17* mRNA expression was observed in bone marrow-derived macrophages (BMDM) [130].

3.2.3 *Increased atherosclerosis in Adam17-deficient mice*

To investigate the role of *Adam17*-deficiency in atherosclerosis we quantified atherosclerotic lesions at oil red O-stained sections of the aortic root of male and female wild-type *Adam17*$^{wt/wt}$.*Ldlr*$^{-/-}$ mice (n = 15/21), heterozygous *Adam17*$^{wt/ex}$.*Ldlr*$^{-/-}$ (n = 19/21) and homozygous *Adam17*$^{ex/ex}$.*Ldlr*$^{-/-}$ (n = 19/16) mice at 20 weeks of age.

In the aortic root, atherosclerosis was significantly increased in *Adam17*$^{ex/ex}$.*Ldlr*$^{-/-}$ compared to *Adam17*$^{wt/wt}$.*Ldlr*$^{-/-}$ mice, were male and female hypomorphic mice developed both approximately 1.5 fold larger atherosclerotic lesions compared to wild-type controls [130].

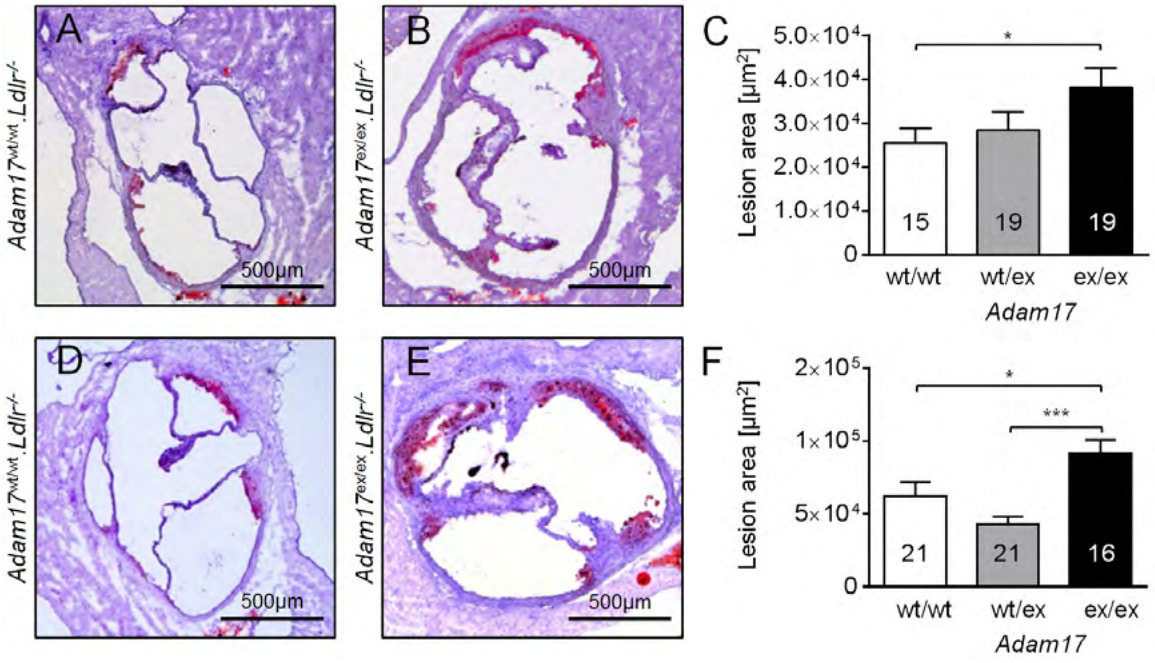

FIGURE 53: Increased atherosclerosis in *Adam17*-deficient mice on the *Ldlr*$^{-/-}$ background. Representative oil red O stainings of aortic roots of male and female (**A/D**) *Adam17*$^{wt/wt}$.*Ldlr*$^{-/-}$ and (**B/E**) *Adam17*$^{ex/ex}$.*Ldlr*$^{-/-}$ mice, respectively. Quantification of atherosclerotic plaque area at the aortic root of male (**C**) and females (**F**) *Adam17*$^{wt/wt}$.*Ldlr*$^{-/-}$(wt/wt), *Adam17*$^{wt/ex}$.*Ldlr*$^{-/-}$(wt/ex) and *Adam17*$^{ex/ex}$.*Ldlr*$^{-/-}$ (ex/ex) mice. Animal numbers are given in the columns. Values are given as mean + SEM. * $p < 0.05$; ** $p < 0.01$ [130].

These findings corresponded with the data from the previous study, demonstrating that reduced *Adam17* expression and activity was associated with increased atherosclerosis at the aortic root in an F2 intercross of atherosclerosis susceptibility B6 and atherosclerosis resistance FVB mice [105].

3.2.4 *Immunohistochemical and immunofluorescence stainings*

To examine the cellular composition of lesions in wild-type *Adam17*$^{wt/wt}$*.Ldlr*$^{-/-}$ and homozygous *Adam17*$^{ex/ex}$*.Ldlr*$^{-/-}$ mice we performed immunohistochemical stainings for CD68 positive macrophages, von Willebrand-factor (vWF) positive endothelial cells and alpha-smooth muscle actin (α-SMA) (Figure 54). Oil red O stainings of wild-type *Adam17*$^{wt/wt}$*.Ldlr*$^{-/-}$ and homozygous *Adam17*$^{ex/ex}$*.Ldlr*$^{-/-}$ mice are also shown.

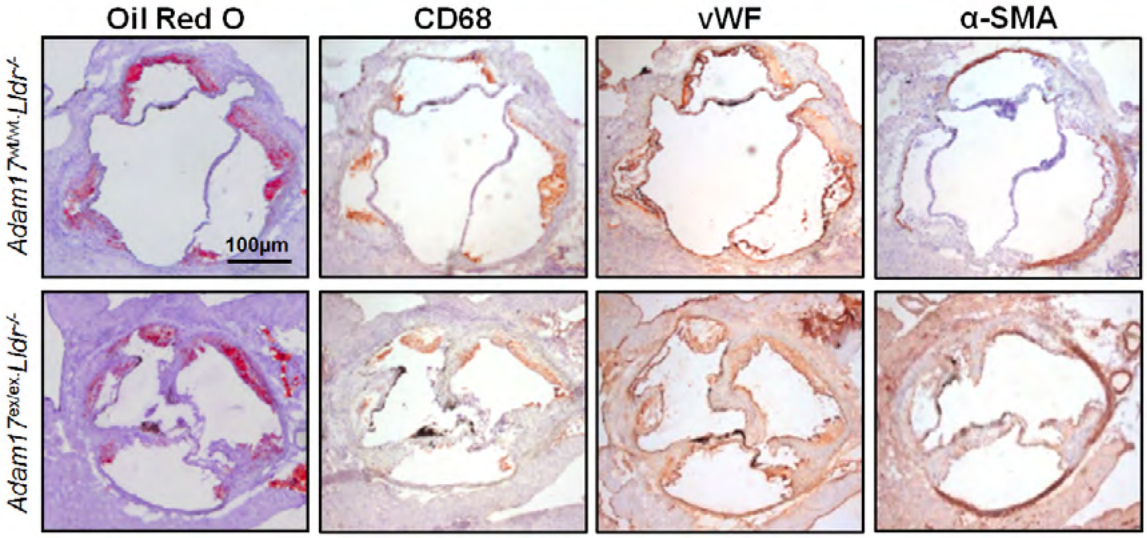

FIGURE 54: Immunohistochemical staining (oil red O, CD68, vWF, α-SMA) of the aortic root of wild-type *Adam17*$^{wt/wt}$*.Ldlr*$^{-/-}$ and homozygous *Adam17*$^{ex/ex}$*.Ldlr*$^{-/-}$ mice.

No differences were observed at the cellular composition, but we observed significantly altered aortic valve morphology (thickening of the aortic valves) of male and female *Adam17*$^{ex/ex}$*.Ldlr*$^{-/-}$ mice compared to heterozygous and wild type littermate controls as previously described in mice (Tie2-Cre/+; *Adam17*$^{Fl/\Delta Ex5}$) with endothelial cell-specific *Adam17* ablation [138].

To investigate, which cells within atherosclerotic lesions expressed ADAM17, and to prioritize cells for subsequent functional studies, we performed immunofluorescence co-stainings in plaques of aortic roots of wild-type C57BL/6 mice with respect to the content of CD68 and Mac2 positive macrophages, von Willebrand-factor (vWF) positive endothelial cells and alpha-smooth muscle actin (α-SMA) [130].

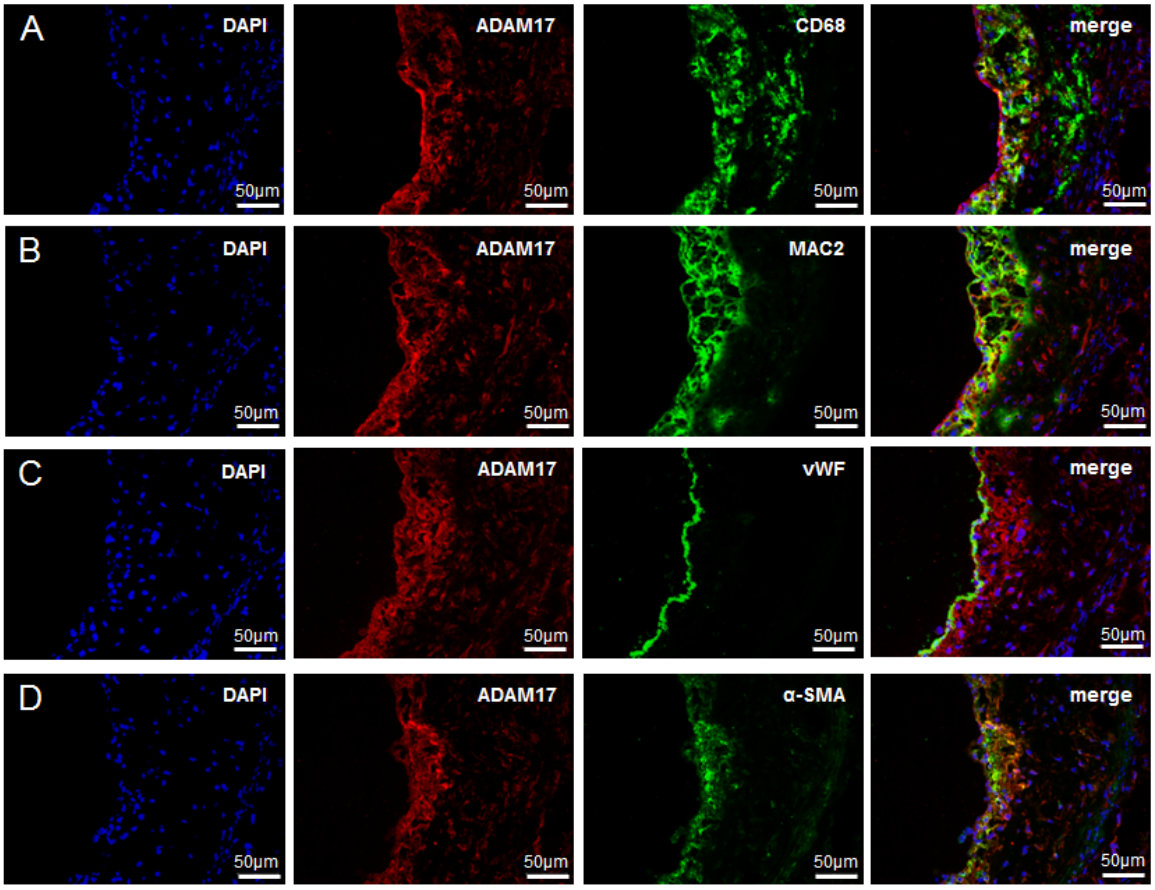

FIGURE 55: Immunofluorescence co-stainings of ADAM17 protein with (**A**) CD68-positive macrophages, with (**B**) MAC2-positive macrophages, with (**C**) von Willebrand-factor (vWF)-positive vascular endothelial cells and with (**D**) Smooth muscle actin (α-SMA)-positive vascular smooth muscle cells in the plaque area of an aortic root of a C57BL/6 mouse [130].

We found that ADAM17 protein was expressed in CD68- and Mac2-positive macrophages, von Willebrand factor-positive endothelial cells, and α-SMA positive vascular smooth muscle cells demonstrating that all key cells involved in atherosclerosis development, expressed this gene [130].

3.2.5 *Adam17 mRNA expression and ADAM17 protein levels in different cell types*

We next investigated the *Adam17* mRNA expression and the ADAM17 protein levels in RAW264.7 macrophages, mouse cardiac endothelial cells (MCEC) and MOVAS vascular smooth muscle cells. Copies of *Adam17* mRNA were normalized to 10^6 copies of *β-actin* house-keeping gene and GAPDH protein levels was used as a control for the western blot analysis.

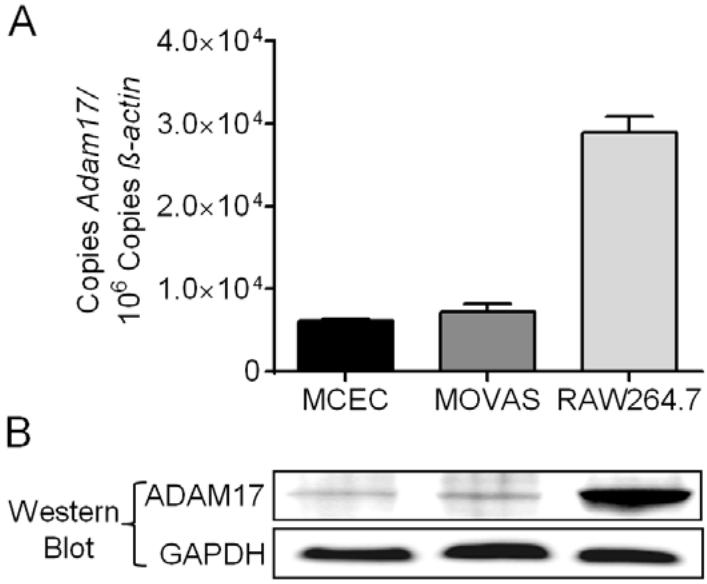

FIGURE 56: Quantification of (**A**) *Adam17* mRNA expression and (**B**) western blot of ADAM17 protein in mouse cardiac endothelial cells (MCEC), vascular smooth muscle cells (MOVAS) and RAW264.7 macrophages [130].

Adam17 mRNA expression was higher in RAW264.7 cells, and in a less degree in vascular smooth muscle cells MOVAS cells and mouse cardiac endothelial cells MCEC cells. On the protein level, highest ADAM17 expression was observed in RAW264.7 macrophages compared to MCEC and MOVAS cells.

3.2.6 *Reduced release of TNFR1 and TNFR2 in plasma of Adam17$^{ex/ex}$.Ldlr$^{-/-}$ mice*

ADAM17 is involved in several physiological and pathophysiological processes including adhesive and proteolytic properties and is also an important mediator of cell signaling which determine cellular fate, proliferation, and growth [121]. Until now, more than 70 substrates of ADAM17 have been identified [122]. The substrates of ADAM17 include membrane receptors, adhesion molecules, growth factors, cytokines and chemokines. Using multiplex technology, we systematically investigated the plasma concentrations of prototypical ADAM17 substrates in wild-type *Adam17*$^{wt/wt}$.*Ldlr*$^{-/-}$ (n = 12), heterozygous *Adam17*$^{wt/ex}$.*Ldlr*$^{-/-}$ (n = 10) and homozygous *Adam17*$^{ex/ex}$.*Ldlr*$^{-/-}$ (n = 12) mice such as soluble tumor necrosis factor receptor 1 (sTNFR1), soluble tumor necrosis factor receptor 2 (sTNFR2), soluble interleukin-6 receptor (sIL-6R), soluble tumor necrosis factor alpha (sTNFα), soluble fractalkine (sFractalkine), soluble interleukin-1 receptor 2 (sIL1-R2), soluble vascular endothelial growth factor receptor 2 (sVEGFR2), soluble CD30 (sCD30) and soluble vascular cell adhesion protein 1 (sVCAM1) [130].

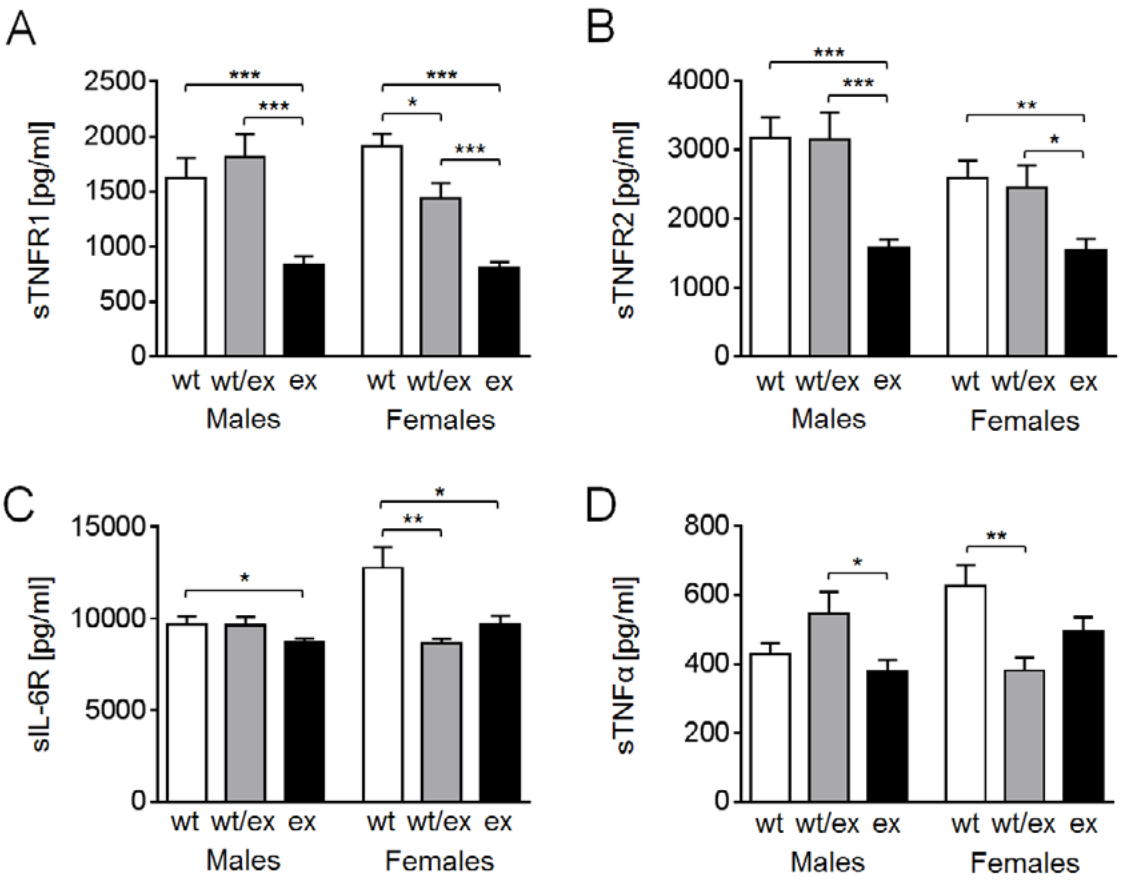

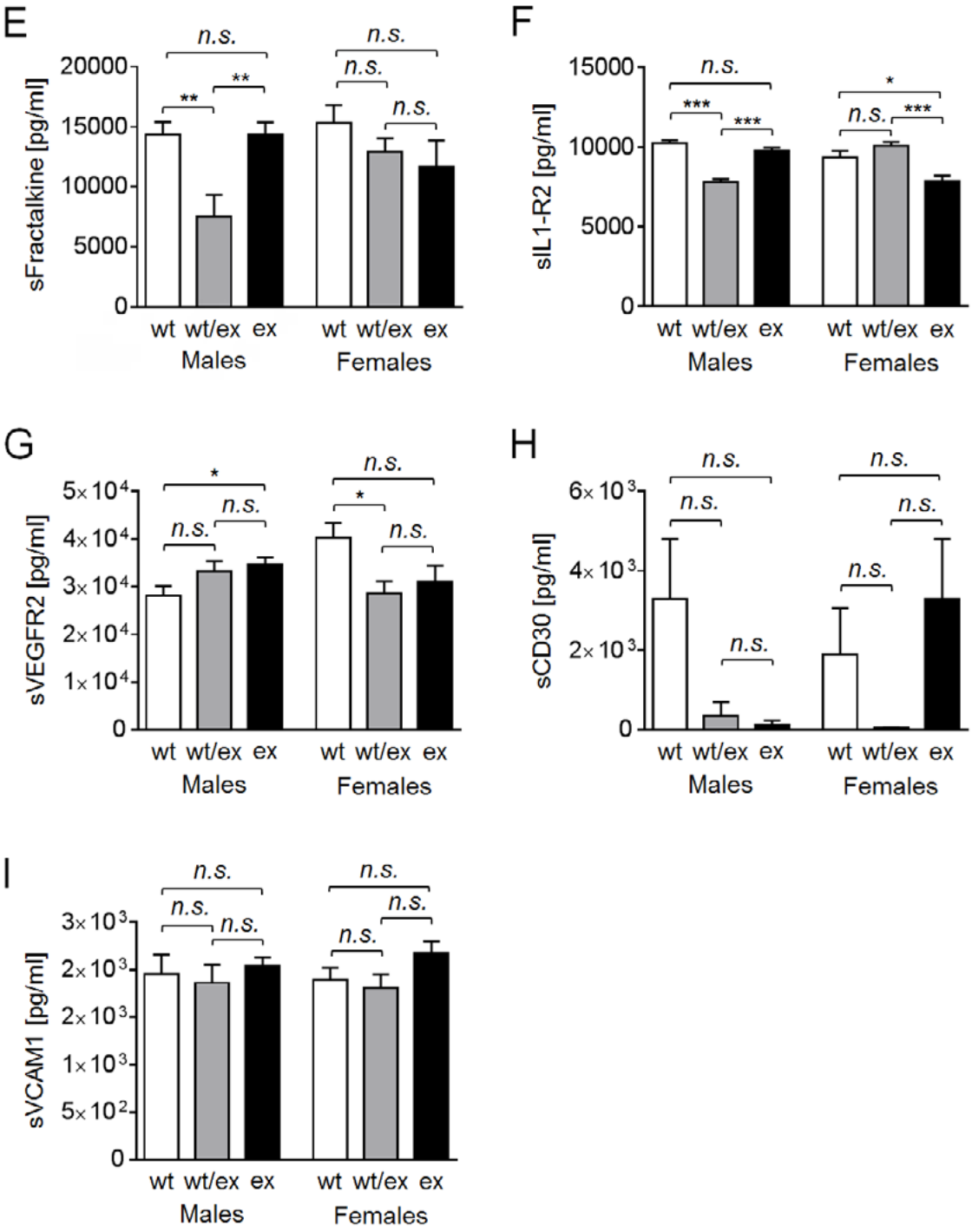

FIGURE 57: Release of ADAM17 protein substrates in plasma. Soluble (s) (**A**), sTNFR1, (**B**), sTNFR2, (**C**), sIL-6R, (**D**), sTNFα, (**E**), sFractalkine, (**F**), sIL-1R2, (**G**), sVEGFR2, (**H**), CD30 and (**I**) sVCAM1 levels in plasma samples of *Adam17*$^{wt/wt}$.*Ldlr*$^{-/-}$ (wt; n = 12), *Adam17*$^{wt/ex}$.*Ldlr*$^{-/-}$ (wt/ex; n = 10) and *Adam17*$^{ex/ex}$.*Ldlr*$^{-/-}$ (ex; n = 12) male and female mice [130].

We detected significantly reduced plasma levels of sTNFR1, sTNFR2 and sIL-6R in male and female *Adam17*$^{ex/ex}$.*Ldlr*$^{-/-}$ mice compared to *Adam17*$^{wt/wt}$.*Ldlr*$^{-/-}$ controls (Figures 57 A-C). For soluble TNFα, we observed a trend toward decreased plasma levels in male and female mice, which did not reach significance (Figure 57 D). sIL1-R2 was significantly reduced only in female *Adam17*$^{ex/ex}$.*Ldlr*$^{-/-}$ mice (Figure 57 E). The release of other ADAM17 substrates (sFractalkine, sVEGFR2, CD30 and sVCAM1) was not significantly altered or inconsistent (Figure 57 E, G-I) [130].

3.2.7 *Plasma levels of ADAM17-independent inflammatory mediators*

We further tested plasma levels of a set of ADAM17-independent inflammatory mediators like soluble interferon-γ (IFN-γ), soluble interleukin-1 beta (IL-1β), soluble interleukin-6 (IL-6), soluble interleukin-10 (IL-10), soluble monocyte chemotactic protein 1 (MCP-1), soluble macrophage inflammatory protein 1α (MIP-1α) and soluble macrophage inflammatory protein 1β (MIP-1β) in wild-type *Adam17*$^{wt/wt}$.*Ldlr*$^{-/-}$ (n = 12), heterozygous *Adam17*$^{wt/ex}$.*Ldlr*$^{-/-}$ (n = 10) and homozygous *Adam17*$^{ex/ex}$.*Ldlr*$^{-/-}$ (n = 12) mice using the Luminex technology [130].

IL-1β and IL-6 are proinflammatory cytokines, IL-10 belongs to the anti-inflammatory cytokines, while MCP-1, MIP-1α, MIP-1β, and RANTES belong to the chemotactic proteins (chemokines) and IFN-γ is an immunoregulatory protein.

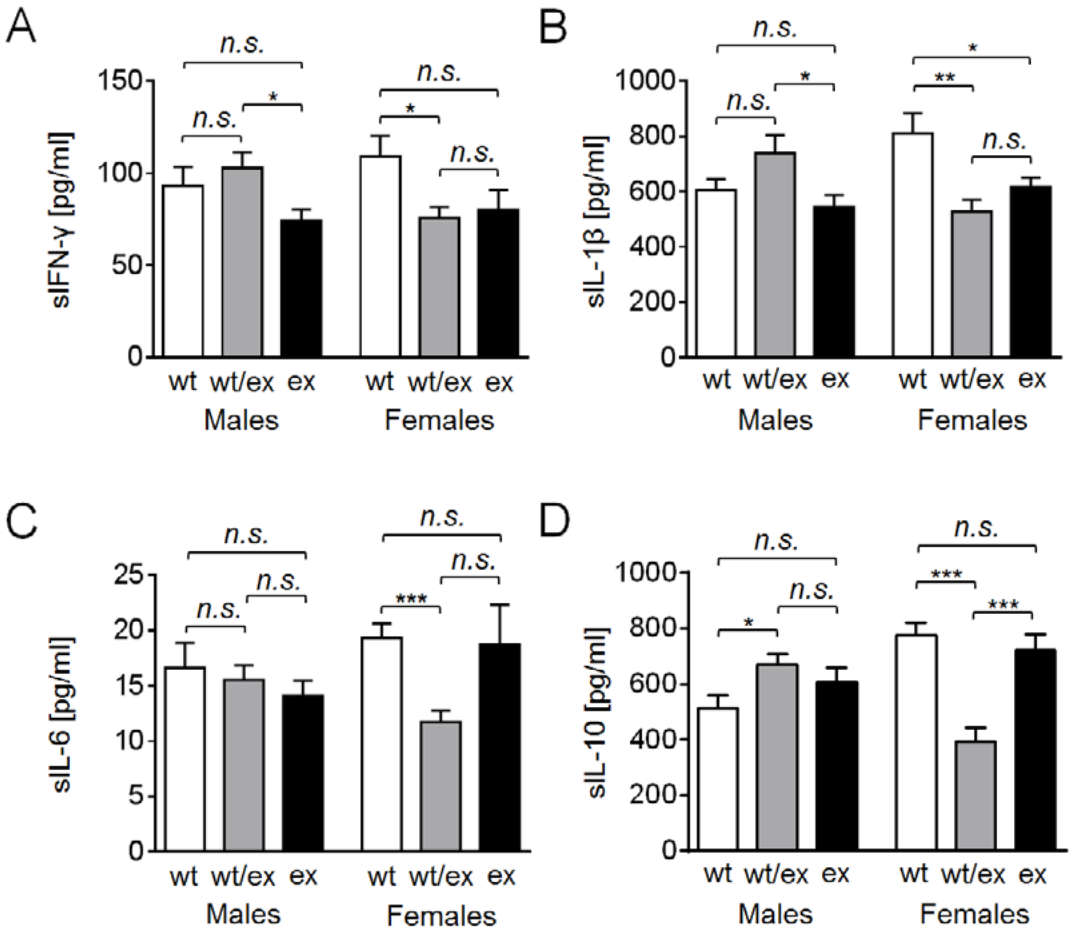

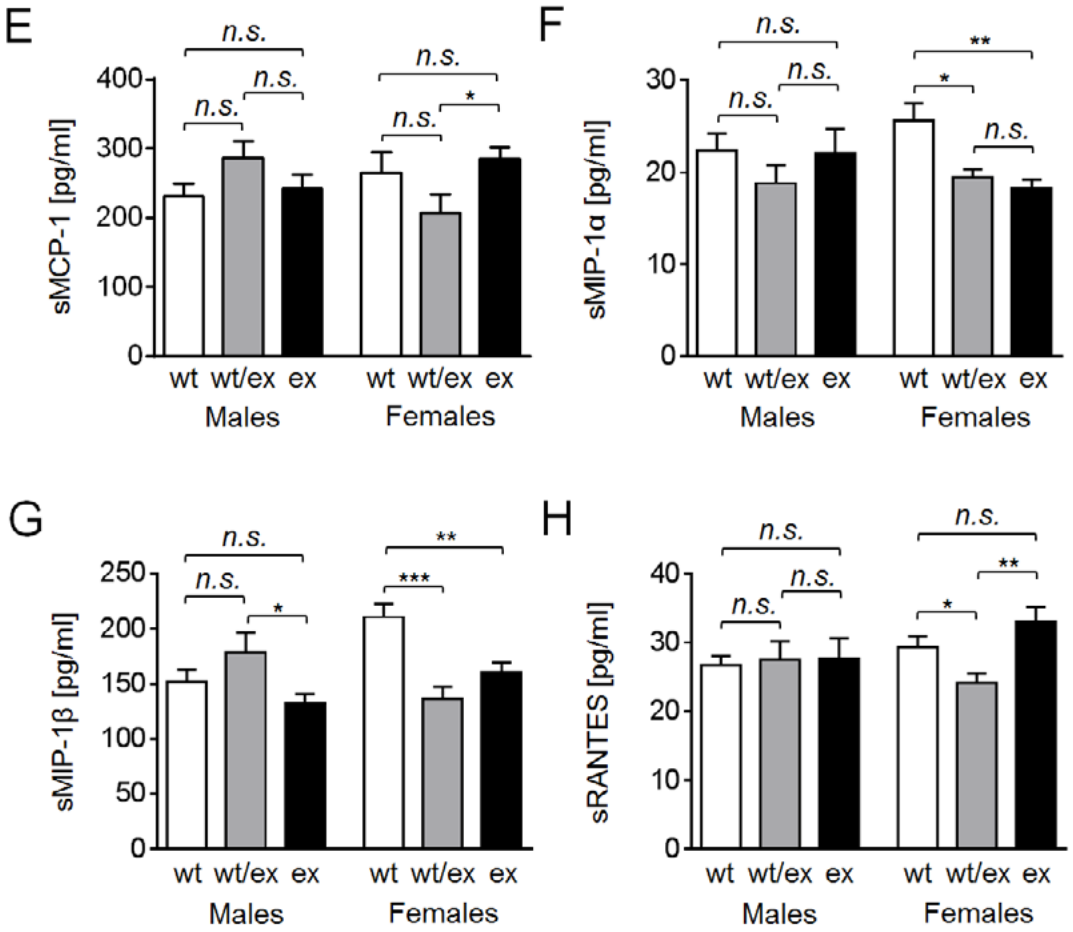

FIGURE 58: Cytokine release in plasma samples of *Adam17*$^{wt/wt}$.*Ldlr*$^{-/-}$, *Adam17*$^{wt/ex}$.*Ldlr*$^{-/-}$ and *Adam17*$^{ex/ex}$.*Ldlr*$^{-/-}$ mice. (**A**) soluble IFN-γ (sIFN-γ), (**B**) sIL-1β, (**C**) sIL-6, (**D**) sIL-10, (**E**) sMCP-1, (**F**) sMIP-1α, (**G**) sMIP-1β, and (**H**) sRANTES levels in plasma samples of *Adam17*$^{wt/wt}$.*Ldlr*$^{-/-}$ (wt, n = 12), *Adam17*$^{wt/ex}$.*Ldlr*$^{-/-}$ (wt/ex, n = 10) and *Adam17*$^{ex/ex}$.*Ldlr*$^{-/-}$ (ex, n = 12) mice. * $p < 0.05$; ** $p < 0.01$; *** $p < 0.001$ [130].

Proinflammatory cytokine IL-1β was significantly decreased in plasma samples of *Adam17*-deficient mice, while IL-6 and IL-10 were unchanged in *Adam17*$^{wt/wt}$.*Ldlr*$^{-/-}$ and *Adam17*$^{ex/ex}$.*Ldlr*$^{-/-}$ male and female mice (Figures 58 B-D). Chemokines MIP-1α (CCL3) and MIP-1β (CCL4) which are formed under pathological conditions and participate in the inflammatory response attracting immune cells to the site of inflammation were significantly less released especially in female mice (Figures 58 F, G). Released soluble MCP-1 and RANTES showed no differences between *Adam17*$^{wt/wt}$.*Ldlr*$^{-/-}$ and *Adam17*$^{ex/ex}$.*Ldlr*$^{-/-}$ male and female mice (Figures 58 E, H).

In summary, we observed no consistent trend between *Adam17*$^{wt/wt}$.*Ldlr*$^{-/-}$, *Adam17*$^{wt/ex}$.*Ldlr*$^{-/-}$ and *Adam17*$^{ex/ex}$.*Ldlr*$^{-/-}$ male and female mice, indicating that *Adam17*-deficiency did not alter inflammatory signaling per se in our atherosclerosis model [130].

3.2.8 *ADAM17 substrate release in the supernatant of BMDM*

For functional validation, we used *in vitro* cell culture of bone marrow-derived macrophages (BMDM) from *Adam17*$^{wt/wt}$.*Ldlr*$^{-/-}$ and *Adam17*$^{ex/ex}$.*Ldlr*$^{-/-}$ mice and quantified ADAM17 substrates, that were differentially released in plasma, in the supernatants with and without stimulation with phorbol 12-myristate 13-acetate (PMA), which is an activator of ADAM17 (Figures 59 A-D) [130].

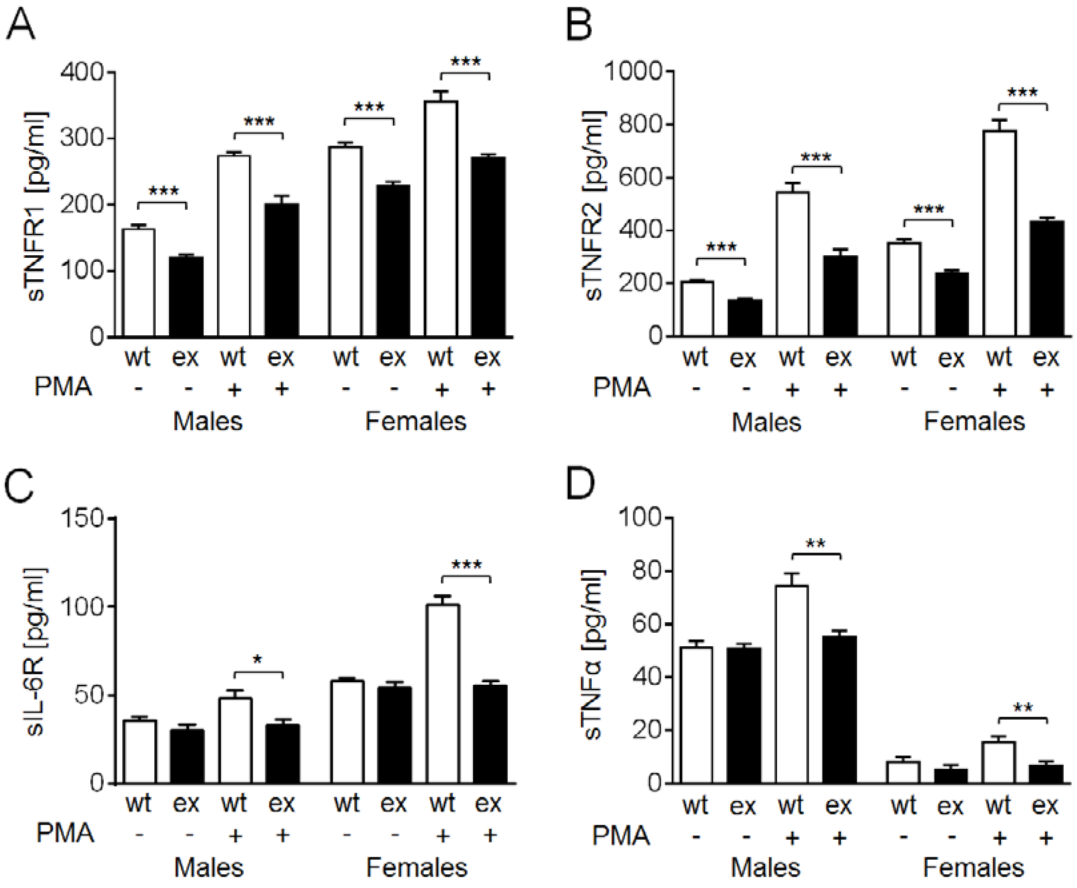

FIGURE 59: Release of ADAM17 substrates in the supernatant of bone marrow derived macrophages. (**A**) sTNFR1, (**B**) sTNFR2, (**C**) sTNFα, and (**D**) sIL-6R levels in the supernatants of macrophages of *Adam17*$^{wt/wt}$.*Ldlr*$^{-/-}$ (wt) and *Adam17*$^{ex/ex}$.*Ldlr*$^{-/-}$ (ex) mice with and without stimulation with phorbol 12-myristate 13-acetate (PMA). * $p < 0.05$; ** $p < 0.01$; *** $p < 0.001$ [130].

Bone marrow-derived macrophages of *Adam17*$^{ex/ex}$.*Ldlr*$^{-/-}$ mice released significantly less sTNFR1 and sTNFR2 compared with macrophages from wild-type controls (Figures 59 A, B). Significant differences of sTNFα and sIL-6R release were only detected after stimulation with PMA, which induced shedding in macrophages from wild-type but not from *Adam17*$^{ex/ex}$.*Ldlr*$^{-/-}$ mice (Figures 59 C, D).

Taken together, these data indicated strongest effects of *Adam17*-deficiency on the shedding of TNF-receptors and of their ligand TNFα [130].

3.2.9 *TNFR1 and TNFR2 signaling in Adam17$^{ex/ex}$.Ldlr$^{-/-}$ Mice*

To investigate whether differential shedding of TNFR1, TNFR2, and TNFα affected their cellular expression levels, we quantified these proteins in whole cell lysates and in the cellular membrane fraction of bone marrow-derived macrophages (BMDM) of wild-type *Adam17*$^{wt/wt}$.*Ldlr*$^{-/-}$ and homozygous *Adam17*$^{ex/ex}$.*Ldlr*$^{-/-}$ mice.

Here, we found that cellular protein levels of ADAM17 were barely detectable in hypomorphic *Adam17*$^{ex/ex}$.*Ldlr*$^{-/-}$ mice compared to wild-type *Adam17*$^{wt/wt}$.*Ldlr*$^{-/-}$ mice validating the hypomorphic *Adam17*$^{ex/ex}$.*Ldlr*$^{-/-}$ mice. Whereas TNFR1 levels were unchanged, cellular TNFα and TNFR2 protein levels were significantly elevated in homozygous *Adam17*$^{ex/ex}$.*Ldlr*$^{-/-}$ macrophages (Figure 60 A, B) [130].

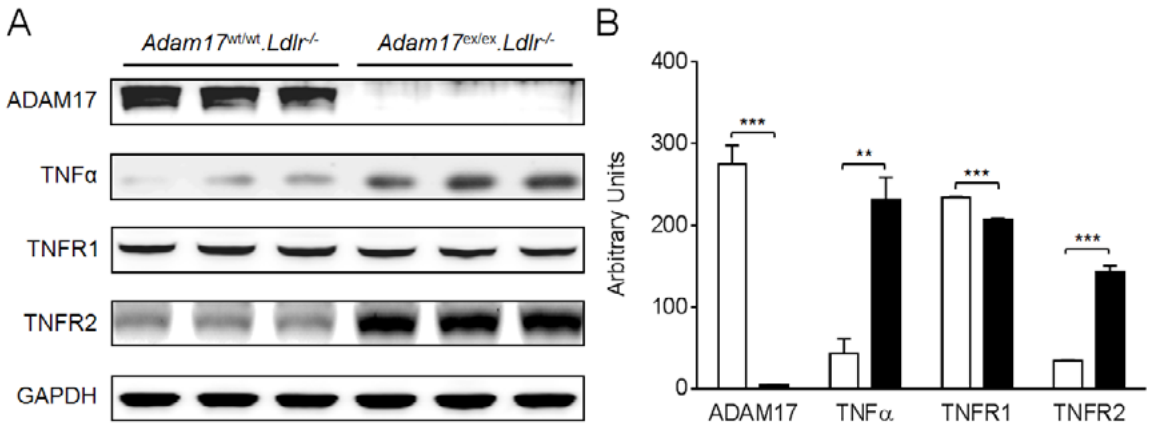

FIGURE 60: (**A**) Western blot and (**B**) densitometric analysis of ADAM17, TNFα, TNFR1, TNFR2, and GAPDH control in whole cell lysates from BMDM of *Adam17*$^{wt/wt}$.*Ldlr*$^{-/-}$ (n = 3) and *Adam17*$^{ex/ex}$.*Ldlr*$^{-/-}$ (n = 3) mice [130].

Whereas TNFR1 is activated through both, membrane-bound TNFα (mTNFα) and soluble TNFα, TNFR2 becomes only activated by mTNFα [177]. To investigate this cell-membrane distribution, bone marrow-derived macrophages from wild-type *Adam17*$^{wt/wt}$.*Ldlr*$^{-/-}$ and homozygous *Adam17*$^{ex/ex}$.*Ldlr*$^{-/-}$ mice were labeled with the cell-impermeable EZ-Link Sulfo-NHS-SS-Biotin and isolated using Dynabeads MyOne Streptavidin C1. As a cell membrane marker we used the Na^+/K^+ ATPase.

Consistently with the results from the whole cell lysates, we observed higher amounts of cell membrane-bound TNFα (mTNFα) as well as cell membrane-bound TNFR2 (mTNFR2) in *Adam17*$^{ex/ex}$.*Ldlr*$^{-/-}$ macrophages compared to control macrophages (Figure 60) whereas TNFR1 membrane distribution was not significantly altered [130].

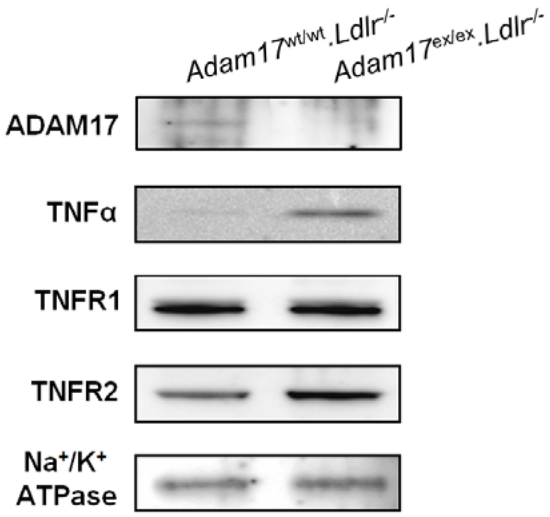

FIGURE 61: Western blots of ADAM17, TNFα, TNFR1, TNFR2, and Na^+/K^+ ATPase as a control in cell membrane fractions of primary BMDMs of *Adam17*$^{wt/wt}$.*Ldlr*$^{-/-}$ (n = 3) and *Adam17*$^{ex/ex}$.*Ldlr*$^{-/-}$ (n = 3) mice [130].

To investigate whether elevated amounts of mTNFα and mTNFR2, thus, resulted in an activation of TNFR2 signaling in *Adam17*-depleted cells, we quantified the phosphorylated form of bone marrow tyrosine kinase in chromosome X (pBMX), which is a downstream marker of TNFR2 but not TNFR1 activation. The endothelial/epithelial tyrosine kinase (Etk/Bmx) is a member of the Btk nonreceptor tyrosine kinase family. Etk and three other members of this family, (Btk, Itk, and Tec) participate in signal transduction stimulated by growth factor receptors, cytokine receptors, G-protein-coupled receptors, antigen receptors, and integrins [178]. This TNFR2-signaling pathway has been shown to positively stimulate cell survival, proliferation, and adhesion [178-180] which is opposite to classical TNFR1 signaling that induces antiproliferative effects. We observed an increase of absolute and also of phosphorylated BMX protein in macrophages of *Adam17*$^{ex/ex}$.*Ldlr*$^{-/-}$ mice, indicating an activation of TNFR2 signaling in these cells [130].

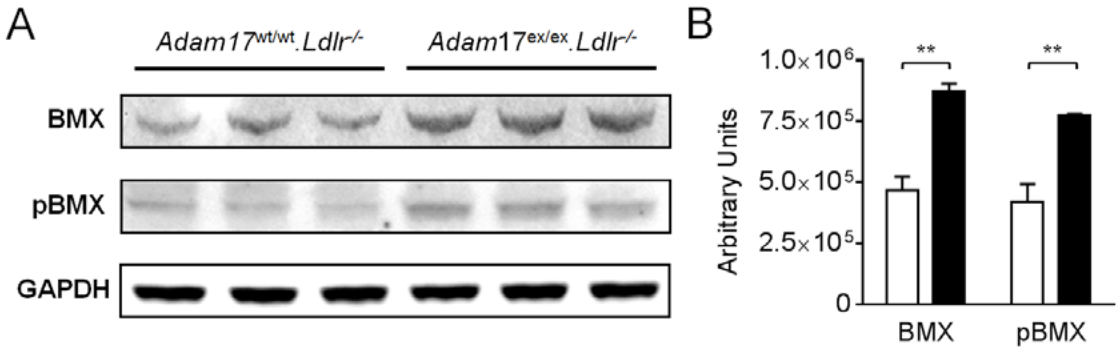

FIGURE 62: (**A**) Western blots and (**B**) densitometric analysis of TNFR2 effector protein BMX and activated phosphorylated BMX (pBMX) in whole cell lysates primary BMDMs of *Adam17*$^{wt/wt}$.*Ldlr*$^{-/-}$ (n = 3) and *Adam17*$^{ex/ex}$.*Ldlr*$^{-/-}$ (n = 3) mice. GAPDH was used as control [130].

3.2.10 *Genome-wide expression profiling in mouse BMDM and aortas validated activation of TNF-signaling*

Cytokines, such as TNFα, in concert with cytokine receptors, such as the ADAM17 substrates TNFR1, TNFR2 and IL-6R, control cellular functions through activating signaling cascades, which finally result in expression changes of gene networks. To investigate whether cell-specific TNFR2 activation is also observed in aortic tissue, and to test whether activation of TNFR2 signaling was relevant for gene expression changes in *Adam17* mutants, we performed transcriptome-wide mRNA expression profiling using Illumina Ref-8 arrays microarrays in primary bone marrowderived macrophages (BMDMs) and aortas of female and male *Adam17*$^{wt/wt}$.*Ldlr*$^{-/-}$ and *Adam17*$^{ex/ex}$.*Ldlr*$^{-/-}$ mice (females n = 4/4; males n = 4/4) [130].

We performed an upstream regulator analysis using the Ingenuity Pathways Analysis (IPA/ www.ingenuity.com) and thereby calculated z-scores.The activation z-score makes predictions about potential regulators by using information about the direction of gene regulation [181]. Its purpose is two-fold: first, similar to the overlap *p-value*, the z-score can be used to determine likely regulators based on statistical significance of the pattern match Second, it can be used to infer the activation state of a putative regulator (i.e. whether the regulator is activated or inhibited) [181]. Subsequently, we performed a gene set enrichment analysis to investigate which cell functions might be affected by *Adam17*-deficiency.

In Table 25, the top three pathways and TNFR2 of the combined upstream analysis in primary BMDM are shown.

TABLE 25: Combined upstream analysis of male and female *Adam17*$^{wt/wt}$.*Ldlr*$^{-/-}$ and *Adam17*$^{ex/ex}$.*Ldlr*$^{-/-}$ mice of bone marrow-derived macrophages (BMDM). Levels of significance and activation z-scores were calculated according to standard procedures of the software [130].

	Macrophages		
	z-Score	***p*-Value**	**Molecules**
TNFα	2.5	1.76×10^{-14}	185
IL1β	2.4	2.63×10^{-14}	149
IFNγ	1.8	2.73×10^{-09}	157
TNFR2	2.2	3.76×10^{-03}	166

In this analysis, we validated a significant induction of TNFα- and TNFR2-signaling pathways in *Adam17*$^{ex/ex}$.*Ldlr*$^{-/-}$ BMDMs (1.76×10^{-14} and 3.76×10^{-03}, respectively) (Table 25).

Subsequently, we performed a combined upstream analysis of male and female *Adam17*$^{wt/wt}$.*Ldlr*$^{-/-}$ and *Adam17*$^{ex/ex}$.*Ldlr*$^{-/-}$ mice in the aortic tissue [130].

TABLE 26: Combined upstream analysis of male and female *Adam17*$^{wt/wt}$.*Ldlr*$^{-/-}$ and *Adam17*$^{ex/ex}$.*Ldlr*$^{-/-}$ mice in aortas. Levels of significance and activation z-scores were calculated according to standard procedures of the software [130].

	Aorta		
	z-Score	***p*-Value**	**Molecules**
TNFα	5.6	2.08×10^{-46}	467
IL1β	6.6	6.41×10^{-32}	448
IFNγ	8.1	1.40×10^{-38}	463
TNFR2	2.5	3.83×10^{-4}	445

Here, we also detected a significant induction of TNFα and TNFR2 signaling ($p = 2.08 \times 10^{-46}$ and $p = 3.83 \times 10^{-4}$, respectively).

With respect to TNFR1 signaling, we only observed a weak activation in macrophages ($p = 1.09 \times 10^{-02}$) and no significant activation in aortas.

Together, data from the transcriptome-wide mRNA expression profiling in BMDMs and aortas indicated a stronger induction of TNFR2 by membrane-bound TNFα than TNFR1 signaling in *Adam17*-deficiency [130].

To determine metabolic, disease-related, and important cell function that might be affected by *Adam17*-deficiency, we performed pathway analysis using the Ingenuity Pathway Analysis (IPA) software. Genes with expression changes of < 0.7 and > 1.3, which were chosen as arbitrary biologically relevant cut off, in aorta and macrophages of wild-type *Adam17*$^{wt/wt}$.*Ldlr*$^{-/-}$ and hypomorphic *Adam17*$^{ex/ex}$.*Ldlr*$^{-/-}$ mice were used. In Table 27, pathways with significant enrichment $p < 10^{-6}$ are listed.

TABLE 27: Gene set enrichment analysis in aorta and bone marrow-derived macrophages (BMDM) of *Adam17*$^{wt/wt}$.*Ldlr*$^{-/-}$ and A*dam17*$^{ex/ex}$.*Ldlr*$^{-/-}$ mice.

Function	**Aorta**	**BMDM**
Cellular growth and proliferation	2.20×10^{-37}	2.62×10^{-24}
Cellular development	2.20×10^{-37}	4.73×10^{-13}
Cellular movement/adhesion	5.11×10^{-36}	8.60×10^{-15}
Cell death and survival	1.14×10^{-19}	2.58×10^{-16}

Together, this analysis predicted *that Adam17*-deficiency controlled cellular growth and proliferation, cellular development, cellular movement/adhesion and cell death and survival which are key cell functions in the development of atherogenesis [1].

3.2.11 *Adam17-deficiency controls cell functions of atherosclerosis in macrophages, endothelial- and smooth muscle cells*

3.2.11.1 *Adam17-deficiency in primary macrophages*

Apoptosis and proliferation are processes that are controlled through both TNF-receptor signalings. Whereas TNFR1 induces apoptosis and reduces proliferation, TNFR2 signalling has been associated with anti-apoptotic and proliferative cellular response [182]. Furthermore, TNFR2 signaling has been shown to increase cell adhesion by inducing the expression of intercellular cell adhesion molecule-1 (ICAM1) in different mouse models [183, 184].

qRT-PCR, immunofluorescence and western blot analysis revealed higher *Adam17* expression in endothelial cells (ECs) as well as in macrophages (MΦ) and vascular smooth muscle cells (SMCs), therefore functional experiments were performed in all three cell types using primary cell lines.

To investigate whether *Adam17*-deficiency controlled cell functions through modulating TNFR2-signalling, we investigated apoptosis in bone marrow-derived macrophages (BMDM) of *Adam17*$^{wt/wt}$.*Ldlr*$^{-/-}$ and *Adam17*$^{ex/ex}$.*Ldlr*$^{-/-}$ mice. To this, BMDMs were stimulated with staurosporine (0.125 µM and 0.25 µM) and cycloheximide (10 ng/ml and 50 ng/ml). The main biological activity of staurosporine is the inhibition of protein kinases through the prevention of ATP binding to the kinase, thereby inducing apoptosis. Cycloheximid's main biological activity is translation inhibition resulting in cell growth arrest and cell death by inhibiting protein biosynthesis at the ribosomes.

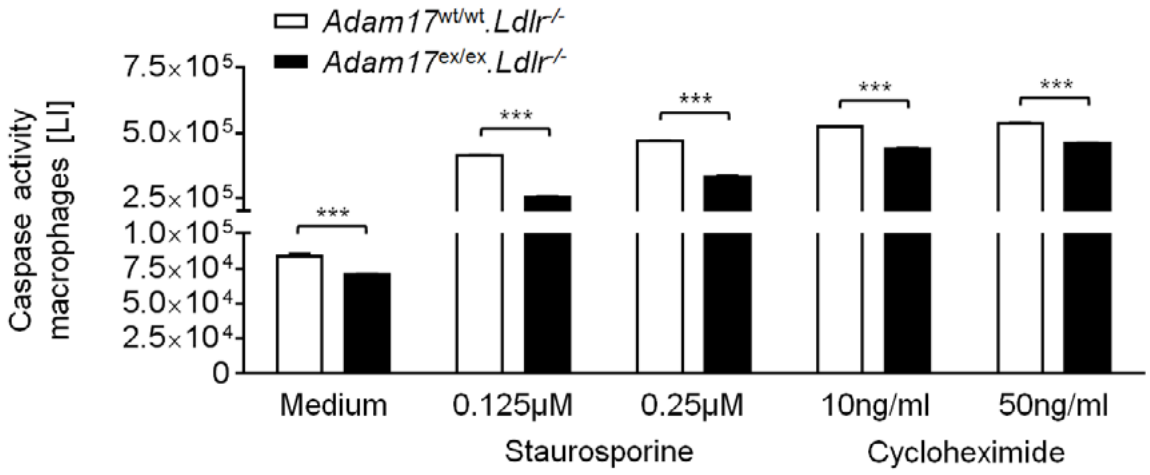

FIGURE 63: Apoptosis assay in bone marrow-derived macrophages of *Adam17*$^{wt/wt}$.*Ldlr*$^{-/-}$ (n = 4) and *Adam17*$^{ex/ex}$.*Ldlr*$^{-/-}$ (n = 4) mice in cell culture medium and after stimulation with staurosporine and cycloheximide. Caspase activity is given as luminescence intensity (LI) [130].

Apoptosis, as determined by caspase-3 activity, was significantly diminished in BMDM of *Adam17*$^{ex/ex}$.*Ldlr*$^{-/-}$ mice compared to *Adam17*$^{wt/wt}$.*Ldlr*$^{-/-}$ mice using different concentrations of staurosporine and cycloheximide (Figure 63).

Furthermore, we tested the proliferation rate of bone marrow-derived macrophages of *Adam17*$^{ex/ex}$.*Ldlr*$^{-/-}$ and *Adam17*$^{wt/wt}$.*Ldlr*$^{-/-}$ mice. Here, we found that primary macrophages of *Adam17*$^{ex/ex}$.*Ldlr*$^{-/-}$ mice proliferated more than cells of *Adam17*$^{wt/wt}$.*Ldlr*$^{-/-}$ controls. Figure 64 shows the proliferation rate

over a time of 96 h in cultured primary BMDMs of *Adam17*$^{wt/wt}$.*Ldlr*$^{-/-}$ (n = 4) and *Adam17*$^{ex/ex}$.*Ldlr*$^{-/-}$ (n = 4) mice and at timepoint 96 h.

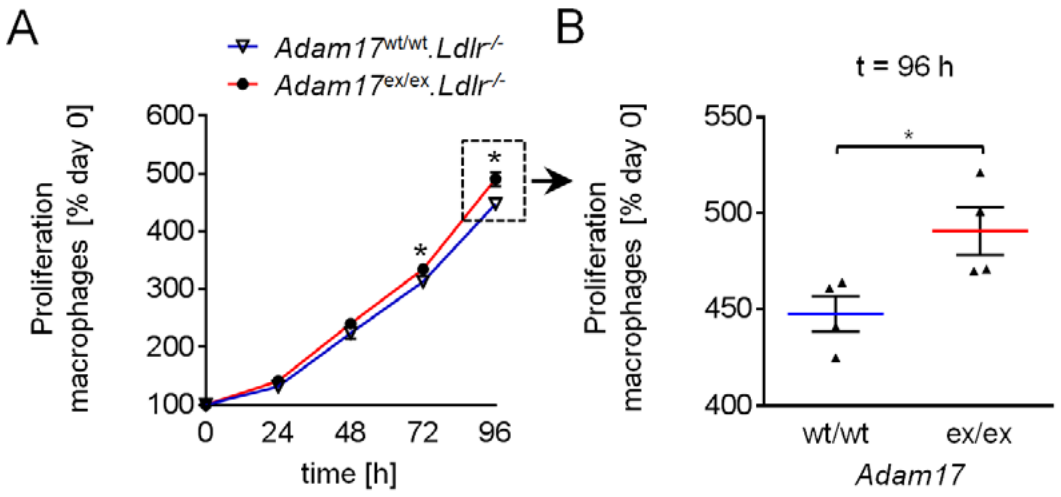

FIGURE 64: Cell proliferation in cultured primary BMDMs of *Adam17*$^{wt/wt}$.*Ldlr*$^{-/-}$ and *Adam17*$^{ex/ex}$.*Ldlr*$^{-/-}$ mice (**A**) over 96 h and (**B**) at time point 96 h. * $p < 0.05$ [130].

Moreover, we performed adhesion experiments with primary macrophages of *Adam17*$^{ex/ex}$.*Ldlr*$^{-/-}$ and *Adam17*$^{wt/wt}$.*Ldlr*$^{-/-}$ mice. Adhesion experiments were performed in quadruplicates of 6 cell lines per genotype that were independently derived from 6 mice. We observed that bone marrow-derived macrophages of *Adam17*$^{ex/ex}$.*Ldlr*$^{-/-}$ mice adhered stronger to matrigel-coated wells than macrophages of control mice (Figure 65 A) [130].

To find out, whether the intercellular adhesion molecule 1 (ICAM1), a substrate of ADAM17, which is expressed by the vascular endothelium, macrophages, and lymphocytes plays a role in adhesion, we examined the protein levels of ICAM1 in whole cell lysates from a pool of primary BMDMs of *Adam17*$^{wt/wt}$.*Ldlr*$^{-/-}$ and a pool of primary BMDMs of *Adam17*$^{wt/wt}$.*Ldlr*$^{-/-}$ mice (Figure 65 B).

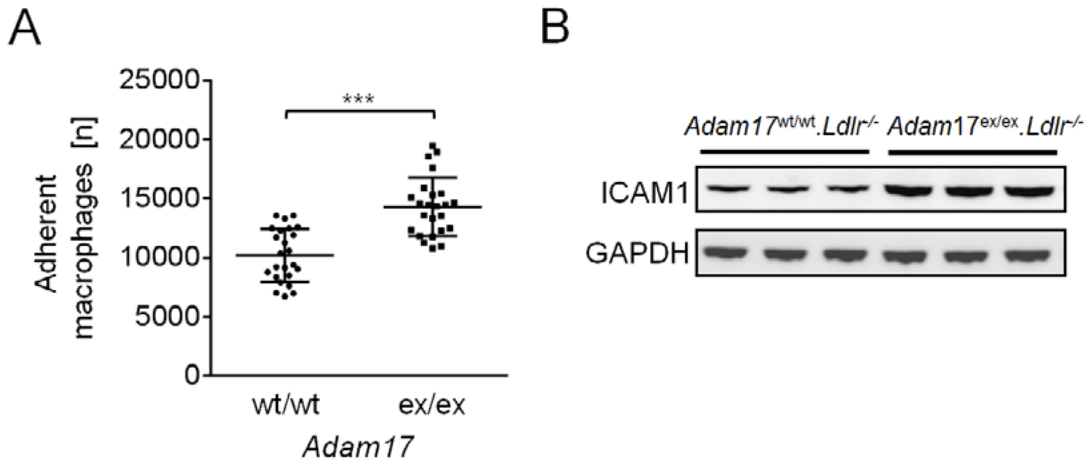

FIGURE 65: (**A**) Adhesion of primary BMDMs of *Adam17*$^{wt/wt}$.*Ldlr*$^{-/-}$ and *Adam17*$^{ex/ex}$.*Ldlr*$^{-/-}$ to matrigel-coated wells. Adhesion experiments were performed in quadruplicates of 6 cell lines per genotype that were independently derived from 6 mice. 3 male and 3 female mice per genotype were used. (**B**) Western blot of ICAM1 and GAPDH control in whole cell lysates of a pool of primary BMDMs of *Adam17*$^{wt/wt}$.*Ldlr*$^{-/-}$ (n = 3) and *Adam17*$^{ex/ex}$.*Ldlr*$^{-/-}$ (n = 3) mice. *** $p < 0.001$ [130].

By this, we could show that, primary macrophages of *Adam17*$^{ex/ex}$.*Ldlr*$^{-/-}$ mice induced higher expression levels of intercellular adhesion molecule 1 (ICAM1) compared to *Adam17*$^{wt/wt}$.*Ldlr*$^{-/-}$ mice (Figure 65 B), which is a plausible explanation for the enhanced adhesion of macrophages of *Adam17*$^{ex/ex}$.*Ldlr*$^{-/-}$ mice [130].

3.2.11.2 *Adam17-deficiency affects apoptosis, proliferation and adhesion in mouse RAW264.7 macrophages and mouse vascular smooth muscle cells MOVAS*

To validate our previous findings in BMDMs with respect to apoptosis, proliferation and adhesion in an independent model, we knocked down *Adam17* in RAW264.7 macrophages using small interfering RNA (siRNA). As a control, we used a scrambled (SCR) oligonucleotides. We obtained ~50 % knockdown efficiency of *Adam17* in RAW264.7 macrophages (Figure 66).

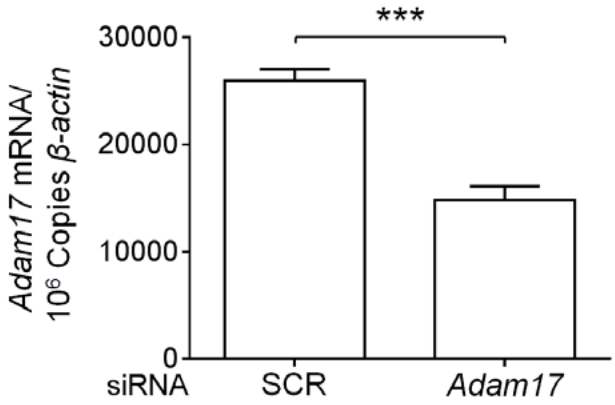

FIGURE 66: Validation of *Adam17* siRNA knockdown efficiency in RAW264.7 macrophages using qRT-PCR after 48 hours. *** $p < 0.001$ [130].

The apoptosis assay in RAW264.7 macrophages after siRNA knock-down of *Adam17* (n = 4) or after using scrambled siRNA control was stimulated with staurosporine (0.25 µmol/l) and cycloheximide (10 ng/ml) and validated that *Adam17* knock-down reduced apoptosis at basal conditions as well as after stimulation with staurosporine and cycloheximide (Figure 67).

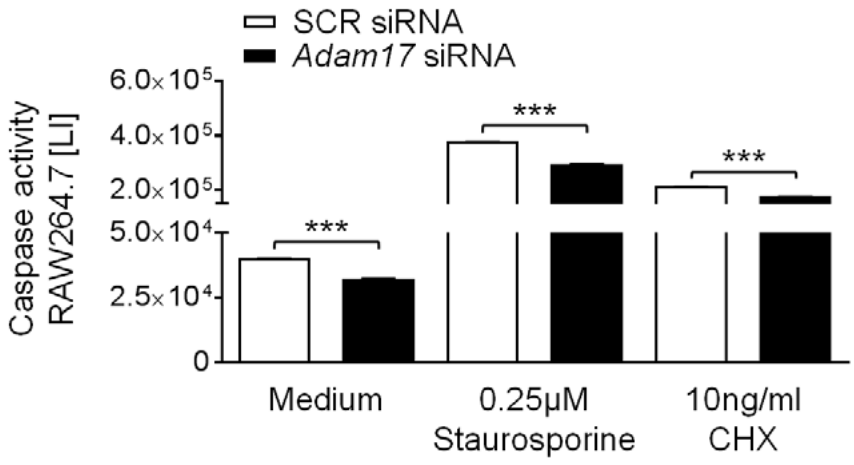

FIGURE 67: Apoptosis assay in RAW264.7 macrophages after siRNA knock-down of *Adam17* and scrambled control siRNA in cell culture medium and after stimulation with staurosporine and cycloheximide (CHX). The caspase activity is given as luminescence intensity. *** $p < 0.001$ [130].

We next examined the proliferation behavior of *Adam17*-depleted RAW264.7 macrophages over a period of 96 hours. We found an increased proliferation of *Adam17* down-regulated macrophages compared to macrophages treated with SCR control siRNA oligonucleotide. Figure 68 A shows the proliferation performance over 96 hours and Figure 68 B at timepoint 96 hours. At time point 96 hours we observed a significant difference between SCR and *Adam17* siRNA treated RAW264.7 macrophages.

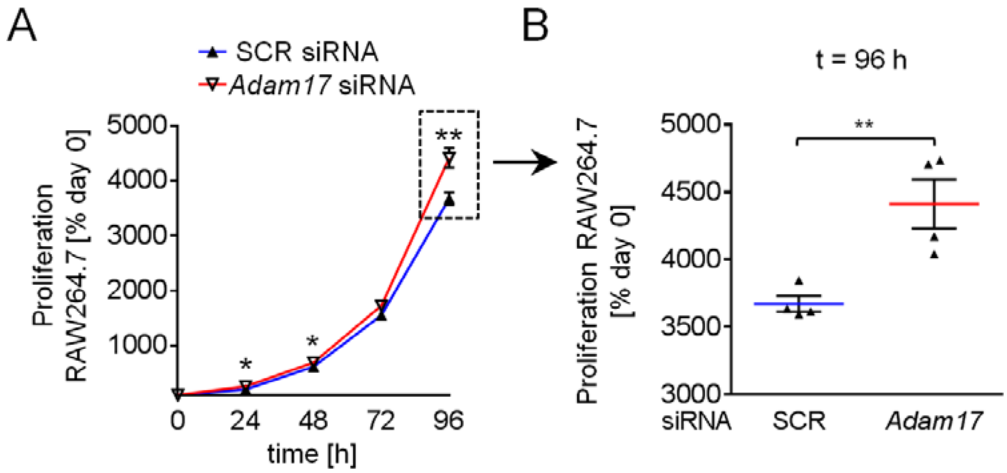

FIGURE 68: Cell proliferation in RAW264.7 macrophages after *Adam17* siRNA mediated (n = 4) knock-down or SCR RNAi (n = 4) control (**A**) over 96 h and (**B**) at timepoint 96 h. * $p < 0.05$; *** $p < 0.001$ [130].

Adhesion experiments were performed with RAW264.7 macrophages on matrigel-coated wells.

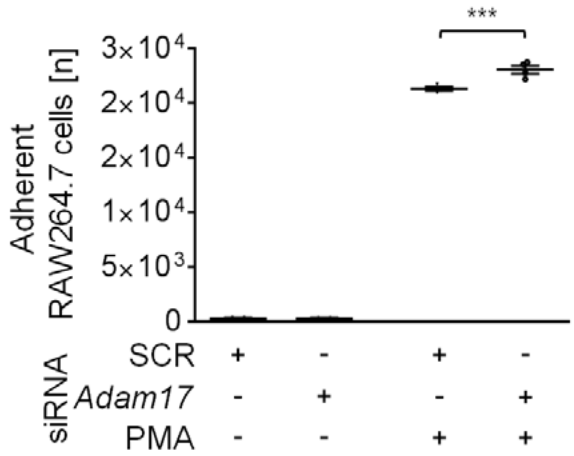

FIGURE 69: Adhesion of RAW264.7 macrophages after siRNA-mediated knockdown of *Adam17* (n = 4) or in SCR RNAi control (n = 4) and with or without stimulation with PMA (100 pmol/ml). *** $p < 0.001$ [130].

RAW264.7 macrophages adhered strongly on matrigel-coated wells only after stimulation with phorbol 12-myristate 13-acetate (PMA), an ADAM17 activator. *Adam17* knockdown in RAW264.7 macrophages resulted in increased adhesion compared to macrophages treated with SCR siRNA, which was consistent with results from *Adam17*-deficient BMDMs.

To resemble an even more physiological situation, we used wild-type primary bone marrow-derived macrophages (BMDMs) and let them to adhere to wild-type mouse primary vascular

endothelial cells (EC). Either BMDMs or vascular ECs or both cell types were treated with siRNAs against *Adam17* or with SCR siRNA control oligonucleotides [130].

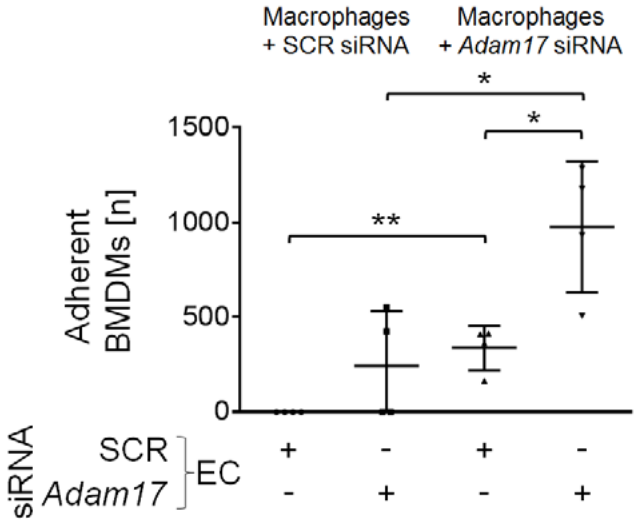

FIGURE 70: Adhesion of wild-type primary bone marrow-derived macrophages (BMDMs) to a wild-type mouse primary vascular endothelial cell line (EC). All adhesion experiments were performed in quadruplicates. * $p < 0.05$; ** $p < 0.01$ [130].

Primary BMDMs treated with *Adam17* siRNA showed stronger adhesion to primary vascular endothelial cells from C57BL/6 mice. Notably, RNAi mediated knockdown of *Adam17* in these endothelial cells further increased adhesion of macrophages, and strongest adhesion was observed when both cell types were treated with siRNA against *Adam17* (Figure 70) [130].

Since, immunofluorescence stainings had also revealed ADAM17 expression in VSMCs, we next depleted *Adam17* in the vascular aortic smooth muscle cell line (MOVAS) using siRNA. We obtained ~50 % knockdown efficiency of *Adam17* in MOVAS vascular smooth muscle cells compared to the scrambled control (SCR).

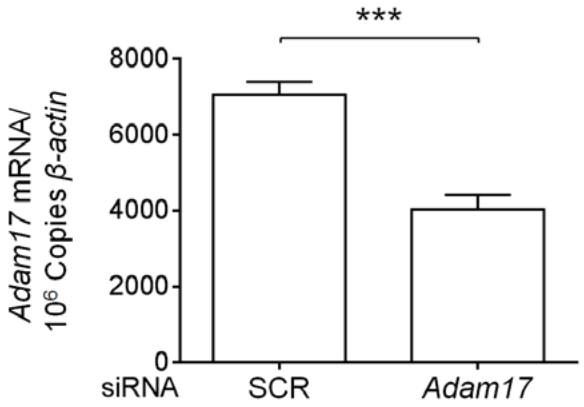

FIGURE 71: Validation of *Adam17* siRNA knockdown efficiency in vascular smooth muscle cells MOVAS using qRT-PCR after 48 hours. *** $p < 0.001$ [130].

We first examined the apoptosis behavior after siRNA-mediated knockdown with *Adam17* siRNA and scrambled (SCR) control oligonucleotides. Apoptosis was stimulated with staurosporine (0.25 µM) and cycloheximide (10 ng/ml).

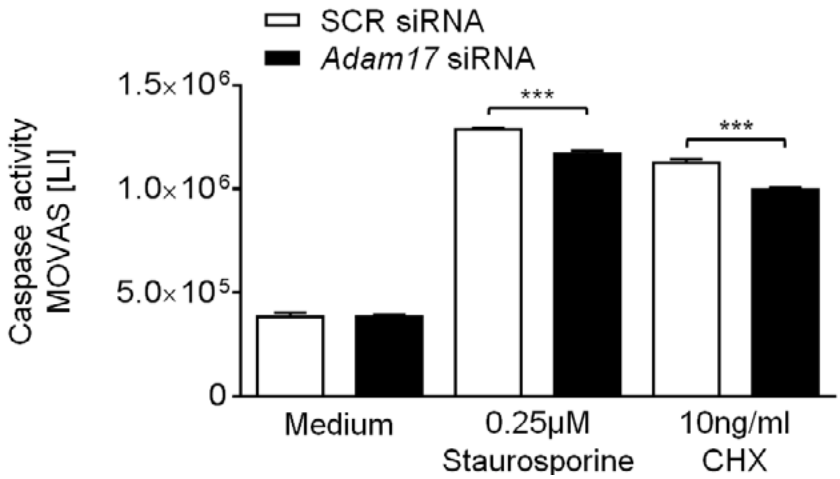

FIGURE 72: Apoptosis assay in vascular smooth muscle cells MOVAS after siRNA knock-down of *Adam17* (n = 4) and scrambled control siRNA (n = 4) in cell culture medium and after stimulation with staurosporine (0.25 µM) and cycloheximide (10 ng/ml). Apoptosis was measured in luminescence intensity (LI). *** $p < 0.001$ [130].

Consistent with the results in BMDM and RAW264.7 cells, the knockdown of *Adam17* resulted in a reduction of apoptosis primarily in transfected MOVAS cells after stimulation with staurosporine and cycloheximide. No major differences were observed in MOVAS cells without stimulation.

Furthermore, we examined also in MOVAS cells the proliferation rate after *Adam17* depletion. Figure 73 A shows the proliferation performance over 96 hours and Figure 73 B at timepoint 96 hours.

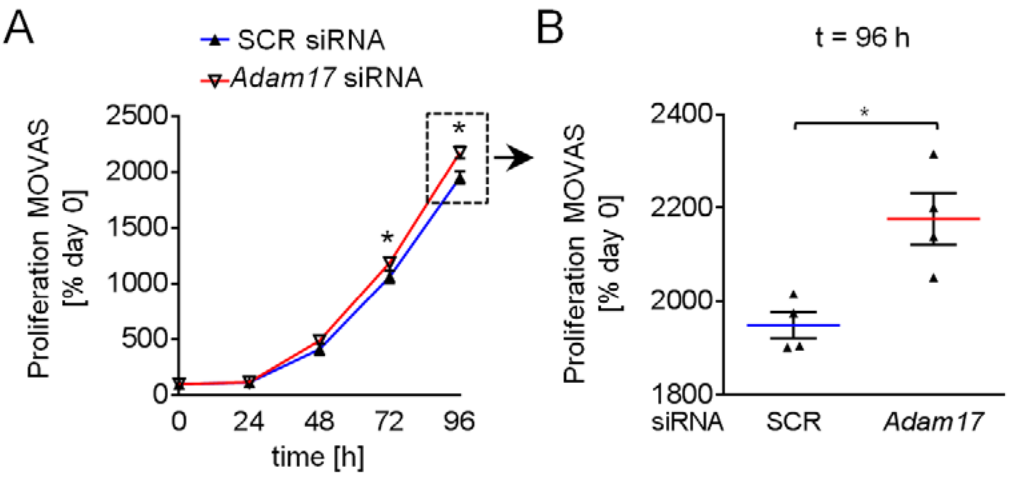

FIGURE 73: Cell proliferation in MOVAS cells after *Adam17* siRNA mediated (n = 4) knock-down or SCR RNAi (n = 4) (**A**) over 96 h and (**B**) at time point 96 h. * $p < 0.05$ [130].

Again, the *Adam17* knockdown in vascular smooth muscle cells MOVAS also resulted in a slight increase in proliferation rates (Figure 73 A). At time point 96 hours we observed a significant difference between SCR and *Adam17* siRNA treated MOVAS cells (Figure 73 B).

3.2.11.3 *Tnfr2 knockdown in Adam17-depleted cells restores cell functions*

Because we had found that TNFR2 signaling was overactivated in the absence of *Adam17*, we next wanted to investigate whether changes of cell functions caused by *Adam17* depletion were dependent on TNFR2. Thus, we performed double-knockdown experiments in RAW264.7 macrophages and MOVAS vascular smooth muscle cells and investigated whether siRNA-mediated co-depletion of both *Tnfr2* and *Adam17* would restore cell functions back to normal. Experiments were performed in both, macrophages and vascular smooth muscle cells.

Figures 74 and 75 show the *Adam17* and *Tnfr2* mRNA expression in RAW264.7 macrophages and vascular smooth muscle cells MOVAS respectively, after transfection with *Adam17* siRNAs, or *Tnfr2* siRNAs, or after double knockdown using *Adam17*/*Tnfr2* siRNAs or using scrambled (SCR) siRNA controls. mRNA expression of *Adam17* and *Tnfr2* was normalized to 10^6 copies of β-*actin* house-keeping gene. Statistical differences were calculated relative to SCR control [130].

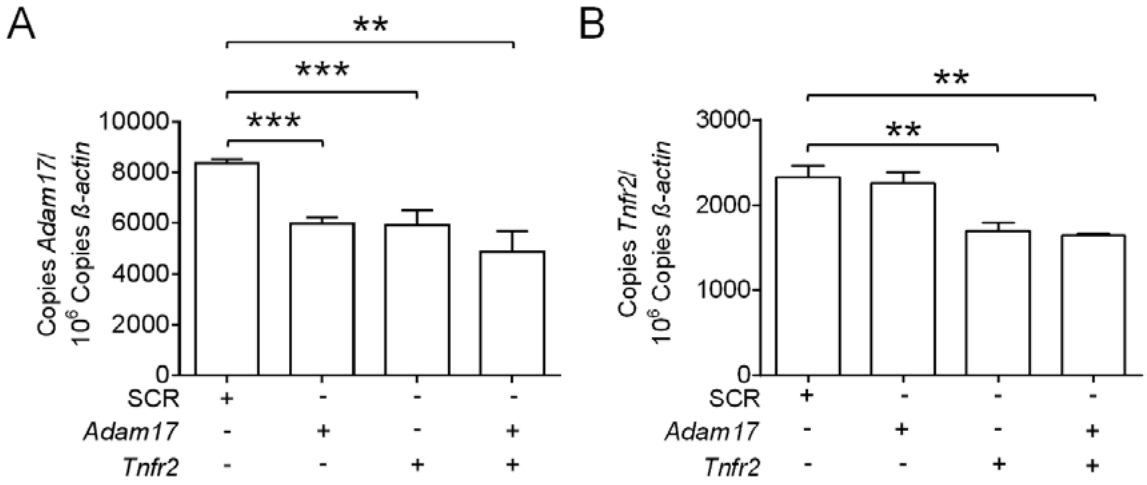

FIGURE 74: Validation of (**A**) *Adam17* and (**B**) *Tnfr2* siRNA knockdown efficiencies in RAW264.7 macrophages used for proliferation and apoptosis experiments after 48 hours. ** $p < 0.01$; *** $p < 0.001$ [130].

Adam17 mRNA expression in RAW264.7 macrophages was significantly reduced after *Adam17* siRNA mediated knockdown as well as after double knockdown with *Tnfr2*. We also observed a significantly reduced *Adam17* mRNA expression after *Tnfr2* siRNA mediated knockdown.

Tnfr2 mRNA expression in RAW264.7 macrophages was significantly reduced after *Tnfr2* siRNA mediated knockdown as well after double knockdown with *Adam17*.

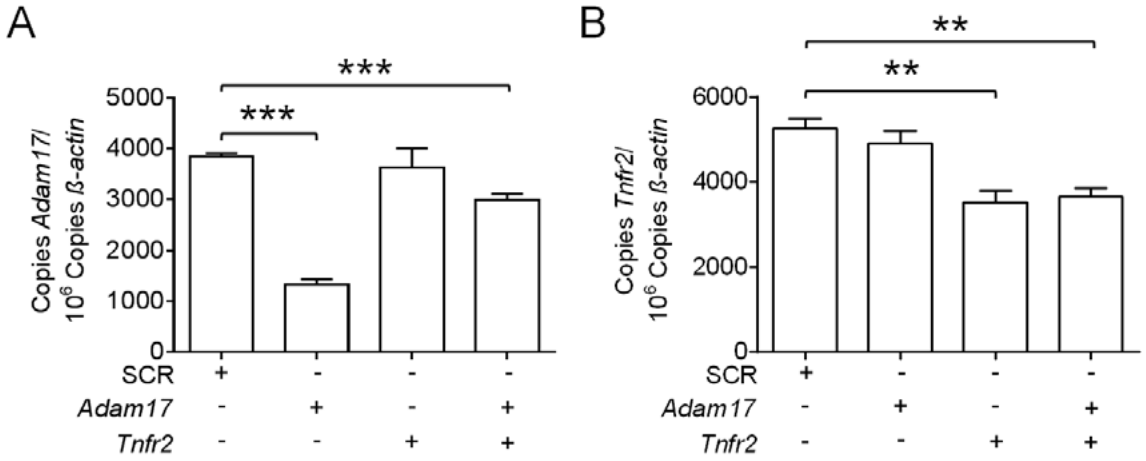

FIGURE 75: Validation of (**A**) *Adam17* and (**B**) *Tnfr2* siRNA knockdown efficiencies in vascular smooth muscle cell line (MOVAS) for proliferation and apoptosis experiments after 48 hours. ** $p < 0.01$; *** $p < 0.001$ [130].

In MOVAS cells *Adam17* mRNA expression was significantly reduced after *Adam17* siRNA mediated knockdown as well as after double knockdown with *Tnfr2*. No *Adam17* mRNA differences were observed after *Tnfr2* siRNA mediated knockdown. *Tnfr2* mRNA expression in MOVAS was significantly reduced only after *Tnfr2* siRNA mediated knockdown as well after double knockdown with *Adam17*.

Figures 76 and 77 show the proliferation rate of RAW264.7 macrophages and MOVAS cells, respectively after *Adam17*, *Tnfr2*, combined *Adam17*/*Tnfr2* and control siRNA mediated knockdown over a period of 96 hours and at time point 96 hours.

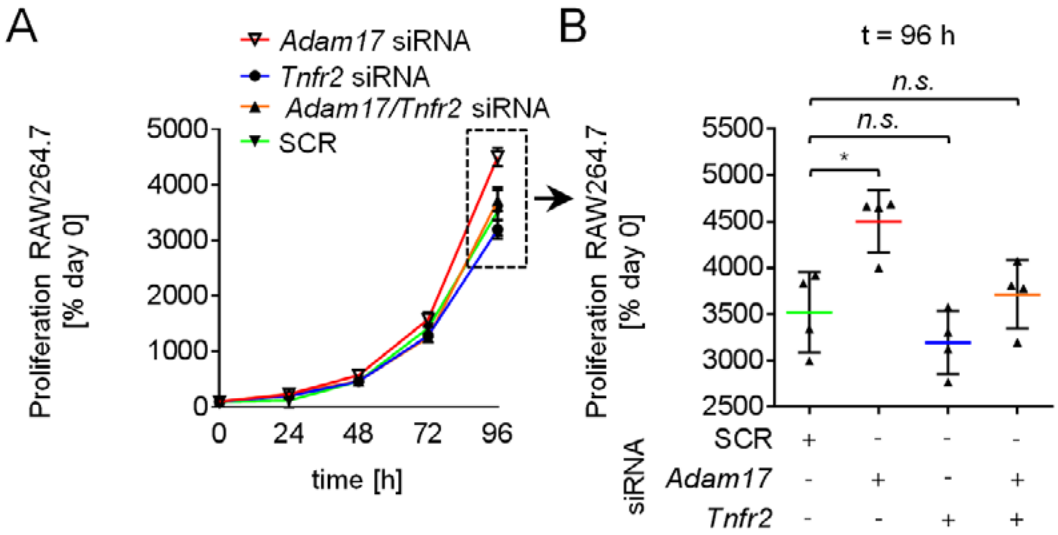

FIGURE 76: Cell proliferation assay (**A**) over 96 h in RAW264.7 macrophages after *Adam17*, *Tnfr2*, *Adam17*/*Tnfr2* and scrambled siRNA mediated knockdown and (**B**) at time point 96 h. * $p < 0.05$ [130].

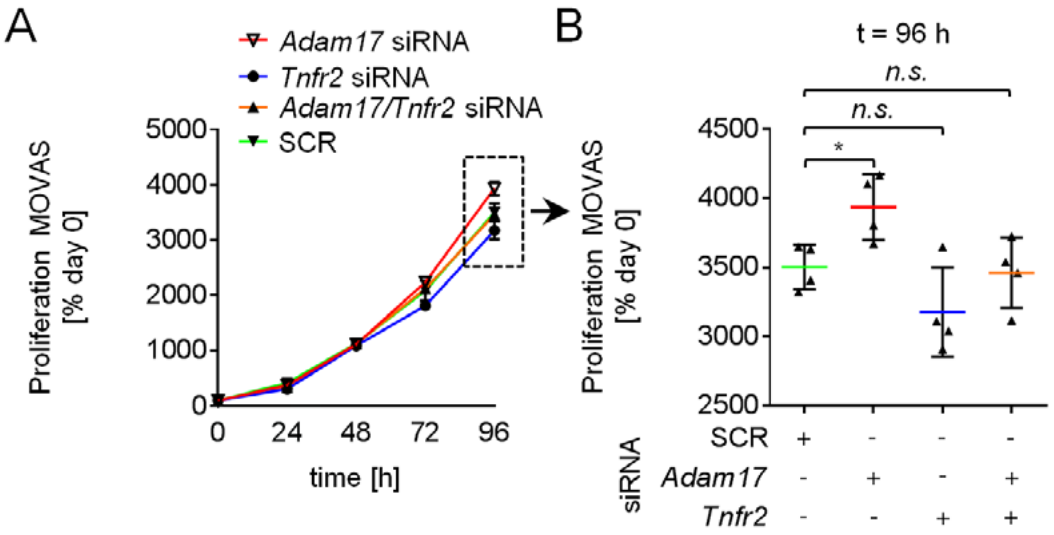

FIGURE 77: Cell proliferation assay (**A**) over 96 h in MOVAS vascular smooth muscle cells after *Adam17*, *Tnfr2*, *Adam17*/*Tnfr2* and scrambled siRNA mediated knockdown and (**B**) at time point 96 h. * $p < 0.05$ [130].

Adam17-deficiency increased proliferation in both cell types, macrophages as well as smooth muscle cells, compared to the scrambled control.*Tnfr2* deficiency led to decreased proliferation and knockdown of *Tnfr2* in *Adam17*-depleted cells attenuated these effects.

Consistently with the results of the proliferation rates, *Tnfr2* depletion also restored the levels of apoptosis in *Adam17*-depleted macrophages and also in vascular smooth muscle cells MOVAS [130].

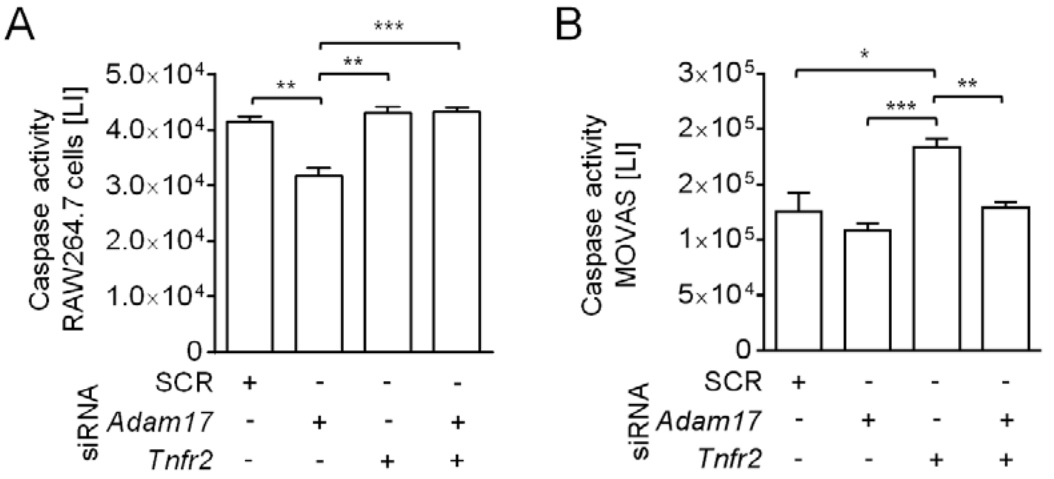

FIGURE 78: Apoptosis in (**A**) RAW264.7 macrophages and (**B**) MOVAS vascular smooth muscle cells after siRNA mediated knock-down with *Adam17*, *Tnfr2*, *Adam17*/*Tnfr2* and SCR control siRNA. * $p < 0.05$; ** $p < 0.01$; *** $p < 0.001$ [130].

Together, these data from the double knockdown experiments support that the proatherogenic cell-specific effects in *Adam17*-depleted cells may depend on TNFR2 signaling [130].

3.2.12 *Effects of Adam17-deficiency on apoptosis (TUNEL) in atherosclerotic lesions*

To translate our *in vitro* findings into the atherosclerosis mouse model, we performed TUNEL (TdT-mediated dUTP Nick-End Labeling) stainings, which measures nuclear DNA fragmentation of apoptotic cells, in order to investigate the *in vivo* apoptotic behavior in the atherosclerotic lesions of the aortic root of wild-type *Adam17*$^{wt/wt}$.*Ldlr*$^{-/-}$ and homozygous *Adam17*$^{ex/ex}$.*Ldlr*$^{-/-}$ mice. Figure 79 shows a negative and a positive control for TUNEL staining of an aortic root.

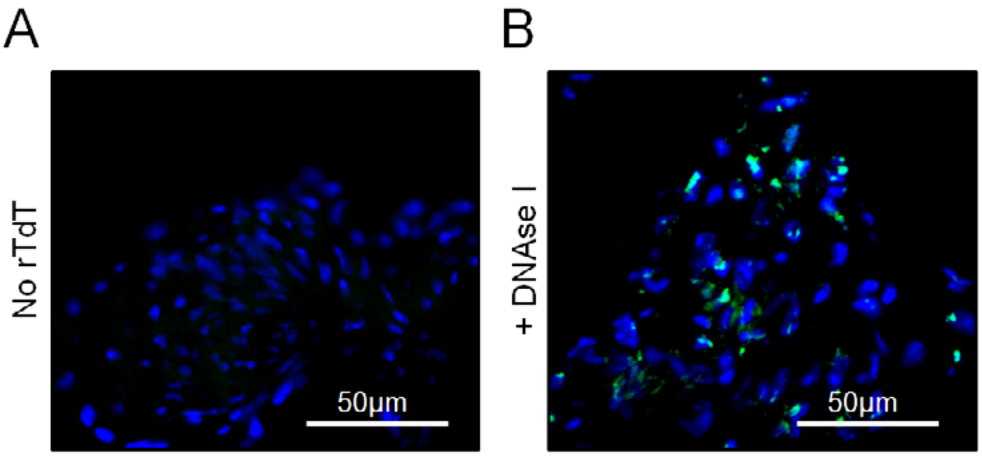

FIGURE 79: Controls for TUNEL staining. (**A**) Negative control for TUNEL staining; no recombinant Terminal Deoxynucleotidyl Transferase (TdT) enzyme was added to the TUNEL reaction. (**B**) Positive control for TUNEL staining; recombinant DNAse I was added prior to staining to cause DNA fragmentation and, thereby, experimentally-induced substrates for TUNEL labeling [130].

For TUNEL experiments, we used aortic roots of 6 wild-type *Adam17*$^{wt/wt}$.*Ldlr*$^{-/-}$ and 6 homozygous *Adam17*$^{ex/ex}$.*Ldlr*$^{-/-}$ male and female mice that were fed a semisynthetic diet for 16 weeks and were sacrificed at 20 weeks of age. Representative TUNEL stainings of *Adam17*$^{wt/wt}$.*Ldlr*$^{-/-}$ and *Adam17*$^{ex/ex}$.*Ldlr*$^{-/-}$ mice are shown in Figure 80. Quantification of TUNEL positive cells was performed in relation to total cell number and plaque area respectively.

TUNEL stainings detected significantly less apoptotic cells (TUNEL^{+}) in lesions of hypomorphic *Adam17*$^{ex/ex}$.*Ldlr*$^{-/-}$ mice in relation to total cell number and the plaque area, corroborating our *in vitro* results (Figure 80 C, D) [130].

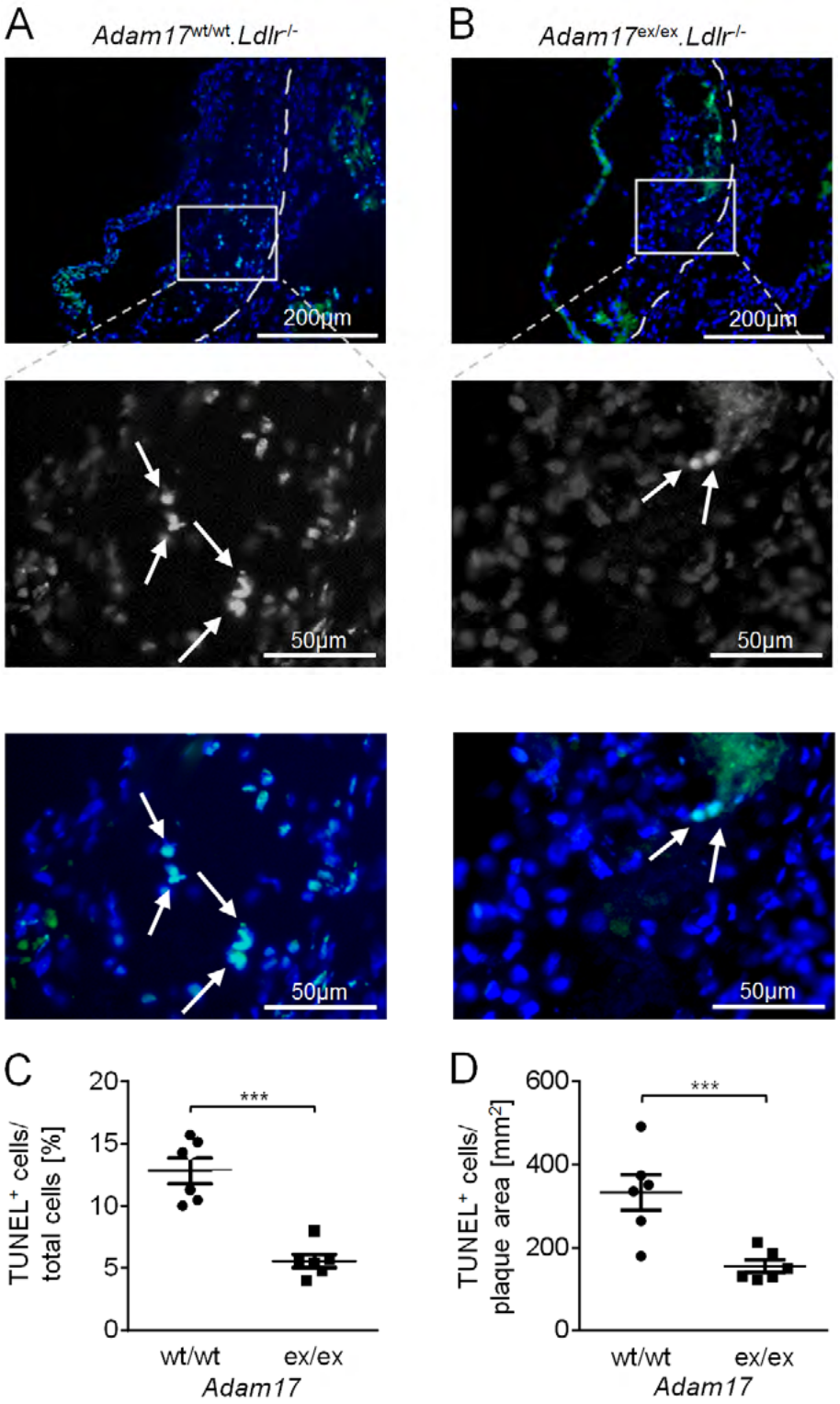

FIGURE 80: Apoptosis in atherosclerotic lesions of *Adam17*$^{wt/wt}$.*Ldlr*$^{-/-}$ and *Adam17*$^{ex/ex}$.*Ldlr*$^{-/-}$ mice. Representative TUNEL stainings for detecting apoptotic cells in the aortic root of (**A**) *Adam17*$^{wt/wt}$.*Ldlr*$^{-/-}$ (n = 6) and (**B**) *Adam17*$^{ex/ex}$.*Ldlr*$^{-/-}$ (n = 6) mice. Areas marked with white boxes in the top panels are depicted in the middle and bottom panels. Arrows indicate representative strongly TUNEL-positive nuclei. Curved white dashed line indicates the border of plaque tissue (left of the line) and arterial wall (right of the line). Apoptotic cells were quantified in (**C**) relation to total cell number and in (**D**) relation to the plaque area. Cell nuclei are marked by DAPI staining (blue). *** $p < 0.001$ [130].

3.2.13 *Effects of Adam17-deficiency on proliferation in atherosclerotic lesions through Ki67 stainings*

To investigate the cellular proliferation in atherosclerotic lesions *in vivo*, we performed immunofluorescence stainings with Ki67 as proliferation marker and co-stainings with Mac2-positive macrophages (MΦ) (Figure 81) and α-SMA positive vascular smooth muscle cells (Figure 82) in aortic lesions of *Adam17*$^{wt/wt}$.*Ldlr*$^{-/-}$ (n = 6) and *Adam17*$^{ex/ex}$.*Ldlr*$^{-/-}$ (n = 6).

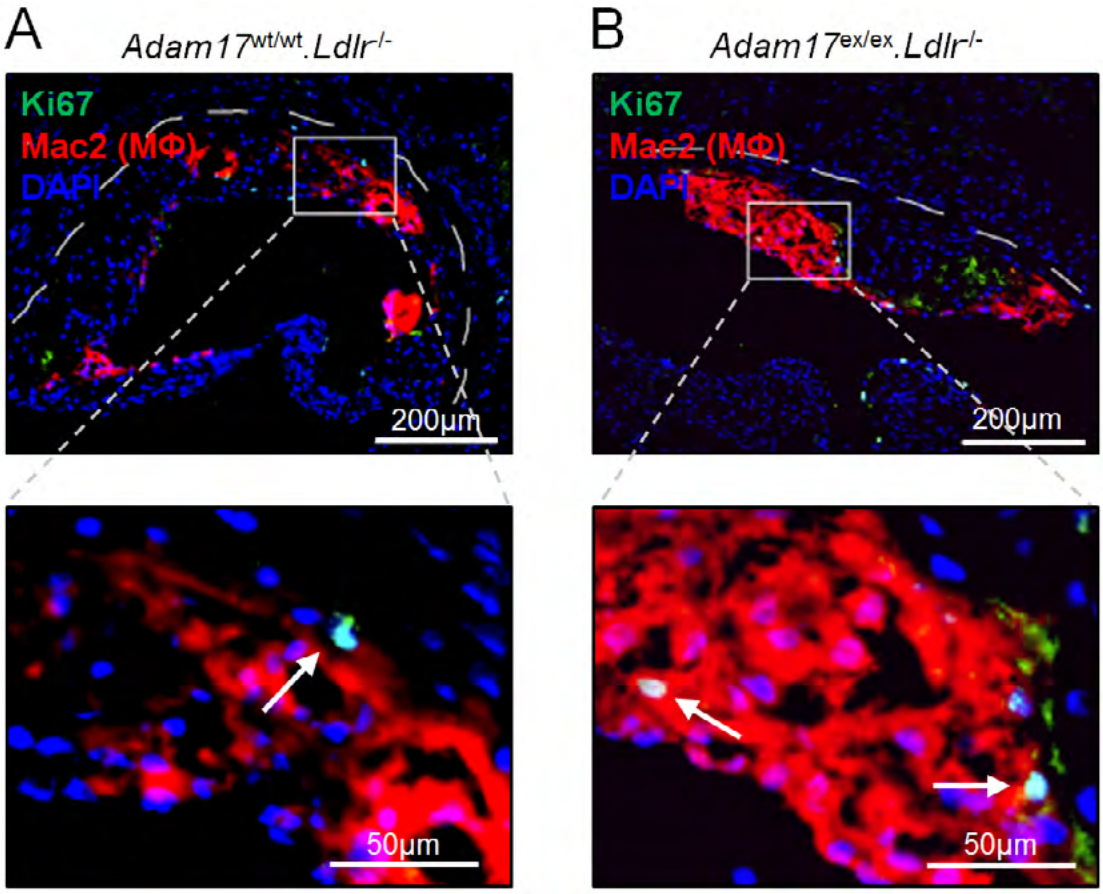

FIGURE 81: Representative immunofluorescence stainings and co-stainings of Ki67-positive (Ki67^{+}) proliferating cells (green) with Mac2-positive (Mac2^{+}) macrophages (red) in the aortic roots of (**A**) *Adam17*$^{wt/wt}$.*Ldlr*$^{-/-}$ and (**B**) *Adam17*$^{ex/ex}$.*Ldlr*$^{-/-}$ *mice*. White arrows indicate proliferating Mac2-positive macrophages. Cell nuclei are marked by DAPI staining (blue) [130].

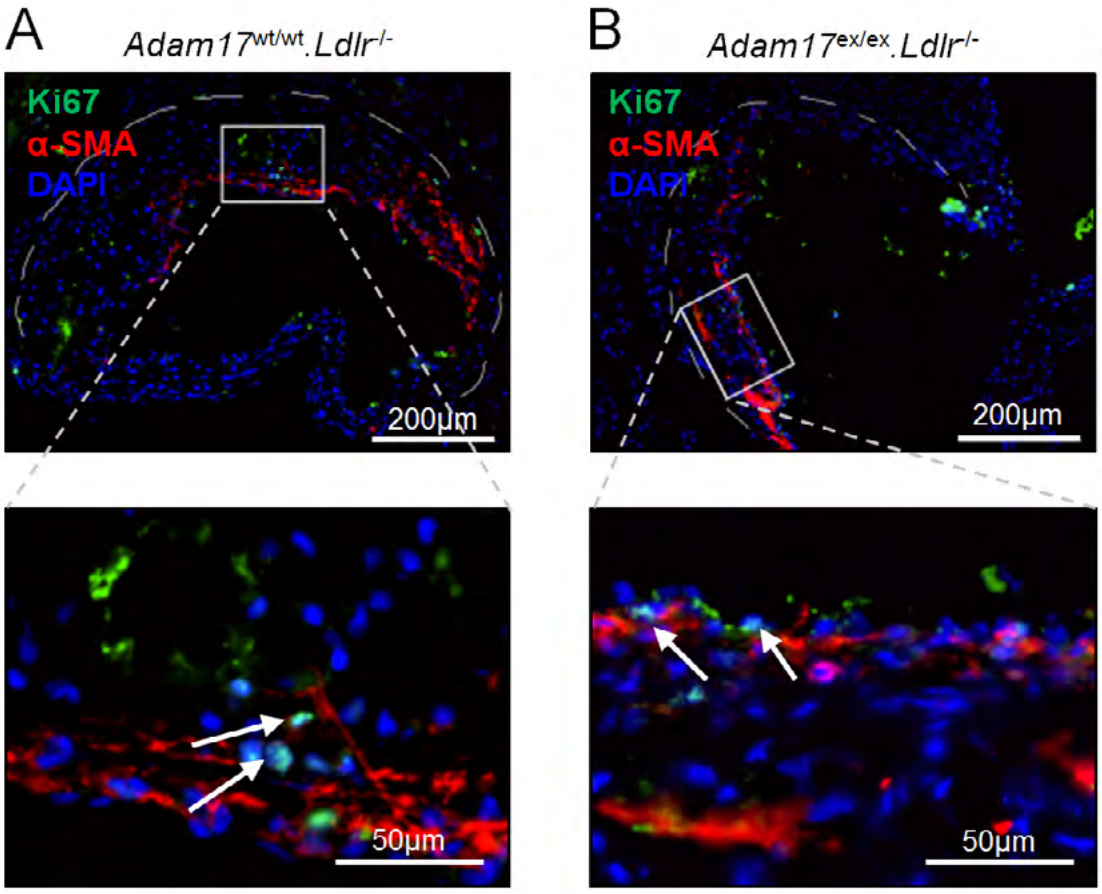

FIGURE 82: Representative immunofluorescence stainings and co-staings of Ki67-positive (Ki67^{+}) proliferating cells (green) with α-SMA-positive smooth muscle cells (red) in the aortic roots of (**A**) *Adam17*$^{wt/wt}$.*Ldlr*$^{-/-}$ and (**B**) *Adam17*$^{ex/ex}$.*Ldlr*$^{-/-}$ mice. White arrows indicate proliferating α-SMA-positive SMCs. Cell nuclei are marked by DAPI staining (blue) [130].

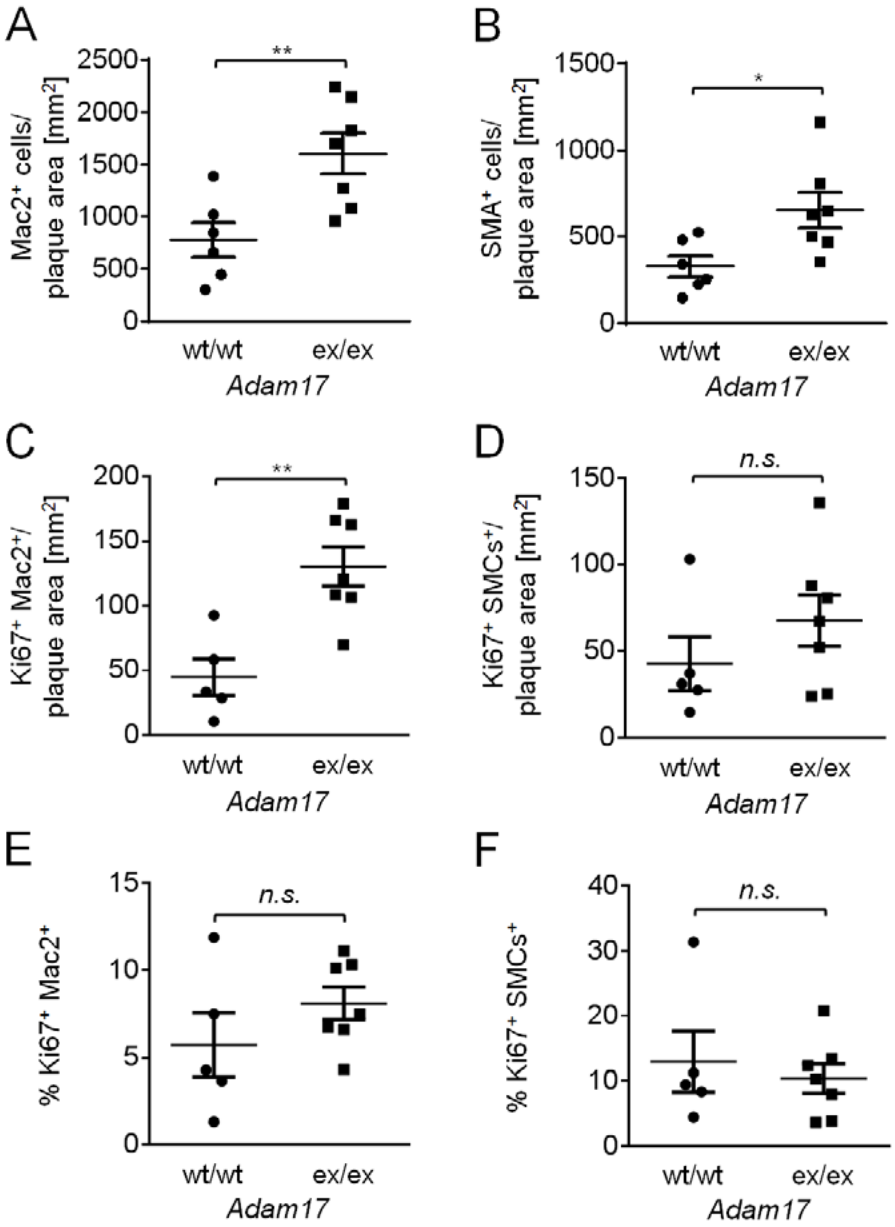

FIGURE 83: Cellular proliferation in atherosclerotic lesions of *Adam17*$^{wt/wt}$.*Ldlr*$^{-/-}$ and *Adam17*$^{ex/ex}$.*Ldlr*$^{-/-}$ mice. (**A**) Quantification of Mac2$^+$ macrophages and (**B**) SMA-positive (SMA$^+$) vascular smooth muscle cells in aortic root plaque areas of *Adam17*$^{wt/wt}$.*Ldlr*$^{-/-}$ (wt/wt; n = 6) and *Adam17*$^{ex/ex}$.*Ldlr*$^{-/-}$ (ex/ex; n = 7) mice. (**C**) Ki67$^+$/Mac2$^+$ double-positive macrophages and (**D**) Ki67$^+$/SMCs$^+$ double-positive vascular smooth muscle cells in aortic root plaque areas of *Adam17*$^{wt/wt}$.*Ldlr*$^{-/-}$ (n = 5) and *Adam17*$^{ex/ex}$.*Ldlr*$^{-/-}$ (n = 7) mice. (**E**) Percentage of Ki67$^+$/Mac2$^+$ cells and (**F**) Ki67$^+$/SMCs$^+$ cells of *Adam17*$^{wt/wt}$.*Ldlr*$^{-/-}$ (n = 5) and *Adam17*$^{ex/ex}$.*Ldlr*$^{-/-}$ (n = 7) mice in relation to the total cell numbers of macrophages or of SMCs, respectively. * $p < 0.05$; ** $p < 0.01$; *** $p < 0.001$, n.s. = not significant [130].

Here, we detected significantly more Mac2-positive macrophages (Figure 83 A) and α-SMA positive vascular smooth muscle cells (SMCs) (Figure 83 B) in lesions of *Adam17*-deficient mice corroborating our results from cultured cells. Ki67 staining revealed higher numbers of proliferating macrophages per plaque area in atherosclerotic lesions of *Adam17*$^{ex/ex}$.*Ldlr*$^{-/-}$ mice (Figure 83 C) and a trend toward increased numbers of proliferating SMCs per plaque area (Figure 83 D) [130].

Neither the ratio of proliferating Ki67-positive Mac2- nor of Ki67-positive SMA-cells in relation to the total number of the respective cell population was significantly different between wild-type *Adam17*$^{wt/wt}$.*Ldlr*$^{-/-}$ and homozygous *Adam17*$^{wt/wt}$.*Ldlr*$^{-/-}$ mice (Figures 83 E, F).

These data are confirmatory of our *in vitro* results, revealing however that the *in vivo* effects on proliferation were rather subtle (Figures 64 A, B; 68 A, B; 73 A, B) and suggested that the higher abundance of macrophages in plaques from *Adam17*-deficient mice (Figure 83 A) might be rather a consequence of resistance to apoptosis (Figures 63, 67) and increased adhesion (Figures 65 A, B; 69; 70). In summary, the histological cellular analysis validated our *in vitro* studies of the mechanisms of *Adam17*-deficiency, thereby establishing ADAM17 as a modulator of atherosclerosis [130].

3 Results – Chapter III –

The ADAM17 metalloprotease maintains arterial elasticity

This work has been published in [146].

3.3 The role of ADAM17 in aneurysm formation

In the second part of this PhD thesis we identified an unexpected protective role of ADAM17 against atherosclerosis. In the absence of *Adam17*, likely due to a deficit in tumour necrosis factor receptor 2 (TNFR2) shedding, the activity of membrane-tethered TNFR2 increased in macrophages and vascular smooth muscle cells (VSMCs) leading to overproliferation, increased adhesive properties, and consequently, to increased atherosclerotic lesions. This atheroprotective function could be attributed to a specific role in cells of the myeloid lineage [185].

To date, *Adam17* has also been studied in the context of other vascular diseases, such as aneurysms. Its role therein remained controversial, with one study reporting reduced ADAM17 expression in aneurysms [140], and other studies showing a positive correlation of expression and aneurysm risk or occurrence [141-143]. In aneurysms the integrity of the arterial wall is compromised by inflammatory processes and other extracellular matrix (ECM)-degrading factors, impairing elastin lamellae that support and transmit mechanical load to the cellular cytoskeleton [144, 145]. Whether and how ADAM17 links to these processes is unknown [146].

Here, we investigated whether mouse *Adam17* was more generally involved in regulating arterial wall integrity. For this, we used the *Adam17* hypomorphic mutant mice (*Adam17*$^{ex/ex}$) carrying an exon-induced translational stop codon leading to strongly decreased ADAM17 activity [132] and drawn comparisons with myeloid-specific or endothelial-specific conditional knockouts in an apolipoprotein E-deficient background (ApoE$^{-/-}$.LysM^{Cre}ADAM17$^{fl/fl}$; ApoE$^{-/-}$.Bmx^{Cre}ADAM17$^{fl/fl}$)[185].

We determined the vascular size by quantifying intra-arterial lumen area in the aortic root, or, separately, arterial wall circumference and wall width in the brachiocephalic artery (BCA) of *Adam17*$^{ex/ex}$.*Ldlr*$^{-/-}$ and control mice. Arterial extracellular matrix (ECM) properties were determined by assessing elastic fibres with Verhoeff van Gieson staining and by quantifying total collagen fibre content by PicroSirius Red imaging using polarized light [186]. Atherosclerotic plaque size was measured as the area of Oil Red-stained tissue in sagittal arterial tissue sections [146].

3.3.1 *Increased aortic root lumen area in Adam17-deficient mice*

First, we quantified the aortic root lumen area in male and female mice of homozygous *Adam17*$^{ex/ex}$.*Ldlr*$^{-/-}$, heterozygous *Adam17*$^{wt/ex}$.*Ldlr*$^{-/-}$ and wild-type *Adam17*$^{wt/wt}$.*Ldlr*$^{-/-}$ mice.

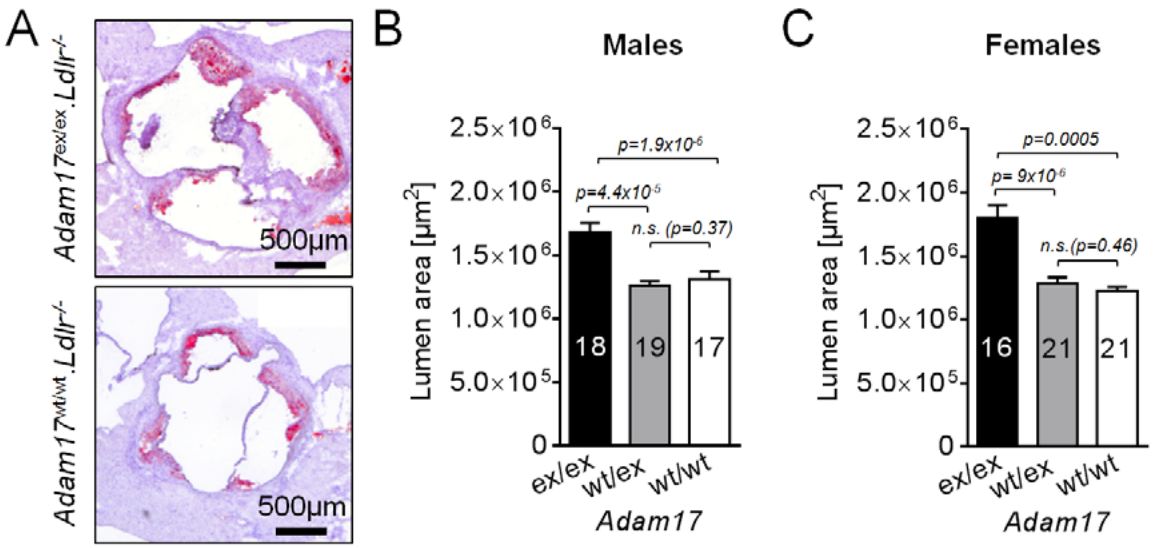

FIGURE 84: (**A**) Representative Oil-Red O stainings of the aortic root of homozygous hypomorphic *Adam17* mutant mice (*Adam17*$^{ex/ex}$.*Ldlr*$^{-/-}$) and *Adam17* wild-type (*Adam17*$^{wt/wt}$.*Ldlr*$^{-/-}$). (**B-C**) Quantification of the lumen area of the aortic root of (B) male and (C) female homozygous *Adam17*$^{ex/ex}$.*Ldlr*$^{-/-}$ (ex/ex), heterozygous *Adam17*$^{wt/ex}$.*Ldlr*$^{-/-}$ (wt/ex) and wild-type *Adam17*$^{wt/wt}$.*Ldlr*$^{-/-}$ (wt/wt) mice [146].

We found that the aortic root lumen area in hypomorphic *Adam17*$^{ex/ex}$.*Ldlr*$^{-/-}$ mutants was increased by 30 % and 40 % in male and female mice compared to wild-type *Adam17*$^{wt/wt}$.*Ldlr*$^{-/-}$, respectively (Figure 84 A-C). These results are in accordance to TACE$^{\Delta Zn/\Delta Zn}$ null mutants, which exhibit markedly enlarged fetal hearts and die at birth [176].

In contrast, in a parallel study myeloid-specific *Adam17* mouse knockouts (ApoE$^{-/-}$Bmx^{CreCre}ADAM$^{fl/fl}$) showed only a trend toward dilation, which did not reach statistical significance, and endothelial-specific depletion (ApoE$^{-/-}$LysM^{Cre}ADAM$^{fl/fl}$) did not show any dilation [185].

To test if *Adam17*-dependent cell wall control was a more general function, we analysed the dimensions of the BCA of *Ldlr*$^{-/-}$ mice [146].

3.3.2 *Atherosclerotic lesions and circumference in the branchiocephalic artery of Adam17-deficient and wild-type mice*

The brachiocephalic artery is the first branch of the aortic arch and divides into the right common carotid artery and the right subclavian artery supplying blood to the right arm, the head and neck (Figure 85).

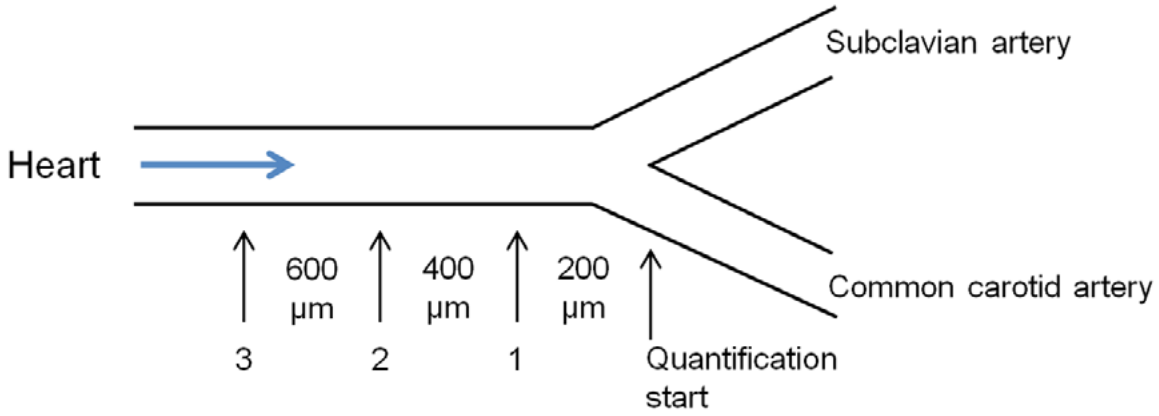

FIGURE 85: Schematic of the quantification of the circumference of the brachiocephalic artery. Transverse cryosections of 10 µm were prepared at three positions (200 µm, 400 µm, and 600 µm proximal to the bifurcation of the BCA with the right common carotid artery and right subclavian artery [99, 146].

We measured the circumference of the brachiocephalic artery at a distance of 200 µm, 400 µm, and 600 µm proximal from the bifurcation of the BCA (1a, 2a, 3a).

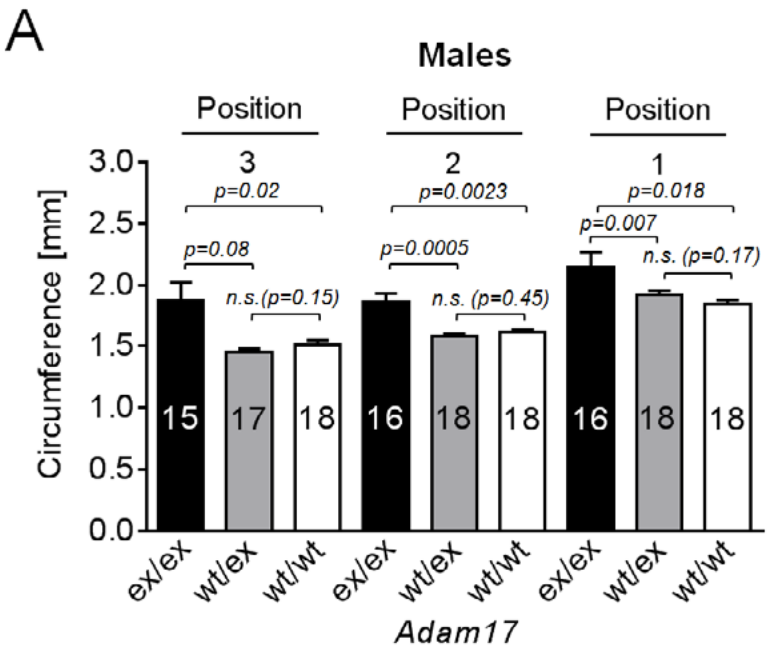

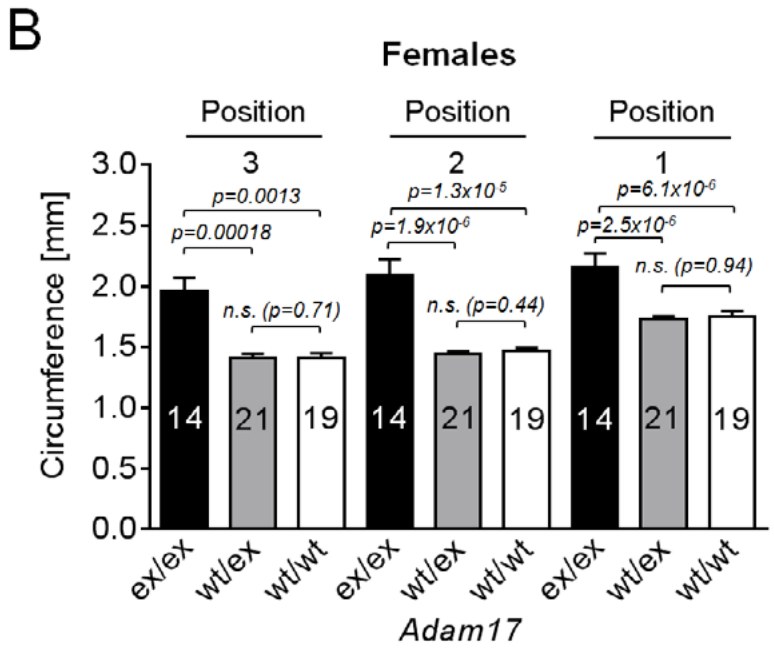

FIGURE 86: Quantification of the circumference of the brachiocephalic artery (BCA) at three different positions in (**A**) male and (**B**) female *Adam17*$^{wt/wt}$.*Ldlr*$^{-/-}$, heterozygous *Adam17*$^{wt/ex}$.*Ldlr*$^{-/-}$ and homozygous *Adam17*$^{ex/ex}$.*Ldlr*$^{-/-}$ mice [146].

Quantification of the circumference of the brachiocephalic artery revealed a significant luminal widening at all three investigated positions in hypomorphic *Adam17*$^{ex/ex}$.*Ldlr*$^{-/-}$ mice in comparison to the heterozygous and the wild-type mice. We had an increase of 39 % and 24 % in female and male respectively, at position 3, 600 µm proximal from the bifurcation of the BCA. At position 2 (400 µm) we observed an increase of 42 % and 15 %, respectively and at position 3 an increase of 23 % and 16 % respectively.

We showed previously, that *Adam17*-deficiency is associated with increased atherosclerotic lesions at the aortic root in male and female mice.

For this, we quantified atherosclerotic lesions in the brachiocephalic artery (BCA) of wild-type *Adam17*$^{wt/wt}$.*Ldlr*$^{-/-}$, heterozygous *Adam17*$^{wt/ex}$.*Ldlr*$^{-/-}$ and homozygous *Adam17*$^{ex/ex}$.*Ldlr*$^{-/-}$ mice. For the quantification of atherosclerosis in the brachiocephalic artery, transverse cryosections of 10 µm were prepared in a proximal direction from the bifurcation with the right common carotid artery and right subclavian artery to the aortic arch at a distance of 200 µm, 400 µm, and 600 µm proximal from the bifurcation of the BCA (1A, 2A, 3A). For the atherosclerosis quantification we used male and female mice of wild-type *Adam17*$^{wt/wt}$.*Ldlr*$^{-/-}$ (n = 17; n = 19), heterozygous *Adam17*$^{wt/ex}$.*Ldlr*$^{-/-}$ (n = 18; n = 21) and homozygous *Adam17*$^{ex/ex}$.*Ldlr*$^{-/-}$ (n = 16; n = 14) mice, respectively (Figure 86) [146].

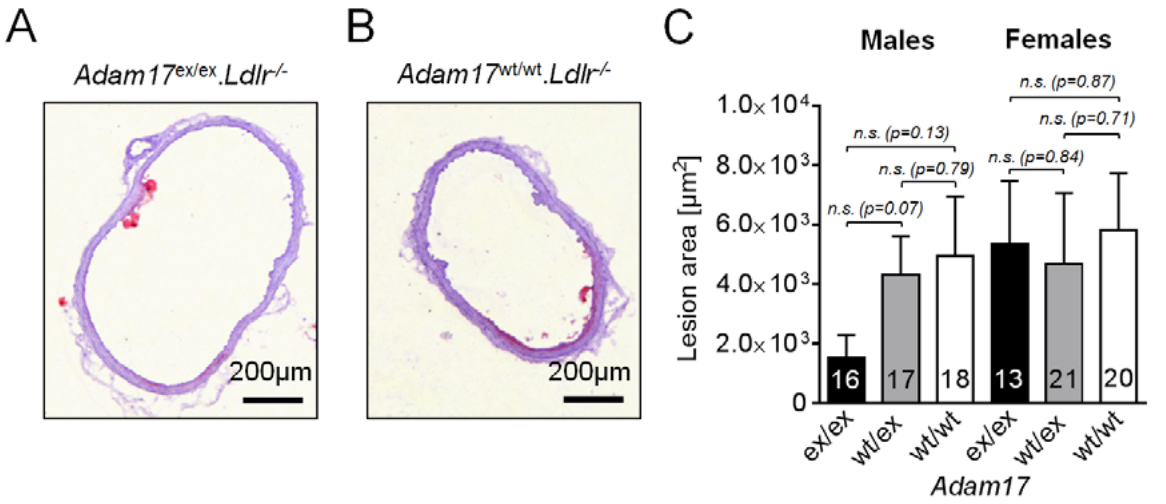

FIGURE 87: Representative oil red O stainings of the brachiocephalic artery (BCA) of (**A**) *Adam17*$^{wt/wt}$.*Ldlr*$^{-/-}$ and (**B**) *Adam17*$^{ex/ex}$.*Ldlr*$^{-/-}$ mice. (**C**) Atherosclerotic lesion quantification in the BCA of wild-type *Adam17*$^{wt/wt}$.*Ldlr*$^{-/-}$ (wt/wt), heterozygous *Adam17*$^{wt/ex}$.*Ldlr*$^{-/-}$ (wt/ex) and homozygous *Adam17*$^{ex/ex}$.*Ldlr*$^{-/-}$ (ex/ex) in male and female mice [146].

Here, we observed no significant differences in the lesion sizes of wild-type *Adam17*$^{wt/wt}$.*Ldlr*$^{-/-}$, heterozygous *Adam17*$^{wt/ex}$.*Ldlr*$^{-/-}$ and homozygous *Adam17*$^{ex/ex}$.*Ldlr*$^{-/-}$ male and female mice (Figure 87).

This suggested that atherosclerotic plaque development and aneurysm onset were regulated independently by ADAM17, at least in the BCA of *Ldlr*$^{-/-}$ mice [146].

3.3.3 *Collagen staining in the brachiocephalic artery*

To explain the luminal widening in the BCAs of *Adam17*-deficient mice, we analyzed the extracellular matrix (ECM). Collagen is the main structural protein in the extracellular space in the various connective tissues in animal bodies. As the main component of connective tissue, it is the most abundant protein in mammals [187], making up from 25 % to 35 % of the whole-body protein content. To examine the collagen structure of wild-type *Adam17*$^{wt/wt}$.*Ldlr*$^{-/-}$ and *Adam17*$^{ex/ex}$.*Ldlr*$^{-/-}$ mice we used the Picrosirius Red (PSR) staining. The arterial wall is composed of a highly ordered structure of cells and extracellular matrix. The tunica media, the middle coat contains SMCs. The media is the thickest layer and provides structural support, vasoreactivity and elasticity. The outer coat, the tunica adventitia, contains mast cells, fibroblasts, nerve endings and microvessels [15]. The ECM makes up to 60 % of the intimal volume and consists of elastic lamellae, smooth muscle cells and three major protein components, including proteoglycans, collagen and multi-adhesive matrix proteins [16]. We examined the collagen structure in brachiocephalic arteries of 3 male and 3 female wild-type *Adam17*$^{wt/wt}$.*Ldlr*$^{-/-}$ and *Adam17*$^{ex/ex}$.*Ldlr*$^{-/-}$ mice. Quantification of the Picrosirius Red staining was imaged using polarized light [146].

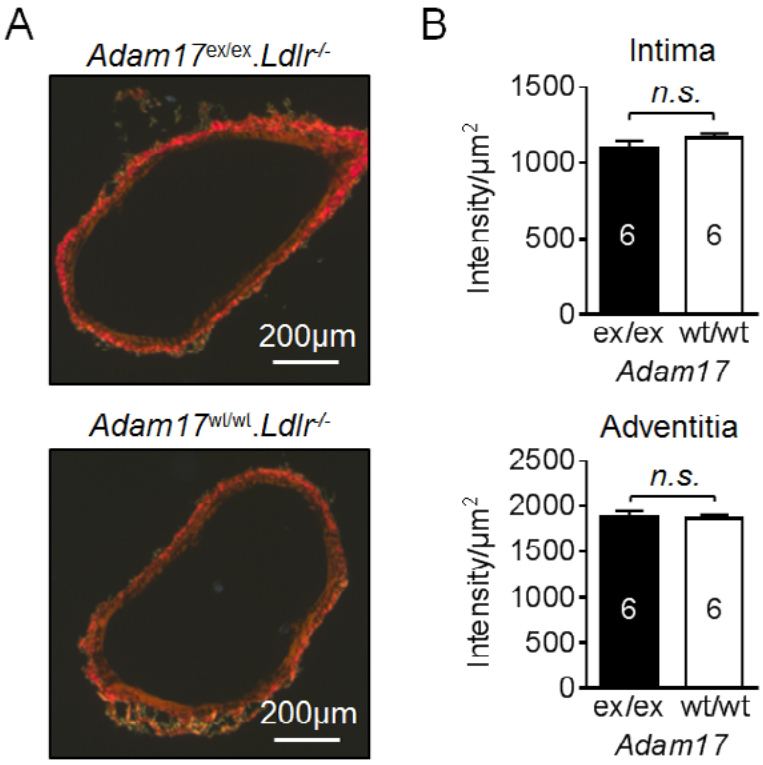

FIGURE 88: (**A**) Representative PicroSirius Red stainings of the BCA of *Adam17*$^{ex/ex}$.*Ldlr*$^{-/-}$ and wild-type *Adam17*$^{wt/wt}$.*Ldlr*$^{-/-}$ mice for visualizing collagen density. (**B**) Quantification of PicroSirius Red intensity by polarization imaging in the intima and adventitia of homozygous *Adam17*$^{ex/ex}$.*Ldlr*$^{-/-}$ (n = 6) and wild-type *Adam17*$^{wt/wt}$.*Ldlr*$^{-/-}$ (n = 6) mice [146].

Based on Picrosirius Red imaging [186], and not distinguishing between different classes of fibres via birefringence colour discrimination [188], total collagen fibre content in the intima and in the adventitia was found to be unaffected in the dilated *Adam17* mutant BCAs [146].

Furthermore, we investigated the arterial wall thickness of BCA sections from *Adam17*$^{ex/ex}$.*Ldlr*$^{-/-}$ (n = 5) and wild-type *Adam17*$^{wt/wt}$.*Ldlr*$^{-/-}$ (n = 5) mice.

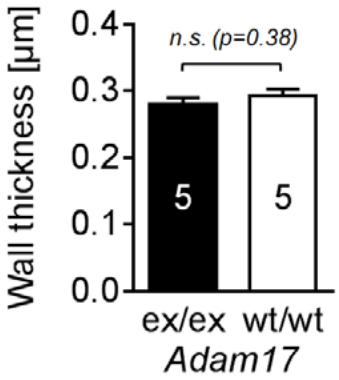

FIGURE 89: Quantification of the arterial wall thickness of BCA sections from *Adam17*$^{ex/ex}$.*Ldlr*$^{-/-}$ (n = 5) and wild-type *Adam17*$^{wt/wt}$.*Ldlr*$^{-/-}$ (n = 5) mice [146].

Here, we did not observe arterial wall thinning in the mutant BCA.

3.3.4 *Elastin staining in the brachiocephalic artery*

In a parallel study, myeloid-specific and conditional endothelial-specific depletion of *Adam17* in ApoE$^{-/-}$Bmx$^{Cre Cre}$ADAM$^{fl/fl}$ or ApoE$^{-/-}$LysM^{Cre}ADAM$^{fl/fl}$ mice caused no significant differences in the lumen area of the BCAs [185]. This indicated that this phenotype might be driven by *Adam17*-deficiency in smooth muscle cells or fibroblasts rather than bone marrow-derived or endothelial cells. Elastic fibres are bundles of proteins (elastin) found in extracellular of connective tissue and produced by fibroblasts and smooth muscle cells in arteries [189]. To examine if elastin fibres hat a different morphology in wild-type and *Adam17*$^{ex/ex}$.*Ldlr*$^{-/-}$ mice we performed Verhoeff's Van Gieson stainings in brachiocephalic arteries of wild-type and *Adam17*-deficient mice (Figure 90).

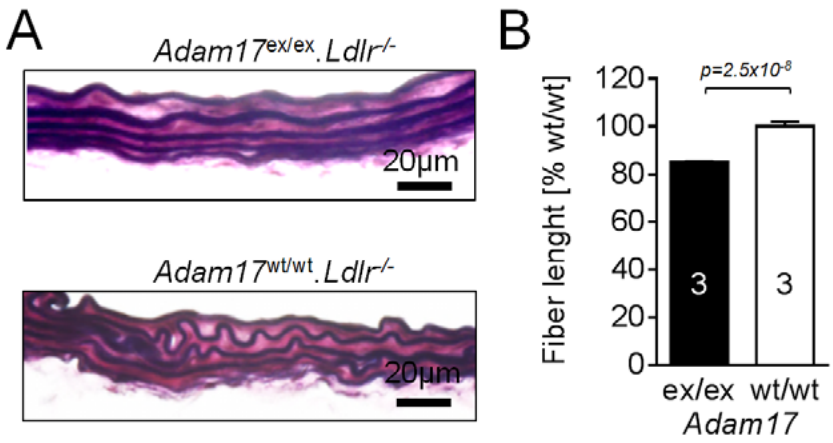

FIGURE 90: (**A**) Representative Verhoeff-van Gieson staining visualizing elastin fibres in the brachiocephalic arteries in *Adam17*$^{wt/wt}$.*Ldlr*$^{-/-}$ (n = 3) und *Adam17*$^{ex/ex}$.*Ldlr*$^{-/-}$ (n = 3) mice. Elastic fibers and cell nuclei are stained black, while other structures are stained red. (**B**) Quantification of elastin fibre length of homozygous *Adam17*$^{ex/ex}$.*Ldlr*$^{-/-}$ (n = 3) and wild-type *Adam17*$^{wt/wt}$.*Ldlr*$^{-/-}$(n = 3) mice. Three fibres were quantified of each animal [146].

Here, we found in *Adam17*$^{wt/wt}$.*Ldlr*$^{-/-}$ mice as well as in *Adam17*$^{ex/ex}$.*Ldlr*$^{-/-}$ the same number of elastic fibres. However, elastin fibres were altered: The elastic fibers of the wild-type BCAs were arranged in wavy bundles, while the elastic fibres in *Adam17*$^{ex/ex}$.*Ldlr*$^{-/-}$ mice were stretched out and showed reduced ondulation. To quantify this phenotypic switch, we determined the length of individual elastic fibers within sub-segments of identical length (20 µm) in BCAs of mutants and wild-type mice [146].

To quantify this phenotypic switch, we determined the length of individual elastic fibres within subsegments of identical length (20 µm) in BCAs of mutants and wild-type mice (n = 3/3).

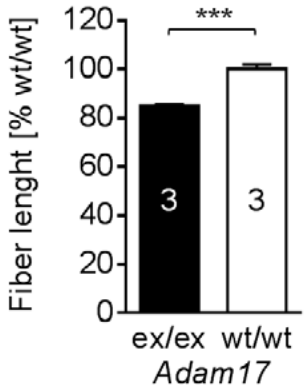

FIGURE 91: Quantification of fiber length of homozygous *Adam17*$^{ex/ex}$.*Ldlr*$^{-/-}$ (ex/ex) and wild-type *Adam17*$^{wt/wt}$.*Ldlr*$^{-/-}$ (wt/wt) mice. *** $p < 0.001$ [146].

We found a significantly reduced unit fibre length in homozygous *Adam17*$^{ex/ex}$.*Ldlr*$^{-/-}$ mice compared to wild-type *Adam17*$^{wt/wt}$.*Ldlr*$^{-/-}$.

Thus, ADAM17 may protect the integrity of the arterial wall by regulating elastin fibre organization [146].

3.3.5 *Differentially expressed genes in aortic tissue of Adam17$^{wt/wt}$.Ldlr$^{-/-}$ and Adam17$^{ex/ex}$.Ldlr$^{-/-}$ mice.*

To get first insights into how ADAM17 controlled arterial wall integrity, we investigated which genes were differentially expressed in aortic tissue of *Adam17$^{ex/ex}$.Ldlr$^{-/-}$* hypomorphic mutants. mRNA microarray profiling revealed not only a set of *bona-fide* atherosclerosis regulators among the top differential abundant transcripts, but also a number of cytoskeletal contractility regulators and factors required for ECM elastogenesis. The latter included the elastin microfibril interfacer *Emilin2*, the elastin-binding laminin/fibronectin-interacting *Fibulin 2*, matrix metalloproteinases MMP3/12, the proteoglycan Syndecan 3, the adhesion molecule and sheer-stress mechanoresponsive *Pecam1* (Figure 92) [146].

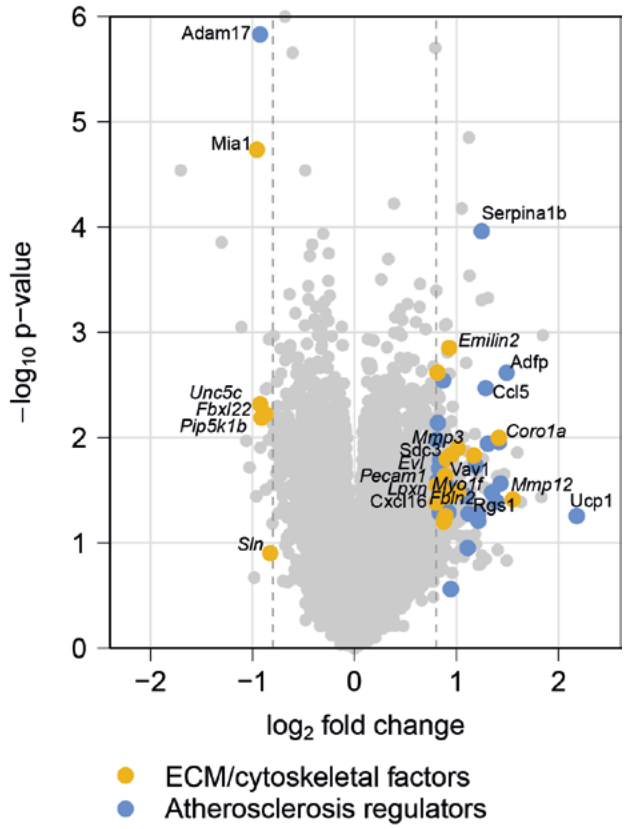

FIGURE 92: Volcano plot of mRNAs differentially abundant in aortas of wild-type *Adam17$^{wt/wt}$.Ldlr$^{-/-}$* and homozygous *Adam17$^{ex/ex}$.Ldlr$^{-/-}$* mice (transcriptome-wide expression profiling by microarrays). Highlighted are genes with a fold change >0.8 which are associated with atherosclerosis (purple; exemplary: uncoupling protein *Ucp1*, Regulator of G Protein Signaling *Rgs1*, C-X-C Motif Chemokine Ligand *Cxcl16*, metalloproteinase *Mmp3*, C-C Motif Chemokine Ligand 5 *Ccl5*, Adipose Differentiation-Related Protein *Adfp*) or with ECM/cytoskeletal regulation (yellow; exemplary: metalloproteinase *Mmp3* and *Mmp12*, Myosin *Myo1f*, Coronin *Coro1a*, *Emilin2*, Syndecan *Sdc3*, *Pecam1*, Fibulin *Fbln2*, *Enah/Vasp-Like Evl*, leupaxin *Lpxn*, melanoma inhibitory activity *Mia1*, *Unc5c*, *Fbxl22*, *Pip5k1b*, Sarcolipin *Sln*). * $p < 0.05$; ** $p < 0.01$; *** $p < 0.001$ [146]

Our combined data reveal a function of ADAM17 in arterial elastin network maintenance, which is separate from the previously known role in atherosclerotic lesion control [146].

4 Discussion

This PhD thesis aims to make a contribution in identifying new determinants of atherosclerosis by investigating two recently reported, yet still uncharacterized, atherosclerosis susceptibility loci on mouse chromosomes 3 and 12. These loci were identified in an intercross of atherosclerosis-susceptible C57BL/6 (B6) and atherosclerosis-resistant FVB mice on the LDL-receptor deficient background (*Ldlr*$^{-/-}$)[104].

As first major result, we identified and moleculary characterized the novel atherosclerosis modifier Pla2g12a at the chromosome 3 locus. As second major result, using a hypomorphic genetic mouse model, we established that Adam17, located at chromosome 12, exhibited protective roles against both, atherosclerosis, as well as aneurysm formation. Both effector genes protect from the disesase by modulating central molecular mechanisms of atherosclerosis, such as adhesion and proliferation of blood and vascular cells.

4.1 Mouse models for understanding human atherosclerosis

In this PhD thesis, we used different mouse models to identify novel candidate genes (*Pla2g12a*) for atherosclerosis susceptibility and to elucidate potential mechanisms of atherogenesis (ADAM17). Over the past 35-40 years, the mouse has become by far the most widely used animal model for atherosclerosis research. Mouse and human genomes are very similar with about 95 % conservation of protein-coding genes. A recent study by Scheidt and colleagues confirmed that about 53-55 % of metabolic and cellular pathways overlapped between the study of mouse candidate CAD risk genes and the list of CAD risk genes from human GWAS, and that 45 of 46 candidate CAD risk genes that were already studied in mouse CAD models showed a consistent role in modifiying disease [190]. With the results of this PhD thesis we show the principal suitability of mouse models in atherosclerosis research for the identification of novel effector genes and make a contribution to understanding different molecular pathways contributing to atherosclerosis.

4.2 *Identification of Pla2g12a as a novel candidate gene of atherosclerosis susceptibility on mouse chromosome 3*

In the first part of this PhD thesis, we identified *Pla2g12a* as a novel atherosclerosis susceptibility gene that determined the risk executed by a genetic locus on mouse chromosome 3. Our study is the first to dissect two overlapping, yet independent female-specific QTL loci for atherosclerosis susceptibility by investigating inheritance patterns from the grandparental F0 generation to female F2 mice. Thereby, and supported by systematic expression QTL analyses, we identify *Pla2g12a* as novel atherosclerosis modifier gene in subcross A, where the atherosclerosis-susceptible B6 risk locus was introduced via B6.*Ldlr*$^{-/-}$ grandfathers. The prioritization of candidate genes in this locus was a multistep process, where gene expression profiling was initially performed in livers of congenic FVB.Chr3$^{B6/B6}$ and FVB mice. Yet, subsequently we validated the results of the profiling in liver and aorta tissues as well as BMDMs of parental C57BL/6 and FVB F0 mice. So, 5 from 7 identified candidate genes that had been identified through liver profiling were, thereby, validated as expressed in aorta and/or BMDMs, and thus in sites that are likely more directly disease-relevant than liver (given the proposed molecular roles of our candidate genes and the absence of a relevant lipid phenotype). Further we found these 5 candidates were differentially expressed also in the aortas and BMDMs (with the same directionality of effects as in liver) in C57BL/6 compared to FVB mice. For eQTL analyses in mice of the F2-generation unlikely only liver probes were at our disposal [104] and an eQTL analysis in vascular tissue could, thus, not performed in the segregating F2 population.

To investigate if the B6-derived genetic variants that promoted atherosclerosis also regulated gene expression *in cis*, we used livers of female F2 mice that were derived from cross A or from cross B, and performed expression quantitative trait locus (eQTL) mapping for the remaining genes. We observed significantly LOD scores for *Pla2g12a*, *Pklr* and *Cth* in cross A and *Vcam1* in cross B. As *Pklr* and *Cth* genes in cross A could be excluded, we concentrated on *Pla2g12a* which co-located with the atherosclerosis LOD score. In subcross B, a LOD score maximum of 4.4 for *Vcam1* was detected and overlapped most closely the location of atherosclerosis-susceptibility. In female mice of the F2-generation, mice carrying two B6-alleles at d3mit57 had 1.5-fold higher *Vcam1* expression levels and developed 1.9-fold more atherosclerosis. *Vcam1* is a well-known regulator of atherogenesis [166] and increased *Vcam1* levels have been shown to promote atherosclerosis [167, 168]. So, our data are consistent with the published literature and make *Vcam1* a likely effector gene in cross B [148].

From the analysis of cross A, *Pla2g12a* emerged as novel candidate atherosclerosis modifier. For better eQTL mapping accuracy in cross A fine-mapping with an additional SNP (rs13464244) led to an increased LOD score maximum for *Pla2g12a* expression of 5.01. Homozygosity for the B6 allele at rs13464244 in F2 females from cross A was associated with decreased mRNA abundance of *Pla2g12a* compared to the FVB genotype at this position and with enlarged atherosclerotic lesions. Furthermore, we observed an inverse correlation of high *Pla2g12a* mRNA expression with smaller atherosclerotic lesion sizes indicating that *Pla2g12a* protects from atherosclerosis.

The Chr3 locus was correlated with atherosclerosis risk only in F2 female progeny of either cross, but not in male F2 mice and, consistently, we observed no eQTLs in male F2 mice for *Pla2g12a* or *Vcam1.* Given that the DNA sequence was identical in mice of the grandparents' generation, an epigenetic regulation and sex-specific regulation of its transmission through the F1 and F2 generations is likely. For example, although the DNA sequence may be the same, histone modifi-

cations of nucleosome enwrapping this DNA, or DNA methylation patterns on regulatory regions could be set differentially on the region in the male and female germline [191, 192]. Also chromatin-based epigenetic patterns are known to be inherited over cell divisions and even over generations [193]. Whether such a mechanism occurs at the identified locus is still speculation. In any case, it might become an important factor in the experimental design for gene discovery in inbred mouse models to consider male or female germline transmission in QTL studies. Furthermore, future profiling of epigenetic imprints in such models may explain at least part of the missing causality of complex traits in existing studies [148, 194-197].

4.2.2 *Pla2g12a-deficiency promotes adhesion between endothelial cells and macrophages*

The potential role of *Pla2g12a*, which belongs to the secreted phospholipase A2 enzymes (sPLA2), has not been investigated in atherogenesis, yet. We thus focussed on PLA2G12A and through immunohistochemical stainings, qPCR analyses and western blots we showed that PLA2G12A was highly expressed in vascular endothelial cells (ECs) and to a lesser extent in macrophages. EC activation is one of the first cellular changes in the vasculature *en route* to atherosclerosis [170, 171] and during atherosclerosis development ECs control adhesion of circulating leukocytes to nascent atherosclerotic lesions [148, 172].

We found that BMDMs from B6 mice, as well as BMDMs derived from Chr3 congenic mice (both with lower *Pla2g12a* expression) were more adhesive than FVB BMDMs. Importantly, we found that depleting *Pla2g12a* from ECs in this adhesion assay further increased adhesion of (untreated) BMDMs to ECs, with a comparable relative increase in adhesion of both B6-derived and FVB-derived BMDMs. These adhesion results were validated in RNAi experiments in RAW264.7 macrophages, to test whether *Pla2g12a* was, thus, a more general determinant of adhesion. These results indicated that PLA2G12A was exhibiting parallel athero-protective roles in macrophages and in ECs. In this adhesion assay upon loss of *Pla2g12a*, mRNA levels of the integrin ligand *Vcam1* did not increase suggesting that the increase in adhesion was due to *Pla2g12a*-dependent processes and independent of indirect transcriptional regulation of *Vcam1* [148].

Our analysis shows that PLA2G12A prevented leukocyte adhesion to endothelial cells in FVB mice, which is one of the earliest events in atherogenesis [166, 167, 198, 199], and establishes *Pla2g12a* as athero-protective factor in this mouse intercross [148].

4.2.3 *Modulation of atherosclerosis through Pla2g12a and Vcam1*

To identify the exact DNA position or epigenetic mark that causes *Pla2g12a* and *Vcam1* misregulation through the female F2 risk alleles is difficult. This study establishes the possibility that VCAM1 and PLA2G12A may modulate atherosclerosis susceptibility by independently controlling a common effector pathway: Induction of the immunoglobulin-superfamily adhesion molecule *Vcam1* on endothelial cells [167] and binding of VCAM1 to integrin $\alpha_4 b_1$ [200] on homing blood mononuclear leukocytes [201] recruits monocytes to growing lesions [171], which is a key step in initiating and promoting atherosclerosis [199]. Consistently, blocking of VCAM1 by an antibody [202] or in a hypomorphic mouse mutant *in vivo* [166] reduced monocyte adhesion on the early atherosclerotic endothelium and reduced lesion size [148].

On the contrary, *Pla2g12a* has not been decisively functionally explored before [203] and no knockout data exist. PLAG12A belongs to the group of secreted phospholipase A2 enzymes [204]. The phospholipase A2 superfamily of enzymes are characterized by their ability to hydrolyze fatty acids at the sn-2 position of glycerophospholipids and generate multiple classes of bioactive lipids [205, 206]. There are five major families of phospholipases: the secretory phospholipases (sPLA2) where the phospholipase of the group 12A belongs (PLA2G12A), the cytosolic (cPLA2) that are Ca^{2+}-dependent, the lysosomal A2 and two major Ca^{2+}-independent groups (iPLA2) and platelet activating factor acetylhydrolase (PAF-AHs)[205]. Adipose-specific PLA2 also belong to the class of PLA2s. Cytosolic PLA2 enzymes are believed to play a major role in the metabolism of arachidonic acid, the iPLA2 family to membrane homeostasis and energy metabolism, and the sPLA2 family to various biological processes [207].

In the meanwhile, secretory PLA2 family consists of 12 isoforms with comparable molecular weights of 16 kDa and three-dimensional structures [205]. Likely due to the secretory nature of this family, existing mouse models of other $sPLA_2$s have revealed diverse, tissue-specific and sometimes contradicting cellular functions [208-212]. Our data now indicate that PLA2G12A may dampen the onset of atherosclerosis via reducing cell-cell adhesive properties in the vascular endothelium. How adhesion changes upon alteration of PLA2G12A levels remain unknown, but we can at least exclude that *Vcam1* expression itself is regulated by *Pla2g12a*. Interestingly, previous reports have shown that some soluble PLA_2s (group IIA) can bind to selective integrin subtypes (avb3, α4b1), where they compete with the integrin ligand VCAM1 for binding [213, 214]. Given that adhesion of macrophages to endothelial cells was increased when *Pla2g12a* was depleted in our own experiments, it is conceptually possible, that PLA2G12A impairs adhesion via impairing integrin signaling, by virtue of blocking the access of the integrin ligand VCAM1 to integrins. Supporting this integrin-binding hypothesis for altering adhesive properties, phospholipase catalytic activity is not needed for this type of interaction of $sPLA_2$'s with integrins [213]. This is relevant, because PLA2G12A's phospholipase activity is known to be very weak compared to other members of this family of secreted phospholipases [215, 216]. Together, *Vcam1* upregulation and *Pla2g12a* down-regulation may converge on activation of integrin-dependent adhesion [148].

4.2.4 *Epistasis analysis*

Epistasis analyses in the F2 generation of our intercrosses revealed no significant interaction between SNPs in the candidate interval on chromosome 3 [104], thus rather speaking against a coordinate regulatory function of *Pla2g12a* and *Vcam1* in atherogenesis. Furthermore, despite the cell-proximal role of PLA2G12A in adhesion control (shown by the RNAi experiments) and the absence of relevant lipid changes, we can at this point not exclude that still unknown factors might change atherosclerosis onset by additional routes. Moreover, we have focused mainly on factors that changed their gene expression dependent on atherosclerosis risk genotype, but we want to note that a number of non-synonymous SNPs exist in the coding regions of the interval in genes that are not identical by descent. Bioinformatic predictions indicate that some may be detrimental to protein function, and *Nes, Gon4l, Tchhl1, Hsd3b2, Pdlim5, Erich3* and *Tnni3k* are potential candidates at this level of analysis. Nevertheless this does not necessarily affect our finding that the change in *Pla2g12a* mRNA abundance is an independent important factor, as demonstrated by functional RNAi experiments in different genetic backgrounds [148].

4.2.5 *Secretory phospholipases A2 as biomarkers*

Supporting a broader relevance of our findings, *sPLA$_2$-IIA* and *-V* genes are clustered in mouse and human in a syntenic region that has been attributed atherosclerosis-susceptible properties [217]. Supporting a broader relevance of our findings, increased secretory phospholipase A_2 as well as lipoprotein-associated phospholipase A_2 have already been identified as biomarkers of cardiovascular risk in population studies with patients with established coronary artery disease (CHD)[205]. This has to be qualified, however, as no SNPs within PLA2G12A itself have been associated with atherosclerosis in humans. Instead, other human SNPs contained in the mouse Chr3 syntenic regions are indeed associated with different endpoints of the disease and some of these associate with loci for atherosclerosis risk factors, such as blood pressure and relevant lipids. Since the orthologues of the relevant human genes were not differentially expressed in our mouse model, and since we found no co-localization of the Chr3 QTL, at least not with lipid phenotypes in mouse, it is thus, however, rather likely that the human genetic variants control atherosclerosis susceptibility through other molecular mechanisms. To date, pharmacological inhibition of conventional sPLA$_2$s (not including PLA2G12A) have been clinically tested and failed in clinical phase III trials in cardiovascular patients and even increased myocardial infarction risk [218]. Therefore, to conclude, atheroprotective roles of some secreted phospholipases like *Pla2g12a* will have to be considered, and stimulation of *Pla2g12a*, not inhibition, might be medically relevant, but whether *Pla2g12a* or also other candidates from the mouse Chr3 interval have to be coordinately induced and repressed remains to be tested [148].

4.3 Mouse chromosome 12 and Adam17

In the second part of this PhD thesis we investigated the effect of *Adam17*-deficiency on atherosclerosis development. This work is the first functional study that describes a causal role of the metalloprotease ADAM17/TACE in atherosclerosis. Our data show that, contrary to what could have been expected from an enzyme that has been implicated mostly in releasing inflammatory effectors from the membrane, ADAM17 exhibits an athero-protective effect *in vivo*. Based on the analysis of *Adam17* hypomorphic knockout mice *in vivo*, and based on biochemical and genome-wide mRNA expression profiling, we describe pro-atherogenic aberrations of apoptosis, proliferation and cell adhesion in all three cell physiologically relevant vascular cell types, namely in macrophages, vascular smooth muscle cells and endothelial cells. We also demonstrate how, mechanistically, ADAM17 executes its athero-protective function: we found that the release of TNFR2 and of TNFα from the cell membrane was impaired in *Adam17*-deficient cells. At the same time the pool of membrane-resident TNFR2 and membrane-resident TNFα were increased in *Adam17*-deficient cells, coinciding with increased TNFR2 pathway signaling and impaired apoptosis, increased proliferation rates of macrophages and vascular smooth muscle cells. Because knocking down *Tnfr2* in *Adam17*-deficient macrophages or SMCs restored levels of apoptosis and cell proliferation back to wild-type levels, we conclude that the control of TNFR2 signaling is an important effector pathway for ADAM17 in protecting from atherosclerosis (Figure 93) [130].

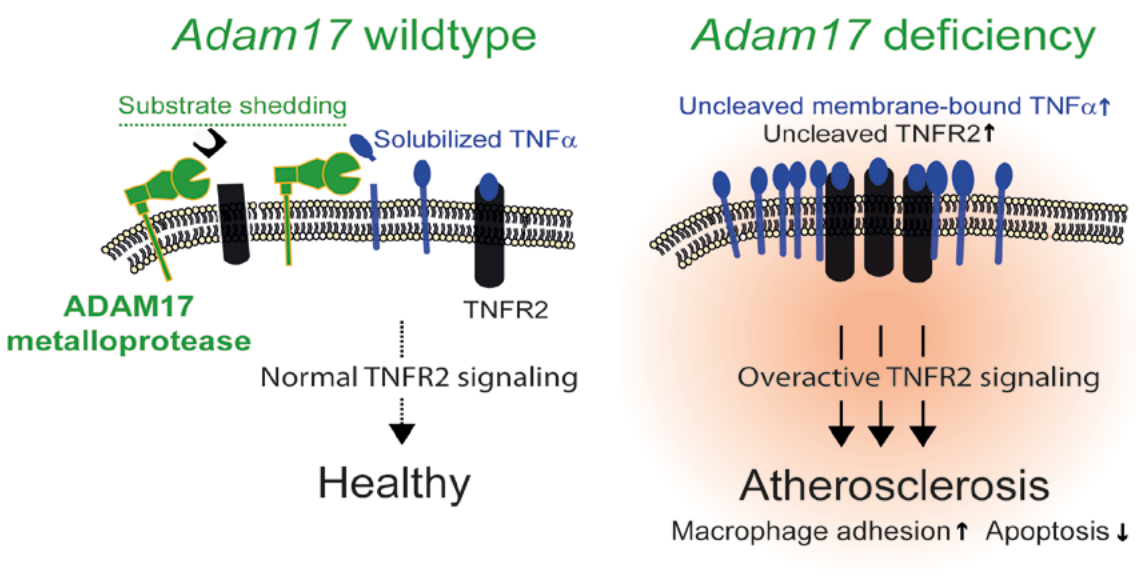

FIGURE 93: Role of ADAM17 in atherosclerosis development [130].

4.3.1 *Adam17 and atherosclerosis*

Since *Adam17* knockout (*Adam17*$^{\Delta Zn/\Delta Zn}$) mice are not viable and die within several hours after birth having severe epithelial abnormalities [131], the direct effect of *Adam17*-deficiency on atherosclerosis development has not been investigated so far. To overcome the limitations of existing mouse models, Chalaris et al. generated hypomorphic *Adam17* mice, which are partially deficient for *Adam17* (*Adam17*$^{ex/ex}$) and have barely detectable levels of ADAM17 in all tissues [132]. To induce atherosclerosis, we backcrossed hypomorphic *Adam17* mice (Adam17$^{ex/ex}$) on the *Ldl* receptor deficient background.

Atherosclerosis studies revealed higher atherosclerotic lesions in both male and female hypomorphic *Adam17*$^{ex/ex}$.*Ldlr*$^{-/-}$ compared to wild-type *Adam17*$^{wt/wt}$.*Ldl*$^{-/-}$ mice. These findings corresponded with the data from a previous study, demonstrating that reduced ADAM17 activity was associated with increased atherosclerosis at the aortic root in an F2 intercross of atherosclerosis-susceptible C57BL/6 and atherosclerosis resistant FVB mice [105]. Although several mouse models with tissue-specific *Adam17*-deficiency have been established [133-138], our study is the first to investigate the direct role of *Adam17*-deficiency in atherosclerosis giving evidence for an atheroprotective effect of ADAM17. The observed intense thickening of the aortic valves in Adam17$^{ex/ex}$.*Ldlr*$^{-/-}$ mice confirmed previous published data [138]. Additionally, the eye, skin and hair defects observed in *Adam17*-deficient mice, previously described by Chalaris et al., were likely caused due to the ADAM17 disturbed release of the heparin-binding epidermal growth factor (HB-EGF) and TGF-α shedding [131].

Until now, the direct effect of *Adam17*-deficiency in atherosclerosis and atherosclerosis development has not been investigated yet. Canault et al. describe an increase of atherosclerotic lesions in an *ApoE*$^{-/-}$ mouse model, where the lesions contain ADAM17-positive cells. But given the fact that *Adam17* is highly expressed in macrophages, and that macrophages are present in atherosclerotic lesions, this is not unexpected [219]. Beyond correlative evidence, the study by Caunault et al, however, did not investigate a causal role of Adam17 in atherosclerosis, for

example, by loss-of-function experiments. Satoh and colleagues demonstrated that both TACE and TNFα were highly expressed in patients with myocarditis [220] and also in peripheral blood mononuclear cells in patients with advanced congestive heart failure [221]. Furthermore, they showed in their studies evidence of increased ADAM17 and TNFα expression in areas of ruptured coronary plaques in patients with myocardial infarction [222]. Due to its well established molecular function in releasing proinflammatory TNFα [120, 131], a protective role of ADAM17 in atherosclerosis might at first seem counterintuitive and this atheroprotective effect seemed somehow to be contradictory to its well-established role in promoting inflammation and cell adhesion [120, 131, 173-175]. However, ADAM17 is also involved in potentially atheroprotective cell functions such as shedding of the receptors for TNFα and of cell adhesion molecules. Given this overall promiscuous nature, it was not obvious before our present study whether the depletion of *Adam17* would push the balance toward a pro- or an antiatherogenic net effect. Our current study corroborates and extends our previous work where we have identified *Adam17* as a candidate gene of atheroprotection using expression quantitative trait locus mapping in mice [105]. In this study, we elucidated the possible mode of action of *Adam17*-deficiency and we provide mechanistic insight into how ADAM17 executes this role [130].

4.3.2 *Adam17-deficiency reduces TNFR1, TNFR2 and TNF-α release in plasma and cells of Adam17$^{ex/ex}$.Ldlr$^{-/-}$ mice*

Adam17-deficiency resulted predominantly in a significant reduction of sTNFR1 and sTNFR2 release in plasma of mice and the supernatant of bone marrow-derived macrophages. Furthermore, the proinflammatory substrates sIL-6R and sTNF-α were also reduced in plasma of the atherosclerosis-prone *Adam17*-deficient mice whereas other ADAM17 substrates were not differentially released. The EGFR- and TNFα pathways are 2 major signaling pathways that are under the control of ADAM17 [120, 131, 223]. Interestingly, in this mouse model, mainly the substrates (TNFR1, TNFR2 and TNFα) of the TNF-α pathway are in this mouse model significantly reduced released. Reduced shedding of TNFR1 and TNFR2 as well as TNFα hints to a role of TNFα signaling in atherogenesis in *Adam17*$^{ex/ex}$*.Ldlr*$^{-/-}$ mice. TNFR1 is ubiquitously expressed and primarily localized to the Golgi apparatus with little surface expression, whereas TNFR2 is predominantly expressed on the cell surface of endothelial and hematopoietic cells [224, 225]. Furthermore, TNFR1 is activated by membrane-bound as well as soluble TNFα, while TNFR2 becomes activated only through membrane-bound TNFα [177]. Protein studies reinforced the hypothesis of enhanced TNFR2 signaling, as higher amounts of TNFα and TNFR2 were detected in whole cell lysate and cell surface proteins of *Adam17*-deficient mice. The enhanced activation of Bmx/Etk, a signaling molecule of the TNFR2 pathway, confirmed this hypothesis even more.

To investigate, if the differences in TNFR1 and TNFR2 levels were due to differential transcriptional regulation, we quantified *Tnfr1* and *Tnfr2* mRNA abundance in *Adam17*-deficient primary macrophages using qPCRs. Since we detected no significant differences in receptor mRNA levels between wildtype and mutant, we conclude that the differences in TNFR1 vs TNFR2 protein levels are not controlled at the level of mRNA expression but might be post-transcriptionally regulated. Given that the rates of TNFR1 and TNFR2 protein delivery to the cell membrane and the rates of TNFR1 and TNFR2 recycling and degradation (via the lysosome) have not been quantified in direct comparison to each other in the literature, we can only speculate about the exact underlying divergence between TNFR1 and TNFR2: It is known that membrane-availability of

TNFR1 is mainly controlled through internalization and subsequent degradation but not through shedding [226]. One can thus speculate that in the *Adam17* hypomorphic mutants, the rate of new TNFR1 production meets equal rates of TNFR1 internalization/degradation, resulting in unchanged net levels of cellular TNFR1 protein despite reduced ADAM17-dependent shedding of TNFR1. On the contrary, membrane-availability of TNFR2 is rather controlled through constitutive shedding [227], which is significantly down-regulated in our *Adam17* hypomorphic mutants. Additionally, Fischer et al have shown that non-cleavable membrane-bound TNFα stabilized membrane protein expression of TNFR2 [227]. Since membrane-bound TNFα is increased in *Adam17*-depleted cells, it is likely that both, the reduced TNFR2 release in cells lacking ADAM17 activity and stabilization through membrane TNFα, might result in increased net levels of TNFR2 protein. Until today, the molecular mechanism of how membrane-bound TNFα stabilizes TNFR2 is unknown and further work will be required to address this aspect.

How does our description of an antiatherogenic function of ADAM17 relate to the literature on the role of TNFα signaling in atherosclerosis? Overall, apart from the onset of atherosclerotic lesions, where TNFα is thought to delay lesion formation via impairing cholesterol accumulation in macrophages [228], the net effect of TNFα signaling seems to promote disease [229-233]. This conclusion based on the studies of atherosclerotic lesions sizes in TNFα-knockout mice and the observation of decreased vascular endothelial cell adhesiveness and decreased inflammatory factor expression in atherosclerotic plaques. In these earlier studies, proatherogenic effects of TNFα were, however, related mostly to the fact that soluble TNFα promotes classical inflammatory TNFR1 signaling [130].

In our present work, we extend these earlier reports by focusing on the membrane-resident mTNFα and TNFR2, which were particularly increased in the absence of ADAM17, likely because of reduced shedding. Previous work had further suggested that mTNFα stabilized membrane protein expression of TNFR2 [227], thus potentially explaining why the levels of membrane TNFR2 but not TNFR1 were higher in the Adam17 mutants. Because it is TNFR2 signaling and not TNFR1 signaling, that is preferentially activated by mTNFα [177], an overactivation of TNFR2 signaling through both higher mTNFα and mTNFR2 protein might, thus, promote atherosclerosis. Consistently, a study by Chandrasekharan et al [234] has shown that *Tnfr2*-deficient mice develop less atherosclerosis on the ApoE$^{-/-}$ background. Together, the activation of TNFR2 signaling seems to be a plausible effector mechanism promoting atherosclerosis in the *Adam17* knockout mice [130].

4.3.3 *Enhanced TNFR2 signaling in hypomorphic Adam17$^{ex/ex}$.Ldlr$^{-/-}$ mice*

TNFR2 signaling has previously been associated with an anti-apoptotic and proliferative cellular response [182] as well as with increased adhesion via the induction of ICAM1 expression in different mouse models [183, 184]. It is those anti-apoptotic, proliferative and pro-adhesive responses that we also see in our *in vitro* and *in vivo* analysis of the *Adam17* mutant: the direction of effects is identical in the *Adam17*$^{ex/ex}$ knockout macrophages, and in the *Adam17* siRNA-treated macrophages, vascular smooth muscle cells and endothelial cells.

Notably, all cell functions that we investigated were restored to normal when depleting TNFR2 in *Adam17*-deficient cells, further supporting an important role of this receptor when *Adam17* is depleted. On the contrary, the observed effects in our *in vitro* and *in vivo* experiments contrasted the functions classically associated with TNFR1 signaling, such as TNFR1-dependent induction of inflammation and apoptosis and reduction of proliferation [235-237], thus further speaking

against TNFR1 as a major effector in our *Adam17* hypomorphic mouse model. Consistent with the results from this study, TNFα and TNFR2 deficiency also led to significantly decreased atherosclerosis in other mouse models [229, 230, 232-234]. TNFα and TNFR2 signaling contribute to the development of atherosclerosis by enhancing cellular processes like proliferation and apoptosis, which are key regulators of atherogenesis [1]. Both processes are highly regulated in *Adam17*$^{ex/ex}$.*Ldlr*$^{-/-}$ mice as was already shown by gene set enrichment and pathway analysis. Increased TNFR2 signaling was already associated with increased cell proliferation [238, 239] and cell survival [130, 240, 241].

In this context, the function of ADAM17 in the vasculature is likely pleiotropic and cell context-dependent and its effect on TNF-signaling is only one of multiple facets of the protease: ADAM17 enzyme activity and substrate specificity are selective and regulated. Similarly complex, the role of proliferation and apoptosis in atherosclerosis is multi-faceted, and inhibition of cellular proliferation and induction of apoptosis, such as ascribed here to ADAM17 function, is not necessarily atheroprotective under all circumstances. For instance, apoptosis in macrophages might indeed attenuate early lesion progression, but can at later stages also induce secondary inflammation and plaque rupture [13] and apoptosis in vascular endothelial cells may be pro-atherogenic [242]. Summarizing, the cell type-specific ADAM17 functions will have to be dissected one by one, and their individual effects integrated, to understand how the net atheroprotective output is achieved. It is likely that also other ADAM17 substrates will modulate atherosclerosis, including adhesion factors that are directly or indirectly shed by ADAM17. We do not claim that control of TNFR2 activity in macrophages and VSMCs is the single effector mechanism for ADAM17's role in protection from atherosclerosis. We also do not claim that TNFR1 has no function at all for *Adam17's* role in atherosclerosis. Reasons to be cautious are data from existing knockouts of other ADAM17 substrates, such as ICAM-1 [243], VCAM-1 [166], CX3CL1 (fractalkine) [153] or IL-1 [244] depletion, which show decreased atherosclerosis. While we did not see consistent changes in the shedding of these substrates, we do note that not all known substrates of ADAM17 have been tested in our study. Thus, it is possible that overall small but coordinated changes in a variety of ADAM17 substrates, other than TNFR2, may add up to an atheroprotective function [130].

4.3.4 *ADAM17 as a therapeutic target.*

Over the past years, ADAM17 has become a therapeutic target in several cancers and inflammatory diseases [245-251]. Here, therapeutic approaches aim to inhibit ADAM17 activity, and several agents are already used in different preclinical models and clinical trials [252]. Results of the current study now show that a general inhibition of ADAM17 may lead to an upregulation of atherosclerosis-associated cell functions by promoting TNFR2 signaling. Similarly, agonists of TNFR2 are considered for depleting insulin-specific autoreactive T cells in type 1 diabetes mellitus treatment [252-254], and our results suggest that an increased atherosclerosis risk might need to be considered as a side effect as well. Although a recent meta-analysis has shown that TNFα inhibition leads to a significant reduction of hard cardiovascular endpoints (relative risk 0.7; $p = 0.005$) in patients with rheumatoid arthritis [255] the exact mechanisms of ADAM17 in the vascular wall of humans and in the pathogenesis of human atherosclerosis remains to be determined [130].

4.4 *The ADAM17 metalloproteinase maintains arterial elasticity*

In the second part of this PhD thesis we found that ADAM17, which is usually regarded as a proinflammatory enzyme, has disease-protective properties in atherosclerosis. In this role, ADAM17 curbs the amount of membrane-bound (yet signaling-active) TNFR2 receptor, in order to avoid overactivation of pro-atherosclerotic TNFα/TNFR2-dependent adhesive and proliferative cellular properties.

In the third part of this PhD thesis we investigated whether mouse *Adam17* was generally involved in regulating arterial wall integrity. Here, we report that ADAM17 exerts another role in vascular biology, namely by functioning as rheostat of arterial wall elasticity. We focused on the brachiocephalic artery (BCA), and we showed that the role in maintaining arterial wall integrity in the BCA is uncoupled from ADAM17-dependent atherosclerotic plaque development. We found no significant differences in plaque size formation between *Adam17* mutants and controls in the brachiocephalic artery.

Employing three complementary genetic mouse mutant models (the hypomorphic [*Adam17*$^{ex/ex}$.*Ldlr*$^{-/-}$] mutant, a conditional myeloid knockout [LysM^{Cre}ADAM17$^{fl/fl}$] and a conditional endothelial knockout [Bmx^{Cre}ADAM17$^{fl/fl}$]), quantifying extracellular matrix (ECM) properties and transcriptionally profiling aortic tissue, we reveal arterial dilation and ECM changes in the absence of *Adam17*. This phenotypic switch was reminiscent of early-phase arterial aneurysm onset. Our data indicate a function of ADAM17 in maintaining a proper elastin network (but not collagen fiber integrity) in arteries.

In the parallel study, neither endothelial (LysM^{Cre}ADAM17$^{fl/fl}$) nor myeloid (Bmx^{Cre}ADAM17$^{fl/fl}$) *Adam17*-depletion showed arterial wall dilation [146, 185]. Only hypomorphic *Adam17*-deficient mutant mice showed approximately up to 15 % increased aortic root mean circumference in male and female mice (*Adam17*$^{ex/ex}$.*Ldlr*$^{-/-}$). Arteria dilated because *Adam17* was required in cells other than macrophages or endothelial cells alone. So it is possible that *ADAM17* executes its role in maintaining the elasticity of the arterial wall through vascular smooth muscle cells (SMCs) or fibroblasts. The elastin network in arteries is deposited largely by vascular smooth muscle cells, which accounts for arterial wall resilience and non-linear elasticity, protects the vessel from rupture and minimizes energy loss through elastic recoiling during cycles of arterial inflation and deflation [144, 146].

4.4.1 *The protective effect of ADAM17 metalloproteinase in arterial elasticity*

The protective role of ADAM17 is corroborated by independent genetic work showing that increased ADAM17 activity reduced coronary arteriole dilation [256] and that conditional deletion of *Adam17* in cardiomyocytes increased left ventricular dilation in pressure-overload models [257]. How ADAM17 molecularly controls arterial elasticity remains open. Our analysis suggested a mixed extracellular matrix-elasticity phenotype, whereby elastin fiber straightened while fiber integrity, number and thickness were unaltered. Collagen fiber composition in the intima and the adventitia of the brachiocephalic artery was unaffected in *Adam17* hypomorphic mice. An interpretation is that reduced fiber elasticity leads to radial dilation of the vessel coinciding with peripheral stretching of the arterial wall [145, 258].

For controlling arterial wall elasticity, TNFα/TNFR signaling, which is an ADAM17 substrate and de-repressed in the *Adam17* mutants (part two of this PhD thesis), could be one the many primary effectors. Indeed, TNFα was found to be anti-elastogenic by increasing the expression of metalloproteinases, which are elastolytic and more abundant and active in human aneurysms [259, 260]. Furthermore, TNFα was found to impair the expression of tropoelastin [261] and enzymes like lysyl oxidase, which cross-links elastin aggregates to mature fibers [262]. To get first insights into how ADAM17 controlled arterial wall integrity, we investigated which genes were differentially expressed in aortic tissue of *Adam17*$^{ex/ex}$.*Ldlr*$^{-/-}$ hypomorphic mutants. mRNA microarray profiling revealed not only atherosclerosis regulators among the top differential abundant transcripts, but also a number of cytoskeletal contractility regulators and factors required for ECM elastogenesis. We detected that the expression of selected metalloproteinases (MMP3/MMP12) was increased while elastin abundance decreased. It will be important to dissect whether and how TNFα and other ADAM17 substrates impact the activity of elastin-regulating factors (such as *emilins* and *fibulins*) and of actomyosin-contractility regulators in smooth muscle cells, mutations in both of which are known genetic determinants also in human aneurysmal syndromes [263, 264]. It has to be said, however, that these observations are only of correlative nature, and that we do not know whether any changes in these genes and ECM-regulators are causal for arterial widening or just the consequence of alterations in Adam17-dependent signaling [146].

Nevertheless, our observations pertain to a specialized and less well-studied function of ADAM17. Given that previous correlative studies on ADAM17 in aneurysm development have been contradictory [140, 141] we think that our findings are of relevance for a broad audience, including biomedical researchers of cardiovascular physiology and disease, as well as cellular and molecular biologists studying receptor-mediated signaling, ECM and cytoskeletal properties and their regulation by enzymes in the context of biomechanical forces.

Although it goes beyond the scope of this study to identify the molecular effectors of how ADAM17 maintains arterial wall elasticity to withstand radial dilation and allow arterial recoil, our mouse model and our candidates stemming from transcriptional profiling may represent a valuable starting point for future mechanistic research. In particular, our experimental system for spontaneous aneurysm development in mouse (*Adam17*$^{ex/ex}$.*Ldlr*$^{-/-}$) may be interesting for the community, as it does not require intravital operations or chemical inducers to trigger aneurysm onset.

In a medically relevant context, ADAM17 inhibitors have already been tested in clinical trials, but have so far failed to pass phase II for various reasons. If ADAM17 inhibitors are administered non-topically, in particular regarding the long-term treatment of cancers or other inflammatory diseases, our study indicates that one should be prepared to monitor side effects in form of artery wall destabilization and aneurysms [146].

Bibliography

[1] Lusis, A.J., *Atherosclerosis.* Nature, 2000. **407**(6801): p. 233-41.

[2] Yuan, C.C., et al., *5′ Nuclease assays for the loci CCR5-+/Delta32, CCR2-V64I, and SDF1-G801A related to pathogenesis of AIDS.* Clin Chem, 2000. **46**(1): p. 24-30.

[3] Lusis, A.J., R. Mar, and P. Pajukanta, *Genetics of atherosclerosis.* Annu Rev Genomics Hum Genet, 2004. **5**: p. 189-218.

[4] Olson, E.N. (2015), Preface. In H. Wang and C. Patterson (Ed.), *Atherosclerosis: Risks, Mechanisms, and Therapies* (p. xvii). Hoboken, New Jersey: Wiley-Blackwell.

[5] Badimon, L., T. Padro, and G. Vilahur, *Atherosclerosis, platelets and thrombosis in acute ischaemic heart disease.* Eur Heart J Acute Cardiovasc Care, 2012. **1**(1): p. 60-74.

[6] Mozaffarian, D., et al., *Heart disease and stroke statistics-2015 update: a report from the american heart association.* Circulation, 2015. **131**(4): p. e29-e322.

[7] Roth, G.A., et al., *Global, Regional, and National Burden of Cardiovascular Diseases for 10 Causes, 1990 to 2015.* J Am Coll Cardiol, 2017. **70**(1): p. 1-25.

[8] *World Health Organisation (WHO) 2017, Fact sheet: Cardiovascular diseases (CVDs), viewed 30.12.2017.* Available from: http://www.who.int/mediacentre/factsheets/fs317/en/.

[9] Townsend, N., et al., *Cardiovascular disease in Europe 2015: epidemiological update.* Eur Heart J, 2015. **36**(40): p. 2673-4.

[10] Townsend, N., et al., *Cardiovascular disease in Europe: epidemiological update 2016.* Eur Heart J, 2016.

[11] Wilkins, E., et al., *European Cardiovascular Disease Statistics 2017. European Heart Network, Brussels.* 2017.

[12] *Federal Statistical Office (Destatis), cases of death in 2015, viewed 29.12.2017.* Available from: https://www.destatis.de/EN/FactsFigures/SocietyState/Health/CausesDeath/CausesDeath.html.

[13] Moore, K.J. and I. Tabas, *Macrophages in the pathogenesis of atherosclerosis.* Cell, 2011. **145**(3): p. 341-55.

[14] Ross, R., J. Glomset, and L. Harker, *Response to injury and atherogenesis.* Am J Pathol, 1977. **86**(3): p. 675-84.

[15] Libby, P., P.M. Ridker, and G.K. Hansson, *Progress and challenges in translating the biology of atherosclerosis.* Nature, 2011. **473**(7347): p. 317-25.

[16] Kingwell, B. and P. Boutouyrie, *Genetic influences on the arterial wall.* Clin Exp Pharmacol Physiol, 2007. **34**(7): p. 652-7.

[17] Haust, M.D., *Arterial endothelium and its potentials.* Adv Exp Med Biol, 1977. **82**: p. 34-51.

[18] Hansson, G.K. and A. Hermansson, *The immune system in atherosclerosis.* Nat Immunol, 2011. **12**(3): p. 204-12.

[19] Skalen, K., et al., *Subendothelial retention of atherogenic lipoproteins in early atherosclerosis.* Nature, 2002. **417**(6890): p. 750-4.

[20] Cyrus, T., et al., *Disruption of the 12/15-lipoxygenase gene diminishes atherosclerosis in apo E-deficient mice.* J Clin Invest, 1999. **103**(11): p. 1597-604.

[21] Esterbauer, H., et al., *Role of vitamin E in preventing the oxidation of low-density lipoprotein.* Am J Clin Nutr, 1991. **53**(1 Suppl): p. 314S-321S.

[22] Esterbauer, H., et al., *Effect of antioxidants on oxidative modification of LDL.* Ann Med, 1991. **23**(5): p. 573-81.

[23] Furchgott, R.F., *Introduction to EDRF research.* J Cardiovasc Pharmacol, 1993. **22 Suppl 7**: p. S1-2.

[24] Vanhoutte, P.M., et al., *Endothelial dysfunction and vascular disease.* Acta Physiol (Oxf), 2009. **196**(2): p. 193-222.

[25] Libby, P., *Inflammation in atherosclerosis.* Nature, 2002. **420**(6917): p. 868-74.

[26] Libby, P. and P.M. Ridker, *Inflammation and atherothrombosis: from population biology and bench research to clinical practice.* Journal of the American College of Cardiology, 2006. **48**(9s1): p. A33-A46.

[27] Singh, R.B., et al., *Pathogenesis of atherosclerosis: A multifactorial process.* Exp Clin Cardiol, 2002. **7**(1): p. 40-53.

[28] Libby, P., P.M. Ridker, and A. Maseri, *Inflammation and atherosclerosis.* Circulation, 2002. **105**(9): p. 1135-43.

[29] Mach, F., *The role of chemokines in atherosclerosis.* Curr Atheroscler Rep, 2001. **3**(3): p. 243-51.

[30] Goldstein, J.L., et al., *Binding site on macrophages that mediates uptake and degradation of acetylated low density lipoprotein, producing massive cholesterol deposition.* Proc Natl Acad Sci U S A, 1979. **76**(1): p. 333-7.

[31] Brown, M.S. and J.L. Goldstein, *Lipoprotein metabolism in the macrophage: implications for cholesterol deposition in atherosclerosis.* Annu Rev Biochem, 1983. **52**: p. 223-61.

[32] Zernecke, A., E. Shagdarsuren, and C. Weber, *Chemokines in atherosclerosis: an update.* Arterioscler Thromb Vasc Biol, 2008. **28**(11): p. 1897-908.

[33] Weber, C. and H. Noels, *Atherosclerosis: current pathogenesis and therapeutic options.* Nat Med, 2011. **17**(11): p. 1410-22.

[34] Raines, E.W. and R. Ross, *Smooth muscle cells and the pathogenesis of the lesions of atherosclerosis.* Br Heart J, 1993. **69**(1 Suppl): p. S30-7.

[35] Owens, G.K., S.M. Vernon, and C.S. Madsen, *Molecular regulation of smooth muscle cell differentiation.* J Hypertens Suppl, 1996. **14**(5): p. S55-64.

[36] Libby, P., et al., *Production of platelet-derived growth factor-like mitogen by smooth-muscle cells from human atheroma.* N Engl J Med, 1988. **318**(23): p. 1493-8.

[37] Palombo, D., et al., *Matrix metalloproteinases. Their role in degenerative chronic diseases of abdominal aorta.* J Cardiovasc Surg (Torino), 1999. **40**(2): p. 257-60.

[38] Lafont, A. and P. Libby, *The smooth muscle cell: Sinner or saint in restenosis and the acute coronary syndromes?* Journal of the American College of Cardiology, 1998. **32**(1): p. 283-285.

[39] Schwartz, S.M., R. Virmani, and M.E. Rosenfeld, *The good smooth muscle cells in atherosclerosis.* Curr Atheroscler Rep, 2000. **2**(5): p. 422-9.

[40] Fuster, V., J.J. Badimon, and L. Badimon, *Clinical-pathological correlations of coronary disease progression and regression.* Circulation, 1992. **86**(6 Suppl): p. III1-11.

[41] Casas, J.P., et al., *Investigating the genetic determinants of cardiovascular disease using candidate genes and meta-analysis of association studies.* Ann Hum Genet, 2006. **70**(Pt 2): p. 145-69.

[42] Assmann, G., H. Funke, and H. Schriewer, *The relationship of HDL-apolipoprotein A-I and HDL-Cholesterol to risk factors of coronary heart disease: initial results of the prospective epidemiological study in company employees in Westfalia.* J Clin Chem Clin Biochem, 1982. **20**(5): p. 287-9.

[43] Tuomilehto, J., K. Kuulasmaa, and J. Torppa, *WHO MONICA Project: geographic variation in mortality from cardiovascular diseases. Baseline data on selected population characteristics and cardiovascular mortality.* World Health Stat Q, 1987. **40**(2): p. 171-84.

[44] Assmann, G., et al., *Assessing risk of myocardial infarction and stroke: new data from the Prospective Cardiovascular Munster (PROCAM) study.* Eur J Clin Invest, 2007. **37**(12): p. 925-32.

[45] Gohlke, H., et al., *CARRISMA: a new tool to improve risk stratification and guidance of patients in cardiovascular risk management in primary prevention.* Eur J Cardiovasc Prev Rehabil, 2007. **14**(1): p. 141-8.

[46] D'Agostino, R.B., Sr., et al., *General cardiovascular risk profile for use in primary care: the Framingham Heart Study.* Circulation, 2008. **117**(6): p. 743-53.

[47] Boomsma, D., A. Busjahn, and L. Peltonen, *Classical twin studies and beyond.* Nat Rev Genet, 2002. **3**(11): p. 872-82.

[48] Austin, M.A., et al., *Risk factors for coronary heart disease in adult female twins. Genetic heritability and shared environmental influences.* Am J Epidemiol, 1987. **125**(2): p. 308-18.

[49] McIlhany, M.L., J.W. Shaffer, and E.A. Hines, Jr., *The heritability of blood pressure: an investigation of 200 pairs of twins using the cold pressor test.* Johns Hopkins Med J, 1975. **136**(2): p. 57-64.

[50] Kyvik, K.O., A. Green, and H. Beck-Nielsen, *Concordance rates of insulin dependent diabetes mellitus: a population based study of young Danish twins.* BMJ, 1995. **311**(7010): p. 913-7.

[51] Colditz, G.A., et al., *A prospective study of parental history of myocardial infarction and coronary artery disease in men.* Am J Cardiol, 1991. **67**(11): p. 933-8.

[52] Lloyd-Jones, D.M., et al., *Parental cardiovascular disease as a risk factor for cardiovascular disease in middle-aged adults: a prospective study of parents and offspring.* JAMA, 2004. **291**(18): p. 2204-11.

[53] Marenberg, M.E., et al., *Genetic susceptibility to death from coronary heart disease in a study of twins.* N Engl J Med, 1994. **330**(15): p. 1041-6.

[54] Zdravkovic, S., et al., *Heritability of death from coronary heart disease: a 36-year follow-up of 20 966 Swedish twins.* J Intern Med, 2002. **252**(3): p. 247-54.

[55] Fischer, M., et al., *Distinct heritable patterns of angiographic coronary artery disease in families with myocardial infarction.* Circulation, 2005. **111**(7): p. 855-62.

[56] Peyser, P.A., et al., *Heritability of coronary artery calcium quantity measured by electron beam computed tomography in asymptomatic adults.* Circulation, 2002. **106**(3): p. 304-8.

[57] O'Donnell, C.J., et al., *Evidence for heritability of abdominal aortic calcific deposits in the Framingham Heart Study.* Circulation, 2002. **106**(3): p. 337-41.

[58] Fox, C.S., et al., *Genetic and environmental contributions to atherosclerosis phenotypes in men and women: heritability of carotid intima-media thickness in the Framingham Heart Study.* Stroke, 2003. **34**(2): p. 397-401.

[59] Brown, M.S. and J.L. Goldstein, *A receptor-mediated pathway for cholesterol homeostasis.* Science, 1986. **232**(4746): p. 34-47.

[60] Biros, E., M. Karan, and J. Golledge, *Genetic variation and atherosclerosis.* Curr Genomics, 2008. **9**(1): p. 29-42.

[61] Lusis, A.J., A.M. Fogelman, and G.C. Fonarow, *Genetic basis of atherosclerosis: part I: new genes and pathways.* Circulation, 2004. **110**(13): p. 1868-73.

[62] Soutar, A.K. and R.P. Naoumova, *Autosomal recessive hypercholesterolemia.* Semin Vasc Med, 2004. **4**(3): p. 241-8.

[63] Schreibman, P.H., D.E. Wilson, and R.A. Arky, *Familial type IV hyperlipoproteinemia.* N Engl J Med, 1969. **281**(18): p. 981-5.

[64] Marcil, M., et al., *Severe familial HDL deficiency in French-Canadian kindreds. Clinical, biochemical, and molecular characterization.* Arterioscler Thromb Vasc Biol, 1995. **15**(8): p. 1015-24.

[65] Mani, A., et al., *LRP6 mutation in a family with early coronary disease and metabolic risk factors.* Science, 2007. **315**(5816): p. 1278-82.

[66] Stitziel, N.O. and C.A. MacRae, *A clinical approach to inherited premature coronary artery disease.* Circ Cardiovasc Genet, 2014. **7**(4): p. 558-64.

[67] Wang, L., et al., *Mutation of MEF2A in an inherited disorder with features of coronary artery disease.* Science, 2003. **302**(5650): p. 1578-81.

[68] Helgadottir, A., et al., *The gene encoding 5-lipoxygenase activating protein confers risk of myocardial infarction and stroke.* Nat Genet, 2004. **36**(3): p. 233-9.

[69] Helgadottir, A., et al., *A variant of the gene encoding leukotriene A4 hydrolase confers ethnicity-specific risk of myocardial infarction.* Nat Genet, 2006. **38**(1): p. 68-74.

[70] Oram, J.F., *HDL apolipoproteins and ABCA1: partners in the removal of excess cellular cholesterol.* Arterioscler Thromb Vasc Biol, 2003. **23**(5): p. 720-7.

[71] International HapMap, C., *A haplotype map of the human genome.* Nature, 2005. **437**(7063): p. 1299-320.

[72] Clancy, S., *Genetic recombination.* Nature Education, 2008. **1**(1): p. 40.

[73] Genomes Project, C., et al., *A global reference for human genetic variation.* Nature, 2015. **526**(7571): p. 68-74.

[74] Wang, W.Y., et al., *Genome-wide association studies: theoretical and practical concerns.* Nat Rev Genet, 2005. **6**(2): p. 109-18.

[75] Matsuzaki, H., et al., *Genotyping over 100,000 SNPs on a pair of oligonucleotide arrays.* Nat Methods, 2004. **1**(2): p. 109-11.

[76] Ozaki, K., et al., *Functional SNPs in the lymphotoxin-alpha gene that are associated with susceptibility to myocardial infarction.* Nat Genet, 2002. **32**(4): p. 650-4.

[77] Consortium, C.A.D., et al., *Large-scale association analysis identifies new risk loci for coronary artery disease.* Nat Genet, 2013. **45**(1): p. 25-33.

[78] Nikpay, M., et al., *A comprehensive 1,000 Genomes-based genome-wide association meta-analysis of coronary artery disease.* Nat Genet, 2015. **47**(10): p. 1121-30.

[79] Myocardial Infarction, G., et al., *Coding Variation in ANGPTL4, LPL, and SVEP1 and the Risk of Coronary Disease.* N Engl J Med, 2016. **374**(12): p. 1134-44.

[80] Webb, T.R., et al., *Systematic Evaluation of Pleiotropy Identifies 6 Further Loci Associated With Coronary Artery Disease.* J Am Coll Cardiol, 2017. **69**(7): p. 823-836.

[81] Helgadottir, A., et al., *The same sequence variant on 9p21 associates with myocardial infarction, abdominal aortic aneurysm and intracranial aneurysm.* Nat Genet, 2008. **40**(2): p. 217-24.

[82] Samani, N.J., et al., *Genomewide association analysis of coronary artery disease.* N Engl J Med, 2007. **357**(5): p. 443-53.

[83] McPherson, R., et al., *A common allele on chromosome 9 associated with coronary heart disease.* Science, 2007. **316**(5830): p. 1488-91.

[84] Holdt, L.M., et al., *ANRIL expression is associated with atherosclerosis risk at chromosome 9p21.* Arterioscler Thromb Vasc Biol, 2010. **30**(3): p. 620-7.

[85] Holdt, L.M., et al., *Alu elements in ANRIL non-coding RNA at chromosome 9p21 modulate atherogenic cell functions through trans-regulation of gene networks.* PLoS Genet, 2013. **9**(7): p. e1003588.

[86] McPherson, R. and A. Tybjaerg-Hansen, *Genetics of Coronary Artery Disease.* Circ Res, 2016. **118**(4): p. 564-78.

[87] Lieb, W. and R.S. Vasan, *Genetics of coronary artery disease.* Circulation, 2013. **128**(10): p. 1131-8.

[88] Beck, J.A., et al., *Genealogies of mouse inbred strains.* Nat Genet, 2000. **24**(1): p. 23-5.

[89] Darvasi, A., *Experimental strategies for the genetic dissection of complex traits in animal models.* Nat Genet, 1998. **18**(1): p. 19-24.

[90] Smith, J., *Quantitative trait locus mapping for atherosclerosis susceptibility.* Curr Opin Lipidol, 2003. **14**(5): p. 499-504.

[91] Paigen, B., et al., *Variation in susceptibility to atherosclerosis among inbred strains of mice.* Atherosclerosis, 1985. **57**(1): p. 65-73.

[92] Nishina, P.M., J. Verstuyft, and B. Paigen, *Synthetic low and high fat diets for the study of atherosclerosis in the mouse.* J Lipid Res, 1990. **31**(5): p. 859-69.

[93] Plump, A.S., et al., *Severe hypercholesterolemia and atherosclerosis in apolipoprotein E-deficient mice created by homologous recombination in ES cells.* Cell, 1992. **71**(2): p. 343-53.

[94] Piedrahita, J.A., L. Gillespie, and N. Maeda, *Production of chimeric hamsters by aggregation of eight-cell embryos.* Biol Reprod, 1992. **47**(3): p. 347-54.

[95] Ishibashi, S., et al., *Hypercholesterolemia in low density lipoprotein receptor knockout mice and its reversal by adenovirus-mediated gene delivery.* J Clin Invest, 1993. **92**(2): p. 883-93.

[96] Ishibashi, S., et al., *The two-receptor model of lipoprotein clearance: tests of the hypothesis in "knockout" mice lacking the low density lipoprotein receptor, apolipoprotein E, or both proteins.* Proc Natl Acad Sci U S A, 1994. **91**(10): p. 4431-5.

[97] Bonthu, S., et al., *Atherosclerosis, vascular remodeling, and impairment of endothelium-dependent relaxation in genetically altered hyperlipidemic mice.* Arterioscler Thromb Vasc Biol, 1997. **17**(11): p. 2333-40.

[98] Stylianou, I.M., et al., *Genetic basis of atherosclerosis: insights from mice and humans.* Circ Res, 2012. **110**(2): p. 337-55.

[99] Teupser, D., A.D. Persky, and J.L. Breslow, *Induction of atherosclerosis by low-fat, semisynthetic diets in LDL receptor-deficient C57BL/6J and FVB/NJ mice: comparison of lesions of the aortic root, brachiocephalic artery, and whole aorta (en face measurement).* Arterioscler Thromb Vasc Biol, 2003. **23**(10): p. 1907-13.

[100] Vignal, A., et al., *A review on SNP and other types of molecular markers and their use in animal genetics.* Genet Sel Evol, 2002. **34**(3): p. 275-305.

[101] Gupta, P.K. and S. Rustgi, *Molecular markers from the transcribed/expressed region of the genome in higher plants.* Funct Integr Genomics, 2004. **4**(3): p. 139-62.

[102] Casa, A.M., et al., *The MITE family heartbreaker (Hbr): molecular markers in maize.* Proc Natl Acad Sci U S A, 2000. **97**(18): p. 10083-9.

[103] Morton, N.E., *Sequential tests for the detection of linkage.* Am J Hum Genet, 1955. **7**(3): p. 277-318.

[104] Teupser, D., et al., *Atherosclerosis quantitative trait loci are sex- and lineage-dependent in an intercross of C57BL/6 and FVB/N low-density lipoprotein receptor$^{-/-}$ mice.* Proc Natl Acad Sci U S A, 2006. **103**(1): p. 123-8.

[105] Holdt, L.M., et al., *Increased ADAM17 mRNA expression and activity is associated with atherosclerosis resistance in LDL-receptor deficient mice.* Arterioscler Thromb Vasc Biol, 2008. **28**(6): p. 1097-103.

[106] Rawlings, N.D. and A.J. Barrett, *Evolutionary families of metallopeptidases.* Methods Enzymol, 1995. **248**: p. 183-228.

[107] Hooper, N.M., *Families of zinc metalloproteases.* FEBS Lett, 1994. **354**(1): p. 1-6.

[108] Bode, W., F.X. Gomis-Ruth, and W. Stockler, *Astacins, serralysins, snake venom and matrix metalloproteinases exhibit identical zinc-binding environments (HEXXHXXGXXH and Met-turn) and topologies and should be grouped into a common family, the 'metzincins'.* FEBS Lett, 1993. **331**(1-2): p. 134-40.

[109] Stocker, W., et al., *The metzincins--topological and sequential relations between the astacins, adamalysins, serralysins, and matrixins (collagenases) define a superfamily of zinc-peptidases.* Protein Sci, 1995. **4**(5): p. 823-40.

[110] Chang, C. and Z. Werb, *The many faces of metalloproteases: cell growth, invasion, angiogenesis and metastasis.* Trends Cell Biol, 2001. **11**(11): p. S37-43.

[111] Bond, J.S. and R.J. Beynon, *The astacin family of metalloendopeptidases.* Protein Sci, 1995. **4**(7): p. 1247-61.

[112] Park, H.I. and L.J. Ming, *Mechanistic studies of the astacin-like Serratia metalloendopeptidase serralysin: highly active (>2000%) Co(II) and Cu(II) derivatives for further corroboration of a "metallotriad" mechanism.* J Biol Inorg Chem, 2002. **7**(6): p. 600-10.

[113] Bjarnason, J.B. and J.W. Fox, *Snake venom metalloendopeptidases: reprolysins.* Methods Enzymol, 1995. **248**: p. 345-68.

[114] Klein, T. and R. Bischoff, *Active metalloproteases of the A Disintegrin and Metalloprotease (ADAM) family: biological function and structure.* J Proteome Res, 2011. **10**(1): p. 17-33.

[115] Kelwick, R., et al., *The ADAMTS (A Disintegrin and Metalloproteinase with Thrombospondin motifs) family.* Genome Biol, 2015. **16**: p. 113.

[116] Seals, D.F. and S.A. Courtneidge, *The ADAMs family of metalloproteases: multidomain proteins with multiple functions.* Genes Dev, 2003. **17**(1): p. 7-30.

[117] Dreymueller, D., S. Uhlig, and A. Ludwig, *ADAM-family metalloproteinases in lung inflammation: potential therapeutic targets.* Am J Physiol Lung Cell Mol Physiol, 2015. **308**(4): p. L325-43.

[118] White, J.M., *ADAMs: modulators of cell-cell and cell-matrix interactions.* Curr Opin Cell Biol, 2003. **15**(5): p. 598-606.

[119] Blobel, C.P. and J.M. White, *Structure, function and evolutionary relationship of proteins containing a disintegrin domain.* Curr Opin Cell Biol, 1992. **4**(5): p. 760-5.

[120] Black, R.A., et al., *A metalloproteinase disintegrin that releases tumour-necrosis factor-alpha from cells.* Nature, 1997. **385**(6618): p. 729-33.

[121] Gooz, M., *ADAM-17: the enzyme that does it all.* Crit Rev Biochem Mol Biol, 2010. **45**(2): p. 146-69.

[122] Scheller, J., et al., *ADAM17: a molecular switch to control inflammation and tissue regeneration.* Trends Immunol, 2011. **32**(8): p. 380-7.

[123] Gonzales, P.E., et al., *Inhibition of the tumor necrosis factor-alpha-converting enzyme by its pro domain.* J Biol Chem, 2004. **279**(30): p. 31638-45.

[124] Schlondorff, J., J.D. Becherer, and C.P. Blobel, *Intracellular maturation and localization of the tumour necrosis factor alpha convertase (TACE).* Biochem J, 2000. **347 Pt 1**: p. 131-8.

[125] Adrain, C., et al., *Tumor necrosis factor signaling requires iRhom2 to promote trafficking and activation of TACE.* Science, 2012. **335**(6065): p. 225-8.

[126] Koenen, R.R., et al., *Regulated release and functional modulation of junctional adhesion molecule A by disintegrin metalloproteinases.* Blood, 2009. **113**(19): p. 4799-809.

[127] Huang, J., L.C. Bridges, and J.M. White, *Selective modulation of integrin-mediated cell migration by distinct ADAM family members.* Mol Biol Cell, 2005. **16**(10): p. 4982-91.

[128] Edwards, D.R., M.M. Handsley, and C.J. Pennington, *The ADAM metalloproteinases.* Mol Aspects Med, 2008. **29**(5): p. 258-89.

[129] Zheng, X., et al., *ADAM17 promotes breast cancer cell malignant phenotype through EGFR-PI3K-AKT activation.* Cancer Biol Ther, 2009. **8**(11): p. 1045-54.

[130] Nicolaou, A., et al., *Adam17 Deficiency Promotes Atherosclerosis by Enhanced TNFR2 Signaling in Mice.* Arterioscler Thromb Vasc Biol, 2017. **37**(2): p. 247-257.

[131] Peschon, J.J., et al., *An essential role for ectodomain shedding in mammalian development.* Science, 1998. **282**(5392): p. 1281-4.

[132] Chalaris, A., et al., *Critical role of the disintegrin metalloprotease ADAM17 for intestinal inflammation and regeneration in mice.* J Exp Med, 2010. **207**(8): p. 1617-24.

[133] Horiuchi, K., et al., *Cutting edge: TNF-alpha-converting enzyme (TACE/ADAM17) inactivation in mouse myeloid cells prevents lethality from endotoxin shock.* J Immunol, 2007. **179**(5): p. 2686-9.

[134] Gravano, D.M., et al., *ADAM17 deletion in thymic epithelial cells alters aire expression without affecting T cell developmental progression.* PLoS One, 2010. **5**(10): p. e13528.

[135] Horiuchi, K., et al., *Conditional inactivation of TACE by a Sox9 promoter leads to osteoporosis and increased granulopoiesis via dysregulation of IL-17 and G-CSF.* J Immunol, 2009. **182**(4): p. 2093-101.

[136] Driscoll, W.S., et al., *Macrophage ADAM17 deficiency augments CD36-dependent apoptotic cell uptake and the linked anti-inflammatory phenotype.* Circ Res, 2013. **113**(1): p. 52-61.

[137] Weskamp, G., et al., *Pathological neovascularization is reduced by inactivation of ADAM17 in endothelial cells but not in pericytes.* Circ Res, 2010. **106**(5): p. 932-40.

[138] Wilson, C.L., et al., *Endothelial deletion of ADAM17 in mice results in defective remodeling of the semilunar valves and cardiac dysfunction in adults.* Mech Dev, 2013. **130**(4-5): p. 272-89.

[139] Yoda, M., et al., *Systemic overexpression of TNFalpha-converting enzyme does not lead to enhanced shedding activity in vivo.* PLoS One, 2013. **8**(1): p. e54412.

[140] Vorkapic, E., et al., *ADAMTS-1 in abdominal aortic aneurysm.* PLoS One, 2017. **12**(6): p. e0178729.

[141] Li, Y., et al., *Analysis of ADAM17 polymorphisms and susceptibility to sporadic abdominal aortic aneurysm.* Cell Physiol Biochem, 2014. **33**(5): p. 1426-38.

[142] Kaneko, H., et al., *Tumor necrosis factor-alpha converting enzyme is a key mediator of abdominal aortic aneurysm development.* Atherosclerosis, 2011. **218**(2): p. 470-8.

[143] Geng, L., et al., *Elevation of ADAM10, ADAM17, MMP-2 and MMP-9 expression with media degeneration features CaCl2-induced thoracic aortic aneurysm in a rat model.* Exp Mol Pathol, 2010. **89**(1): p. 72-81.

[144] Wagenseil, J.E. and R.P. Mecham, *Vascular extracellular matrix and arterial mechanics.* Physiol Rev, 2009. **89**(3): p. 957-89.

[145] Humphrey, J.D., E.R. Dufresne, and M.A. Schwartz, *Mechanotransduction and extracellular matrix homeostasis.* Nat Rev Mol Cell Biol, 2014. **15**(12): p. 802-12.

[146] Nicolaou, A., et al., *The ADAM17 Metalloproteinase Maintains Arterial Elasticity.* Thromb Haemost, 2018. **118**(1): p. 210-213.

[147] Yuan, Y., et al., *Improvements in Genomic Technologies: Application to Crop Genomics.* Trends Biotechnol, 2017. **35**(6): p. 547-558.

[148] Nicolaou, A., et al., *Quantitative trait locus mapping in mice identifies phospholipase Pla2g12a as novel atherosclerosis modifier.* Atherosclerosis, 2017. **265**: p. 197-206.

[149] Teupser, D., et al., *Effect of macrophage overexpression of murine liver X receptor-alpha (LXR-alpha) on atherosclerosis in LDL-receptor deficient mice.* Arterioscler Thromb Vasc Biol, 2008. **28**(11): p. 2009-15.

[150] Allain, C.C., et al., *Enzymatic determination of total serum cholesterol.* Clin Chem, 1974. **20**(4): p. 470-5.

[151] Paigen, B., et al., *Quantitative assessment of atherosclerotic lesions in mice.* Atherosclerosis, 1987. **68**(3): p. 231-40.

[152] Plump, A.S., C.J. Scott, and J.L. Breslow, *Human apolipoprotein A-I gene expression increases high density lipoprotein and suppresses atherosclerosis in the apolipoprotein E-deficient mouse.* Proc Natl Acad Sci U S A, 1994. **91**(20): p. 9607-11.

[153] Teupser, D., et al., *Major reduction of atherosclerosis in fractalkine (CX3CL1)-deficient mice is at the brachiocephalic artery, not the aortic root.* Proc Natl Acad Sci U S A, 2004. **101**(51): p. 17795-800.

[154] Pang, Z.J., Y. Chen, and F.Q. Xing, *Effect of L929 cell-conditioned medium on antioxidant capacity in RAW264.7 cells.* Br J Biomed Sci, 2001. **58**(4): p. 212-6.

[155] Stephenson, M.L. and P.C. Zamecnik, *Inhibition of Rous sarcoma viral RNA translation by a specific oligodeoxyribonucleotide.* Proc Natl Acad Sci U S A, 1978. **75**(1): p. 285-8.

[156] Elbashir, S.M., et al., *Duplexes of 21-nucleotide RNAs mediate RNA interference in cultured mammalian cells.* Nature, 2001. **411**(6836): p. 494-8.

[157] Sachidanandam, R., et al., *A map of human genome sequence variation containing 1.42 million single nucleotide polymorphisms.* Nature, 2001. **409**(6822): p. 928-33.

[158] Venter, J.C., et al., *The sequence of the human genome.* Science, 2001. **291**(5507): p. 1304-51.

[159] Chen, X. and P.F. Sullivan, *Single nucleotide polymorphism genotyping: biochemistry, protocol, cost and throughput.* Pharmacogenomics J, 2003. **3**(2): p. 77-96.

[160] El Housni, H., et al., *Single-nucleotide polymorphism genotyping by melting analysis of dual-labeled probes: examples using factor V Leiden and prothrombin 20210A mutations.* Clin Chem, 2003. **49**(10): p. 1669-72.

[161] Dupuis, J. and D. Siegmund, *Statistical methods for mapping quantitative trait loci from a dense set of markers.* Genetics, 1999. **151**(1): p. 373-86.

[162] Ott, J., J. Wang, and S.M. Leal, *Genetic linkage analysis in the age of whole-genome sequencing.* Nat Rev Genet, 2015. **16**(5): p. 275-84.

[163] Bregman, A., et al., *Promoter elements regulate cytoplasmic mRNA decay.* Cell, 2011. **147**(7): p. 1473-83.

[164] Price, A.L., et al., *Single-tissue and cross-tissue heritability of gene expression via identity-by-descent in related or unrelated individuals.* PLoS Genet, 2011. **7**(2): p. e1001317.

[165] Adzhubei, I.A., et al., *A method and server for predicting damaging missense mutations.* Nat Methods, 2010. **7**(4): p. 248-9.

[166] Cybulsky, M.I., et al., *A major role for VCAM-1, but not ICAM-1, in early atherosclerosis.* J Clin Invest, 2001. **107**(10): p. 1255-62.

[167] Cybulsky, M.I. and M.A. Gimbrone, Jr., *Endothelial expression of a mononuclear leukocyte adhesion molecule during atherogenesis.* Science, 1991. **251**(4995): p. 788-91.

[168] Nakashima, Y., et al., *Upregulation of VCAM-1 and ICAM-1 at atherosclerosis-prone sites on the endothelium in the ApoE-deficient mouse.* Arterioscler Thromb Vasc Biol, 1998. **18**(5): p. 842-51.

[169] Galkina, E. and K. Ley, *Vascular adhesion molecules in atherosclerosis.* Arterioscler Thromb Vasc Biol, 2007. **27**(11): p. 2292-301.

[170] Gimbrone, M.A., Jr. and G. Garcia-Cardena, *Vascular endothelium, hemodynamics, and the pathobiology of atherosclerosis.* Cardiovasc Pathol, 2013. **22**(1): p. 9-15.

[171] Mestas, J. and K. Ley, *Monocyte-endothelial cell interactions in the development of atherosclerosis.* Trends Cardiovasc Med, 2008. **18**(6): p. 228-32.

[172] Tabas, I., G. Garcia-Cardena, and G.K. Owens, *Recent insights into the cellular biology of atherosclerosis.* J Cell Biol, 2015. **209**(1): p. 13-22.

[173] Bech-Serra, J.J., et al., *Proteomic identification of desmoglein 2 and activated leukocyte cell adhesion molecule as substrates of ADAM17 and ADAM10 by difference gel electrophoresis.* Mol Cell Biol, 2006. **26**(13): p. 5086-95.

[174] Garton, K.J., et al., *Stimulated shedding of vascular cell adhesion molecule 1 (VCAM-1) is mediated by tumor necrosis factor-alpha-converting enzyme (ADAM 17).* J Biol Chem, 2003. **278**(39): p. 37459-64.

[175] Tsakadze, N.L., et al., *Tumor necrosis factor-alpha-converting enzyme (TACE/ADAM-17) mediates the ectodomain cleavage of intercellular adhesion molecule-1 (ICAM-1).* J Biol Chem, 2006. **281**(6): p. 3157-64.

[176] Shi, W., et al., *TACE is required for fetal murine cardiac development and modeling.* Dev Biol, 2003. **261**(2): p. 371-80.

[177] Grell, M., et al., *The transmembrane form of tumor necrosis factor is the prime activating ligand of the 80 kDa tumor necrosis factor receptor.* Cell, 1995. **83**(5): p. 793-802.

[178] Pan, S., et al., *Etk/Bmx as a tumor necrosis factor receptor type 2-specific kinase: role in endothelial cell migration and angiogenesis.* Mol Cell Biol, 2002. **22**(21): p. 7512-23.

[179] Qiu, Y. and H.J. Kung, *Signaling network of the Btk family kinases.* Oncogene, 2000. **19**(49): p. 5651-61.

[180] Chen, S., et al., *Tyrosine kinase BMX phosphorylates phosphotyrosine-primed motif mediating the activation of multiple receptor tyrosine kinases.* Sci Signal, 2013. **6**(277): p. ra40.

[181] Kramer, A., et al., *Causal analysis approaches in Ingenuity Pathway Analysis.* Bioinformatics, 2014. **30**(4): p. 523-30.

[182] Pimentel-Muinos, F.X. and B. Seed, *Regulated commitment of TNF receptor signaling: a molecular switch for death or activation.* Immunity, 1999. **11**(6): p. 783-93.

[183] Lucas, R., et al., *Crucial role of tumor necrosis factor (TNF) receptor 2 and membrane-bound TNF in experimental cerebral malaria.* Eur J Immunol, 1997. **27**(7): p. 1719-25.

[184] Bertok, S., et al., *Characterization of TNF receptor subtype expression and signaling on pulmonary endothelial cells in mice.* Am J Physiol Lung Cell Mol Physiol, 2011. **300**(5): p. L781-9.

[185] van der Vorst, E.P., et al., *Contrasting effects of myeloid and endothelial ADAM17 on atherosclerosis development.* Thromb Haemost, 2017. **117**(3): p. 644-646.

[186] MacKenna, D.A., J.H. Omens, and J.W. Covell, *Left ventricular perimysial collagen fibers uncoil rather than stretch during diastolic filling.* Basic Res Cardiol, 1996. **91**(2): p. 111-22.

[187] Di Lullo, G.A., et al., *Mapping the ligand-binding sites and disease-associated mutations on the most abundant protein in the human, type I collagen.* J Biol Chem, 2002. **277**(6): p. 4223-31.

[188] Lattouf, R., et al., *Picrosirius red staining: a useful tool to appraise collagen networks in normal and pathological tissues.* J Histochem Cytochem, 2014. **62**(10): p. 751-8.

[189] Liu, X., et al., *Elastic fiber homeostasis requires lysyl oxidase-like 1 protein.* Nat Genet, 2004. **36**(2): p. 178-82.

[190] von Scheidt, M., et al., *Applications and Limitations of Mouse Models for Understanding Human Atherosclerosis.* Cell Metab, 2017. **25**(2): p. 248-261.

[191] Hennig, W. and A. Weyrich, *Histone modifications in the male germ line of Drosophila.* BMC Dev Biol, 2013. **13**: p. 7.

[192] Guo, F., et al., *The Transcriptome and DNA Methylome Landscapes of Human Primordial Germ Cells.* Cell, 2015. **161**(6): p. 1437-52.

[193] Margueron, R. and D. Reinberg, *Chromatin structure and the inheritance of epigenetic information.* Nat Rev Genet, 2010. **11**(4): p. 285-96.

[194] Farh, K.K., et al., *Genetic and epigenetic fine mapping of causal autoimmune disease variants.* Nature, 2015. **518**(7539): p. 337-43.

[195] Rakyan, V.K., et al., *Epigenome-wide association studies for common human diseases.* Nat Rev Genet, 2011. **12**(8): p. 529-41.

[196] Johannes, F., et al., *Assessing the impact of transgenerational epigenetic variation on complex traits.* PLoS Genet, 2009. **5**(6): p. e1000530.

[197] Ost, A., et al., *Paternal diet defines offspring chromatin state and intergenerational obesity.* Cell, 2014. **159**(6): p. 1352-64.

[198] Conway, D.E. and M.A. Schwartz, *Flow-dependent cellular mechanotransduction in atherosclerosis.* J Cell Sci, 2013. **126**(Pt 22): p. 5101-9.

[199] Hajra, L., et al., *The NF-kappa B signal transduction pathway in aortic endothelial cells is primed for activation in regions predisposed to atherosclerotic lesion formation.* Proc Natl Acad Sci U S A, 2000. **97**(16): p. 9052-7.

[200] Elices, M.J., et al., *VCAM-1 on activated endothelium interacts with the leukocyte integrin VLA-4 at a site distinct from the VLA-4/fibronectin binding site.* Cell, 1990. **60**(4): p. 577-84.

[201] Luster, A.D., R. Alon, and U.H. von Andrian, *Immune cell migration in inflammation: present and future therapeutic targets.* Nat Immunol, 2005. **6**(12): p. 1182-90.

[202] Huo, Y., A. Hafezi-Moghadam, and K. Ley, *Role of vascular cell adhesion molecule-1 and fibronectin connecting segment-1 in monocyte rolling and adhesion on early atherosclerotic lesions.* Circ Res, 2000. **87**(2): p. 153-9.

[203] Murakami, M., et al., *Cellular arachidonate-releasing function of novel classes of secretory phospholipase A2s (groups III and XII).* J Biol Chem, 2003. **278**(12): p. 10657-67.

[204] Murakami, M., et al., *A new era of secreted phospholipase A(2).* J Lipid Res, 2015. **56**(7): p. 1248-61.

[205] Rosenson, R.S. and E. Hurt-Camejo, *Phospholipase A2 enzymes and the risk of atherosclerosis.* Eur Heart J, 2012. **33**(23): p. 2899-909.

[206] Burke, J.E. and E.A. Dennis, *Phospholipase A2 biochemistry.* Cardiovasc Drugs Ther, 2009. **23**(1): p. 49-59.

[207] Shridas, P. and N.R. Webb, *Diverse Functions of Secretory Phospholipases A2.* Advances in Vascular Medicine, 2014. **2014**: p. 11.

[208] Murase, R., et al., *Group X Secreted Phospholipase A2 Releases omega3 Polyunsaturated Fatty Acids, Suppresses Colitis, and Promotes Sperm Fertility.* J Biol Chem, 2016. **291**(13): p. 6895-911.

[209] Sato, H., et al., *The adipocyte-inducible secreted phospholipases PLA2G5 and PLA2G2E play distinct roles in obesity.* Cell Metab, 2014. **20**(1): p. 119-32.

[210] Taketomi, Y., et al., *Mast cell maturation is driven via a group III phospholipase A2-prostaglandin D2-DP1 receptor paracrine axis.* Nat Immunol, 2013. **14**(6): p. 554-63.

[211] Yamamoto, K., et al., *The role of group IIF-secreted phospholipase A2 in epidermal homeostasis and hyperplasia.* J Exp Med, 2015. **212**(11): p. 1901-19.

[212] Cormier, R.T., et al., *Secretory phospholipase Pla2g2a confers resistance to intestinal tumorigenesis.* Nat Genet, 1997. **17**(1): p. 88-91.

[213] Saegusa, J., et al., *Pro-inflammatory secretory phospholipase A2 type IIA binds to integrins alphavbeta3 and alpha4beta1 and induces proliferation of monocytic cells in an integrin-dependent manner.* J Biol Chem, 2008. **283**(38): p. 26107-15.

[214] Fujita, M., et al., *Proinflammatory secreted phospholipase A2 type IIA (sPLA-IIA) induces integrin activation through direct binding to a newly identified binding site (site 2) in integrins alphavbeta3, alpha4beta1, and alpha5beta1.* J Biol Chem, 2015. **290**(1): p. 259-71.

[215] Gelb, M.H., et al., *Cloning and recombinant expression of a structurally novel human secreted phospholipase A2.* J Biol Chem, 2000. **275**(51): p. 39823-6.

[216] Singer, A.G., et al., *Interfacial kinetic and binding properties of the complete set of human and mouse groups I, II, V, X, and XII secreted phospholipases A2.* J Biol Chem, 2002. **277**(50): p. 48535-49.

[217] Welch, C.L., et al., *Localization of atherosclerosis susceptibility loci to chromosomes 4 and 6 using the Ldlr knockout mouse model.* Proc Natl Acad Sci U S A, 2001. **98**(14): p. 7946-51.

[218] Nicholls, S.J., et al., *Varespladib and cardiovascular events in patients with an acute coronary syndrome: the VISTA-16 randomized clinical trial.* JAMA, 2014. **311**(3): p. 252-62.

[219] Canault, M., et al., *The TNF alpha converting enzyme (TACE/ADAM17) is expressed in the atherosclerotic lesions of apolipoprotein E-deficient mice: possible contribution to elevated plasma levels of soluble TNF alpha receptors.* Atherosclerosis, 2006. **187**(1): p. 82-91.

[220] Satoh, M., et al., *Expression of tumor necrosis factor-alpha--converting enzyme and tumor necrosis factor-alpha in human myocarditis.* J Am Coll Cardiol, 2000. **36**(4): p. 1288-94.

[221] Satoh, M., et al., *Increased expression of tumor necrosis factor-alpha converting enzyme and tumor necrosis factor-alpha in peripheral blood mononuclear cells in patients with advanced congestive heart failure.* Eur J Heart Fail, 2004. **6**(7): p. 869-75.

[222] Satoh, M., et al., *The expression of TNF-alpha converting enzyme at the site of ruptured plaques in patients with acute myocardial infarction.* Eur J Clin Invest, 2008. **38**(2): p. 97-105.

[223] Sunnarborg, S.W., et al., *Tumor necrosis factor-alpha converting enzyme (TACE) regulates epidermal growth factor receptor ligand availability.* J Biol Chem, 2002. **277**(15): p. 12838-45.

[224] Bradley, J.R., S. Thiru, and J.S. Pober, *Disparate localization of 55-kd and 75-kd tumor necrosis factor receptors in human endothelial cells.* Am J Pathol, 1995. **146**(1): p. 27-32.

[225] Vandenabeele, P., et al., *Two tumour necrosis factor receptors: structure and function.* Trends Cell Biol, 1995. **5**(10): p. 392-9.

[226] Higuchi, M. and B.B. Aggarwal, *TNF induces internalization of the p60 receptor and shedding of the p80 receptor.* J Immunol, 1994. **152**(7): p. 3550-8.

[227] Fischer, R., et al., *Ligand-induced internalization of TNF receptor 2 mediated by a di-leucin motif is dispensable for activation of the NFkappaB pathway.* Cell Signal, 2011. **23**(1): p. 161-70.

[228] Schreyer, S.A., C.M. Vick, and R.C. LeBoeuf, *Loss of lymphotoxin-alpha but not tumor necrosis factor-alpha reduces atherosclerosis in mice.* J Biol Chem, 2002. **277**(14): p. 12364-8.

[229] Branen, L., et al., *Inhibition of tumor necrosis factor-alpha reduces atherosclerosis in apolipoprotein E knockout mice.* Arterioscler Thromb Vasc Biol, 2004. **24**(11): p. 2137-42.

[230] Canault, M., et al., *Exclusive expression of transmembrane TNF-alpha in mice reduces the inflammatory response in early lipid lesions of aortic sinus.* Atherosclerosis, 2004. **172**(2): p. 211-8.

[231] Ohta, H., et al., *Disruption of tumor necrosis factor-alpha gene diminishes the development of atherosclerosis in ApoE-deficient mice.* Atherosclerosis, 2005. **180**(1): p. 11-7.

[232] Xiao, N., et al., *Tumor necrosis factor-alpha deficiency retards early fatty-streak lesion by influencing the expression of inflammatory factors in apoE-null mice.* Mol Genet Metab, 2009. **96**(4): p. 239-44.

[233] Boesten, L.S., et al., *Tumor necrosis factor-alpha promotes atherosclerotic lesion progression in APOE*3-Leiden transgenic mice.* Cardiovasc Res, 2005. **66**(1): p. 179-85.

[234] Chandrasekharan, U.M., et al., *Decreased atherosclerosis in mice deficient in tumor necrosis factor-alpha receptor-II (p75).* Arterioscler Thromb Vasc Biol, 2007. **27**(3): p. e16-7.

[235] Loetscher, H., et al., *Human tumor necrosis factor alpha (TNF alpha) mutants with exclusive specificity for the 55-kDa or 75-kDa TNF receptors.* J Biol Chem, 1993. **268**(35): p. 26350-7.

[236] Tartaglia, L.A., et al., *A novel domain within the 55 kd TNF receptor signals cell death.* Cell, 1993. **74**(5): p. 845-53.

[237] Micheau, O. and J. Tschopp, *Induction of TNF receptor I-mediated apoptosis via two sequential signaling complexes.* Cell, 2003. **114**(2): p. 181-90.

[238] Grell, M., et al., *TNF receptor type 2 mediates thymocyte proliferation independently of TNF receptor type 1.* Eur J Immunol, 1998. **28**(1): p. 257-63.

[239] Tartaglia, L.A., et al., *The two different receptors for tumor necrosis factor mediate distinct cellular responses.* Proc Natl Acad Sci U S A, 1991. **88**(20): p. 9292-6.

[240] Fontaine, V., et al., *Neurodegenerative and neuroprotective effects of tumor Necrosis factor (TNF) in retinal ischemia: opposite roles of TNF receptor 1 and TNF receptor 2.* J Neurosci, 2002. **22**(7): p. RC216.

[241] Shen, Y., R. Li, and K. Shiosaki, *Inhibition of p75 tumor necrosis factor receptor by antisense oligonucleotides increases hypoxic injury and beta-amyloid toxicity in human neuronal cell line.* J Biol Chem, 1997. **272**(6): p. 3550-3.

[242] Stoneman, V.E. and M.R. Bennett, *Role of apoptosis in atherosclerosis and its therapeutic implications.* Clin Sci (Lond), 2004. **107**(4): p. 343-54.

[243] Kitagawa, K., et al., *Involvement of ICAM-1 in the progression of atherosclerosis in APOE-knockout mice.* Atherosclerosis, 2002. **160**(2): p. 305-10.

[244] Kirii, H., et al., *Lack of interleukin-1beta decreases the severity of atherosclerosis in ApoE-deficient mice.* Arterioscler Thromb Vasc Biol, 2003. **23**(4): p. 656-60.

[245] Dekkers, P.E., et al., *The effect of a metalloproteinase inhibitor (GI5402) on tumor necrosis factor-alpha (TNF-alpha) and TNF-alpha receptors during human endotoxemia.* Blood, 1999. **94**(7): p. 2252-8.

[246] Grootveld, M. and M.F. McDermott, *BMS-561392. Bristol-Myers Squibb.* Curr Opin Investig Drugs, 2003. **4**(5): p. 598-602.

[247] Zhou, B.B., et al., *Targeting ADAM-mediated ligand cleavage to inhibit HER3 and EGFR pathways in non-small cell lung cancer.* Cancer Cell, 2006. **10**(1): p. 39-50.

[248] Fridman, J.S., et al., *Selective inhibition of ADAM metalloproteases as a novel approach for modulating ErbB pathways in cancer.* Clin Cancer Res, 2007. **13**(6): p. 1892-902.

[249] Thabet, M.M. and T.W. Huizinga, *Drug evaluation: apratastat, a novel TACE/MMP inhibitor for rheumatoid arthritis.* Curr Opin Investig Drugs, 2006. **7**(11): p. 1014-9.

[250] Morimoto, Y., K. Nishikawa, and M. Ohashi, *KB-R7785, a novel matrix metalloproteinase inhibitor, exerts its antidiabetic effect by inhibiting tumor necrosis factor-alpha production.* Life Sci, 1997. **61**(8): p. 795-803.

[251] Moss, M.L., L. Sklair-Tavron, and R. Nudelman, *Drug insight: tumor necrosis factor-converting enzyme as a pharmaceutical target for rheumatoid arthritis.* Nat Clin Pract Rheumatol, 2008. **4**(6): p. 300-9.

[252] Arribas, J. and C. Esselens, *ADAM17 as a therapeutic target in multiple diseases.* Curr Pharm Des, 2009. **15**(20): p. 2319-35.

[253] Ban, L., et al., *Selective death of autoreactive T cells in human diabetes by TNF or TNF receptor 2 agonism.* Proc Natl Acad Sci U S A, 2008. **105**(36): p. 13644-9.

[254] Faustman, D. and M. Davis, *TNF receptor 2 pathway: drug target for autoimmune diseases.* Nat Rev Drug Discov, 2010. **9**(6): p. 482-93.

[255] Roubille, C., et al., *The effects of tumour necrosis factor inhibitors, methotrexate, non-steroidal anti-inflammatory drugs and corticosteroids on cardiovascular events in rheumatoid arthritis, psoriasis and psoriatic arthritis: a systematic review and meta-analysis.* Ann Rheum Dis, 2015. **74**(3): p. 480-9.

[256] Dou, H., et al., *Role of Adipose Tissue Endothelial ADAM17 in Age-Related Coronary Microvascular Dysfunction.* Arterioscler Thromb Vasc Biol, 2017. **37**(6): p. 1180-1193.

[257] Fan, D., et al., *A Disintegrin and Metalloprotease-17 Regulates Pressure Overload-Induced Myocardial Hypertrophy and Dysfunction Through Proteolytic Processing of Integrin beta1.* Hypertension, 2016. **68**(4): p. 937-48.

[258] Ingber, D.E., *Mechanical signaling and the cellular response to extracellular matrix in angiogenesis and cardiovascular physiology.* Circ Res, 2002. **91**(10): p. 877-87.

[259] Takagi, H. and T. Umemoto, *Matrix metalloproteinases synthesized in autosomal dominant polycystic kidney disease play a role in development of a concurrent abdominal aortic aneurysm.* Med Hypotheses, 2005. **64**(4): p. 778-81.

[260] Lu, H. and M. Aikawa, *Many faces of matrix metalloproteinases in aortic aneurysms.* Arterioscler Thromb Vasc Biol, 2015. **35**(4): p. 752-4.

[261] Kahari, V.M., et al., *Tumor necrosis factor-alpha down-regulates human elastin gene expression. Evidence for the role of AP-1 in the suppression of promoter activity.* J Biol Chem, 1992. **267**(36): p. 26134-41.

[262] Rodriguez, C., et al., *Lysyl oxidase (LOX) down-regulation by TNFalpha: a new mechanism underlying TNFalpha-induced endothelial dysfunction.* Atherosclerosis, 2008. **196**(2): p. 558-64.

[263] Lindsay, M.E. and H.C. Dietz, *The genetic basis of aortic aneurysm.* Cold Spring Harb Perspect Med, 2014. **4**(9): p. a015909.

[264] Jeremy, R.W., et al., *Perturbations of mechanotransduction and aneurysm formation in heritable aortopathies.* Int J Cardiol, 2013. **169**(1): p. 7-16.

Publications

Nicolaou, A., Zhao, Z, Northoff, B.H., Kohlmaier, A., Sass K., Rose-John, S., Steffens, S., Weber, C., Teupser, D., Holdt, L.M. (2017). ***The* ADAM17 *Metalloprotease Maintains Arterial Elasticity. Thromb Haemost. 2018; 118(1): 210-213.***

Nicolaou, A., Northoff, B.H., Sass, K., Ernst, J., Kohlmaier, A., Krohn, K., Wolfrum, C., Teupser, D., Holdt, L.M. (2017). ***Quantitative trait locus mapping in mice identifies phospholipase Pla2g12a as novel atherosclerosis modifier. Atherosclerosis 265: 197-206.***

Nicolaou, A., Zhao, Z., Northoff, B.H., Sass, K., Herbst, A., Kohlmaier, A., Chalaris, A., Wolfrum, C., Weber, C., Steffens, S., Rose-John S., Teupser D., Holdt, L.M. (2017). ***Adam17 Deficiency Promotes Atherosclerosis by Enhanced TNFR2 Signaling in Mice. Arteriosclerosis, thrombosis, and vascular biology 37, 247-257.***

Holdt, L.M., Stahringer, A., Sass, K., Pichler, G., Kulak, N.A., Wilfert, W., Kohlmaier, A., Herbst, A., Northoff, B.H., **Nicolaou, A.,** Gäbel G., Beutner F., Scholz M., Thiery J., Musunuru K., Krohn K., Mann M., Teupser D. (2016). ***Circular non-coding RNA ANRIL modulates ribosomal RNA maturation and atherosclerosis in humans. Nature communications 7, 12429.***

Holdt, L.M., von Delft, A., **Nicolaou, A.,** Baumann, S., Kostrzewa, M., Thiery, J., Teupser, D. (2013). ***Quantitative trait loci mapping of the mouse plasma proteome (pQTL). Genetics 193, 601-608.***

Presentations

Lecture Presentations

Adam17-Deficiency Promotes Atherosclerosis in a Mouse Model by Enhanced TNFR2 Signaling

Alexandros Nicolaou, Bernd Henrik Northoff, Andreas Herbst, Kristina Sass, Joachim Thiery, Stefan Rose-John, Daniel Teupser, Lesca Miriam Holdt

13th Annual Meeting of the German Society for Clinical Chemistry and Laboratory Medicine (DGKL), Mannheim, 28th-30th September 2016

Poster Presentations

Identification of Cd5l and Fcrl1 as Potential Candidate Genes of Atherosclerosis Susceptibility in Mice and Men.

Alexandros Nicolaou, Lesca M. Holdt, Markus Scholz, Janja Nahrstaedt, Inke König, Jeanette Erdmann, Heribert Schunkert, Joachim Thiery, Daniel Teupser

8th Leipzig Research Festival for Life Sciences,
Leipzig, 18th December 2009

Identification of Elovl6 as Novel Candidate Gene of Atherosclerosis Susceptibility in Mice.

Alexandros Nicolaou, Lesca M. Holdt, Joachim Thiery, Daniel Teupser

9th Leipzig Research Festival for Life Sciences,
Leipzig, 17th December 2010

Elovl6 a Novel Candidate Gene of Atherosclerosis Susceptibility in Mice and Men

Alexandros Nicolaou, Lesca M. Holdt, Uta Ceglarek, Andreas Peter, Joachim Thiery, Daniel Teupser

17th Lipid Meeting Leipzig,
Leipzig, 09th-10th December 2011

Identification of Elovl6 as a Candidate Gene of Atherosclerosis Susceptibility in Mice and Men.

Alexandros Nicolaou, Lesca M. Holdt, Daniel Teupser

10th Leipzig Research Festival for Life Sciences,
Leipzig, 16th December 2011

Novel Candidate Genes of Atherosclerosis Susceptibility at Mouse Chromosome 3

Alexandros Nicolaou, Joachim Thiery, Daniel Teupser, Lesca M. Holdt

9th Annual Meeting of the German Society for Clinical Chemistry and Laboratory Medicine (DGKL), Mannheim, 26th-29th September 2012

Pla2g12a and Elovl6 as Novel Candidate Genes of Atherosclerosis Susceptibility in Mouse Chromosome 3

Alexandros Nicolaou, Kristina Sass, Bernd H. Northoff, Joachim Thiery, Daniel Teupser, Lesca M. Holdt

10th Annual Meeting of the German Society for Clinical Chemistry and Laboratory Medicine (DGKL), Dresden, 23th-26th October 2013

The Effects of Metalloproteinase ADAM17 on Atherosclerosis

Alexandros Nicolaou, Kristina Sass, Bernd H. Northoff, Joachim Thiery, Stefan Rose-John, Daniel Teupser, Lesca M. Holdt

18th Lipid Meeting Leipzig,
Leipzig, 05th-0th December 2013

Identification of two Novel Candidate Genes of Atherosclerosis Susceptibility on Mouse Chromosome 3: Pla2g12a and Elovl6

Alexandros Nicolaou, Kristina Sass, Bernd H. Northoff, Daniel Teupser, Lesca M. Holdt

Arteriosclerosis, Thrombosis, and Vascular Biology 2014 Scientific Sessions,
Toronto, 01th-03th May 2014

The Role of Metalloproteinase ADAM17 in Atherosclerosis

Alexandros Nicolaou, Bernd-Henrik Northoff, Kristina Sass, Joachim Thiery, Stefan Rose-John, Daniel Teupser, Lesca Miriam Holdt

11th Annual Meeting of the German Society for Clinical Chemistry and Laboratory Medicine (DGKL), Mannheim, 24th-27th September 2014

Enhanced TNFR2 Signaling in Hypomorphic Adam17-Deficient Mice

Alexandros Nicolaou, Bernd Henrik Northoff, Andreas Herbst, Kristina Sass, Joachim Thiery, Stefan Rose-John, Daniel Teupser, Lesca Miriam Holdt

12th Annual Meeting of the German Society for Clinical Chemistry and Laboratory Medicine (DGKL), Leipzig, 14th-17th October 2015

Awards

Poster Awards

Identification of Cd5l and Fcrl1 as Potential Candidate Genes of Atherosclerosis Susceptibility in Mice and Men.

Alexandros Nicolaou, Lesca M. Holdt, Markus Scholz, Janja Nahrstaedt, Inke König, Jeanette Erdmann, Heribert Schunkert, Joachim Thiery, Daniel Teupser

8th Leipzig Research Festival for Life Sciences,
Leipzig, 18th December 2009

Acknowledgements

Firstly, I would like to express my sincere gratitude to Prof. Dr. med. Daniel Teupser for the opportunity to do my doctoral thesis at the Institute of Laboratory Medicine of the University Hospital Munich and the excellent support through all the years.

At the same moment I would like to thank Ms. Prof. Dr. med. Dr. rer. nat. Lesca M. Holdt without whom the present work would not have been possible. The excellent support as well as the regular critical discussions and the many helpful suggestions have contributed decisively to my work. Her enthusiasm for scientific work, her patience, motivation, and immense knowledge was a continuous support of my Ph.D study. Lesca, you have been a great advisor and mentor for my Ph.D study.

I would like to thank Wolfgang Wilfert, Bernd Northoff and Anika Stahringer who have accompanied me during my entire time at the institute.

I would like to thank Bernd Northoff for the endless hours in the preparation of mice, the trips to Switzerland and all the stimulating discussions.

Anika Stahringer, the good soul of the cell culture, who helped me with the planning, design and execution of complicated cell culture experiments.

I would like to thank Wolfgang Wilfert, the “man of all jobs” who satisfied nearly all my requests in the lab. Without your cooperation many experiments could not have been realized. Thank you for your help and friendship.

Kristina Sass who showed me the world of immunohistochemistry.

Alexander Kohlmaier, thank you for correcting the manuscript of my thesis and the published manuscripts; for your helpful and interesting suggestions.

My neighbor in the last years Andreas Herbst for all the stimulating discussions and the constructive criticism in the preparation of the publications.

Last but not the least, I would like to thank my parents for their continued support and my life partner Franziska for the support and the patience over the whole years.

Affidavit / Eidesstattliche Versicherung

Ich erkläre hiermit an Eides statt, dass ich die vorliegende Dissertation mit dem Thema

„Identification of novel atherosclerosis modifiers in mice“

selbstständig verfasst, mich außer der angegebenen keiner weiteren Hilfsmittel bedient und alle Erkenntnisse, die aus dem Schrifttum ganz oder annähernd übernommen sind, als solche kenntlich gemacht und nach ihrer Herkunft unter Bezeichnung der Fundstelle einzeln nachgewiesen habe.

Ich erkläre des Weiteren, dass die hier vorgelegte Dissertation nicht in gleicher oder ähnlicher Form bei einer anderen Stelle zur Erlangung eines akademischen Grades eingereicht wurde.

München, den 01.10.2019

Alexandros Nicolaou

Appendix

TABLE 28: Antibodies and their dilutions used for Western blot (WB) and immunohistochemistry (IHC).

Antibody	Supplier	Catalogue number	Primary/secondary antibody	Mono-/ polyclonal	Host	Dilution	WB	IHC
ADAM17	Abcam	ab2051	primary	p	Rabbit	1:1000	+	
TNF-α	Abcam	ab9739	primary	p	Rabbit	1:500	+	
PLA2G12A	Proteintech	160009-1-AP	primary	p	Rabbit	1:500	+	+
ELOVL6	BioCat	AP6524a	Primary	p	Rabbit	1:500	+	+
Na+/K+-ATPase	Cell Signaling	#3010S	primary	p	Rabbit	1:1000	+	
TNFR1	Abcam	ab64006	primary	p	Rabbit	1:3000	+	
TNFR2	Novus Biologicals	H7133-D01P	primary	p	Rabbit	1:1000	+	
BMX	Santa Cruz	sc-8874	primary	p	Goat	1:1000	+	
pBMX	Origene	TA325277	primary	p	Rabbit	1.500	+	
GAPDH	Fitzgerald	10R-G109a	primary	m	Mouse	1:10000	+	
Peroxidase labeled Anti Mouse	Vector laboratories	PI-2000	secondary	p	Horse	1:6000	+	
Peroxidase labeled Anti Rabbit	Vector laboratories	PI-1000	secondary	p	Goat	1:6000	+	
α-SMA	Abcam	ab5694	primary	p	Rabbit	1:200		+
CD68	Serotec	MCA1957	primary	m	Rat	1:10		+
vWF	DakoCytomation	A0082	primary	p	Rabbit	1:200		+
STAR72	Serotec	-	secondary	p	Goat	1:50		+
Anti-rabbit Ig	Vector laboratories	MP-7401	secondary	-	Rabbit	undiluted		+
Anti-mouse Ig	Vector laboratories	MP-7402	secondary	-	Mouse	undiluted		+

TABLE 29: Primers and TaqMan probes used for the qRT-PCR (*: 6-FAM; # TAMRA).

Gene	NM Number	Primer Probes	Sequence
Fdps	NM_134469.3	5′- primer	5′-TGTAAGCCGCAAACATCTTG-3′
		3′- primer	5′-CAATTTCTGGTTTCCCATTCATT-3′
		probe	5′*-CCGGGAGAATCCGCGTTGAAGAACA-#3′
Pklr	NM_001099779	5′- primer	5′-GTGGAGGCTTCCTTCAAGTG-3′
	NM_013631	3′- primer	5′-AGGTCGGTAGCGAGACAGAA-3′
		probe	5′*-TGTGCCGCAGCCATCATTGTGCT-#3′
Pmvk	NM_026784	5′- primer	5′-GAGGTAACATCTGTGCTCTCCTG-3′
	NM_027348	3′- primer	5′-GGAAGTCCAAGCCATGCTC-3′
		probe	5′*-TCTCTGGTCCACTCAAGGAGGAGTATGCTCG-3′
Them4	NM_029431	5′- primer	5′-TGCTGAGAAACTGCGCTATG-3′
		3′- primer	5′-GACTTTCTCAGAAGAAAATAACCTCCT-3′
		probe	5′*-CCTGCGCACTCTTGGGGCCAC-#3′
Selenbp2	NM_019414	5′- primer	5′-TCTCCAGGGTAATGGCAAAG-3′
		3′- primer	5′-GTAGCCCATTGGAGATGCAC-3′
		probe	5′*-TGCTGCTGGATGGGGAGACCTTCG-#3′
Gm129	NM_001033302	5′- primer	5′-AGGTAGCCGGCACCAGAT-3′
		3′- primer	5′-TTTGGCCCATCTTCTCTAGG-3′
		probe	5′*-CAAGCACTTTCCCAGCCACCACGGT-#3′
Vcam1	NM_011693.3	5′- primer	5′-CTCTGGGAAGCTGGAACGAAG-3′
		3′- primer	5′-CCAGGGGGCCACTGAATTGAATC-3′
		probe	5′*-CCACGTGGACATCTACTCTTTCCCCAAGG-#3′
Abcd3	NM_008991	5′- primer	5′-AGCACAAGCTAGTCCCTTGG-3′
		3′- primer	5′-TTGCTAAAGGAACATGATCAAACT-3′
		probe	5′*-CCCTGGTGCTGGAGAAATCATCAATACAGACAC-#3′
Elovl6	NM_130450	5′- primer	5′-CAGCAAAGCACCCGAACTA-3′
		3′- primer	5′-AGGAGCACAGTGATGTGGTG-3′
		probe	5′*-CTGAGGAAACAGAAACTGATCTTCCTGCACTGG-#3′
Pla2g12a	NM_023196	5′- primer	5′-TGAGCTCTAGGAATGACGGGTTTAA-3′
	NM_183423	3′- primer	5′-TAGAAGATGGAAAACGGGGATGAG-3′
		probe	5′*-CTGTGCGCTATCTGCTGCTGAGGTTGTG-#3′
Agxt2l1	NM_027907	5′- primer	5′-CAGCTCGGGCATGGAATA-3′
	NM_001163587	3′- primer	5′-AGCACAGCCAAGCCAACT-3′
		probe	5′*-TCAATACGTATGGAGGAAATCCAGTGTCTTGTGC-3′
Adh7	NM_009626	5′- primer	5′-AGAAGACGTTCCTGTTTGCAG-3′
		3′- primer	5′-ACAGCCGCTTTGCACTTAAT-3′
		probe	5′*-CACACACCCAGGAGAGGCAGGATGG-#3′
Adh4	NM_011996	5′- primer	5′-ACAAACCTCTGTGGAAAACTCC-3′
		3′- primer	5′-AAATTGATCTTCCTTTGCAGGT-3′
		probe	5′*-ACTATTGATCAGGAGCTCATGGAAGACAGAACCA-#3′
Gbp3	NM_018734	5′- primer	5′-TGGAGAGCGAAAAGGAGATG-3′
		3′- primer	5′-TGAATCCTTCAATAAGCAGTTCTTC-3′
		probe	5′*-AGGGAGCAGGAGAAGATGCTGGAGCAC-#3′

Gene	NM Number	Primer Probes	Sequence
Ccbl2	NM_173763	5′- primer	5′-ATTCAAAAACGCCAAACGAA-3′
		3′- primer	5′-AGGATCCGCAGCCAACTTA-3′
		probe	5′*-AGGCCTGGACAGCAATGTGTGGGTTG-#3′
Acadm	NM_007382	5′- primer	5′-TGTCGAACACAACACTCGAAA-3′
		3′- primer	5′-CTGCTGTTCCGTCAACTCAA-3′
		probe	5′*-CTCACAAGCAGGAGCCCGGATTAGGGT-#3′
Cth	NM_145953.2	5′- primer	5′-GAGGATGAACAGGACCTTCTTG-3′
		3′- primer	5′-CAGCTTTGACTCGAACTTTTAAGG-3′
		probe	5′*-ACCTGGATCGAGCTTTGAAGGCAGCG-#3′
Adam17	NM_009615.4	5’-primer	5’-GGAAAGGGAAGCCATGTACAGTAG-3’
		3’-primer	5’-CGCTCAATTACGTCCTGTACTCG-3’
		probe	5’F-GCGACATGAATGGCAAATGTGAGAAACG-3’T
TNF-α	NM_013693	5’-primer	5’-CCACCACGCTCTTCTGTCTACTG-3’
		3’-primer	5’-TGGGCCATAGAACTGATGAGAGG-3’
	NM_001278601	probe	5’F-CGGTCCCCAAAGGGATGAGAAGTTCCC-3’T
Tnfrsf1a	NM_011609.4	5’-primer	5’-GCCCGAAGTCTACTCCATCATTTG-3’
		3’-primer	5’-GCTGAAGGCTGGGGAGGG-3’
		probe	5’F-CGTGCCTGTCAAAGAGGAGAAGGCTGGA-3’T
Tnfrsf1b	NM_011610.3	5’-primer	5’-CAGTTTCGTACATGTTTGAGCTGC-3’
		3’-primer	5’-CACACACTCGGTTCTGCTGTTTAG-3’
		probe	5’F-TACCACTGACCAGGTGGAGATCCGCG-3’T
Gapdh	NM_001289726	5’-primer	5’-TGTCCGTCGTGGATCTGACG-3’
		3’-primer	5’-CCAAGATGCCCTTCAGTGGG-3’
		probe	5’F-GGCCTGGAGAAACCTGCCAAGTATGATGAC-3’T
Icam1	NM_010493	5’-primer	5’-CCCACGCTACCTCTGCTC-3’
		3’-primer	5’-GATGGATACCTGAGCATCACC-3’
		probe	5’-TGGCCCTGGTCACCGTTGTGATCCCT-3’
Lox	NM_010728.2	5’-primer	5’-CTCCTGGGAGTGGCACAG-3’
		3’-primer	5’-CTTGCTTTGTGGCCTTCAGC-3’
		probe	5’-CAGCCACTATGACCTGCTTGATGCCAACAC-3’
β-Actin		5’-primer	5’-GAGAAGCTGTGCTATGTTGCTC-3’
		3’-primer	5’-AGGAAGAGGATGCGGCA-3’
		probe	5’-AGACTTCGAGCAGGAGATGGCCA -3’

TABLE 30: SNPs, bp position, primers and probes used for genotyping (*: 6-FAM; # TAMRA).

SNP	Mbp	Primer/Probes	Sequence
rs4224041	87	5′- primer	5′-CATTCCCTCTCAAGTGTTCCTCATGT-3′
		3′- primer	5′-CCTCGAAAGAGTCTGAACATTGTGTTC-3′
		probe	5′*-TTGGTGAACAGCCCCCA-#3′
rs3683384	110	5′- primer	5′-TGTCACTCTCAGAATTGCCTAGGCAG-3′
		3′- primer	5′-ATCTGACACCTCCCCATCCCTATC-3′
		probe	5′*-TAGGCACCCAAGACTTGAG-#3′
rs13459071	115	5′- primer	5′-CTGTCTAGCTGCTCCACCGTGC-3′
		3′- primer	5′-TTGGTACCTGAGTTCAGCACAGCC-3′
		probe	5′*-TGATCATTGTCCTGAGTGTCT-#3′
rs30132365	116 (*Vcam1*)	5′- primer	5′-GCACAAGTAGGCTTTTGGCTTCTGTT-3′
		3′- primer	5′-TGTGGTCTCCATCATCCAAGGTCAT-3′
		probe	5′*-TGGTTTGTGGCAAACACAG-#3′
rs36523879	122	5′- primer	5′-ATGTATTCACTTTGCAGCCCTAGGATG-3′
		3′- primer	5′-ACGGTAGGACGGGAAGCTATTCTTTC-3′
		probe	5′*-GATACAGAAGTCCCAAACCCA-#3′
rs13424644	129.3 (*Elovl6*)	5′- primer	5′-TCTTTGACTATTGGATTGCCTCAGTGTC-3′
		3′- primer	5′-TTCTGGGCTGTCATCATGATCTCC-3′
		probe	5′*-CGATCCTGCCAATGCAACT-#3′
rs30635946	129.6 (*Pla2g12a*)	5′- primer	5′-CAGGAAAAGCCTTGCTGAAGTGTGA-3′
		3′- primer	5′-TCAGAAAGCTCAATACCCACCAACCA-3′
		probe	5′*-CTCTTCACGGCACACCC-#3′
rs31282710	130	5′- primer	5′-CATTGGGAAAGTGTTAGCAGCAAACC-3′
		3′- primer	5′-ACTTCTAAGCCCAACGCTCATTCCAT-3′
		probe	5′*-ACAAATAAGATCGCATTGTCTGT-#3′
rs30359806	140	5′- primer	5′-AGAGACTTAGTAATTGCTCCTCATTCCTG-3′
		3′- primer	5′-TAGTCAAGCTGTAATTCTGCCAGTTAATG-3′
		probe	5′*-TATCACCAGGGTCCATACGA-#3′
rs30102565	150	5′- primer	5′-CTTGATATCATGCCAATTGCTCTGTCAT-3′
		3′- primer	5′-TGTAGGAAATAGCAGGCTTCTCAAGGT-3′
		probe	5′*-CATTATTTGGCACATTCTTCCT-#3′
rs31598641	160	5′- primer	5′-CTTCCTCATTTATCAAGGATACTCCCCTC-3′
		3′- primer	5′-TATTCCTGTCTGACAATCATGGCTAATGA-3′
		probe	5′*-GGAATTCATACAACAGGTTGAG-#3′